UNIVERSITÉ DU QUÉBEC

IMPACTS DE L'HÉTÉROGÉNÉITÉ DU PAYSAGE SUR LE COUVERT NIVAL DES ENVIRONNEMENTS AGRO-FORESTIERS ET BORÉALS DANS L'EST DU CANADA

IMPACT OF LANDSCAPE HETEROGENEITY ON SNOW COVER IN AGRO-FORESTED AND BOREAL ENVIRONMENTS IN EASTERN CANADA

THÈSE PRÉSENTÉE
COMME EXIGENCE PARTIELLE DU
DOCTORAT EN SCIENCES DE L'ENVIRONNEMENT

OFFERT PAR L'UNIVERSITÉ DU QUÉBEC À MONTRÉAL
EN ASSOCIATION AVEC
L'UNIVERSITÉ DU QUÉBEC À TROIS-RIVIÈRES

PAR
VASANA SANDAMALI DHARMADASA

JUILLET 2023

UNIVERSITÉ DU QUÉBEC

DOCTORAT EN SCIENCES DE L'ENVIRONNEMENT (PH. D.)

Programme offert par l'Université du Québec à Montréal (UQAM)

en association avec

l'Université du Québec à Chicoutimi (UQAC)

l'Université du Québec à Rimouski (UQAR)

l'Université du Québec en Abitibi-Témiscamingue (UQAT)

et l'Université du Québec à Trois-Rivières (UQTR)

Direction de recherche :

Christophe Kinnard	Directeur de recherche
Michel Baraër	Codirecteur de recherche

Jury d'évaluation :

Christophe Kinnard	Directeur de recherche
Michel Baraër	Codirecteur de recherche
Karem Chokmani	Président de jury
John Pomeroy	Évaluateur externe
Vincent Vionnet	Évaluateur externe

Thèse soutenue le 12 juin 2023

DEDICATION

ලොකු මිනිහෙකු නොව,
හොඳ මිනිහෙකු වන්නට කියා දුන්,
ආදරණීය අම්මාට සහ තාත්තාට

To my parents,
Thank you for believing in me!

ACKNOWLEDGEMENTS

First, I would like to thank Christophe Kinnard for giving me the opportunity to work as a PhD student under his supervision in Canada. I am grateful to both my supervisors, Christophe Kinnard and Michel Baraër for their guidance, support, advices, encouragements, and for always being available for all my queries for the past several years. It has been a great pleasure working with you!

I am also thankful to the members of the jury, John Pomeroy, Vincent Vionnet, and Karem Chokmani for allocating their time to evaluate my dissertation.

I extend my sincere thanks to Catarina Leote F. Pio for her exceptional problem-solving skills and technical support throughout my PhD journey.

A special thanks to Pierre-Andre Bordeleau for all the support he provided with drone-related things.

To all my friends in GlacioLab, thank you for your technical and moral support, and all the beautiful and memorable moments we shared on and off the field; Hadi, Okan, Saida, Lisane, Hafsa, Ghada, Matthieu, Maxime, Arthur, Shahab, Amex, and Olivier. Specially Okan and Hadi, thank you for always being there for me, this journey would have been much harder without you guys. Thank you, Lizzie, for being an awesome housemate and friend, and introducing me to the joys of gardening. Thank you, Maxime and Pumba, for all the nice times, and especially for helping me overcome my fear of dogs! Thank you, Hung, for all the good and fun discussions of random forest modeling and R. To Darshil, Vrutti, Rushali, Sameera, Varun, and Anjali; thank you for bringing

home a little closer to heart. To my Sri Lankan friends; Sue, Pavi, Kumudu, Jeewa, Prash, and Mano, thank you for your encouragement and love regardless of where you are.

To Saida, who will always be remembered as one of the most beautiful and strong women I have ever met in my life, rest in peace, my dear friend.

To my family, I am always grateful for your endless support and unconditional love. To my better half, Nimalan, thank you for your love and laughter and for having my back through thick and thin.

This research was funded by the Canada Research Chair program, grant number 231380 (Christophe Kinnard), and the Natural Sciences and Engineering Research Council of Canada, NSERC discovery grant CRSNG-RGPIN-2015-03844 (Christophe Kinnard).

TABLE OF CONTENTS

LIST OF FIGURES

Figure **Page**

LIST OF TABLES

Table **Page**

RÉSUMÉ

Le paysage a une influence notable sur la couverture neigeuse et l'hydrologie dans les régions dominées par la neige. Cela a été bien documenté dans des paysages comme les Prairies canadiennes, les régions de la Cordillère et l'Arctique. Cependant, relativement peu de publications ont été faites sur la variabilité de la couverture neigeuse et les interactions météorologiques et climatiques de la neige dans des régions comme le Québec, dans l'est du Canada, qui a un climat et des caractéristiques physiographiques différents (c'est-à-dire un climat continental humide avec des paysages agro-forestiers dans les basses terres du Saint-Laurent et des paysages forestiers boréaux dans le bouclier canadien) par rapport aux régions où la plupart des études sur la couverture neigeuse ont été réalisées. Ces différences dans le climat et les caractéristiques physiographiques suggèrent que les conclusions d'autres régions peuvent ne pas être facilement transférables à cette région, indiquant la nécessité d'études supplémentaires pour mieux comprendre la dynamique de la couverture neigeuse dans l'est du Canada. La connaissance de la dynamique de la couverture neigeuse dans cette région est cruciale, en raison des implications profondes qu'elle a pour la région, y compris son rôle vital dans la régulation de l'afflux de réservoirs pour l'hydroélectricité et son influence sur la probabilité d'inondations au printemps.

Dans ce contexte, cette thèse vise à combler cette lacune de connaissances en explorant comment l'hétérogénéité du paysage module la couverture neigeuse à l'échelle microscopique (<100 m) dans le sud du Québec, à l'est du Canada, en combinant des mesures de lidar à haute résolution et des mesures détaillées de météorologie et de flux d'énergie. Représentant le paysage typique, la distribution spatiale des profondeurs de neige dans deux sites agro-forestiers dans les basses terres du fleuve Saint-Laurent et un site forestier boréal sur le bouclier canadien ont été surveillés par détection et

télémétrie de la lumière des véhicules aériens sans pilote (UAV lidar). En vue d'utiliser le UAV lidar pour observer les profondeurs de neige pour la première fois dans cette région, cette étude a évalué l'exactitude des profondeurs de neige dérivées du UAV lidar dans les environnements agro-forestiers par rapport au site forestier boréal et a fourni des recommandations pour les futures applications. En utilisant les données dérivées du UAV lidar, les effets topographiques et végétaux sur l'accumulation de neige sur chaque site ont été analysés avec des modèles de forêt aléatoire. Une nouvelle méthode d'interpolation a également été introduite pour résoudre les effets de sous-échantillonnage sur les profondeurs de neige interpolées finales par des techniques de télédétection aérienne dans les environnements conifères. En se concentrant sur les environnements agro-forestiers largement peu étudiés, la partition d'énergie entre les champs forestiers et ouverts a été caractérisée par une approche basée sur des mesures, en particulier en tenant compte de la neige soufflée et de la sublimation.

Les résultats de cette étude démontrent l'utilisation prometteuse de la télédétection lidar par drone pour surveiller les surfaces terrestres et enneigées sous une couverture végétale variable avec une précision raisonnable à des échelles plus fines. Les résultats mettent en évidence les différences de comportement de l'enneigement et des processus associés induits par le paysage et fournissent une identification et un classement utiles des variables/processus qui influencent la variabilité de la profondeur de neige entre et au sein des paysages agro-forestiers et boréaux. Par exemple, les résultats de l'analyse de régression suggèrent que la topographie sous-jacente (y compris la micro-topographie et les caractéristiques topographiques importantes telles que les canaux) et la redistribution du vent de la neige le long des lisières forestières sont les principales variables/processus régissant la variabilité de la profondeur de neige dans les paysages agro-forestiers, par rapport à l'influence dominante de la variabilité spatiale de la structure forestière sur les profondeurs de neige dans le paysage boréal. Ces résultats seront bénéfiques pour le développement et l'application de modèles physiquement basés pour des estimations précises de la dynamique du manteau neigeux dans de tels

environnements. De plus, les profondeurs de neige estimées à l'aide du nouvel algorithme d'interpolation sur le site forestier boréal montrent que cette méthode d'interpolation qui combine l'interpolation spatiale et intègre les tendances systématiques dans l'accumulation de neige à l'échelle du paysage, de la canopée par rapport aux lacunes et à l'intra-canopée peut résoudre la variabilité à petite échelle et réduire ainsi la probable surestimation des profondeurs de neige sous la canopée par les données aéroportées. En outre, les flux d'énergie entre les zones ouvertes, forestières et lacunaires dans le paysage agroforestier ont montré des différences considérables dans les flux d'énergie entre les sites, avec la radiation nette dominant le bilan énergétique de la surface enneigée. L'analyse a montré une plus grande influence de la radiation à ondes longues sur la variabilité du bilan d'énergie pendant la période d'accumulation, tandis que les flux de chaleur latente et l'absorption de la radiation solaire dominent pendant la fonte du manteau neigeux. L'influence de la neige soufflée sur le bilan d'énergie dans la zone ouverte balayée par le vent a également été observée grâce aux effets de rétroaction négatifs pendant la période d'accumulation. Les différentes conditions de manteau neigeux et de bilan d'énergie entre les zones ouvertes et forestières des paysages agro-forestiers mises en évidence dans cette étude pourraient avoir d'importantes implications pour les modèles d'infiltration de la fonte des neiges et pour l'hydrologie à l'échelle du bassin versant. Cette recherche apporte une contribution importante à la connaissance de la dynamique de la couverture neigeuse induite par le paysage dans ces environnements, ce qui sera utile pour la prévision des crues, la gestion de l'eau et les pratiques de gestion des terres.

Mots-clés : Lidar UAV; variabilité de la profondeur de neige; environnements agro-forestiers; environnements boréaux; sous-échantillonnage sous la canopée; partitionnement de l'énergie; transport de neige par le vent

ABSTRACT

Landscape has a notable influence on snow cover and hydrology in snow-dominated regions. This has been well documented in the landscapes like Canadian prairies, Cordillera regions, and the Arctic. However, relatively little has been published about snow cover variability and snow-meteorological and snow-climate interactions in regions like Québec, eastern Canada, which has different climate and physiographic settings (i.e., humid continental climate with agro-forested landscapes in the St. Lawrence lowlands and boreal forested landscapes in the Canadian Shield) compared to regions where most of the snow cover studies have been performed. These differences in climate and physiographic settings suggest that findings from other regions may not be easily transferable to this region, underscoring the need for further studies to better understand the dynamics of snow cover in eastern Canada. The knowledge of snow cover dynamics in this region is crucial due to the profound implications it has for the region, including its vital role in regulating reservoir inflow for hydroelectricity and its influence on the likelihood of spring floods.

In this context, this thesis aims to bridge this knowledge gap by exploring how landscape heterogeneity modulates the snow cover at the microscale (< 100 m) level in southern Québec, eastern Canada by combining high-resolution lidar and detailed meteorological and energy flux measurements. Representing the typical landscape, the spatial distribution of snow depths in two agro-forested sites in the St. Lawrence river lowlands and one boreal forested site on the Canadian Shield were monitored by Unmanned Aerial Vehicle Light Detection and Ranging (UAV lidar). In view of utilizing UAV lidar to monitor snow depths for the first time in this region, this study evaluated the accuracy of UAV lidar-derived snow depths in agro-forested environments compared to the boreal forested site and provided recommendations for

future applications. Utilizing the UAV lidar-derived data, topographic and vegetation effects on snow accumulation at each site were analyzed with random forest models. A new interpolation method was also introduced to resolve the effects of under-sampling on final interpolated snow depths by airborne remote sensing techniques in coniferous environments. Focusing on largely understudied agro-forested environments, energy partitioning of forested versus open fields was characterized by a measurement-based approach, while particularly considering blowing snow and sublimation.

The results of this study demonstrate the promising use of UAV lidar to monitor ground and snow surfaces under varying vegetation covers with reasonable accuracy at finer scales. Results highlight the difference in snowpack behaviors and associated processes induced by the landscape and provide a useful identification and ranking of variables/processes that are influencing snow depth variability between and within agro-forested and boreal landscapes. For instance, results from the regression analysis suggest that the underlying topography (including the microtopography and prominent topographical features such as canals) and the wind-redistribution of snow along forest edges are the prime variables/processes governing the snow depth variability in agro-forested landscapes compared to the dominant influence of spatial variability of forest structure on snow depths in the boreal landscape. These findings will be beneficial for the development and application of physically-based models for accurate estimates of snowpack dynamics in such environments. Moreover, the snow depths estimated using the new interpolation algorithm in the boreal forested site show that this interpolation method that combines spatial interpolation and incorporates systematic trends in snow accumulation at the landscape, canopy versus gaps, and intra-canopy scales can resolve the small-scale variability and thereby reduce the likely overestimation of snow depths under the canopy by airborne data. Furthermore, energy fluxes between open, forest, and gap areas in the agro-forested landscape showed considerable differences in energy fluxes between the sites, with net radiation dominating the snow surface energy balance.

Analysis showed the greater influence of longwave radiation on the variability of the energy balance during the accumulation period, while latent heat fluxes and solar radiation absorption dominance during snowpack melting. The influence of blowing snow on the energy budget in the wind-swept open area was also observed through negative feedback effects during the accumulation season. The different snowpack and energy balance conditions between the open and forested patches of agro-forested landscapes highlighted in this study could have important implications for snowmelt infiltration patterns and resulting catchment-scale hydrology. This research provides an important contribution to the knowledge of landscape-induced snow cover dynamics in these environments which will be useful in flood forecasting, water management, and land management practices.

Keywords: UAV lidar; snow depth variability; agro-forested environments; boreal environments; under-sampling under-canopy; energy partitioning; blowing snow

INTRODUCTION

Motivation and Relevance

In cold climate regions, snow cover represents a major part of the terrestrial water storage during the winter season and produces a significant spring runoff with the onset of snowmelt. In addition, being a strong insulator, the snow cover protects the soil from extreme air temperature variations by substantially reducing the frost depth in soils compared to bare surfaces. Moreover, due to its high reflectivity and insulation properties, the interaction of snow cover with the atmosphere dramatically alters the energy exchange between the surface and the atmosphere (Brown, 2011). All these aspects shape snow accumulation and ablation into a significant variable in the hydrological processes of cold regions. Snow accumulation and the timing, intensity, and duration of snowmelt are deeply dependent on meteorological and physiographic variables such as regional climate, elevation, presence or absence of vegetation, and forest structure (Golding and Swanson, 1986; Elder et al., 1998; Pomeroy et al., 1998a; Varhola et al., 2010a; Roth and Nolin, 2017; Zheng et al., 2018; Koutantou et al., 2022). For instance, an increase in snow accumulation is reported with increasing elevation due to adiabatic cooling and orographic enhancement of precipitation while a reduced spring snowmelt flooding is observed due to different melting rates along the elevation gradients (Pomeroy et al., 1998a; Jost et al., 2007; Grünewald et al., 2014; Shaw et al., 2020). Higher snow accumulation on northerly slopes in the northern hemisphere is documented due to reduced melting rates associated with reduced incoming solar radiation and the opposite is observed in the southern hemisphere, i.e., higher snow depths and reduced melt rates on southerly slopes (Baños et al., 2011; Hopkinson et al., 2012a; Revuelto et al., 2016; Schirmer and Pomeroy, 2020; Shaw et al., 2020). In general, shallower snow depths were observed on steeper slopes depending on exposure to wind and radiation (Golding and Swanson, 1986; Shaw et al., 2020).

Evaluating snowpack conditions in forested regions is particularly important as the snowmelt-dominated, forested watersheds contribute approximately 60 % of the global freshwater runoff (Moeser et al., 2015). Moreover, the spatial arrangement of different forest stands and forest versus open/agricultural areas play a significant role in altering the spatial distribution of the snow cover and thereby the regional hydrology (Winkler et al., 2005; Aygün et al., 2020). For instance, in the province of Québec, Canada where the second-largest maxima of snow accumulation in North America is reported (Brown et al., 2003), forest covers about 50 % of its land area (Government of Canada, 2018) while in the southern part of the province, in the St-Lawrence lowlands and Appalachian piedmont, forests are intertwined with mosaics of agricultural fields (i.e., agro-forested landscape). Differential snow accumulation and melt patterns in these landscape units are expected to have a greater influence on regional hydrology (Aygün et al., 2020; Aygün et al., 2022).

Generally, compared to open areas, forest cover reduces the incoming shortwave radiation, increases longwave radiation, dampens wind speed, and hence reduces turbulent heat transfers within the canopy (Prévost et al., 1991; Pomeroy and Gray, 1994; Tarboton, 1994; Pomeroy and Dion, 1996; Pomeroy and Granger, 1997; Pomeroy et al., 1998a; Pomeroy et al., 1998b; Helgason and Pomeroy, 2012). In turn, the snowpack dynamics within a forest differ from that in an open area. Depending on the canopy density, forested areas reportedly accumulate less snow than adjacent open areas due to canopy interception and sublimation losses and undergo slower snowmelt rates due to shading by the canopy in dry climates while the melt appears faster in a humid climate, due to increased longwave radiation with higher canopy density, a phenomenon known as the radiative paradox (Golding and Swanson, 1986; Pomeroy and Granger, 1997; Hopkinson et al., 2004; Varhola et al., 2010a; Lundquist et al., 2013; Roth and Nolin, 2017; Zheng et al., 2018). In addition, forests can also influence differential snow accumulation by preferential deposition of wind-blown snow along the forest edges (Essery et al., 2009; Currier and Lundquist, 2018). Several authors reported substantial differences in snow accumulation and melt patterns in forest clearings or gaps compared to adjacent forests and open areas (e.g., Winkler et al., 2005; Musselman et al., 2008; Revuelto et al., 2015; Roth and Nolin, 2017; Mazzotti et al., 2019). Small gaps (~2–5 times the tree height diameter) are often still sheltered by trees and accumulate more snow due to reduced exposure to wind, while large gaps are exposed to wind erosion that eventually reduces the overall snow accumulation (Golding and Swanson, 1986; Pomeroy and Gray, 1994; Pomeroy et al., 2002; Woods et al., 2006; Pomeroy et al., 2012; Broxton et al., 2015; Conway et al., 2018). Snow accumulation and ablation also differ significantly between different forest stands with distinct structural differences, due to the impact of forest structure on the energy balance, dominated by radiative heat fluxes (Winkler et al., 2005). Accumulation and ablation rates generally decline with increasing canopy density and leaf area (Pomeroy et al., 2002). Within a forest stand, snow accumulation increases with increased distance from the tree stem due to reduced interception, whereas the melt rate decreases due to the reduced influence of longwave radiation emitted by the tree canopy (Pomeroy and Dion, 1996; Musselman et al., 2008; Revuelto et al., 2015; Zheng et al., 2019). Accounting for this snow depth variability and the knowledge of energy exchanges between snow, atmosphere, and the ground is important when estimating snowmelt dynamics of the snowpack in these environments (Liston and Elder, 2006; Trujillo et al., 2007; Varhola et al., 2010a; Clark et al., 2011; Mas et al., 2018).

Given the importance of accounting for the spatial variability of the snow cover, the most frequently utilized techniques to observe snowpack variations are in-situ observations and/or remote sensing techniques. The traditional, ground-based, and mostly manual process of monitoring snow depths is expensive, labor-intensive, time-consuming, potentially dangerous, and can also disturb the snowpack and influence subsequent measurements (Deems et al., 2013). Even when available, and despite its accuracy, point measurements may not be representative of a larger area (Dong, 2018). Nevertheless, a number of studies in the literature used point scale measurements of snow depth and density to statistically model spatial variability of snow depth and snow water equivalent, SWE (Elder et al., 1991; Elder et al., 1998; Brown et al., 2018). However, during the past several decades, remote sensing has become a powerful and efficient approach for monitoring snowpacks in areas located in remote and inaccessible environments. A variety of airborne (manned and unmanned) and terrestrial remote sensing techniques using satellite, radar, laser (lidar, light detection and ranging), and photogrammetry data have been developed ever since (Dong, 2018). Among these techniques, laser scanning and photogrammetry are prominent for their ability to capture high-resolution micro (< 100 m) and mesoscale (100 m–10 km) variability (Deems et al., 2013). Compared to traditional photogrammetric approaches, topographic data from lidar feature lower systematic and stochastic uncertainties due to its ability to accurately map in cast shadows and to better cope with low contrast surfaces such as fresh snow (Eitel et al., 2016; Harder et al., 2020). Lidar data sets from airborne platforms are increasingly used to estimate snow depth by differencing snow-covered and snow-free elevation products (Hopkinson et al., 2004; Deems et al., 2006; Trujillo et al., 2007; Baños et al., 2011; Hopkinson et al., 2012a; Hopkinson et al., 2012b; Deems et al., 2013; Harpold et al., 2014; Kirchner et al., 2014; Eitel et al., 2016; Zheng et al., 2016; Zheng et al., 2018). Due to the strong penetration ability of lidar through the forest canopy, this technology is efficient for detecting the snow cover under the canopy and deriving forest metrics such as LAI (leaf area index), canopy cover, gap fraction, etc., which play a significant role in shaping snow dynamics in forested environments (Morsdorf et al., 2006; Richardson et al., 2009; Varhola et al., 2010b; Varhola et al., 2012; Fieber et al., 2014; Qin et al., 2017; Currier and Lundquist, 2018; Zheng et al., 2018; Mazzotti et al., 2019; Harder et al., 2020; Jacobs et al., 2021). However, the density of ground return lidar points in forested environments depends on the canopy type and architecture, laser spot size, laser pulse rate, scan angle of the laser sensor, flying height, and flying speed. For example, higher pulse rates provide more laser shots, while smaller scan angles and a lower flight altitude increase the probability of canopy penetration (Hyyppä et al., 2005; Wallace et al., 2012; Deems et al., 2013). Under-sampling of snow depths under dense canopies by airborne lidar surveys is reported by many authors (e.g., Varhola et al., 2010b; Hopkinson et al., 2012b; Harpold et al., 2014; Tinkham et al., 2014; Broxton et al., 2015; Zheng et al., 2016; Mazzotti et al., 2019; Zheng et al., 2019; Jacobs et al., 2021; Koutantou et al., 2022). Addressing this under-sampling under dense canopies and consequent effects on snow depth interpolations is still a growing area of research (Tinkham et al., 2014; Zheng et al., 2016; Koutantou et al., 2022). Nevertheless, validation of the snow depth products from remote sensing techniques with in-situ measurements shows that the lidar technique gives promising results in capturing accurate snow depths.

Given the importance of understanding energy exchanges between snow, the atmosphere, and the ground, many of the snow physics models developed for hydrological applications are in fact based on energy budget estimation. These models have undergone significant improvements since their early developments, with the addition of new parameterizations for turbulent energy transfer (Andreas et al., 2010), blowing snow (Pomeroy et al., 1993; Liston et al., 2007; Pomeroy et al., 2007), and snow metamorphism (Lehning et al., 2002). However, despite these advances, snowmelt models do not consistently produce acceptable results in all environments, which is partly due to the inability to robustly simulate the snowpack processes and snow-atmosphere-ground interactions (Rutter et al., 2009). However, there is potential to improve the accuracy of these models through the availability of calibration data. By reducing the parameter uncertainty and thereby offsetting model deficiencies, calibration data can help improve the snowmelt model performances (Essery et al., 2009). This highlights the importance of having detailed meteorological and/or energy flux measurements in different environments.

Despite the notable influence of landscape on snow cover and hydrology (Whitfield and Cannon, 2000), relatively little has been published about snow cover variability and snow-meteorological and snow-climate interactions in regions such as Québec compared to Canadian prairies (e.g., Pomeroy and Gray, 1994; Helgason and Pomeroy, 2012; Harder et al., 2016; Harder et al., 2018; Harder et al., 2020) and Cordillera regions (e.g., Hopkinson et al., 2012b; Roth and Nolin, 2019; Harder et al., 2020; Schirmer and Pomeroy, 2020). It is partly due to the lack of detailed and simultaneous micrometeorological and snow observations (Brown, 2010; Sena et al., 2017; Sena et al., 2019; Aygün et al., 2020). Sena et al. (2019) noted that while the existing snow survey network in Québec is adequate to model the spatial variability of SWE at a regional scale (10 km x 10 km), it is inadequate at the local scale (300 m x 300 m) due to the reduced and uneven number of stations. To date, compared to extensive manual sampling or ground-based sensors (e.g., existing snow survey network in Québec (Sena et al., 2019) and snow surveys in Montmorency experimental watershed (Parajuli et al., 2021; Royer et al., 2021; Bouchard et al., 2022)), limited use of remote sensing techniques (Brown and Goodison, 1996; Chokmani et al., 2005; Chokmani et al., 2013; Valence et al., 2022) is reported in snow depths/SWE monitoring in Québec. Sena et al. (2017) emphasized that remote sensing approaches still require improvements in the province of Québec. Moreover, the lack of field studies simultaneously measuring snow mass and energy balance in open and forest patches hampers the holistic understanding of snowpack dynamics and makes it difficult to validate the modeling efforts in the region (Brown, 2010; Sena et al., 2017; Aygün et al., 2020; Paquotte and Baraer, 2021). As such, much uncertainty still exists about the micro and mesoscale spatial variability of snow cover and associated snow-meteorological interactions in Québec.

Moreover, compared to climate and physiographic settings in which most snow cover studies have been performed (e.g., fully-humid continental climate in prairies, mild-wet climate in Cordillera's coast), southern Québec is characterized by a humid continental climate with agro-forested landscapes in the St. Lawrence lowlands and boreal forested landscapes in the Canadian Shield (Québec Ministry of Forests, Wildlife, and Parks (MFFP)). These differences in climate and physiographic settings suggest that findings from other regions may not be easily transferable to this region, underscoring the need for further studies to better understand the dynamics of snow cover in southern Québec. The knowledge of snow cover dynamics in this region is crucial due to the profound implications it has for the region, including its vital role in regulating reservoir inflow for hydroelectricity (Hydro-Québec, 2023) and its influence on the likelihood of spring floods- e.g., 2017 and 2019 spring floods- (Teufel et al., 2019; Turcotte et al., 2019; Zahmatkesh et al., 2019).

The main objective of this thesis is to bridge this knowledge gap by exploring how landscape heterogeneity modulates the snow cover at the microscale (< 100 m) level in southern Québec, eastern Canada by combining high-resolution lidar and detailed meteorological and energy flux measurements.

Research Objectives, Scope and Importance

This research seeks to examine and better understand how the snow cover responds to meteorological forcing and how landscape heterogeneity modulates the snow distribution. Two paired forested (deciduous and mixed) and agricultural sites (Sainte-Marthe and Saint-Maurice) and one boreal forested site (Forêt Montmorency) were selected as study sites representing the typical landscape of southern Québec. Sainte-Marthe and Saint-Maurice are located in the St. Lawrence river lowlands where its fertile soil makes it an ideal environment for intensive farming practices. Mosaics of agricultural and forested areas, which are referred to as agro-forested landscapes (Jobin et al., 2014; Aygün et al., 2020), are very common in this part of the province of Québec. Forêt Montmorency is a boreal forest farther north on the Canadian Shield. Forest gaps associated with clear-cutting and regeneration practices are common in this area.

In view of utilizing UAV lidar to monitor snow depths for the first time in this region, this study first aims to evaluate the accuracy of UAV lidar-derived snow depths in the agro-forested environments compared to boreal forested site and provide recommendations for future applications. Then, we seek to assess the small-scale spatial variability of snow depths between and within these different landscapes by UAV lidar data and discuss the landscape impacts on the snow depths. Next, we aim to introduce an interpolation algorithm to resolve the effects of under-sampling on final interpolated snow depths by airborne remote sensing techniques in coniferous environments. Finally, we seek to characterize the energy fluxes of forested versus open fields in the agro-forested landscape, particularly considering blowing snow and sublimation, which are largely understudied in southern Québec. Since there are a limited number of studies that have focused on agro-forested environments compared to boreal forested environments to date, it is expected that the findings of this project would make an important contribution to the knowledge of snow cover dynamics in such environments.

The following specific objectives were formulated to pursue the aforementioned purpose of the study.

Objective 1: Investigate how accurate the lidar-derived snow depths are in open versus forested environments with different canopy covers.

Despite the growing interest in the use of UAV lidar scanning for snow depth monitoring, there is still a need for evaluating the accuracy of UAV lidar data and lidar-derived snow depths in different land covers compared to those obtained by ALS. Previously, Harder et al. (2020) evaluated the UAV lidar-derived snow depth accuracies in mountain and prairie environments in western Canada, and Jacobs et al. (2021) in mixed-hardwood-forest and open-field land covers in the eastern USA. There has been no application of UAVs in agro-forested environments such as in eastern Canada. This objective aims to answer the following questions:

1-a) How does the accuracy of snow depths vary between open and forested environments?

It is hypothesized that the accuracy of snow depths will be higher in open areas compared to forested areas due to likely disturbances for lidar measurements by the canopy. It is expected higher accuracy in snow depths in deciduous forests than in coniferous forests due to the abundance of leafless deciduous trees in winter.

1-b) How can the accuracy of lidar-based snow depth measurements be improved?

It is hypothesized that a well-formulated flight plan and careful boresight calibration will improve the accuracy of the lidar data by reducing navigational errors and boresight errors. It is also thought that an application of a strip alignment method will improve accuracy by reducing misalignment between lidar flight strips.

Objective 2: Characterize the small-scale variability of snow depth between and within the forested and open environments using lidar-derived data.

Spatial variability of snow depth at small scales depends on topography, microtopography, vegetation type, and vegetation density (Varhola et al., 2010a; Koutantou et al., 2022). Snow spatial variability also occurs on more than one scale due to different processes acting over multiple scales (Deems et al., 2006; Clark et al., 2011). Thus, snow accumulation patterns and scaling behavior vary in different environments (e.g., open versus forested). However, little has been published about how terrain and vegetation characteristics influence snow heterogeneity in different landscapes, especially in agro-forested environments, by using UAV lidar. This objective aims to answer the following questions:

2-a) How does snow accumulation vary between and within forested and open environments?

It is hypothesized that more snow accumulation in deciduous forest stands than in coniferous forests due to the absence of leaves in winter. It is also expected that deciduous forest stands to have a more homogeneous snow depth distribution than in coniferous forests, where snow accumulation will be highly heterogeneous, notably due to snow accumulation increasing away from tree stems due to the reduction of interception and sublimation losses (Pomeroy and Dion, 1996). Deciduous forests are expected to have higher snow accumulation than the adjacent open field due to small canopy interception losses and wind sheltering inside the forest. On the other hand, coniferous forests are expected to accumulate less snow compared to open fields due to canopy snow storage losses. It is assumed that the forest gaps and forest edges will account for higher snow accumulation than the adjacent forest or open fields due to the reduction of wind speed, interception losses, and absence of snow erosion compared to open fields.

2-b) What are the relationships between snow depth, topography, and vegetation structure?

It is hypothesized that the effect of elevation on snow accumulation is absent in relatively flat areas such as Sainte-Marthe and Saint-Maurice, whereas the opposite occurs in areas that have more pronounced topography (e.g., Montmorency). Vegetation structure is expected to be the prime driver of the spatial variability of snow depths in absence of the elevation effect in relatively flat sites. It is also expected microtopography to influence snow depth patterns at small scales. Snow accumulation is expected to increase with decreasing vegetation densities due to fewer interception losses.

Objective 3: Develop an interpolation method to resolve the effects of under-sampling under the canopy in coniferous environments by UAV lidar.

Under-sampling of snow depth by ALS and UAV lidar methods in presence of dense canopies such as coniferous stands is well documented (Tinkham et al., 2014; Zheng et al., 2019). Consequently, this under-sampling causes overestimation in interpolated snow depth in such environments (Tinkham et al., 2014; Zheng et al., 2016). Thus, there is a need for a more sophisticated gap-filling algorithm to resolve intra-canopy snow depth variability and thereby avoid likely overestimation of under-sampled under-canopy snow depths. This objective aims to answer the following question:

3-a) How does the distance between sampled and unsampled points affect the snow depth estimates?

It is hypothesized that the accuracy of snow depth estimates in unsampled locations will be degraded with the increasing distance between sampled and unsampled points.

It is also expected that accounting for systematic trends within the canopy helps interpolate sparse lidar snow depth points.

Objective 4: Analyze snow energy partitioning between forested and open environments.

The lack of field studies simultaneously measuring snow mass and energy balance in open and forest areas hinder our ability to validate modeling efforts and limit our ability to develop a comprehensive understanding of snowpack dynamics in agro-forested landscapes (Brown, 2010; Sena et al., 2017; Paquotte and Baraer, 2021). Moreover, blowing snow flux measurements and their influence on the snowpack mass and energy budget are largely understudied in agro-forested, temperate environments. This objective aims to answer the following questions:

4-a) How do the snow energy fluxes vary between forested and open environments?

It is hypothesized an increase of net incoming longwave radiation to the snow surface due to the longwave emittance by trees and a decrease in shortwave radiation due to partial shading from the canopy in forests. Since the canopy dampens the wind speeds, turbulent fluxes are expected to play a lesser role in the surface energy balance below the canopy. In larger open fields where an adequate fetch length is available for the development of higher winds, turbulent fluxes are expected to dominate the energy budget whereas, in smaller openings, net radiation is expected to be dominant. However, in spring, when longer daylight is available, net radiation is expected to dominate in both environments. Although, shading by trees and reduced turbulent fluxes in forests expect to cause slower melt rates under the canopy compared to open fields.

4-b) How important are the sublimation energy losses from snow surfaces and blowing snow transport in these environments?

High sublimation (latent heat) energy losses are hypothesized in large open areas where higher winds are prevalent compared to forested areas. However, it is expected that snow surface sublimation to be reduced during blowing snow events due to the increased moisture content in the air layer above the snowpack from the sublimation of blowing snow particles.

Thesis Outline

This dissertation consists of four main chapters related to each objective defined in the section "Research Objectives, Scope, and Importance".

CHAPTER I aims to achieve the 1st objective of the dissertation by employing UAV lidar surveys with a Geo-MMS UAV lidar system (Geodetics, 2019) in Sainte-Marthe, Sainte-Maurice agro-forested sites, and Montmorency coniferous forested site and assessing the accuracy of the point clouds and subsequent snow depth products. The effect of boresight calibration on the collected data was first investigated. Then, an automatic strip alignment algorithm implemented in BayesStripAlign (Bayesmap Solutions, 2020) was tested on lidar data to assess whether it can improve upon the manual boresight calibration procedure. We used several ground control points (some manmade, some permanent structures) to evaluate the absolute accuracy of lidar point clouds. Strip alignment and a repeated survey were used to evaluate the inter-strip accuracy and relative accuracy of overlapping point clouds (e.g., winter and summer), respectively. Then, the accuracy of the snow depths was assessed relative to manual snow depth measurements at the sites. Differences in accuracies in open versus forested and deciduous versus coniferous forests, sources of uncertainties, and recommendations to improve accuracies were explored and discussed.

CHAPTER II seeks to accomplish the 2nd objective of the dissertation by exploring the spatial variability of the snow depths derived by UAV lidar in CHAPTER I in the aforementioned sites. A random forest model (Breiman, 2001) was applied to snow depth, topographic variables, vegetation descriptors, and forest edge matrices derived from lidar data to investigate the effect of these variables on the spatial variability of snow depth at each site. The scaling behavior of snow depths was explored by semi-variogram analysis (Webster and Oliver, 2007). This chapter provides a comprehensive analysis of inter (agro-forested versus coniferous) and intra (open versus forest) site variability of snow depths.

CHAPTER III intends to accomplish 3rd objective of the dissertation. To achieve this objective the processed lidar data in Montmorency in CHAPTER I was used. Development of the interpolation method consisted of tree segmentation, canopy delineation, taking into account systematic trends such as landscape trend, under-canopy versus forest gap snow depth trend, and intra-canopy trend, and implementing spatial interpolation techniques on the residuals of these trends. As such, four interpolation methods were employed by combining landscape trend, under-canopy versus forest gap trend, intra-canopy trend, and spatial interpolation techniques. The performance of interpolation methods was evaluated by cross-validation while progressively increasing the distance between sampled and unsampled points. Based on the results, this chapter provides recommendations on the use of tested interpolation methods depending on the distance between sampled and unsampled points (i.e., point density).

CHAPTER IV is associated with the 4th objective of the dissertation. Automatic weather station measurements from an open agricultural area, a mixed wood forest (mostly deciduous), and a forest clearing in Sainte-Marthe were used to estimate energy budget components for the 2020–2021 winter in this chapter. Raw measurements were visually inspected, and missing, and/or suspected erroneous values were screened, inventoried, and gap-filled accordingly prior to computing energy fluxes. The energy balance for snowpacks in three sites was calculated using the energy balance equation developed by Anderson (1976). This chapter compares measurement-based snow energy partitioning between open ground, forest, and forest clearing and discusses the influence of blowing snow on the energy budget in open areas based on blowing snow measurements.

CHAPTER I

AN ACCURACY ASSESSMENT OF SNOW DEPTH MEASUREMENTS IN AGRO-FORESTED ENVIRONMENTS BY UAV LIDAR

Vasana Dharmadasa [1,2,3], Christophe Kinnard [1,2,3] and Michel Baraër [4]

[1] Department of Environmental Sciences, University of Québec at Trois-Rivières, Trois-Rivieres, QC G8Z 4M3, Canada

[2] Center for Northern Studies (CEN), Quebec City, QC GV1 0A6, Canada

[3] Research Centre for Watershed-Aquatic Ecosystem Interactions (RIVE), University of Québec at Trois-Rivières, Trois-Rivieres, QC G8Z 4M3, Canada

[4] Department of Construction Engineering, École de Technologie Supérieure, Montreal, QC H3C 1K3, Canada

Corresponding author: vasana.sandamali.dharmadasa@uqtr.ca

This article has been published in the Special Issue " Remote Sensing in Snow and Glacier Hydrology" of *Remote Sensing* (doi: 10.3390/rs14071649).

Abstract

This study assesses the performance of UAV lidar system in measuring high-resolution snow depths in agro-forested landscapes in southern Québec, Canada. We used manmade, mobile ground control points in summer and winter surveys to assess the absolute vertical accuracy of the point cloud. Relative accuracy was determined by a repeat flight over one survey block. Estimated absolute and relative errors were within the expected accuracy of the lidar (~5 and ~7 cm, respectively). The validation of lidar-derived snow depths with ground-based measurements showed a good agreement, however with higher uncertainties observed in forested areas compared with open areas. A strip alignment procedure was used to attempt the correction of misalignment between overlapping flight strips. However, the significant improvement of inter-strip relative accuracy brought by this technique was at the cost of the absolute accuracy of the entire point cloud. This phenomenon was further confirmed by the degraded performance of the strip-aligned snow depths compared with ground-based measurements. This study shows that boresight calibrated point clouds without strip alignment are deemed to be adequate to provide centimeter-level accurate snow depth maps with UAV lidar. Moreover, this study provides some of the earliest snow depth mapping results in agro-forested landscapes based on UAV lidar.

Keywords: UAV lidar; boresight calibration; strip alignment; agro-forested landscapes; ground control points

1.1 Introduction

One of the key features of snow accumulation is the spatial variability of the snow cover. At a broader scale, quantifying the spatial distribution of snow depth is vital to address the current behavior and the future of the cryosphere (Barnett et al., 2005). At the watershed or smaller scales, accounting for the spatial variability of snow depth is crucial to estimate the amount and timing of spring runoff (Clark et al., 2011). Rapid changes in the amount, extent, timing, and duration of the snow cover in cold regions with changing climatic conditions—mainly in response to warming temperatures and rain-on-snow events (NSIDC, 2019; Sturm et al., 2017)—call for a better knowledge of the quantification of snow distribution (Aygün et al., 2020a).

Given the importance of accounting for the spatial variability of the snow cover, the most frequently utilized techniques to observe snowpack variations are in situ observations and/or remote sensing. The traditional, ground-based, and mostly manual process of monitoring snow characteristics is expensive, extremely labor-intensive, time-consuming, and potentially dangerous. Additionally, it can disturb the snowpack and influence subsequent measurements (Deems et al., 2013). Even when available, and despite its accuracy, point measurements may not be representative of a larger area (Dong, 2018). Nevertheless, during the past several decades, remote sensing techniques that surmounted most of the aforementioned drawbacks have become a powerful and efficient approach for monitoring snowpack in remote environments. A variety of airborne and terrestrial remote sensing techniques developed using satellite, radar, laser (lidar: Light detection and ranging), and photogrammetry data have been extensively used in a variety of cryospheric studies (Dong, 2018; Tsai et al., 2019). Among these techniques, airborne (manned and unmanned) laser scanning has become increasingly popular due to its ability to capture high-resolution micro (<100 m) and mesoscale (100 m–10 km) variability, as well as to detect snow cover/ground under canopy due to its strong penetration ability (Currier and Lundquist, 2018; Deems et al., 2013; Harder et al., 2020; Harpold et al., 2014; Hopkinson et al., 2012b; Hopkinson et al., 2004; Jacobs et al., 2021; Mazzotti et al., 2019; Morsdorf et al., 2006; Zheng et al., 2016; Zheng et al., 2018). In recent years, there has been a growing interest in the use of unmanned aerial vehicle (UAV) laser scanning for small scale high-resolution mapping, due to its potential to deliver dense and high-quality point clouds with minimal occlusion in forested areas compared with airborne laser scanning (ALS) (Broxton et al., 2015; Currier and Lundquist, 2018; Glira et al., 2016; Harder et al., 2020; Mazzotti et al., 2019; Michele et al., 2016; Painter et al., 2016; Pajares, 2015). Snow depths from lidar data are commonly estimated by differencing snow-covered and snow-free elevation products (Deems et al., 2006; Deems et al., 2013; Hopkinson et al., 2012a; Hopkinson et al., 2012b; Hopkinson et al., 2004; Kirchner et al., 2014; Trujillo et al., 2007). Usually, ground-based manual measurements are used as ground truth data to validate the lidar-derived snow depth products (Deems et al., 2013; Dong, 2018). However, as with any other measuring technique, UAV laser scanning is not exempt from errors.

In general, the UAV lidar system comprises three instruments: A laser device, an inertial measurement unit (IMU) that continuously records platform orientation, and high precision airborne global positioning system (GNSS, global navigation satellite system), which records the three-dimensional position of the platform (Deems et al., 2013; Li et al., 2019). Moreover, the system requires a GNSS base station installed at a known location and in the vicinity of the airborne platform (preferably within 50 km), which operates simultaneously to differentially correct, and thus improve the precision of the airborne GNSS data (Gatziolis and Andersen, 2008). Error sources of UAV lidar mapping can broadly be classified into boresight errors, navigational errors, terrain-induced errors, vegetation-induced errors, and post-processing errors (Deems et al., 2013; Pilarska et al., 2016). Boresight errors occur due to offset and angular differences between the lidar and IMU origins. The origin difference vector is called boresight shift or lever-arm offset, and the three angles between the lidar and IMU axes are called boresight angles (Geodetics, 2019a; Pilarska et al., 2016). UAV lidar systems are more prone to boresight angular errors, due to their lower sensor installation precision and stability than lidars used onboard manned aircrafts (Li et al., 2019; Zhang et al., 2019). Precise calibration of lever-arm offsets and boresight angles can reduce the boresight errors (Li et al., 2019; Ravi et al., 2018). While lever-arm offsets can usually be accurately measured after system assembling or from drawings (Li et al., 2019), boresight angle errors should be calibrated manually (Geodetics, 2019a) or using automated methods (De Oliveira Junior and Dos Santos, 2019; Li et al., 2019; Ravi et al., 2018; Zhang et al., 2019).

Errors associated with GNSS and IMU can result in navigational errors. These navigational errors can be minimized with IMU calibration, as well as GNSS accuracy enhancements methods, such as differential global positioning system (DGPS), real-time kinematic (RTK), precise point positioning (PPP) or post-processing kinematic (PPK) (Deems et al., 2013). Another method to reduce random errors caused by GNSS and IMU is the strip adjustment, which fundamentally decreases the discrepancies between flight strips. The strip adjustment (or strip alignment) technique has proven to be very successful with ALS data (Glira et al., 2015; Kumari et al., 2011), and implementing it on UAV data remains an active area of research (Chen et al., 2021; Glira et al., 2016). One of the reasons that this technique is not (yet) very popular among UAV users is that the readily available strip adjustment algorithms require raw data of the laser scanner, which is often not accessible for most end-users through the UAV lidar system (Glira et al., 2016; Zhang et al., 2019).

Terrain-induced errors are mostly positional errors that occur due to complex terrain and steep terrain slopes. Flight planning can help in reducing these terrain-induced errors to some extent by minimizing oblique incident laser shots on steep slopes (Deems et al., 2013). The presence of canopy and/or sub-canopy can reduce the number of laser shots reaching the ground or snowpack surface, and thus result in observation gaps. The density of ground return lidar points depends on the canopy type and architecture, laser spot size, laser pulse rate, scan angle, flying height, and flying speed, i.e., higher pulse rates provide more laser shots, while smaller scan angles and a lower flight altitude increase the probability of canopy penetration (Deems et al., 2013; Hyyppä et al., 2005; Wallace et al., 2012). Therefore, a proper flight planning can minimize errors to some degree. Post-processing errors are predominantly caused by misclassification of the raw point cloud (misclassifying the terrain points as non-terrain and/or vice versa). Point cloud classification algorithms are often highly automated. As a result, the magnitude of error depends on the type of filter used, local terrain geometry, the height and type of vegetation, the presence of manmade structures, such as buildings, and the accuracy of the measured elevation (Deems et al., 2013; Evans and Hudak, 2007; Yilmaz et al., 2018).

Moreover, there is a lack of studies evaluating the accuracy of UAV lidar point data and lidar-derived snow depth maps with and without different vegetation covers. To our knowledge, two studies estimated the UAV-based lidar snow depth measurement accuracy to date (Harder et al., 2020; Jacobs et al., 2021). Harder et al. (2020) compared snow depth estimates between UAV lidar versus structure-from-motion (SfM) technique using manual snow depth measurements in mountain and prairie environments in western Canada. Jacobs et al. (2021) explored the capability of UAV lidar to estimate shallow snow depths in mixed-hardwood-forest and open-field land covers in the eastern USA through the comparison of simultaneous field-based snow depth measurements. Both studies showcased the ability of UAV lidar to effectively quantify the small scale snow depth variability.

The overall motivation for this work is to understand and assess the performance of UAV lidar system in measuring high-resolution snow depths in agro-forested landscapes. Moreover, to our knowledge, this study is the first of its kind that utilized the UAV laser scanning technique to measure small scale snow depth variability in southern Québec, Canada, which houses distinct land use patterns of alternating agricultural fields and forest patches. These mosaics of forests and agricultural fields are referred to as agro-forested landscapes in southern Québec (Aygün et al., 2020b; Jobin et al., 2014). In addition to boresight calibration, a strip alignment method was applied to the data to test whether it can improve the accuracy of data by partly correcting high-frequency IMU errors (random errors). First, this paper discusses the data collection and processing workflow, including the sources of errors and the refinement methods implemented in this study. Then, an assessment of the absolute and relative accuracy of the lidar data, an evaluation of the accuracy of snow depth maps with manual measurements in the open field versus forested environments, and an investigation of the applicability of strip alignment with UAV lidar data are presented.

1.2 Materials and Methods

1.2.1 Study Sites

Three sites that represent the main land use and cover patterns in southern Québec were selected to test the ability of UAV lidar to measure snow depths in open and vegetated areas (Figure 1.1). Sainte-Marthe (45.4°N, 74.2°W) is a paired agricultural and dense deciduous forested site (Paquotte and Baraer, 2021), where the forested area comprises sugar maple (*Acer saccharum*), red maple (*Acer rubrum*) with no or sparse understory, and a small conifer plantation to the Southwest. Saint-Maurice (46.4°N, 72.5°W) is a paired agricultural and high to moderate dense mixed forested site, and the forested area comprises poplar (*Populus x canadensis*), red maple (*Acer rubrum*), white pine (*Pinus strobus*), and balsam fir (*Abies balsamea*) with sparse understory. The forested areas in these sites overlie undulating glacial till sediments that are often associated with rougher microtopography, whereas the agricultural fields are associated with flatter glaciomarine or fluvioglacial sediments (Québec Ministry of Forests, Wildlife, and Parks (MFFP), Québec Research and Development Institute for the Agri-

Environment (IRDA), and La Financière Agricole du Québec (FADQ)). The main crop type in the agricultural areas of these two agro-forested sites is soya. Irrigation canals and streams that flow through these open agricultural areas form distinct terrain characteristics in the exposed agricultural fields. Forêt Montmorency (hereafter Montmorency; 47.3°N, 71.1°W) is a site with dense boreal forest interspersed with large gaps. The dominant tree types in this site are balsam fir (*Abies balsamea*), black spruce (*Picea mariana*), and white spruce (*Picea glauca*) with no understory. Adjacent to the forest is an open area hosting the NEIGE-FM snow research station, which hosts a variety of precipitation gauges and snowpack measuring sensors, and is part of the World Meteorological Organization's (WMO) Global Cryosphere Watch (GCW) surface network (Royer et al., 2021). Montmorency has a combination of glacial till and fluvioglacial soil types. Table 1.1 outlines the physiographic and climatic conditions at each site. Climatic data presented here were based on the climate averages (1981–2010) from the Environment and Climate Change Canada (2021) meteorological stations closest to each site (station climate ID 7016470, 7017585, and 7042388 for Sainte-Marthe, Saint-Maurice, and Montmorency, respectively). Land use datasets were obtained from the MFFP. For interpretation purposes, open agricultural areas in Sainte-Marthe and Saint-Maurice and the small open area in Montmorency (NEIGE-FM site) are referred to as "field" hereafter.

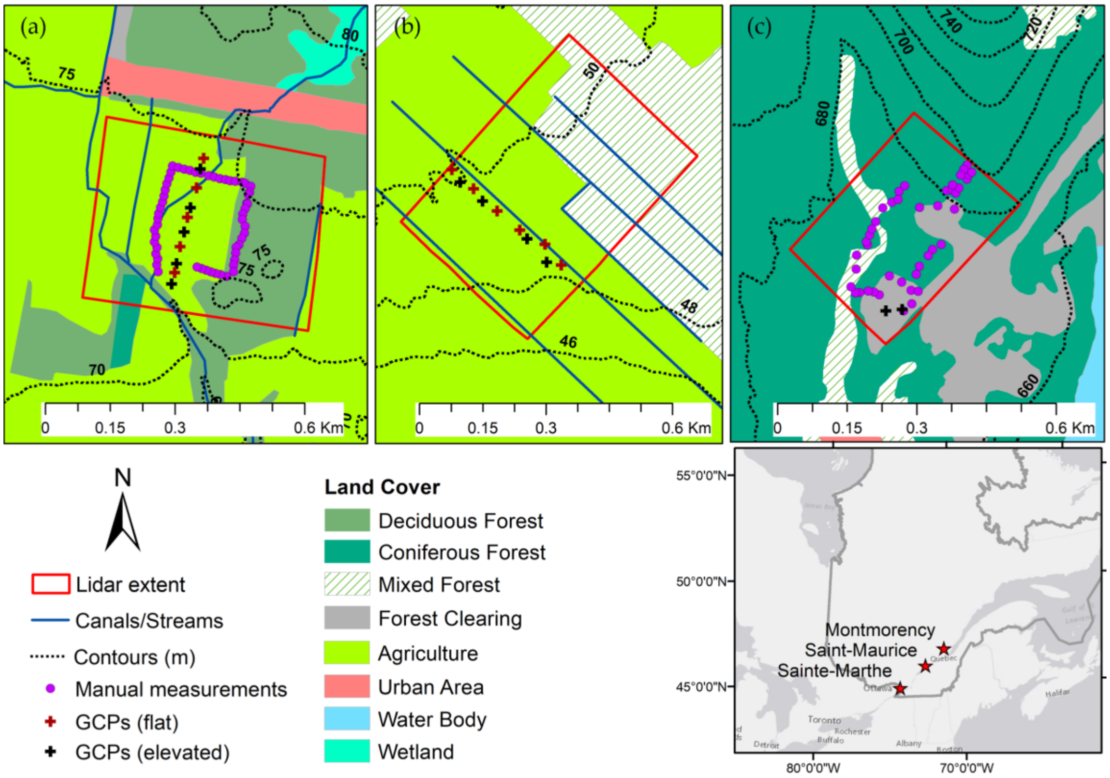

Figure 1.1. Overview of the study sites with lidar survey extents. (**a**) Sainte-Marthe; (**b**) Saint-Maurice; and (**c**) Montmorency. Manual measurement and ground control point (GCP) locations are also shown. (Manual measurements in Saint-Maurice could not be retrieved due to a probe malfunctioning, thus they are not shown). Contour intervals deliberately differed between sites for interpretation purposes.

Table 1.1. Site characteristics and field campaign details.

	Sainte-Marthe	Saint-Maurice	Montmorency
Elevation range, m	70–78	46–50	670–700
MAAT, °C	6.0	4.7	0.5
Total precipitation, mm	1000	1063	1600
Snowfall/Total Precipitation, %	15	16	40
Winter season	November–March	November–March	October–April
Lidar extent, km^2	0.22	0.25	0.12
Snow-off flight date	11 May 2020	02 May 2020	13 June 2019
Snow-on flight date	12 March 2020	11 March 2020	29 March 2019

Average snow depth, m	0.32	0.60	1.40
Number of manual measurements	56	- [a]	43

MAAT: Mean annual air temperature; [a]: Manual snow depth measurements could not be retrieved due to a probe malfunctioning.

1.2.2 Data Acquisition

Field campaigns were carried out in summer for the snow-free surface and in winter for the snow-covered surface with UAV lidar (Table 1.1) in 2019 and 2020. Simultaneous manual snow depth measurements were taken on the same day of the winter–UAV lidar flights to later validate the UAV-derived snow depths. Winter surveys were targeted to capture near-peak snow accumulation. Figure 1.2 depicts the site conditions during snow-off and snow-on surveys.

Figure 1.2. (**a**) Sainte-Marthe site during summer survey and (**b**) during winter survey; (**c**) presence of basal ice layer in Sainte-Marthe field; (**d**) Saint-Maurice site during summer survey and (**e**) during winter survey; (**f**) Montmorency site during summer survey and (**g**) during winter survey; (**h**) local snow accumulation in a forest gap in Montmorency boreal forest.

1.2.2.1 Lidar System

A Geo-MMS lidar mapping payload mounted onto a DJI M600 Pro UAV platform was used for the surveys (Figure 1.3). This Geo-MMS UAV lidar system is manufactured by Geodetics Inc., San Diego, USA and is comprised of a Velodyne VLP-16 lidar sensor coupled to a real-time, dual-antenna GNSS aided inertial navigation system (INS). The INS, called Geo-iNAV, is comprised of a tactical MG364 Quartz Micro

Electro Mechanical (MEMS) IMU, a high performance dual-core processor, a data recorder, and two dual-frequency GNSS receivers. The VLP-16 sensor uses 16 infrared lasers (wavelength of 905 nm) each pulsating at 18.08 kHz and retrieves measurements up to 600,000 points/s in dual return mode, with a 3 cm precision at 50 m above ground level (AGL) (VelodyneLiDAR, 2018). The Geo-iNAV INS provides positional accuracy of 5 cm in horizontal and 10 cm in vertical dimensions with a 0.1 and 0.3° accuracy in roll/pitch and heading, respectively (Geodetics, 2018). Based on the manufacturer specifications, the Geo-MMS can meet a ±5 cm (RMS, root mean square) accuracy of the point cloud. The UgCS flight control software (2019) developed by SPH Engineering, Latvia was used to generate terrain-following flight paths with respect to an underlying shuttle radar topography mission digital elevation model (SRTM DEM). Flight parameters were optimized to reduce overall INS errors and maximize the mapping efficiency in the forested areas. Maximum flight time with one battery set was conservatively limited to 15 min. Depending on the extent of the surveying area, our flight plans included multiple return flight paths with two or three battery exchanges. Flight parameters used for the surveys are outlined in Table 1.2.

Figure 1.3. UAV lidar system.

Table 1.2. Flight parameters.

Flying speed	3 m/s
Flight altitude	40 m AGL
Lidar RPM	1200
Field of view	145°
Distance between parallel flight lines	64 m
Ground overlap	20%
Point density	603 points/m^2

1.2.2.2 Ground Control Points (GCPs)

GCPs were used to assess the absolute accuracy of lidar data (in the vertical dimension, z) in all three survey areas. In the Montmorency site, two permanent structures were utilized as GCPs, whereas at other sites, in the absence of static structures, two types of temporary targets, circular-shaped elevated (1 m diameter) ones, and square-shaped flat (0.5 x 0.5 m) ones (Figure 1.4) were employed. Elevated targets were used in both winter and summer surveys, while flat targets were only used in summer surveys. Locations of the GCPs are shown in Figure 1.1. Geographical coordinates of the GCPs were measured using PPK surveys. Each target was surveyed at 1 Hz for 5 min using a FOIF A30 GNSS receiver. Each static survey was post-processed relative to another A30 base receiver deployed at each site. Figure 1.2d,f shows the deployment of A30 base stations in Saint-Maurice and Montmorency. Nominal horizontal and vertical accuracies of the PPK surveys were 3 and 3.5 mm, respectively.

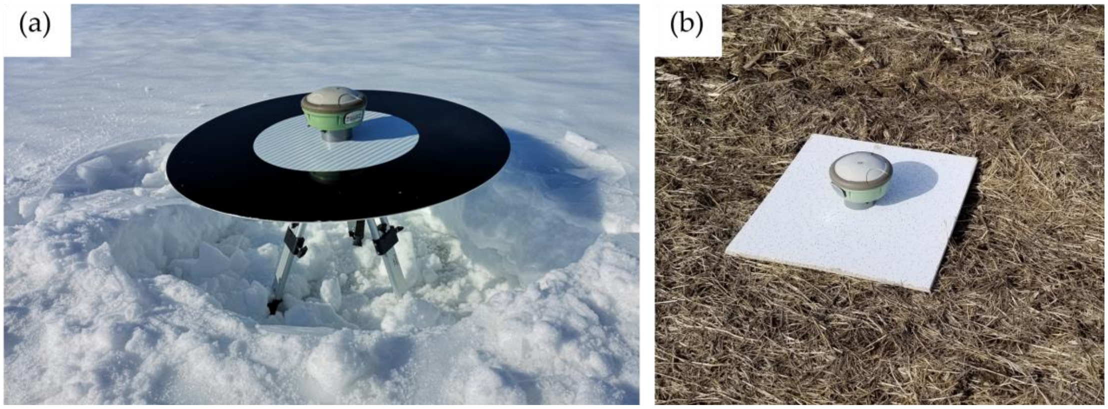

Figure 1.4. Manmade GCPs: (**a**) Elevated and (**b**) flat. Photos were taken after the lidar surveys with FOIF A30 GNSS receiver on the target surface.

1.2.2.3 Ground Validation Surveys

To assess the lidar-derived spatially distributed snow depth retrievals, we used ground-based manual snow depth measurements taken simultaneously with the lidar flight (Table 1.1). Snow depth transects were taken in a manner that effectively samples the different vegetation types and pronounced topographical characteristics at the respective sites (Figure 1.1). Snow depths were measured using a Magna probe (Sturm and Holmgren, 2018) in Sainte-Marthe and Saint-Maurice and a snow tube in Montmorency. The Magna probe automatically measures and stores the snow depth in a data logger. Unfortunately, the snow depth measurements at Saint-Maurice were lost due to a probe malfunctioning, which prevented the data recording. At each location, five measurements were taken and averaged to achieve more representative snow depths. Measurements were taken as one point in the center, and four points 1 m away from the center in a diagonal cross shape. The geographical coordinates of the center measurement were obtained using RTK surveys relative to a FOIF A30 base receiver deployed at each site (Figure 1.2d,f). Nominal horizontal and vertical accuracies of the rover points relative to the base in RTK mode are 8 and 15 mm. RTK signal can be degraded in forested areas due to the multipath error (Valbuena et al., 2010). Therefore, positional accuracy was expected to be lower than the nominal accuracy in forested areas, especially in Montmorency.

1.2.3 Data Processing

Figure 1.5 presents the workflow developed to produce snow depth from lidar data.

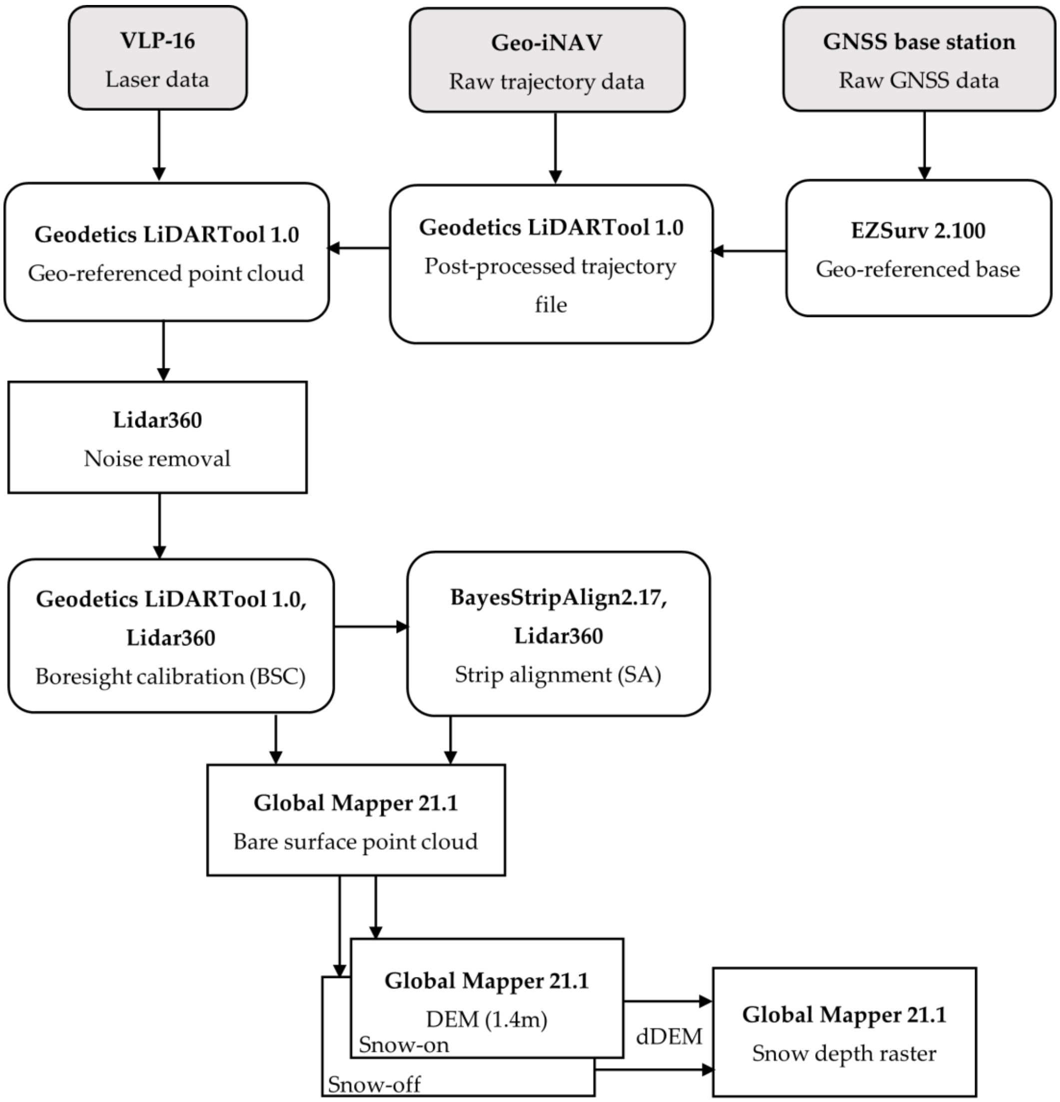

Figure 1.5. Data processing workflow of lidar data. Each box shows the software used (bold) with the corresponding end product.

1.2.3.1 GNSS Data Processing

Post-processing of GNSS data was carried out in EZSurv software (Effigis, 2019). Base station locations varied between flights. The base station of the first survey in Sainte-Marthe was geo-referenced to the closest available geodetic marker (Ministry of Energy and Natural Resources, 2020). Due to the unavailability of geodetic markers in the vicinity of the other two sites, the processing of base stations of the first surveys (summer or winter, no matter which one was conducted first, see Table 1.1) was carried out using the PPP option in EZSurv. Since the location of the GNSS base station changed on the second survey, we used three permanent structures—reference post—(light post, two logger boxes of weather instrument) in the vicinity of the three sites as reference points to co-register the two lidar surveys conducted in summer and winter. In summary, the GNSS data processing of the snow-off and snow-on surveys involved two steps:

(1) First survey: PPP of the base, then PPK of the reference post, drone, and GCPs;

(2) Second survey: PPK of the reference post, calculate the coordinates of the new base using the positional shift of the reference post relative to the first survey, PPK of the drone, and GCPs using the corrected base coordinates.

Manual snow depth measurements were processed as RTK and registered to the reference post. The standard deviation of PPP computed and further processed base stations was consistently lower than 0.01 m. The uncertainty of RTK manual snow depth survey points varied among sites and their respective land cover (field and forest). Horizontal standard deviation in Sainte-Marthe forest ranged between 0.327–3.091 m with RTK float solutions (low quality and less confident) and 0.003–0.081 m with RTK fixed solutions in the field. The higher range of values in the forest implies the higher uncertainty of GNSS measurements in the forest. In Montmorency, the average horizontal RTK accuracy was 0.008 m. Horizontal standard deviation in Montmorency forest ranged between 0.002–0.034 m and 0.002–0.007 m in the field, both with RTK fixed solutions. Nevertheless, the uncertainty of RTK solutions in Montmorency forest could be significantly higher than the values indicated here due to the multipath effect (Hopkinson et al., 2004; Valbuena et al., 2010).

1.2.3.2 Raw Lidar Data Processing

A geo-referenced lidar point cloud requires post-processing of IMU and GNSS data. First, high-frequency raw trajectory data (x,y,z, heading, pitch, roll) from the Geo-iNAV INS was post-processed in the Geodetics proprietary software LiDARTool (Geodetics, 2019b) with PPK correction. The PPK option regenerates a significantly more accurate trajectory file by correcting the onboard GNSS data with the GNSS base station data (Geodetics, 2019b). Then, this post-processed trajectory file was merged with the raw laser data to produce a geo-referenced x,y,z point cloud. To reduce the noise level of lidar data, the outer beams of the VLP-16 lidar, where the noise level is highest (Geodetics, 2019b), were discarded from processing (i.e., only the laser beams between ±8° from the full ±15° vertical field of view were used in processing). The outlier removal tool in LiDAR360 (GreenValley-International, 2020) removed the remaining low and high noisy data present in lidar data (Figure 1.5).

1.2.3.3 Boresight Calibration

As depicted in Figure 1.5, while lidar direct geo-referencing with post-processed trajectory and GNSS data is quite precise in the position and orientation of each point cloud, it can be prone to errors if the alignment of the laser sensor to the INS is not precisely known. Quite often, the manufacturer’s calibrated boresight shift and angles of the laser frame to the platform body frame can be slightly offset upon reassembling of the laser sensor on the Geo-iNAV system. This problem can be solved by a boresight calibration. Once calibrated, these values remain constant as long as the lidar sensor payload is not disassembled (Geodetics, 2019b). For this purpose, we first manually and precisely measured the lever arm distances between the laser sensor and IMU center. To find the boresight angles, the manufacturer recommends a manual adjustment with a trial-and-error procedure (Geodetics, 2019b). To achieve this, test flights were carried out in the University of Québec at Trois-Rivières premises in April 2019 by flying the Geo-MMS system in different directions over a flat roof and an inclined surface to calibrate the boresight angles (Figure 1.6a). Processing and visualization of the data collected by the system were carried out in Geodetics LiDARTool and LiDAR360, respectively. The test flights were conducted with the nominal boresight angles (90, 0, −90° in roll, pitch, heading) and the misalignment between flight strips was analyzed in all three rotational axes. Calibration of the boresight angles was initiated with the heading angle. Two opposite direction strips covering the roof edges were selected, plotted together, and the top view alignment was checked. Since the roof edges seem to be misaligned (Figure 1.6b), the nominal heading angle was increased in a small step of 1° (90, 0, −91° in roll, pitch, heading) and the flight strips were re-processed in LiDARTool. Then, the re-processed flight strips were checked to inspect the impact of the angle change along the roof edges from a top view of the roof. Generally, if two flight strips become more aligned/converged compared with nominal values and if there was still room for convergence, the heading angle was increased in small steps in the same direction (e.g., −92°), otherwise, the angle was increased in the opposite direction (e.g., −89°). Then, the step size was progressively narrowed (e.g., down to 0.1°) when the two strips started converging. This process was continued until a good alignment between flight strips along the heading was achieved (Figure 1.6c). Once the heading angle was calibrated, and by maintaining the calibrated heading angle, the same procedure was followed to calibrate the pitch and roll angles by checking the misalignment of adjacent flight strips over the inclined surface in the side view in LiDAR360 (Figure 1.6d,e). The calibrated boresight angles obtained from this procedure for our system were 90.1, 0.28, and −90.6° in roll, pitch, and heading, respectively. Figure 1.6c,e illustrates the noteworthy improvement of the alignment of the flight strips after boresight calibration. Then, these boresight angle values were used to process data collected from all the flights in this study.

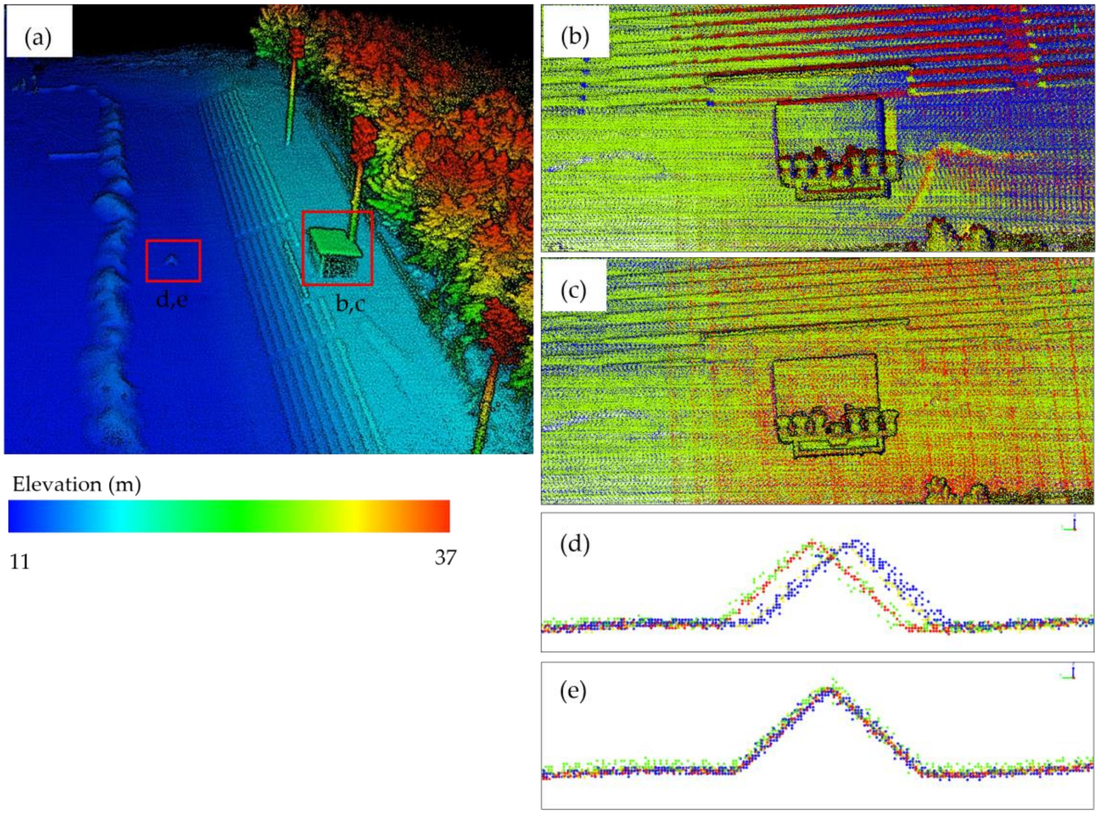

Figure 1.6. An example plot of the boresight calibration procedure. (**a**) 3D view of the calibration site, lidar point cloud is colorized by elevation (roof structure and inclined surface are demarcated in red squares with relevant letters); (**b**) top view of the roof structure for nominal boresight angles and (**c**) for calibrated boresight angles; (**d**) cross-section view of the inclined surface for nominal boresight angles and (**e**) for calibrated boresight angles. Points scanned from different strips have different colors (red, blue, yellow, and green).

1.2.3.4 Strip Alignment

We tested an automatic strip alignment algorithm implemented in BayesStripAlign 2.17 software developed by BayesMap solutions, USA, (2020) to assess whether it can improve upon the manual boresight calibration procedure. The strip alignment algorithm in BayesStripAlign registers overlapping lidar flight strips and uses relative displacement calculated between those overlapping strips to correct both relative and absolute geometric errors. The goal of the process is to have the smallest possible absolute corrections, while achieving the maximum relative accuracy. The algorithm uses a spatially adaptive approach to address time-dependent effects, such as drifts and oscillations (i.e., high-frequency IMU drifts and oscillations), which cannot be corrected with a classical sensor calibration, and thus effectively reduces the discrepancies between flight strips. Within the algorithm, systematic effects are absorbed by the x and y lever arms, boresight angles, and internal distortion corrections. The high-frequency components of the random walk IMU noise are mainly treated by high-frequency drift corrections. After testing the algorithm with different combinations of aforementioned parameters on the flight strips, the best alignment of overlapping flight strips was found for the automated calibration and correction of the y lever arm, boresight angles, and use of a rigorous model to capture internal distortions and with 5 s intervals for high-frequency drift corrections. This combination of parameters found for our dataset was reviewed and verified by the software developer. BayesStripAlign allows for the control of the absolute accuracy of corrected point cloud using GCP information. The version used in this study includes the automatic detection of GCPs based on local terrain roughness and the calculation of bias using interpolated and gridded lidar data. Each point at GCP locations is weighed using inverse terrain roughness before the absolute accuracy statistics are computed. Unfortunately, the automatic detection of GCPs based on this roughness method did not work well with the elevated GCPs used, and thus this option was excluded from the analysis.

1.2.3.5 Bare Surface Points Classification

Snow depth mapping requires a classification of the point clouds into the bare surface, ground (from summer survey) or snow (from winter survey). We used the multiscale curvature classification (MCC) algorithm (Evans and Hudak, 2007) implemented in the commercial Global Mapper software (2020) to classify bare surface points. The Global Mapper lidar module identifies possible ground points by employing a morphological filter prior to the application of the MCC algorithm. The morphological filter uses three user-defined parameters of the maximum height difference, expected terrain slope, and maximum building width. MCC uses two user-defined parameters, bin size and minimum height difference from the local mean. Parameters of the algorithm were adjusted according to the vertical spread of the flight strips over open terrain, the local slope of the terrain and streams, and the presence/absence of buildings. A bin size of 0.5 m, a minimum height difference of 0.2 m, a maximum height difference of 10 m, expected terrain slope of 10° in Sainte-Marthe and Saint-Maurice sites and 20° in Montmorency, and a maximum building width of 10 m were found as the optimum parameters for the sites in both seasons. To classify the bare surface points of streams and visible snowbanks, the algorithm was implemented by selecting these areas manually and adjusting the abovementioned parameters to 0.5 m, 0.35–0.45 m, 10 m, 40–70°, and 10 m, respectively. Following a careful inspection of the classified bare surface points, some misclassified points in forested areas were manually reclassified as bare surface.

1.2.3.6 Snow Depth Maps

Snow depth rasters were produced by differencing winter and summer DEMs. DEMs were generated by aggregating bare surface points at each site to a grid resolution of 1.4 m using the binning method in Global Mapper. This method takes the average of the bare surface points that fall inside a grid cell, rather than interpolating. Observation gaps in the point cloud were assigned as no data (i.e., no interpolation method was used to fill the gaps in the DEMs). With the high point density obtained from UAV lidar, this method would ensure that the generated DEMs were of reasonable representations of the true ground/snow surfaces. The grid resolution of 1.4 m was selected based on the manual sampling strategy outlined in Section 1.2.2.3 (i.e., five measurements at each sampling location represented a 1.4 × 1.4 m ($\sqrt{1^2+1^2}$) grid cell) and aimed at minimizing the effect of GNSS positional errors on manual measurements. As final filtering, spurious negative snow depths were set to zero as they are physically impossible and needed to be filtered out (Hopkinson et al., 2012a). Negative snow depths were found along the access roads, stream banks, and forested areas. Negative snow depths along access roads could be due to the snow clearing operations in winter. Compressed grasses or shrubs due to snow, and/or misclassification errors, and local changes in topography could be the reason for negative snow depths along stream banks and in forests. However, all these values are rather small in magnitude, accounting for a small portion of the total area (<0.1%) sampled and had a negligible effect on our snow depth statistics. DEMs and snow depth maps derived before applying the strip alignment (i.e., rasters derived after manual boresight calibration only) are denoted as "BSC" and those derived after applying the strip alignment are denoted as "SA".

1.2.4 Data Analysis

We assessed the accuracy of UAV lidar in terms of absolute and relative accuracies in the vertical direction (z). The absolute accuracy was determined by comparing the GNSS elevation of the GCPs with those obtained from the lidar data. The relative accuracy between the overlapping flight strips was obtained as a direct output from BayesStripAlign. In addition, one repeat summer flight was conducted on the same day in Sainte-Marthe and used to further assess the spatial distribution of relative errors of the lidar data. The relative accuracy statistics were calculated for the DEM created by differencing the two repeat summer DEMs. The manual snow depth measurements were finally used to validate the lidar-derived snow depth maps. The lidar-derived snow depth error was estimated by comparing each manual measurement to its corresponding 1.4 m grid cell snow depth. The locations of the GCPs and manual measurements are indicated in Figure 1.1. The error metrics employed to assess accuracies, include the mean (bias), standard deviation (sd), and root mean square error (RMSE).

1.3 Results

1.3.1 Accuracy Assessment of Lidar Point Cloud

1.3.1.1 Absolute Accuracy of Lidar Data

Absolute error statistics calculated for the lidar point cloud are presented in Figure 1.7. Generally, SA shows an inferior performance, with higher RMSE values than BSC. All BSC results show that the RMSE values are closer to the nominal accuracy of the lidar system (0.05 m), while the majority of the SA RMSE values are higher.

With the BSC method, winter surveys consistently show a lower RMSE, bias, and sd than summer surveys in both Sainte-Marthe and Montmorency. In contrast, the absolute accuracy was slightly better in summer than winter at Saint-Maurice. With the exception of Montmorency, the other two sites generally exhibit a small bias compared with the spread (sd) for both seasons with the BSC method. The SA method exhibits a different pattern: The winter RMSE, bias, and sd are higher at Saint-Maurice and Montmorency than in summer, while Sainte-Marthe shows an opposite tendency. On the other hand, the SA method appears to consistently increase the bias of the BSC data.

Moreover, it seems to decrease the summer sd of the BSC data, but increase it in winter, except in Sainte-Marthe.

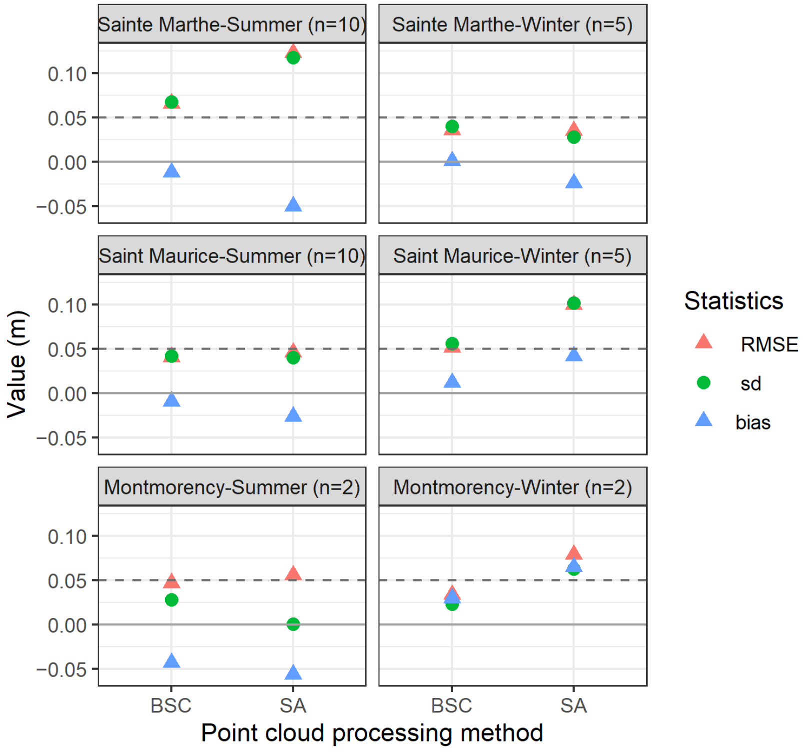

Figure 1.7. Absolute error statistics of lidar point clouds. Plots are segmented by site (rows), data processing method (columns), and error statistics (colors). The grey dashed line is the expected accuracy of the lidar system. *n* denotes the number of GCPs. BSC: Boresight calibrated point cloud; SA: Boresight + strip-aligned point cloud. (Bias was calculated as lidar-derived DEM elevation – GNSS elevation at GCPs).

1.3.1.2 Relative Accuracy of Lidar Data

The relative RMSE error is a combination of errors from two co-registered point clouds at the same location. The expected uncorrelated relative error for lidar data is approximately 7 cm ($\sqrt{5^2+5^2}$). As seen from Figure 1.8, SA significantly improved the inter-strip relative accuracy of the BSC data. For example, the large biases in Sainte-Marthe summer and Montmorency winter BSC data were notably reduced after the application of SA. All SA statistics are closer to zero, and well below the nominal error of lidar data.

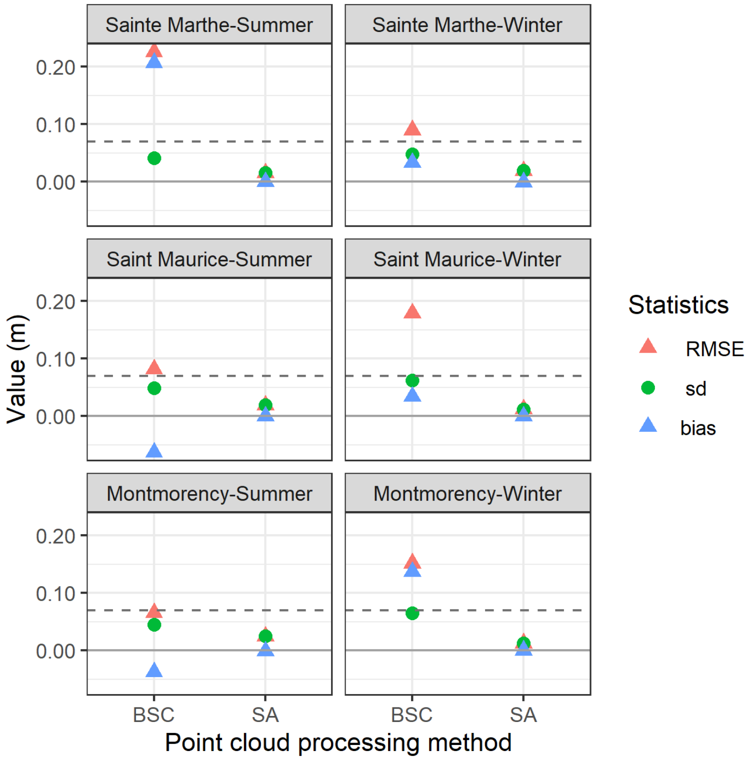

Figure 1.8. Relative error statistics between overlapping flight strips.

Repeat flight statistics provide an insight into the probable error values we could expect in snow depth maps, as shown in Figure 1.9. Accuracy statistics show that relative errors are larger (Figure 1.9a) and more variable (Figure 1.9b) in the forested area compared with the field area. SA appears to consistently increase the BSC bias, while decreasing the BSC sd, partly in line with the inter-strip relative statistics found in Figure 1.8. The estimated RMSE values for the two processing methods in all landscape units are well below the nominal error (Figure 1.9a).

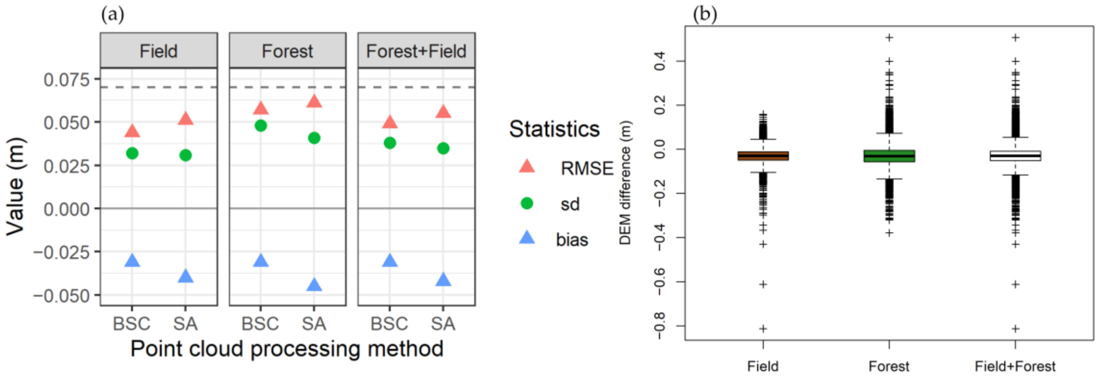

Figure 1.9. (**a**) Relative error statistics from repeat flights in field, forest, and the combined landscape for the two point cloud processing methods; (**b**) relative error distribution in field, forest, and the combined landscape of the BSC data.

1.3.2 Accuracy Assessment of Snow Depth Maps

1.3.2.1 Lidar-Derived Snow Depth Maps

Snow depth maps were produced for four cases corresponding with the BSC and SA methods and their bias-corrected versions (BSC_BC and SA_BC; BC: Bias-corrected). The bias-corrected DEMs were produced by directly subtracting the bias estimated from the absolute accuracy assessment (Figure 1.7) to each winter and summer DEM before deriving the snow depth map. Figure 1.10 shows the snow depth maps derived from UAV lidar data. The overall snow depth patterns among the different processing methods did not significantly differ, thus only the maps from the BSC processing method are shown here.

The highest snow depths are found at the colder and more humid Montmorency site, specifically in forest gaps (Figure 1.10: Number 4). Higher snow accumulation in streams (Figure 1.10: Number 1) and along the forest edges (Figure 1.10: Number 2) is apparent at the two agro-forested sites. Access roads in Sainte-Marthe and Montmorency (Figure 1.10: Number 3) are snow-free due to snow clearing operations.

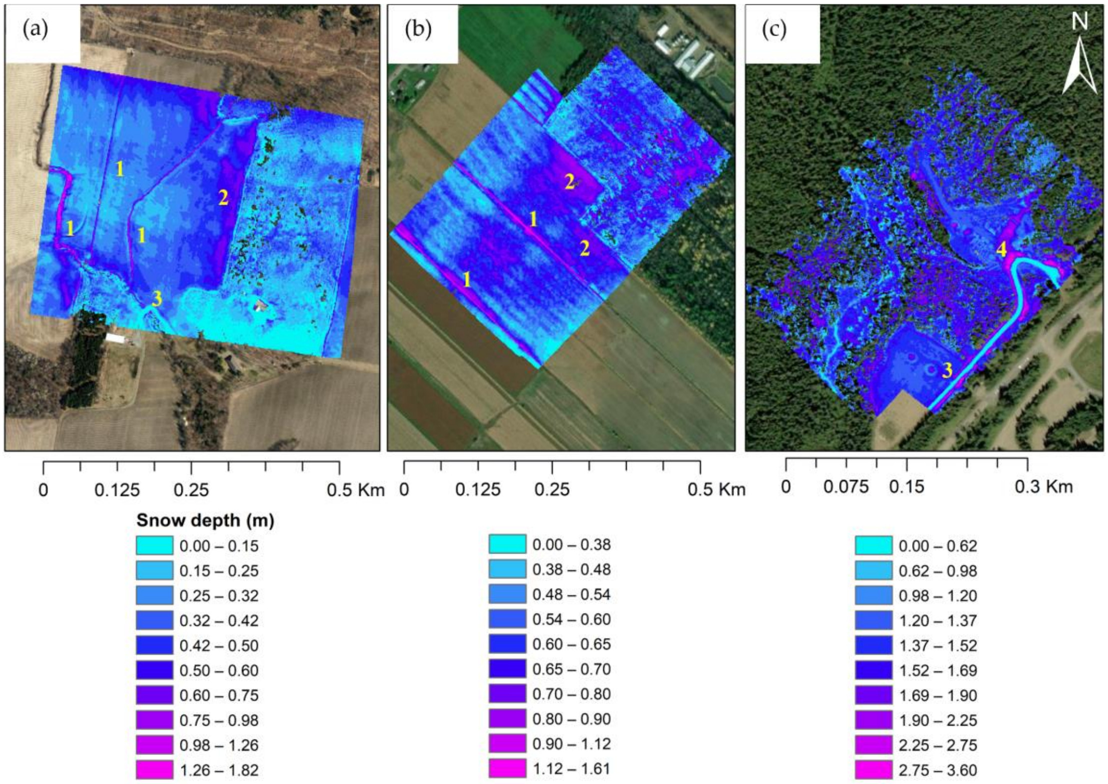

Figure 1.10. UAV lidar-derived snow depth maps. (**a**) Sainte-Marthe; (**b**) Saint-Maurice; and (**c**) Montmorency. Features 1 to 4 are discussed in the text.

1.3.2.2 Snow Depth Validation

The validation of UAV lidar-derived snow depths with manually sampled ground measurements is shown as boxplots in Figure 1.11. The boxplots illustrate the discrepancy between the lidar and manual snow depths in the field and forest at each site for the four processing methods, BSC, BSC_BC, SA, and SA_BC.

As seen in Figure 1.11, boxplots of the Sainte-Marthe field, forest, and Montmorency field show on average a consistent overestimation (positive bias) of lidar snow depths, whereas in Montmorency forest, lidar snow depths seem to be mostly underestimated for all methods. Owing to their different characteristics, field and forest areas in the two sites show contrasting behaviors in terms of lidar snow depth accuracy. In Sainte-

Marthe, field snow depths consistently show a higher error dispersion (RMSE = 0.16–0.22 m) than the adjacent deciduous forest (RMSE = 0.079–0.12 m). On the other hand, the small open field in Montmorency exhibits a smaller and less dispersed error (RMSE = 0.043–0.17 m) than the adjacent boreal forest (RMSE = 0.19–0.22 m). The influence of vegetation type is apparent in Figure 1.11, where the leaf-less deciduous forest in Sainte-Marthe has a smaller RMSE (0.079–0.12 m) compared with evergreen coniferous trees of Montmorency (0.19–0.22 m).

Sainte-Marthe BSC and BSC_BC show a similar performance in both field and forest (Figure 1.11 a,b). This suggests that the small bias of ≤1 cm in each DEM (Figure 1.7) does not contribute significantly to errors in the final snow depth map. Compared with BSC, SA displays higher RMSE and bias in both field and forest at this site. Despite the slightly better RMSE and bias values of the SA_BC method in comparison with SA, its performance remains inferior to the BSC and BSC_BC methods. In contrast with Sainte-Marthe, BSC_BC shows a lower RMSE and bias in Montmorency field, but a higher RMSE and bias in Montmorency forest, compared with BSC. However, similar to Sainte-Marthe, SA results in a substantial increase in RMSE and bias in the field, but only a minor change in the forest. SA_BC statistics are better than SA in the field, but are still higher than the BSC_BC method. Moreover, the SA_BC method in Montmorency forest shows the highest RMSE and bias among all cases.

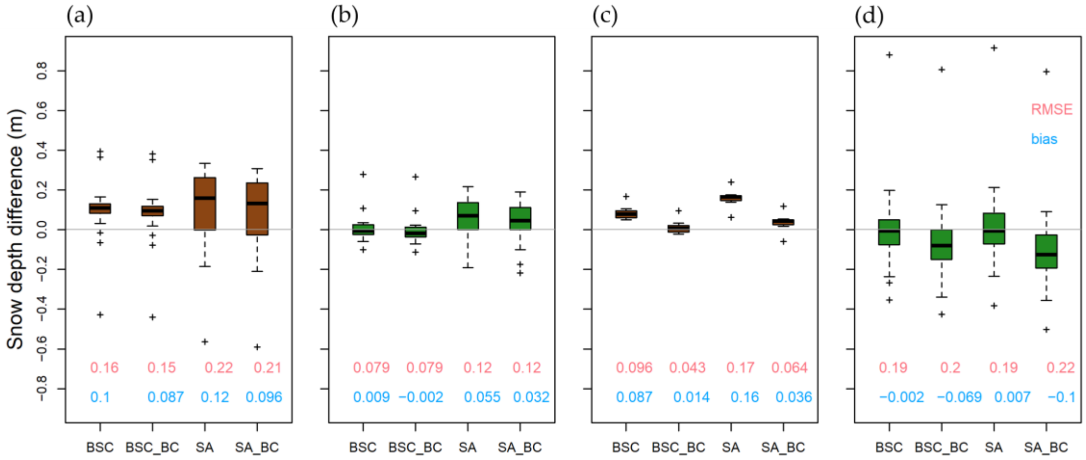

Figure 1.11. Distribution of the differences between lidar and manual snow depth for the different point cloud processing methods. (**a**) Sainte-Marthe field; (**b**) Sainte-Marthe forest; (**c**) Montmorency field; and (**d**) Montmorency forest. BSC: Boresight calibrated point cloud; SA: Boresight + strip-aligned point cloud; BSC_BC: Bias-corrected BSC data; SA_BC: Bias-corrected SA data. Outliers are indicated by "+" symbol in boxplots.

1.4 Discussion

As previously mentioned, error sources in lidar mapping can stem from boresight errors, navigational errors, terrain-induced errors, vegetation-induced errors, and post-processing errors (Deems et al., 2013; Pilarska et al., 2016). In this study, boresight errors were minimized by a careful boresight calibration. Furthermore, navigational errors posed by the system were minimized by implementing fine alignment (IMU calibration by maneuvering the Geo-MMS through several turns at different velocities prior to the system entering the scanning area (Geodetics, 2019a)), deploying a base station at each site, and using the PPK post-processing technique to correct the Geo-MMS positions. The elevation ranges were small at all sites, as were the slopes (mean grid slopes are 3, 2, and 7° in Sainte-Marthe, Saint-Maurice, and Montmorency, respectively). Therefore, terrain-induced errors are assumed to be minimum. Flight parameters, such as flight height, lidar rotational speed (RPM), overlap, and scan angle were optimized to obtain maximum penetration and minimum occlusion of lidar in the forested area, and thus mitigating errors posed by vegetation. Extensive manual inspection was conducted after each ground point classification to identify any misclassification errors and correct them when necessary. In addition, there could be errors in lidar-derived snow depth products due to changes in microtopography between snow-off and snow-on surveys. For instance, changes of the soil surface due to freezing, possible plowing in agricultural fields, compression of vegetation by snow, and state of understory vegetation could cause spurious and/or negative lidar snow depths (Harder et al., 2020; Jacobs et al., 2021). Since our snow-off surveys were carried out shortly after the last snowfall with leaf-off deciduous canopy and sub-canopy conditions, and before the growing season begins, it is expected to have minimal changes to the soil surface and minimum effects from vegetation to ground retrievals (Evans et al., 2009; Hopkinson et al., 2004). A good agreement with the lidar-derived snow depths with manually sampled ground measurements in this study implies that these errors, if present, were small overall. Our results demonstrate that while there are still errors in UAV lidar, as with any measuring technique, they are within the expected system accuracy and consistent.

1.4.1 Comparison of Lidar Point Cloud Accuracy to Previous Studies

Similar to the findings of Harder et al. (2020), our BSC absolute accuracy statistics (Figure 1.7) generally show a better performance in winter. In contrast, SA absolute accuracy statistics showed an inferior performance in winter (except in Sainte-Marthe), most probably due to reduced micro topographical contrasts in the winter point clouds that are used by the strip aligning algorithm to match strip segments. The number of GCPs may also have impacted the accuracy assessment. For example, the use of only two GCPs in Montmorency might not be sufficient to assess the notably high bias observed in Montmorency. Despite this, all BSC results show RMSE values closer to the nominal error of the lidar system (0.05 m), which implies that the collected data were of acceptable accuracy. As expected, SA substantially reduced elevation (z) discrepancies between flight strips. This implies that the application of strip alignment effectively helped in rectifying the misalignment between corresponding segments of overlapping BSC strips. However, the results suggest that this significant improvement in relative accuracy brought by SA was at the cost of the absolute accuracy of lidar data.

Relative error statistics in Figure 1.9 show that the errors are generally higher and more variable in the forest than in the field area. Lidar data are expected to be more prone to errors in the forest depending on the canopy cover density, the presence of sub-canopy cover, and the lidar ability to penetrate through canopy gaps and reach the ground/snow surface. This observation is analogous to previous studies (Harder et al., 2020; Jacobs et al., 2021), which observed a higher RMSE in the presence of vegetation compared with open areas in their studies. Moreover, Jacobs et al. (2021) noted that reduced lidar returns combined with sampling issues contributed to the higher uncertainty of snow depths in the forest compared with open areas in their study.

1.4.2 Sources of Uncertainty in Lidar-Derived Snow Depths

In general, the snow depth validation error statistics (Figure 1.11) exhibited higher values than the probable errors estimated from the relative accuracies (Figure 1.9) across all sites. These higher errors can be explained by site characteristics.

1.4.2.1 Sainte-Marthe Snow Depths

The higher and more variable snow depth RMSE in the Sainte-Marthe field compared with the adjacent deciduous forest can be explained by the deep, narrow canals/streams in the field (Figures 1.1 and 1.10) and the presence of basal ice layers in the snowpack. The notable positive bias in lidar-derived snow depths indicates an overestimation of snow depths by UAV lidar, mostly in the field, as shown by the distinctive higher lidar snow depths for measurements in the area shaded in brown color in Figure 1.12 (measurement ID 1–31 and 51–56). In contrast, Jacobs et al. (2021) and Harder et al. (2020) reported slightly low (negative) biases of lidar snow depths compared with manual soundings in a field by UAV lidar in Durham, the United States and Alberta and Saskatchewan, Canada respectively (however, these authors have not reported a presence of basal ice layer in their study sites). As both summer and winter DEMs in this study have biases less than 1 cm, which causes minimal systematic bias in the final snow depth maps, this remaining bias of the lidar snow depths can be attributed to the presence of the ice layers. We observed a 2–10 cm thick ice layer at the base of the snowpack in the field during manual measurements (Figure 1.2c), which limited the ability of the probe to reach the soil surface. Therefore, in these cases, the lidar measurements are in fact deemed to be more accurate than the manual soundings. As well, as can be observed from Figure 1.10, snow depths in the streams are twice as deep as the adjacent terrain since snow drifting fills the canals. At locations where the central snow depth manual measurement was directly inside the streams, the average of the five manual measurements was significantly higher or lower than the average lidar snow depths (refer to the range of snow depths at ID 2, 4, 6, 8, 10 in Figure 1.12), which reflected in higher outlier values (i.e., indicated as “+” in boxplots) of field boxplots in Figure 1.11a. This is thought to be the main reason for the high variability of errors in the field.

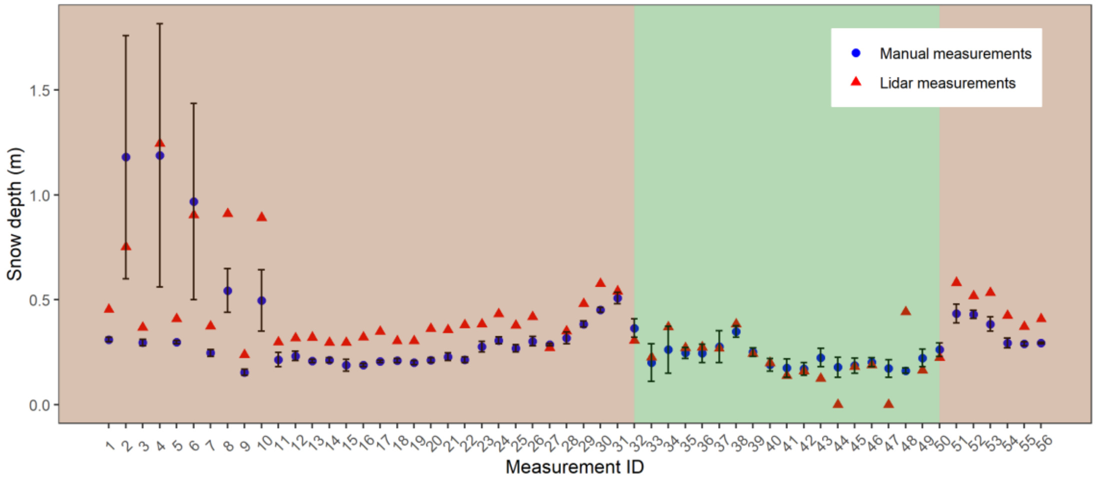

Figure 1.12. Variability of manual and lidar snow depth measurements in Sainte-Marthe. Error bars represent the minimum and maximum snow depth values of the five manual measurements taken at each sampling location and blue dots denote the average value of the five measurements. Measurements in the field (ID 1–31 and 51–56) and the forest (ID 32–50) are demarcated by brown and green colored shadings, respectively.

1.4.2.2 Montmorency Snow Depths

Similar to Sainte-Marthe, Montmorency field lidar snow depths show a positive bias. This could also be due to the presence of an ice layer and the snow tube's limited penetration ability (Jacobs et al., 2021). Compared with the field, forest lidar snow depth biases are only slightly greater (Sainte-Marthe) and lower (Montmorency) than from the manual soundings in both sites. This contrasts with previous findings from UAV lidar in the forest (Harder et al., 2020; Jacobs et al., 2021; Proulx et al., 2022), where they observed a notable underestimation (negative bias) of lidar snow depths than from the manual measurements compared with the open field. In their studies, the causes of these differences were partially attributed to the snow probe's ability to penetrate the soil and vegetation, e.g., Jacobs et al. (2021) and Proulx et al. (2022) suggested that the overprobing by the Magna probe into the thick leaf litter layer present in the forest might have caused the higher average Magna probe snow depths than lidar snow depths. Compared with Sainte-Marthe, Montmorency's snow depth validation in the coniferous forest does not show a large bias, but a larger dispersion (sd) which increases the RMSE. This larger variation (sd) is attributed to be mainly associated with positional errors caused by multipath effects that are reportedly occurring in areas with thick canopy cover (Hopkinson et al., 2012b; Hyyppä et al., 2005; Valbuena et al., 2010). Apart from the errors propagated from individual DEMs, misclassification errors in forested areas, and small branches that are compressed by snow can also cause errors in lidar snow depths. However, the higher RMSE in Montmorency has a comparatively smaller impact due to the deeper snowpack observed at the site, i.e., the relative RMSE error (RMSE/mean snow depth) in Montmorency (0.068–0.135) is much lower than the relative error (0.321–0.420) in Sainte-Marthe where the snowpack is shallower.

1.4.3 Comparison of Lidar Snow Depth Accuracy to Previous Studies

When the strip alignment is not used, the UAV lidar system is able to capture snow depths with a RMSE< 0.16 m in an open environment (including a basal ice layer) and a RMSE< 0.19 m in forests with different canopy covers. This is comparable with previous efforts with UAV lidar (0.09–0.17 m from open to coniferous environment) (Harder et al., 2020; Jacobs et al., 2021) and airborne lidar (0.09–0.35 m from open to coniferous environment) (Broxton et al., 2019; Harpold et al., 2014; Hopkinson et al., 2004; Painter et al., 2016; Tinkham et al., 2014; Zheng et al., 2016). Therefore, despite potential inaccuracies within the coniferous forested area, our results show that UAV lidar can be an efficient technique to capture high-resolution, on-demand snow maps within complex agro-forested landscapes.

1.4.4 Use of GCPs in UAV Lidar

While authors as Harder et al. (2020) have suggested that the low bias of UAV lidar errors, without incorporating GCPs, would remove the need of deploying GCPs at the site, we believe that at least a few GCPs are required in natural environments, such as Sainte-Marthe and Saint-Maurice, where distinct manmade structures, such as buildings and roof structures are not present to control for systematic biases in repeat flights. In these environments, GCPs would ensure an absolute check of the lidar dataset and provide a quantitative assessment of the bias, and thus would help in correcting the bias of the data. Csanyi and Toth (2007) also highlighted the importance of using well-defined lidar-specific GCPs for applications with high accuracy requirements (e.g., survey-grade mapping). They showed that using specifically designed lidar targets (1 m radius circular-shaped elevated targets) could improve the lidar flight strip accuracies. Furthermore, they mentioned that in the absence of three-dimensional ground information, such as buildings and roof structures at site, the information from mobile lidar specific ground control targets can be used in or after the strip adjustment process to correct the remaining absolute errors in the corrected strips.

1.4.5 Use of Strip Alignment for UAV Lidar

Our results showed that while the SA algorithm improved the relative accuracy of the point clouds, its ultimate impact was to degrade the snow depth validation compared with the simple BSC method, even after bias correction. This observation was consistent in both field and forested areas, and at all sites. Possible reasons for this inferior performance can be attributed to the limitations of the algorithm used. The software version did not support the elevated GCPs used in this study, and thus did not use the GCP information during strip alignment, which led to degrading the absolute errors of the point cloud. It is not surprising that the SA exacerbated errors in winter, as there were fewer or no microtopographic features for the strip aligning algorithm to match the point cloud segments reliably in winter. Therefore, our results indicate that the SA implemented in this study is not suitable for similar UAV lidar applications, especially for monitoring snow depths. The main reason for using BayesStripAlign was for its ability to directly use the las and trajectory files rather than raw data from the laser scanner (Glira et al., 2016), which is not currently retrievable from the Geo-MMS system. However, our results could be used to improve the BayesStripAlign SA algorithm for further UAV applications in snow-covered landscapes.

1.5 Conclusions

This study demonstrated the ability of UAV lidar to measure snow depth variability under varying vegetation covers with reasonable accuracy. However, the observation gaps in ground returns in the coniferous forest imply that, despite the higher point density returned by the UAV lidar compared with ALS, airborne remote sensing techniques alone are not able to retrieve a comprehensive snow depth distribution pattern under a coniferous canopy. A combination of UAV lidar and ground-based manual measurement (or under and above canopy UAV lidar as demonstrated by Hyyppä et al. (2020)) might be beneficial to obtain more representative and extensive snow depths in coniferous environments.

The results showed that the strip alignment approach we used was not suitable for UAV lidar, since it degraded the absolute accuracy of the point clouds. The dataset would potentially benefit from a strip alignment algorithm that incorporates GCPs in the alignment procedure and/or uses that information in a 3D (x,y,z) adjustment of the point cloud.

Nevertheless, it can be concluded from the results that a careful boresight calibration can provide centimeter-level accuracy of lidar data without SA enhancement.

Therefore, boresight calibration should receive paramount attention in the data processing workflow. Moreover, a well-formulated flight plan plays a critical role in reducing system errors. Utilizing two or more turning maneuvers allows for better tuning of the IMU. Furthermore, flying at a lower altitude and slower speed reduces the impact of uncertainty in the boresight angles. Flight planning should also address weather conditions, for instance, flying the Geo-MMS in windy conditions (wind speeds higher than 8 m/s according to specifications) would degrade the sensor accuracies. The deployment of GCPs ensures an absolute check of data in the absence of distinct structures visible from airborne sensors. Importantly, a successful ground point classification is critical to the final accuracy of the snow depth maps. A manual inspection of the geo-referenced point cloud is advisable following automatic classification, preferably with geo-tagged imagery if available.

The methodological framework presented in this paper provides a valuable contribution to the UAV lidar accuracy assessments for snow research, which is reproducible in similar environments.

Acknowledgments

The authors extend their appreciation to the members of GlacioLab for their help during the fieldwork. Moreover, the authors are grateful to the Sainte-Marthe municipality, Québec, Canada and members of NEIGE_FM, Forêt Montmorency, Québec, Canada.

References

Aygün, O., Kinnard, C., and Campeau, S. (2020a). Impacts of climate change on the hydrology of northern midlatitude cold regions. Progress in Physical Geography: Earth and Environment, 44(3), 338–375. doi:10.1177/0309133319878123

Aygün, O., Kinnard, C., Campeau, S., and Krogh, S. A. (2020b). Shifting hydrological processes in a Canadian agroforested catchment due to a warmer and wetter climate. Water, 12(3), 739.

Barnett, T. P., Adam, J. C., and Lettenmaier, D. P. (2005). Potential impacts of a warming climate on water availability in snow-dominated regions. Nature, 438(7066), 303–309. doi:10.1038/nature04141

Bayesmap Solutions. (2020). BayesStripAlign 2.1 Software Manual. Retrieved from Mountain View, CA, USA: http://bayesmap.com/

Blue Marble Geographics. (2020). Global Mapper. Retrieved from Hallowell, ME, USA: www.bluemarblegeo.com/knowledgebase/global-mapper

Broxton, P., Leeuwen, W. J. V., and Biederman, J. (2019). Improving snow water equivalent maps with machine learning of snow survey and lidar measurements. Water Resources Research, 55, 3739–3757. doi:10.1029/2018WR024146

Broxton, P. D., Harpold, A. A., Biederman, J. A., Troch, P. A., Molotch, N. P., and Brooks, P. D. (2015). Quantifying the effects of vegetation structure on snow accumulation and ablation in mixed-conifer forests. Ecohydrology, 8, 1073–1094.

Chen, Z., Li, J., and Yang, B. (2021). A strip adjustment method of UAV-borne lidar point cloud based on DEM features for mountainous area. Sensors, 21(8), 2782. doi:10.3390/s21082782

Clark, M., Hendrikx, J., Slater, A., Kavetski, D., Anderson, B., Cullen, N. J., et al. (2011). Representing spatial variability of snow water equivalent in hydrologic and land surface models: A review. Water Resources Research, 47, W07539. doi:10.1029/2011WR010745

Csanyi, N., and Toth, C. K. (2007). Improvement of lidar data accuracy using lidar-specific ground targets. Photogrammetric Engineering & Remote Sensing, 73(4), 385–396.

Currier, W. R., and Lundquist, J. D. (2018). Snow depth variability at the forest edge in multiple climates in the western United States. Water Resources Research, 54(11), 8756–8773. doi:10.1029/2018WR022553

De Oliveira Junior, E. M., and Dos Santos, D. R. (2019). Rigorous calibration of UAV-based LiDAR systems with refinement of the boresight angles using a point-to-plane approach. Sensors, 19(23), 5224. doi:10.3390/s19235224

Deems, J. S., Fassnacht, S. R., and Elder, K. J. (2006). Fractal distribution of snow depth from lidar data. Journal of Hydrometeorology, 7, 285–297.

Deems, J. S., Painter, T. H., and Finnegan, D. C. (2013). Lidar measurement of snow depth: a review. Journal of Glaciology, 59(215), 467–479. doi:10.3189/2013JoG12J154

Dong, C. (2018). Remote sensing, hydrological modeling and in situ observations in snow cover research: a review. Journal of Hydrology, 561, 573–583. doi:10.1016/j.jhydrol.2018.04.027

Effigis. (2019). EZSurv User Manual Retrieved from Montreal, QC, Canada: http://www.onpoz.com/

Environment and Climate Change Canada. (2021). Canadian Climate Normals 1981-2010, Edited. Retrieved August 10, 2020 https://climate.weather.gc.ca/

Evans, J., Hudak, A. T., Faux, R., and Smith, A. M. S. (2009). Discrete return lidar in natural resources: Recommendations for project planning, data processing, and deliverables. Remote Sensing, 1, 776–794. doi:10.3390/rs1040776

Evans, J. S., and Hudak, A. T. (2007). A multiscale curvature algorithm for classifying discrete return LiDAR in forested environments. IEEE Transactions on Geoscience and Remote Sensing, 45(4), 1029–1038 doi:10.1109/TGRS.2006.890412

Gatziolis, D., and Andersen, H.-E. (2008). A guide to lidar data acquisition and processing for the forests of the Pacific Northwest. Retrieved from Portland, USA: https://www.fs.fed.us/pnw/pubs/pnw_gtr768.pdf

Geodetics, I. (2018). Geo-iNAV®,Geo-RelNAV®,Geo-PNT®,Geo-Pointer™,Geo-hNAV™,Geo-MMS™ and Geo-RR™ Commercial User Manual (Document 20134 Rev X). Retrieved from San Diego, CA, USA: https://geodetics.com/

Geodetics, I. (2019a). Geo-MMS User Manual (Document 20160 Rev B). Retrieved from San Diego, CA, USA: https://geodetics.com/

Geodetics, I. (2019b). LiDARTool™ User Manual (Document 20149 Rev I). Retrieved from San Diego, CA, USA: https://geodetics.com/

Glira, P., Pfeifer, N., Briese, C., and Ressl, C. (2015). A correspondence framework for ALS strip adjustments based on variants of the ICP algorithm. Journal of Photogrammetry, Remote Sensing and Geoinformation Science, 4, 275–289.

Glira, P., Pfeifer, N., and Mandlburger, G. (2016). Rigorous strip adjustment of UAV-based laserscanning data including time-dependent correction of trajectory errors. Photogrammetric Engineering and Remote Sensing, 82, 945–954.

GreenValley-International. (2020). LiDAR360 User Guide. Retrieved from Berkeley, CA, USA: https://greenvalleyintl.com/software/lidar360/

Harder, P., Pomeroy, J., and Helgason, W. (2020). Improving sub-canopy snow depth mapping with unmanned aerial vehicles: Lidar versus structure-from-motion techniques. The Cryosphere, 14, 1919–1935. doi:10.5194/tc-14-1919-2020

Harpold, A. A., Guo, Q., Molotch, N., Brooks, P. D., Bales, R., Fernandez-Diaz, J. C., et al. (2014). Lidar-derived snowpack data sets from mixed conifer forests across the Western United States. Water Resources Research, 50, 2749–2755.

Hopkinson, C., Collins, T., Anderson, A., Pomeroy, J., and Spooner, I. (2012a). Spatial snow depth assessment using lidar transect samples and public GIS data layers in the Elbow River watershed, Alberta. Canadian Water Resources Journal, 37(2), 69–87.

Hopkinson, C., Pomeroy, J., Debeer, C., Ellis, C., and Anderson, A. (2012b). Relationships between snowpack depth and primary lidar point cloud derivatives in a mountainous environment. Paper presented at the Remote Sensing and Hydrology, Jackson Hole, Wyoming, USA, 27–30 September 2010.

Hopkinson, C., Sitar, M., Chasmer, L., and Treitz, P. (2004). Mapping snowpack depth beneath forest canopies using airborne lidar. Photogrammetric Engineering & Remote Sensing, 70(3), 323–330.

Hyyppä, E., Hyyppä, J., Hakala, T., Kukko, A., Wulder, M. A., White, J. C., et al. (2020). Under-canopy UAV laser scanning for accurate forest field measurements. ISPRS Journal of Photogrammetry and Remote Sensing, 164, 41–60. doi:10.1016/j.isprsjprs.2020.03.021

Hyyppä, H., Hyyppä, J., Kaartinen, H., Kaasalainen, S., Honkavaara, E., and Rönnholm, P. (2005). Factors affecting the quality of DTM generation in forested areas. Paper presented at the Proceedings of the ISPRS Workshop Laser scanning 2005, Enschede, the Netherlands, 12–14 September 2005.

Jacobs, J. M., Hunsaker, A. G., Sullivan, F. B., Palace, M., Burakowski, E. A., Herrick, C., et al. (2021). Snow depth mapping with unpiloted aerial system lidar observations: a case study in Durham, New Hampshire, United States. The Cryosphere, 15(3), 1485–1500. doi:10.5194/tc-15-1485-2021

Jobin, B., Latendresse, C., Baril, A., Maisonneuve, C., Boutin, C., and Côté, D. (2014). A half-century analysis of landscape dynamics in southern Québec, Canada. Environmental Monitoring and Assessment, 186(4), 2215–2229. doi:10.1007/s10661-013-3531-6

Kirchner, P. B., Bales, R. C., Molotch, N. P., Flanagan, J., and Guo, Q. (2014). Lidar measurement of seasonal snow accumulation along an elevation gradient in the southern Sierra Nevada, California. Hydrology and Earth System Sciences, 18, 4261–4275.

Kumari, P., Carter, W. E., and Shrestha, R. L. (2011). Adjustment of systematic errors in ALS data through surface matching. Advances in Space Research, 47(10), 1851–1864. doi:10.1016/j.asr.2010.12.015

Li, Z., Tan, J., and Liu, H. (2019). Rigorous boresight self-calibration of mobile and UAV LiDAR scanning systems by strip adjustment. Remote Sensing, 11(4), 442. doi:10.3390/rs11040442

Mazzotti, G., Currier, W., Deems, J. S., Pflug, J. M., Lundquist, J. D., and Jonas, T. (2019). Revisiting snow cover variability and canopy structure within forest stands: Insights from airborne lidar data. Water Resources Research, 55, 6198–6216. doi:10.1029/2019WR024898

Michele, C., Avanzi, F., Passoni, D., Barzaghi, R., Pinto, L., Dosso, P., et al. (2016). Using a fixed-wing UAS to map snow depth distribution: An evaluation at peak accumulation. The Cryosphere, 10, 511–522. doi:10.5194/tc-10-511-2016

Ministry of Energy and Natural Resources. (2020). Geodetic network map. Retrieved February 05, 2019 https://geodesie.portailcartographique.gouv.qc.ca/

Morsdorf, F., Kötz, B., Meier, E., Itten, K. I., and Allgöwer, B. (2006). Estimation of LAI and fractional cover from small footprint airborne laser scanning data based on gap fraction. Remote Sensing of Environment, 104, 50–61.

NSIDC. (2019). State of the cryosphere Retrieved October 20, 2020 https://nsidc.org/cryosphere/sotc/

Painter, T., Berisford, D., Boardman, J., Bormann, K. J., Deems, J., Gehrke, F., et al. (2016). The Airborne Snow Observatory: Fusion of scanning lidar, imaging spectrometer, and physically-based modeling for mapping snow water equivalent and snow albedo. Remote Sensing of Environment, 184, 139–152.

Pajares, G. (2015). Overview and current status of remote sensing applications based on Unmanned Aerial Vehicles (UAVs). Photogrammetric Engineering and Remote Sensing, 81, 281–329.

Paquotte, A., and Baraer, M. (2021). Hydrological behavior of an ice-layered snowpack in a non-mountainous environment. Hydrological Processes, 36(1), e14433. doi:10.1002/hyp.14433

Pilarska, M., Ostrowski, W., Bakula, K., Górski, K., and Kurczynski, Z. (2016). The potential of light laser scanners developed for unmanned aerial vehicles-The review and accuracy. ISPRS - International Archives of the Photogrammetry, Remote Sensing and Spatial Information Sciences, 87–95.

Proulx, H., Jacobs, J. M., Burakowski, E. A., Cho, E., Hunsaker, A. G., Sullivan, F. B., Palace, M.; Wagner, C. (in review, 2022). Comparison of in-situ snow depth measurements and impacts on validation of unpiloted aerial system lidar over a mixed-use temperate forest landscape. preprint. The Cryosphere Discuss., Copernicus Publications. doi:10.5194/tc-2022-7

Ravi, R., Shamseldin, T., Elbahnasawy, M., Lin, Y.-J., and Habib, A. (2018). Bias impact analysis and calibration of UAV-based mobile LiDAR system with spinning multi-beam laser scanner. Applied Sciences, 8(2), 297. doi:10.3390/app8020297

Royer, A., Roy, A., Jutras, S., and Langlois, A. (2021). Review article: Performance assessment of radiation-based field sensors for monitoring the water equivalent of snow cover (SWE). The Cryosphere, 15(11), 5079–5098. doi:10.5194/tc-15-5079-2021

SPH-Engineering. (2019). UgCS Desktop application version 3.2 (113) User Manual. Retrieved from Baložu Pilsēta, Latvia: www.ugcs.com

Sturm, M., Goldstein, M. A., and Parr, C. (2017). Water and life from snow: A trillion dollar science question. Water Resources Research, 53(5), 3534–3544. doi:10.1002/2017wr020840

Sturm, M., and Holmgren, J. (2018). An automatic snow depth probe for field validation campaigns. Water Resources Research, 54(11), 9695–9701. doi:10.1029/2018WR023559

Tinkham, W. T., Smith, A. M. S., Marshall, H., Link, T., Falkowski, M., and Winstral, A. (2014). Quantifying spatial distribution of snow depth errors from lidar using random forest. Remote Sensing of Environment, 141, 105–115. doi:10.1016/j.rse.2013.10.021

Trujillo, E., Ramı´rez, J. A., and Elder, K. J. (2007). Topographic, meteorologic, and canopy controls on the scaling characteristics of the spatial distribution of snow depth fields. Water Resources Research, 43, W07409, 1–17.

Tsai, Y.-L. S., Dietz, A., Oppelt, N., and Kuenzer, C. (2019). Remote sensing of snow cover using spaceborne SAR: A review. Remote Sensing, 11(12), 1456. doi:10.3390/rs11121456

Valbuena, R., Mauro, F., Rodriguez-Solano, R., and Manzanera, J. A. (2010). Accuracy and precision of GPS receivers under forest canopies in a mountainous environment. Spanish Journal of Agricultural Research, 8(4), 1047–1057.

VelodyneLiDAR. (2018). VLP-16 User Manual. Retrieved from San Jose, USA: https://www.velodynelidar.com

Wallace, L. O., Lucieer, A., and S.Watson, C. (2012). Assessing the feasibility of UAV-based lidar for high resolution forest change detection. Paper presented at the ISPRS Congress, Melbourne, Austrailia, 25 August–1 September 2012.

Yilmaz, C. S., Yilmaz, V., and Güngör, O. (2018). Investigating the performances of commercial and non-commercial software for ground filtering of UAV-based point clouds. International Journal of Remote Sensing, 39(15–16), 5016–5042. doi:10.1080/01431161.2017.1420942

Zhang, X., Gao, R., Sun, Q., and Cheng, J. (2019). An automated rectification method for unmanned aerial vehicle LiDAR point cloud data based on laser intensity. Remote Sensing, 11(7), 811. doi:10.3390/rs11070811

Zheng, Z., Kirchner, P. B., and Bales, R. C. (2016). Topographic and vegetation effects on snow accumulation in the southern Sierra Nevada: A statistical summary from lidar data. The Cryosphere, 10, 257–269.

Zheng, Z., Ma, Q., Qian, K., and Bales, R. C. (2018). Canopy effects on snow accumulation: observations from lidar, canonical-view photos, and continuous ground measurements from sensor networks. Remote Sensing, 10, 1769. doi:10.3390/rs10111769

CHAPTER II

TOPOGRAPHIC AND VEGETATION CONTROLS OF THE SPATIAL DISTRIBUTION OF SNOW DEPTH IN AGRO-FORESTED ENVIRONMENTS BY UAV LIDAR

Vasana Dharmadasa [1,2,3,5], Christophe Kinnard [1,2,3] and Michel Baraër [4,5]

[1] Department of Environmental Sciences, University of Québec at Trois-Rivières, Trois-Rivieres, QC G8Z 4M3, Canada

[2] Center for Northern Studies (CEN), Quebec City, QC GV1 0A6, Canada

[3] Research Centre for Watershed-Aquatic Ecosystem Interactions (RIVE), University of Québec at Trois-Rivières, Trois-Rivieres, QC G8Z 4M3, Canada

[4] Department of Construction Engineering, École de Technologie Supérieure, Montreal, QC H3C 1K3, Canada

[5]CentrEau, the Québec Water Management Research Centre, Québec City, QC GV1 0A6, Canada

Corresponding author: vasana.sandamali.dharmadasa@uqtr.ca

This article has been published in *The Cryosphere* (doi: 10.5194/tc-17-1225-2023).

Abstract

Accurate knowledge of snow depth distributions in forested regions is crucial for applications in hydrology and ecology. In such a context, understanding and assessing the effect of vegetation and topographic conditions on snow depth variability is required. In this study, the spatial distribution of snow depth in two agro-forested sites and one coniferous site in eastern Canada was analyzed for topographic and vegetation effects on snow accumulation. Spatially distributed snow depths were derived by unmanned aerial vehicle light detection and ranging (UAV lidar) surveys conducted in 2019 and 2020. Distinct patterns of snow accumulation and erosion in open areas (fields) versus adjacent forested areas were observed in lidar-derived snow depth maps at all sites. Omnidirectional semi-variogram analysis of snow depths showed the existence of a scale break distance of less than 10 m in the forested area at all three sites, whereas open areas showed comparatively larger scale break distances (i.e., 11–14 m). The effect of vegetation and topographic variables on the spatial variability in snow depths at each site was investigated with random forest models. Results show that the underlying topography and the wind redistribution of snow along forest edges govern the snow depth variability at agro-forested sites, while forest structure variability dominates snow depth variability in the coniferous environment. These results highlight the importance of including and better representing these processes in physically based models for accurate estimates of snowpack dynamics.

2.1 Introduction

Knowledge of spring snowpack conditions is essential to accurately estimate water availability and flood peaks following the onset of melt (Hopkinson et al., 2004). Many studies showed that addressing the spatial distribution of snow depth prior to melting is more important than spatial differences in melt behavior when estimating snowmelt dynamics of the snowpack (e.g., Schirmer and Lehning, 2011; Egli et al., 2012). Evaluating snowpack conditions in forested regions is particularly crucial as the forest cover significantly modifies snow accumulation and ablation processes due to canopy interception and changes energy balance processes within the canopy. These changes produce a marked effect on downstream hydrographs (Roth and Nolin, 2017). In addition, forests can also influence differential snow accumulation by preferential deposition of wind-blown snow along the forest edges (Essery et al., 2009; Currier and Lundquist, 2018).

Spatial variability of the snow cover is mainly controlled by topography, vegetation type, and vegetation density (Golding and Swanson, 1986; Jost et al., 2007; Varhola et al., 2010a; Koutantou et al., 2022). With the advent of remote sensing techniques, airborne (piloted and unpiloted) laser (lidar: light detection and ranging) scanning techniques have been extensively used to monitor snowpacks due to their strong penetration ability through the canopy to detect underlying snow cover/ground (Hopkinson et al., 2004; Morsdorf et al., 2006; Hopkinson et al., 2012b; Deems et al., 2013; Harpold et al., 2014; Zheng et al., 2016; Currier and Lundquist, 2018; Zheng et al., 2018; Mazzotti et al., 2019; Harder et al., 2020; Jacobs et al., 2021). Lidar scanning also typically allows capturing micro variability and allows producing high resolution (<10 m) snow depth/cover maps (e.g., Deems et al., 2013; Harder et al., 2020; Koutantou et al., 2021; Dharmadasa et al., 2022).

Snow spatial variability can occur on more than one scale due to different processes acting over multiple scales (Deems et al., 2006; Clark et al., 2011). Several studies emphasized a multiscale behavior of snow depths with two distinct regions (scales) separated by a scale break at a location varying from meters to tens of meters, with a more strongly spatially correlated snow depth structure before the scale break (Deems et al., 2006; Fassnacht and Deems, 2006; Trujillo et al., 2007; Deems et al., 2008; Trujillo et al., 2009; Mott et al., 2011; Schirmer and Lehning, 2011; Helfricht et al., 2014; Clemenzi et al., 2018; Mendoza et al., 2020a; Mendoza et al., 2020b). In turn, this suggests the existence of different combinations of processes controlling the snow accumulation, and distribution over these two distinct scales. For instance, these studies emphasized that canopy interception causes a short scale break distance in forested areas (9–12 m) where the effect of wind redistribution is minimal (Deems et al., 2006; Trujillo et al., 2007). Comparatively longer distances (15–65 m) were reported in tundra regions and explained by the interaction of wind, vegetation, and terrain roughness (Trujillo et al., 2009), while shorter distances (6 m and 20 m) in non-vegetated areas are explained by the interaction of the wind with terrain roughness in sheltered and exposed mountain slopes, respectively (Mott et al., 2011; Schirmer and Lehning, 2011). The estimation of this scale break location is important when choosing the horizontal resolution required for remotely sensed or in situ data collection efforts, and model scales in order to represent the snowpack variability at different scales.

In addition to the scaling properties of snow distribution, the relationship between snow depth, topography, and forest structure is also an important aspect for understanding/assessing small-scale snow heterogeneity in forested environments. The need to quantify these complex relationships has inspired the development of numerous empirical models (e.g., Anderton et al., 2004; Winkler et al., 2005; Grünewald et al., 2013) and process-based models (e.g., Hedstrom and Pomeroy, 1998; Liston and Elder, 2006; Mazzotti et al., 2020a; Mazzotti et al., 2020b). While process-based models are applicable to a wide range of conditions, they do require an extensive amount of input data. Contrarily, empirical models are useful in establishing a general relationship between the variables and provide a first-order estimate of their effects on snow processes. However, they do not explicitly account for governing processes, and thus may not make accurate predictions under specific conditions (Varhola et al., 2010a). Nevertheless, the use and effectiveness of empirical models like multiple linear regressions (MLR) (Jost et al., 2007; Lehning et al., 2011; Grünewald et al., 2013; Revuelto et al., 2014; Zheng et al., 2016; Zheng et al., 2018) and binary regression trees (BRT) (Elder et al., 1995; Elder et al., 1998; Winstral et al., 2002; Anderton et al., 2004; Molotch et al., 2005; Baños et al., 2011; Revuelto et al., 2014) to relate snow depth/SWE patterns with terrain and land cover predictors is well documented. Compared to linear methods, tree-based methods have the ability to describe more complex and nonlinear relationships between snow depth and landscape variables (Erxleben et al., 2002; Veatch et al., 2009; Bair et al., 2018). In recent years, random forest (RF) models, an ensemble machine learning algorithm that combines several randomized decision trees and aggregates their predictions, have gained popularity in water science and hydrological applications (Tyralis et al., 2019). The use of the ensemble bagging approach in RF models reduces overfitting, which is a well-known issue with traditional decision trees, and provides more accurate and unbiased error estimates (Breiman, 2001). As yet, there is only a handful of studies that used RF models to estimate snow depths/SWE (Bair et al., 2018; Yang et al., 2020) other than those that used RF algorithm to quantify the relative importance of predictor variables (Zheng et al., 2016) or to predict spatially distributed lidar vertical errors (Tinkham et al., 2014).

To our knowledge, to date, there are only a few previous studies that estimated snow depths by unpiloted aerial vehicle (UAV) based lidar (Harder et al., 2020; Cho et al., 2021; Jacobs et al., 2021; Koutantou et al., 2021; Dharmadasa et al., 2022). None of them explicitly examined how terrain and vegetation characteristics influence snow heterogeneity in different landscapes. From previous studies, Koutantou et al. (2022)

used UAV lidar data on two opposing slopes with a heterogeneous forest cover at a high spatio-temporal scale to show the effect of canopy structure and solar radiation on snow dynamics, excluding the effect of microtopography. The main objective of this paper is to study the small-scale spatial variability of snow depth by UAV lidar and investigate the terrain (including the effect of microtopography) and vegetation controls on this snow depth heterogeneity in an agro-forested and a boreal landscape. The study sites are based in southern Québec, Canada, where forests intertwined with mosaics of open agricultural fields in low-lying lands (agro-forested landscapes) play a significant role in altering the spatial distribution of the snow cover (Aygün et al., 2020). Much uncertainty still exists about the micro and meso scale spatial variability of snow cover and associated hydrological processes in these landscapes, partly due to lack of detailed and simultaneous micrometeorological and snowpack observations (Brown, 2010; Sena et al., 2017; Valence et al., 2022). To our knowledge, there has been no application of UAV laser scanning to investigate the small-scale snow cover heterogeneity in this type of landscape. This study will specifically explore: (1) how the snow accumulation and its scaling characteristics vary between and within forested and open environments, and (2) the relationship between snow depth, topography, and forest structure in different sites. Motivated by previous works (Currier and Lundquist, 2018; Mazzotti et al., 2019), we specifically investigate how the forest edges modulate the accumulation patterns in agro-forested environments. Given the relatively flat topography in these environments, we hypothesize that preferential accumulation along forest edges may represent a significant factor of spatial variability in snow depth.

2.2 Data and Methods

2.2.1 Study Sites

Small-scale snow depth heterogeneity was investigated at three selected sites that represent the typical landscape in southern Québec (Figure 2.1). Sainte-Marthe and

Saint-Maurice are agro-forested sites located in the St. Lawrence River lowlands. Irrigation canals and streams flowing through the open agricultural areas are very common in these agro-forested landscapes. The main crop type in the agricultural areas is soya. The forested area in Sainte-Marthe consists of a dense deciduous forest with sugar maple (*Acer saccharum*), red maple (*Acer rubrum*), and a small conifer plantation to the southwest. Saint-Maurice has a high to moderate dense mixed forest with poplar (*Populus x canadensis*), red maple, white pine (*Pinus strobus*), and balsam fir (*Abies balsamea*) being the dominant tree species. Forêt Montmorency (hereafter Montmorency) is a dense boreal forest with balsam fir, black spruce (*Picea mariana*), and white spruce (*Picea glauca*) tree species farther north on the Canadian Shield. Forest gaps associated with clear-cutting and regeneration practices are common in this area. Adjacent to the forest is an open area hosting the NEIGE-FM snow research station, which hosts a variety of precipitation gauges and snowpack measuring sensors, and is part of the World Meteorological Organization's (WMO) station network (Royer et al., 2021). Table 2.1 summarizes the physiographic and climatic conditions at each site. Land use information presented in Figure1 was obtained from the Québec Ministry of Forests, Wildlife, and Parks (MFFP). For interpretation purposes, open agricultural areas in Sainte-Marthe and Saint-Maurice and the small open area in Montmorency (NEIGE-FM site) are referred to as "field" herein.

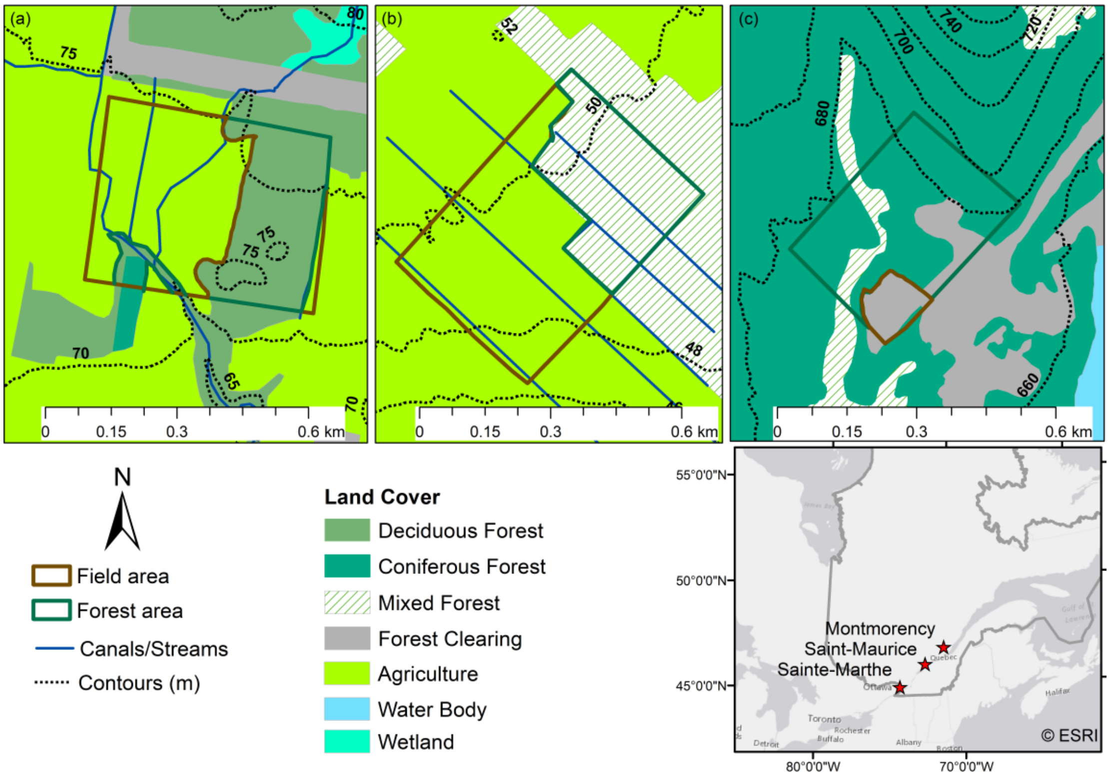

Figure 2.1. Overview of the study sites with lidar survey extents. Field and forest areas within each lidar extent are delineated with brown and green colors, respectively. **(a)** Sainte-Marthe, **(b)** Saint-Maurice and **(c)** Montmorency. Contour intervals intentionally differ between sites for better readability. (Adapted from Dharmadasa et al. (2022))

Table 2.1. Site characteristics and lidar data collection information (Adapted from Dharmadasa et al. (2022))

	Sainte-Marthe	Saint-Maurice	Montmorency
Elevation range, m	70–78	46–50	670–700
MAAT, °C	6.0	4.7	0.5
Total precipitation, mm/yr	1000	1063	1600
Snowfall/Total Precipitation, %	15	16	40
Winter season	November–March	November–March	October–April
Lidar survey extent, km^2	0.22	0.25	0.12

Forest area/Total area, %	40	40	92
Forest type	Deciduous	Mixed	Boreal
Mean canopy density, %	>80	60–80	60–80
Snow-on flight date	12 March 2020	11 March 2020	29 March 2019
Snow-off flight date	11 May 2020	02 May 2020	13 June 2019

MAAT= mean annual air temperature. Climatic data presented here were based on the climate averages (1981–2010) at the nearest Environment and Climate Change Canada (2021b) meteorological stations to the sites (Station climate ID 7016470, 7017585, and 7042388 for Sainte-Marthe, Saint-Maurice, and Montmorency). None of the snow-on flights were conducted right after a storm.

Although the lidar data acquisition years are different between agro-forested sites and boreal forest due to logistical reasons, the study years are representative of the long-term climatological conditions at the sites (Supplement Figure S2.1), and hence allowed us for inter-site comparison of snow depths.

2.2.2 Data Processing

All lidar surveys were performed with a GeoMMS system mounted onto a DJI M600 Pro UAV platform. The GeoMMS system is comprised of a Velodyne VLP-16 lidar sensor, a real-time dual-antenna global navigation satellite system (GNSS) aided inertial navigation system (INS) for precise heading, and a tactical MG364 inertial measurement unit (IMU). The nominal accuracy of the point cloud provided by GeoMMS is ±5 cm (RMS, root mean square) (Geodetics, 2018) whereas the nominal uncorrelated relative error of two lidar point clouds is approximately ±7 cm ($\sqrt{5^2+5^2}$). Flight paths for the surveys were prepared in UgCS flight control software (Sph-Engineering, 2019) and the flight parameters were optimized to reduce overall INS errors and maximize the mapping efficiency in the forested areas. Table 2.2 outlines the flight parameters and equipment settings used in surveys.

Raw lidar data sets collected from the flights were post-processed in Geodetics LiDARTool (Geodetics, 2019) with post-processing kinematic (PPK) correction. The

PPK option regenerated a significantly more accurate trajectory file by combining the onboard GNSS data with GNSS base station data. Then, this post-processed trajectory file was merged with the raw laser data to produce a geo-referenced x,y,z point cloud. Noise removal was applied next. We also employed a trial-and-error, manual boresight calibration method to correct for boresight errors in the data, as recommended by the manufacturer (Geodetics, 2019). The final post-processed point clouds have a vertical absolute accuracy range of 3–6 cm and a relative accuracy range of 4–6 cm (Dharmadasa et al., 2022).

To classify the bare surface points, we used the multiscale curvature algorithm (Evans and Hudak, 2007) implemented in the commercial Global Mapper software (Blue Marble Geographics, 2020). Parameters of the algorithm were adjusted according to the vertical spread of the flight strips over open terrain, the local slope of the terrain and canals/streams, and the presence/absence of buildings. The reader is referred to Dharmadasa et al. (2022) for a comprehensive overview of the UAV lidar system and post-processing of raw data.

Table 2.2. Flight parameters and equipment settings

Flight parameters		Equipment settings	
Flying speed	3 m s^{-1}	Wavelength	905 nm
Flight altitude	40 m AGL	Laser pulse repetition rate	18.08 kHz
Field of view (horizontal)	145°	Field of view (vertical)	±15°
Distance between parallel flight lines	64 m	Laser RPM	1200
Ground overlap	20 %	Return type	Dual
Point density	603 points m^{-2}		

2.2.2.1 Snow Depth Maps

Snow depth maps were obtained by differencing winter (snow-on) and summer (snow-off) digital elevation models (DEMs) generated from bare surface points at each site. Bare surface points were aggregated to a grid resolution of 1.4 m using the binning method in Global Mapper (Blue Marble Geographics, 2020). This grid resolution was selected based on the manual snow depth sampling strategy used by Dharmadasa et al. (2022) to validate the snow depth maps and aimed to minimize the effect of positional errors of the manual measurements made with GNSS. The manual sampling strategy consisted of five snow depth measurements taken at each sampling location in a diagonal cross shape at 1 m apart, and the average of these five measurements represents a 1.4x1.4 m ($\sqrt{1^2 + 1^2}$) grid cell. As final filtering, spurious negative snow depths were set to zero, as they are physically inconsistent and need to be filtered (Hopkinson et al., 2012a). Negative snow depths accounted for a very small portion of the total area (<0.1 %) sampled and had a negligible effect on the statistics derived from the snow depth maps. The validation of UAV lidar snow depths with manual measurements showed a RMSE of 0.079–0.160 m in the deciduous forested environment, and 0.096–0.190 m in the coniferous forested environment (Dharmadasa et al., 2022), which is comparable to previous efforts with UAV lidar (Harder et al., 2016; Jacobs et al., 2021) and airborne lidar (Harpold et al., 2014; Painter et al., 2016). More details about the snow depth validation can be found in Dharmadasa et al. (2022).

2.2.2.2 Terrain Metrics

To typify the terrain characteristics, we derived four variables from the summer DEM, i.e., elevation (*Elevation*), slope (*Slope*), aspect (*Aspect*), and topographic wind sheltering index (*TWSI*) at 1.4 m resolution (Supplement Figure S2.2–S2.4). Topographic variables other than elevation need to be considered when studying areas that encompass a small elevation range (Zheng et al., 2016), such as our sites. *Elevation* was obtained directly from the DEM, while *Slope* and *Aspect* were derived using ArcGIS 10.2 software. *Slope* was calculated as the first derivative of the DEM, while *Aspect* was derived in two orthogonal components, i.e., west-east (*Aspect_WE*) and south-north (*Aspect_SN*) exposures. *Aspect_WE* (west-negative, east-positive) and *Aspect_SN* (south-negative, north-positive) were calculated directly as the sine and cosine of the aspect, respectively. The *TWSI* was produced using the RSAGA package in CRAN. This variable considers the sheltering effects of the local topography in the dominant wind direction. Several studies showed that *TWSI* is a good measure to characterize sheltering and exposure of the local terrain providing a reasonable representation of the local wind field and thus the redistribution of snow by wind (Winstral et al., 2002; Winstral and Marks, 2002; Plattner et al., 2004; Molotch et al., 2005). Negative *TWSI* values correspond to terrain exposure and positive values to sheltering from the wind. *TWSI* is similar to the Sx parameter used by Revuelto et al. (2014), but the *TWSI* is calculated based on prescribed dominant wind directions, in contrast to the eight directions used by them. Dominant wind directions were extracted from hourly wind data for the study period considered (winter season in each study year as indicated in Table 2.1) at each site (Figure 2.2). Wind data was collected from an automatic weather station located 1.4 km away from the Sainte-Marthe site and the closest Environment Canada wind measuring stations at the other sites. The closest station to Saint-Maurice (climate ID 7018561) was 19 km away from the site and 0.25 km away from the Montmorency site (climate ID 7042395) (ECCC, 2021a).

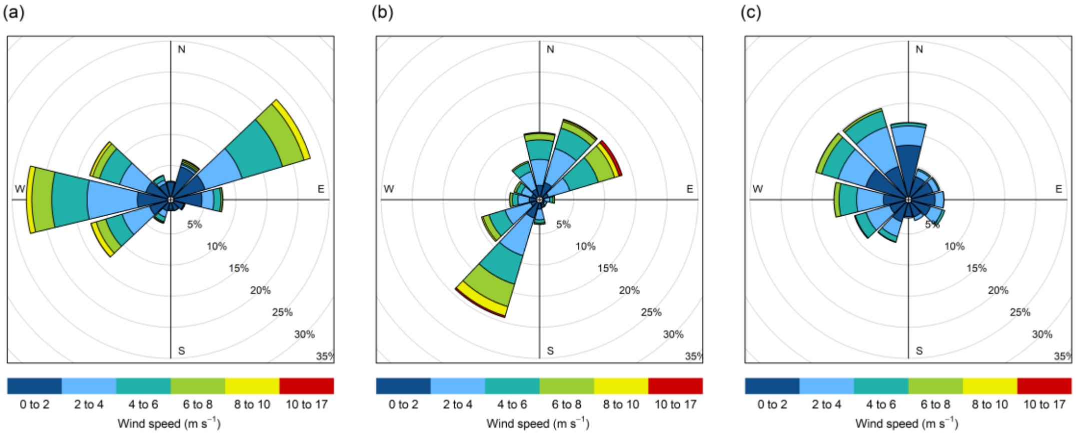

Figure 2.2. Winter period wind rose plots of the sites. **(a)** Sainte-Marthe, **(b)** Saint-Maurice and **(c)** Montmorency

2.2.2.3 Vegetation Descriptors

Vegetation-related variables were rasterized from the classified winter point cloud in LiDAR360 (Greenvalley-International, 2020). The forestry module of LiDAR360 contains tools that allow users to calculate essential forest metrics and accurately extract individual tree parameters like crown diameter, crown area, and tree diameter by breast height from airborne lidar data. In this study, the leaf area index (*LAI*), canopy cover (*CC*), and gap fraction (*GF*) were estimated at 1.4 m resolution for the forest cover higher than 2 m (Supplement Figure S2.2–S2.4). A 2 m height threshold was selected as canopies >2 m has been shown to have a strong influence on snow accumulation (Varhola et al., 2010b; Zheng et al., 2016; Zheng et al., 2019). The function used to calculate *LAI* is based on the Beer-Lambert law (Richardson et al., 2009). The estimated *LAI* is contingent on the average scan angle, *GF,* and extinction coefficient. *GF*, the amount of open area within the canopy which is not blocked by branches or foliage, is calculated as the total number of ground points to the total number of lidar points within a grid cell. *CC*, which is defined as the percentage of vertical projection of forest canopy to the forest land area (Jennings et al., 1999), is calculated as the total number of vegetation returns to total returns (Morsdorf et al., 2006), ($CC = 1 - GF$). Refer to Richardson et al. (2009) and Morsdorf et al. (2006) for the equations used by LiDAR360 to estimate the forest metrics. In addition, canopy height (CH) was derived by subtracting the DEM from the digital surface model (DSM).

2.2.2.4 Site Variable

A binary variable, *Site* representing forested (1), and field (0) pixels was derived to investigate systematic effects, if any, of land cover that was not captured by vegetation or terrain metrics (Supplement Figure S2.2–S2.4). This variable was derived by manually mapping field and forested area boundaries at each site (as indicated in Figure 2.1) in ArcGIS 10.2 software. After delineating forest and field boundaries, the area inside the forest boundary was assigned a value of 1, and the area inside the field boundary was assigned a value of 0.

2.2.2.5 Forest Edge Descriptors

We investigated forest edge effects on snow accumulation using an approach inspired from Currier and Lundquist (2018) and Mazzotti et al. (2019) using Matlab software. Analogous to their analyses, we added directionality to forest edges to examine if preferential snow accumulation occurred windward or leeward of forest edges due to snow redistribution by wind or reduced ablation due to shading from the forest. Pixels were first classified as north-facing (NFE) when they were within a maximum search distance d_{max} northward of the forest edge. Forest edges (the boundary between field and forest areas) were extracted from the *Site* variable. Based on previous results by Currier and Lundquist (2018), d_{max} was set to 2H, where H is the typical tree height derived from the canopy height model at each site. The 2H distance reflects the typical shading of the ground by the canopy. H is 15 m in Sainte-Marthe, 20 m in Saint-Maurice, and 12 m in Montmorency. A tolerance of ±45° was used for the search direction for *NFE*. Pixels were further classified as windward (*WFE*) and leeward (*LFE*) when they were within a maximum search distance of the forest edge in the dominant wind direction. A range of search directions was used to constrain the dominant wind directions at each site, based on wind roses (Figure 2.2). Two dominant wind cones, 270±15°, and 50±15° were used in Sainte-Marthe, and one dominant wind cone in Saint-Maurice (210±15°) and Montmorency (310±15°). d_{max} was initially varied between 6–10H for pixels in open terrain based on Currier and Lundquist (2018), which represents the typical length scale of preferential snow accumulation at the forest edge. After a few trials, a final value of 10H was retained, which showed the highest correlation with snow depth. Moreover, the 10H distance at each site (150 m, 200 m, and 120 m in Sainte-Marthe, Saint-Maurice, and Montmorency respectively) encompassed the preferential snow accumulation seen along the forest edges on the lidar-derived snow depth maps. A maximum search distance of 1H was used for pixels within the forest in order to detect if preferential accumulation from blowing snow penetrated the forest. This value was chosen based on visual observations in the field, which suggested limited penetration of blowing snow inside the forest. Figure 2.3 shows a schematic illustration of the forest edge parameters described.

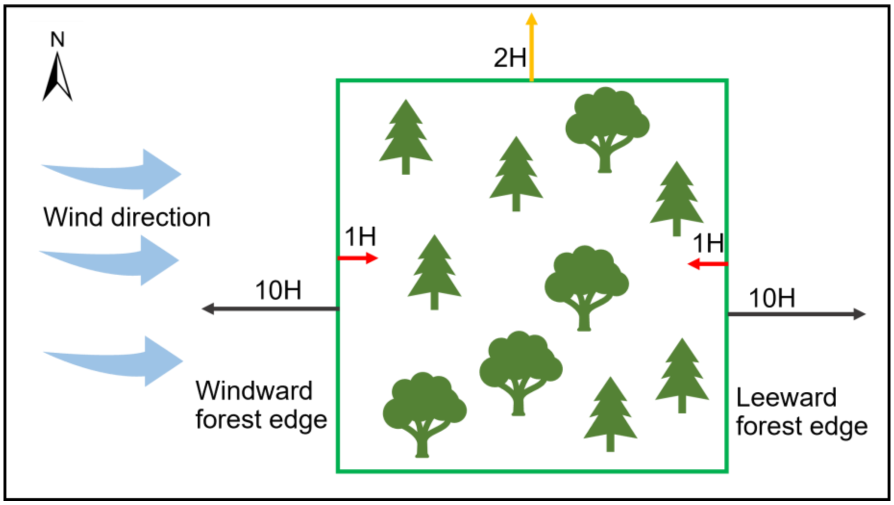

Figure 2.3. Graphical illustration of forest edges and respective maximum search

distances, dmax. 10H indicates the maximum search distance in the open field from the forest edge in windward and leeward direction, 1H indicates the maximum search distance in the forest from the forest edge in the windward and leeward direction, and 2H indicates the maximum search distance northward of the forest edge, for shading effects.

A new index of proximity to the forest edge, *FE*, was calculated by scaling the distance between each pixel and the forest edge (d) by the maximum search distance, d_{max}:

$$FE = \frac{d_{max} - d}{d_{max}} \qquad \text{Equation 2.1}$$

FE (either *NFE*, *WFE,* or *LFE*, depending on the initial classification) is equal to one when a pixel is situated on the forest edge and equal to zero when it is located at, or beyond the maximum search distance d_{max}. The novelty of this approach is to derive a continuous predictor of forest edge proximity while considering the dominant wind direction, as opposed to the simpler binary classification introduced by Currier and Lundquist (2018). Maps of the forest edge descriptors for each site can be found in supplement Figure S2.2–S2.4.

2.2.3 Data Analysis

Data analysis was primarily focused on assessing the small-scale snow depth heterogeneity at the selected sites. Lidar-derived snow depth data were analyzed for inter (agro-forested versus coniferous) and intra (field versus forest) site variability. First, the scale dependence of snow depth variability was explored using semi-variogram analysis. Then, the site-specific topographic and vegetation control on the snow depth spatial heterogeneity was examined with RF regression models. All the statistical analyses were performed in R software.

2.2.3.1 Spatial Correlation Analysis

To analyze the small-scale spatial variability of the snow depth map in each study site, omnidirectional semi-variograms were used. Semi-variogram analysis allows constraining the dominant scales of snow depth variability and to compare them between land cover types and sites. Canals/streams were discarded from the snow depth maps for this analysis to ensure stationarity of the surface. i.e., snow depths in canals/streams would have a unidirectional spatial correlation which could alter the relationship of the overall terrain by introducing biases. In addition, omnidirectional semi-variograms of snow depth were compared with those obtained from bare earth topography in the field and topography+vegetation surface (DSM, bare earth topography+trees) in the forest to investigate the influence of topography and vegetation interactions on snow depth. Moreover, directional semi-variograms of snow depth were also computed to establish possible influences of dominant wind directions on snow depth variability at each site.

The semi-variogram $\gamma(r)$ is expressed as:

$$\gamma(r_k) = \frac{1}{2N(r_k)} \sum_{(i,j)\in N(r_k)} \{z_i - z_j\}^2 \qquad \text{Equation 2.2}$$

Where r is the lag distance of bin k, $N(r_k)$ is the total number of pairs of points in the k^{th} bin and z_i and z_j are the snow depth values at two different point locations i and j (Webster and Oliver, 2007).

Half of the maximum point pairs distance (Sun et al., 2006) was taken as the maximum lag distance for the semi-variogram calculations with 50 log-width bins. Log-width distance bins provide equal bin widths when semi-variograms are transformed to log-log scale, and help resolve the semi-variogram at short length scales by allowing greater bin density at shorter lag distance compared to linear-width bins (Deems et al., 2006).

In the case of scale invariance, the semi-variogram can be described by a power law:

$$\gamma(r) = ar^{b} \qquad \text{Equation 2.3}$$

Where a and b are coefficients selected to minimize the squared residuals.

To identify scale breaks in semi-variograms, the following steps were implemented following a similar approach suggested by Mendoza et al. (2020a).

- First, a change point analysis was conducted on the semi-variograms in log-log space using the ecp package in R (James and Matteson, 2014) to identify possible break points, which allows delineating sections of the semi-variogram with similar trends.

- Then, linear least square regression models were fitted in log-log space for each cluster of points identified in step 1.

- Finally, we checked whether the changes in the slopes of the log-log linear models were larger than 20 % and that the 95 % confidence limits of the slopes did not overlap, and verified that the R2 was greater than 0.9. If all these conditions were fulfilled, the existence of a scale break was confirmed.

2.2.3.2 Random Forest Model

To investigate the effect of vegetation and topographic variables on the spatial variability of snow depth, we applied RF regression models on rasters derived from lidar data. Generally, in a RF model, two-thirds of the sample data (in-bag) are used to train the model, while the remaining one-third (out-of-bag, OOB) is used to estimate how well the trained model performs. This in-bag and OOB sampling procedure is akin to the much used k-fold cross-validation approach (Probst and Boulesteix, 2017; Tyralis et al., 2019). As such, model performance statistics (mean square error, MSE and variance explained) are derived from the OOB predictions, which give an independent error assessment of the model (Breiman, 2001). The RF algorithm also calculates the predictor importance (importance of a variable), by estimating how much the prediction error increases when OOB data for the respective variable is permuted while all others are left unchanged (Liaw and Wiener, 2002). i.e., how much the prediction error increases (or decreases) when the variable of interest is removed (included) from the RF model.

The RF analyses were conducted in R with grid resolutions of 1.4 m at all sites. Data were not separated into discrete training and test sets so that we would not create an artificial bias by data splitting. As such, all data were inputted into the RF model and the error metrics were calculated on the OOB samples as described above. As a precautionary measure, we excluded collinear variables prior to building the RF models using the variance inflation factor (VIF) function in R. This was done mainly because our objective was to investigate the relative contribution of different variables to snow depth variability in forest versus the field, rather than deriving a model with maximum predictive capacity. While RF can handle collinearity in a predictive mode, collinearity makes it difficult to separately evaluate the predictive power (variable importance) of the predictors (Bair et al., 2018). The number of trees in the ensemble (ntree) and the number of variables at each node (mtry) were tuned before training each RF model.

We used the following procedure to identify the potential predictors of RF models at each site. *Elevation* was discarded from the analysis since the elevation range at all sites was too small (Table 2.1) to produce any meaningful local orographic effect on precipitation, or adiabatic effects on air temperature, (e.g., Mazzotti et al. (2019)), and could mask other local topographic effects on accumulation related to slope, aspect and terrain roughness (wind sheltering), due to collinearity. In addition, irrespective of the variable type, collinear variables were identified and discarded prior to building the RF models at all sites. As such, the topographical variables *Slope, Aspect_WE, Aspect_SN,* and *TWSI* were used at all sites. However, the vegetation descriptors (*LAI*, *CC*, *GF*, and *CH*) were strongly intercorrelated (with correlation coefficient, r of 0.82–1.00) and hence could not be used together in a predictive model, at least not without compromising the interpretation of variable importance in the RF model. Therefore, *LAI* was selected as the most representative forest structure indicator in the RF analysis as, it has been shown to be a strong predictor of snow accumulation in forests (Hedstrom and Pomeroy, 1998; Pomeroy et al., 1998; Broxton et al., 2015; Lendzioch et al., 2016). Moreover, a sensitivity analysis showed that the choice of forest structure descriptor has a negligible impact on the performance (R^2) of RF models (Supplement Table S2.1). The selection of the windward and leeward forest edge descriptors (*WFE* and *LFE*) was guided by the landscape setting at each site. In Sainte-Marthe, both *WFE* and *LFE* have large extents (Supplement Figure S2.2) but are collinear due to the two dominant and opposed wind directions. Including both variables in the RF model would thus compromise the interpretation of the variable importance. Hence, we opted to use the *WFE* only in the final RF analysis. In Saint-Maurice, *LFE* has only a few pixels (Supplement Figure S2.3) and was hence omitted. In Montmorency, *LFE* seemingly has more influence on snow depth variability with its larger extent than the *WFE* (Supplement Figure S2.4). This is also more logical as the open areas in Montmorency constitute a large gap within an overall forested environment, so deposition is expected leeward of the forest edge with little remobilization (erosion) within the gap. *NFE* was used at all sites to see the effect of forest edge shading on the snow depth variability.

The RF model results were first examined for the relative importance of predictor variables (variable importance), which has proven to be useful for evaluating the relative contribution of input variables (Tyralis et al., 2019). Then, the partial relationships of the predictors with snow depth were examined and presented. Partial dependence functions are typically used to help interpret models produced by machine learning models such as RF (Jerome, 2001). It is a better alternative to variable dependence. Each partial plot was generated by integrating out the effects of all variables beside the covariate of interest. Partial dependence data in each plot were constructed by selecting points evenly spaced along the distribution of the variable of interest. This subsampling helps to cut down computational time substantially. We used the default subsampling of 51 points in our analysis. The performance of RF models in terms of OOB statistics was compared between the different land cover types and sites. Additionally, we discuss RF model performances compared to traditional MLR models.

2.3 Results

2.3.1 General Snow Accumulation Patterns

Figure 2.4 depicts the snow depth maps derived from UAV lidar data at the study sites. Montmorency shows the highest overall snow accumulation. Higher snow accumulation in canals/streams (area 1 in Figure 2.4a, b) and along the forest edge (area 2 in Figure 2.4a, b) is evident in Sainte-Marthe and Saint-Maurice, whereas in Montmorency, forest gaps (area 4 in Figure 2.4c) seem to accumulate more snow. The highest snow depth in Montmorency corresponds to localized, artificial snow piles adjacent to the main road as observed during the field campaign (area 5 in Figure 2.4c). Concentric snow accumulation patterns around the double fence precipitation gauges are also noticeable in Montmorency snow depth map (area 6 in Figure 2.4c). Compared to the other two sites, the Montmorency snow depth map comprises more data gaps in the forested area. Paved roads in Sainte-Marthe (area 3 in Figure 2.4a) and Montmorency (area 3 in Figure 2.4c) and the area surrounding the small house (area 7 in Figure 2.4a) in the forest at Sainte-Marthe appear snow-free due to the snow clearing operations, as confirmed in field campaigns. Snow clearing in the proximity of the house in Sainte-Marthe accounts for a significant portion of zero and/or small snow depths (Figure 2.4d) and biases the mean snow depth in the forest. When this portion is discarded, the mean snow depth in the forest increases from 0.250 to 0.275 m. In Sainte-Marthe, the mean snow depth in the field area is higher than that in the adjacent forested area (Figure 2.4d), whereas, at the other two sites, mean snow depths in the field and forest are similar considering the measurement error of the lidar system (Figure 2.4e, f). A nonparametric Wilcoxon rank-sum test (Wilcoxon, 1945) was applied to test whether snow depths within forested and field areas were statistically different from each other. To remove spatial autocorrelation, snow depths were subsampled every 20 m (larger than the scale break distances found by semi-variogram analysis, Figure 2.5). The results confirmed that snow depth in the Sainte-Marthe field was statistically greater than that in the forest and in the other two sites differences were not statistically significant.

Snow depths in Sainte-Marthe are lower on average (mean forest = 0.250 m; mean field = 0.374 m) than in Saint-Maurice (mean forest = 0.591 m; mean field = 0.600 m). The snow depth is more variable in the forest (higher coefficient of variation, CV) than in the field in Sainte-Marthe and Montmorency, which is not the case in Saint-Maurice, where the coefficient of variation in the field is slightly larger than in the forest.

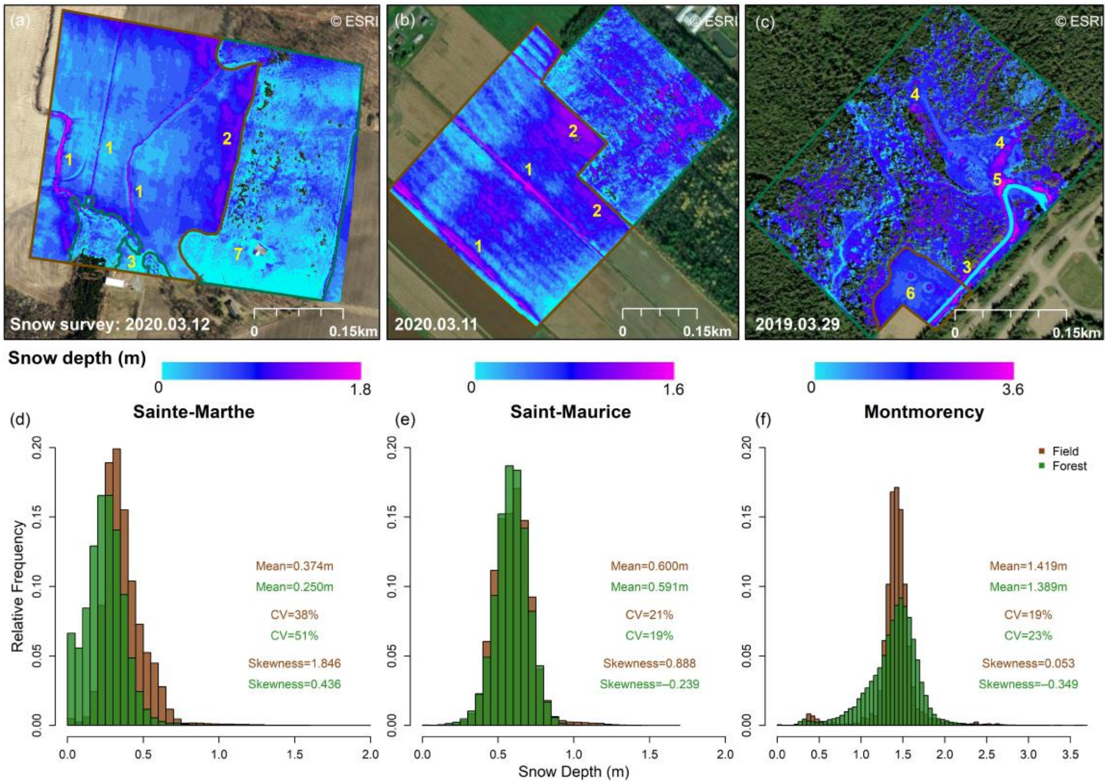

Figure 2.4. UAV-lidar-derived snow depth maps (grid size 1.4 m) and histograms of snow depth distribution. **(a, d)** Sainte-Marthe map with snow surveying date and histogram; **(b, e)** Saint-Maurice map with snow surveying date and histogram; **(c, f)** Montmorency map with snow surveying date and histogram. Field and forest areas are demarcated with brown and green colors in snow depth maps respectively. Histograms are derived according to these boundaries. Features 1 to 7 are discussed in the text.

2.3.2 Spatial Correlation Analysis

Omnidirectional semi-variograms of snow depth, bare earth topography, and topography+vegetation surface at the study sites are shown on a log-log scale in Figure 2.5. Semi-variograms were discretely developed for field and forested areas to assess the effect of land cover on the snow depth variability. Overall, forested areas show more variable (higher semi-variance values) snow depths than field snow depths at all sites. Snow depths seem to be more variable in coniferous forests than in deciduous and mixed forests. Snow depth in forested areas at all three sites shows a typical multi-scaling behavior, where the semi-variance between neighboring snow depths increases rapidly up to a scale break located at distances less than 10 m (Figure 2.5a, b and c), followed by a slower increase thereafter. Similarly, field snow depths exhibit multi-scaling behavior with comparatively larger scale break distances, with Montmorency showing two scale break distances (Figure 2.5a, b and c). Topography+vegetation surfaces show the highest semi-variance with scale break distances similar to forest snow depths (Figure 2.5d, e and f). Sainte-Marthe bare earth topography does not exhibit a distinct scale break (Figure 2.5d). In contrast, the bare earth topography at the other two sites shows multi-scaling behavior with scale break distances larger than 10 m (Figure 2.5e, f).

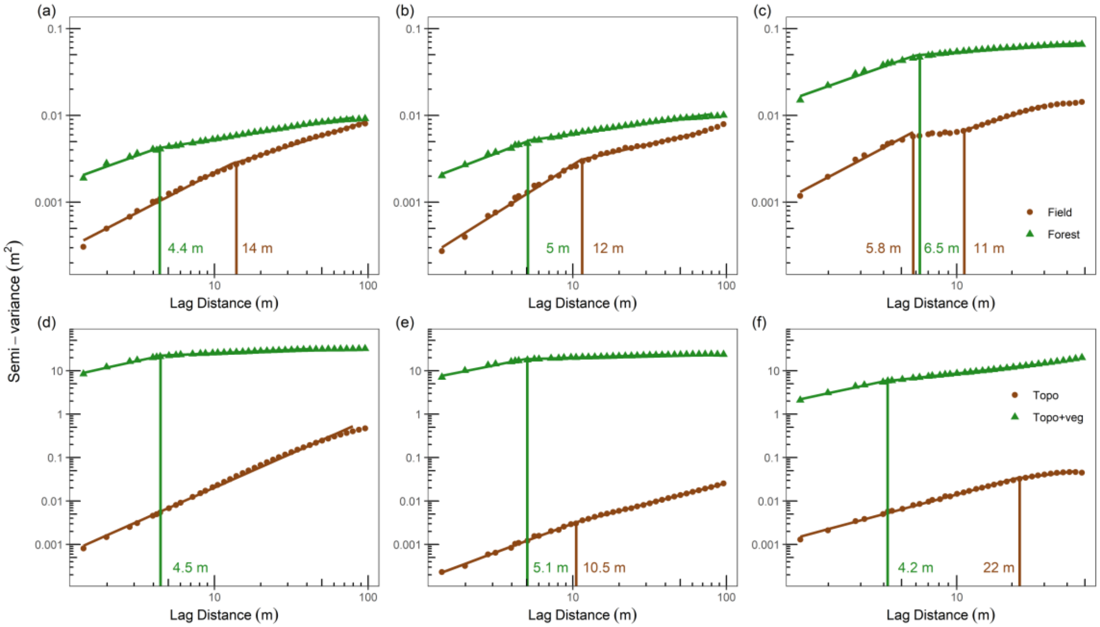

Figure 2.5. Omnidirectional semi-variogram for the field and forested areas for **(a)** Sainte-Marthe snow depth, **(b)** Saint-Maurice snow depth, **(c)** Montmorency snow depth, **(d)** Sainte-Marthe bare earth topography and topography+vegetation, **(e)** Saint-Maurice bare earth topography and topography+vegetation and **(f)** Montmorency bare earth topography and topography+vegetation. In the figure, Topo denotes bare earth topography and Topo+veg denotes topography+vegetation surface. Vertical lines indicate the dominant scale breaks, and trend lines represent significant ($p<0.05$) log-

log linear models with $R^2 > 0.9$ (see methods).

Figure 2.6 shows directional semi-variograms of snow depth derived for field and forested areas at each site. Sainte-Marthe field snow depths show an isotropic behavior (Figure 2.6a) whereas Sainte-Marthe forest shows an anisotropic behavior along the west-east direction (Figure 2.6d). In contrast, both Saint-Maurice field and forest snow depths show distinct anisotropic behaviors. Saint-Maurice field snow depths show a narrow anisotropic pattern along northwest-southeast and a broad anisotropic pattern along southwest-northeast directions (Figure 2.6b) whereas forest snow depths show an anisotropic pattern along the southwest-northeast direction (Figure 2.6e). Neither field nor forest snow depths in Montmorency show strong anisotropic behavior (Figure 2.6c, f).

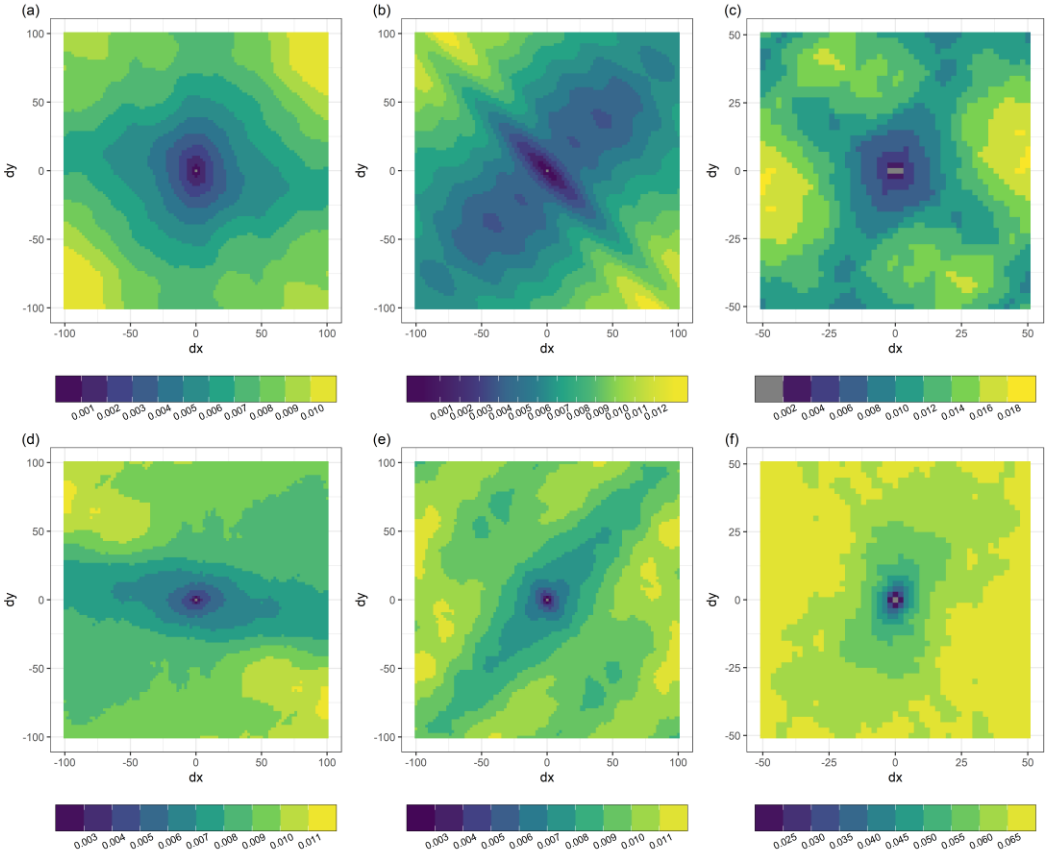

Figure 2.6. Directional semi-variogram of snow depth in **(a)** Sainte-Marthe field, **(b)** Saint-Maurice field, **(c)** Montmorency field, **(d)** Sainte-Marthe forest, **(e)** Saint-Maurice forest and **(f)** Montmorency forest

2.3.3 Random Forest Analysis

2.3.3.1 Relative Importance of Topography and Vegetation on Snow Depth Variability

The relative importance of predictor variables in Figure 2.7 summarizes the relative contribution of the different topographic, vegetation, and forest edge effects on snow depth spatial variability at each site. i.e., how much the prediction error decreases if the variable at interest is included in the RF model compared to when it is excluded. Within the full domain (field+forest), windward forest edge proximity (*WFE*) has the strongest influence on snow depth variability in both Sainte-Marthe (0.99) and Saint-Maurice (0.97), and the north-facing forest edge proximity (*NFE*) has the least influence (0.30 and 0.23). However, topographic wind sheltering (*TWSI*) exerts an equally strong impact on snow depth as *WFE* in Sainte-Marthe (0.99) compared to that in Saint-Maurice (0.70). In Montmorency, *LAI* and *NFE* have the highest (0.99) and least (0.07) impacts, respectively, on snow depth variability for the full domain. The importance of variables somewhat changes when forests and fields are modelled independently, implying different dominant factors/processes acting in each environment. For instance, in Sainte-Marthe, the *TWSI* dominates (0.74) snow depth variability in the forest, followed by *LAI* (0.36), *WFE* (0.36), and *Slope* (0.31). In Sainte-Marthe field, *WFE* (0.94), *TWSI* (0.87), and *Slope* (0.62) are the most important variables. In Saint-Maurice *WFE* (0.33), *TWSI* (0.25), and *LAI* (0.21) have the highest influence on snow depth variability within the forest, whereas in the adjacent field *WFE* (0.99), *TWSI* (0.64), and *Slope* (0.39) predominate. In Montmorency, the importance of *LAI* (0.97), *TWSI* (0.41), and *Slope* (0.25) is higher for snow depths within the coniferous forest with gaps whereas the snow depths in the small field are mostly influenced by *LFE* (0.27), *TWSI* (0.23), and *Slope* (0.18).

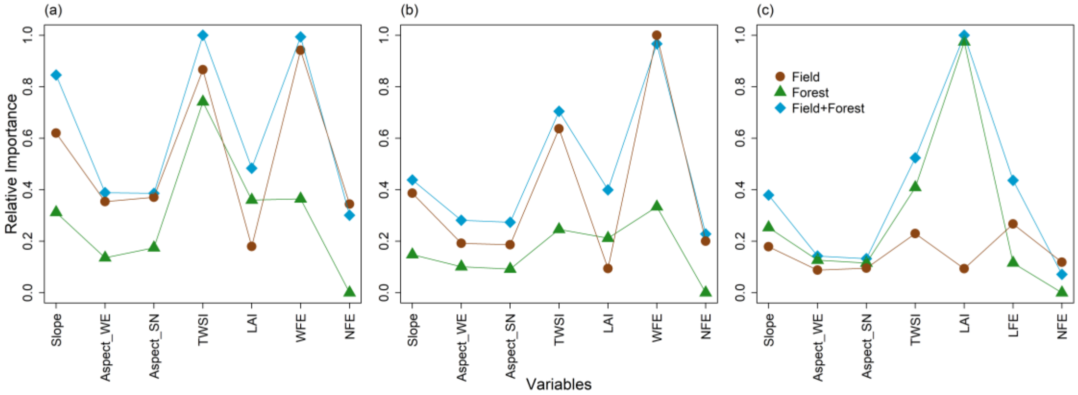

Figure 2.7. Relative importance of variables (scaled between 0 and 1) in predicting snow depths. **(a)** Sainte-Marthe, **(b)** Saint-Maurice and **(c)** Montmorency

2.3.3.2 Partial Relationships of Predictor Variables with Snow Depth

As seen in Figure 2.8, all variables exhibit mostly nonlinear relationships with snow depth across all sites. Spearman rank correlation coefficients (ρ) were used to quantify the strength of the partial relationships and reported in the graphs. A positive ρ indicates an increasing monotonic trend and a negative ρ indicates a decreasing one. Note that the positive *LAI* values in field areas correspond to a few isolated *LAI* pixels along the forest edges, the boundary between field and forest. In general, at all sites and despite the magnitude of the correlation, the two slope aspect variables (*Aspect_WE* and *Aspect_SN*) as well as forest shading represented by the north-facing forest edge proximity (*NFE*) have the least effect on snow depth variability (i.e., a relatively flat partial relationship on Figure 2.8). Moreover, all the relationships between landscape descriptors and snow depth for the overall domain in Montmorency (field+forest, blue curves on Figure 2.8c), except *NFE*, are governed by the respective variable behavior in the forest, probably due to the large extent of forest at this site.

With regards to topographical control, all sites show increasing snow depths with increasing slopes in the field, forest, and field+forest (positive ρ values in Figure 2.8a, b, and c). The general relationship of snow depth with *TWSI* suggests that increased topographic sheltering from the wind (increasing *TWSI* values), leads to enhanced snow accumulation. At the two agro-forested sites (Figure 2.8a, b), the greatest contribution to the overall field+forest *TWSI*-snow depth relation comes from field snow depths.

As for the influence of vegetation, there is a decrease in snow depths in response to increasing *LAI* at all sites, although the relation is comparatively weak ($\rho = -0.65$) in the Sainte-Marthe forest. Snow depth at the two agro-forested sites shows a general increase in response to increasing distance towards the windward forest edge (*WFE*), except within the Saint-Maurice forest. An increase of snow depth with *WFE* in Sainte-Marthe forest indicates more snow at the edge and decreasing inward the forest, which reflects blowing snow penetration from the field inside the forest. The increase in snow depth with *WFE* within the Sainte-Maurice forest for *WFE* > ~0.8 could also reflect the limited penetration of blowing snow from the field inside the forest. In Montmorency, the field snow depth shows a non-linear relation with *LFE*, probably due to the influence of instrumentation at the NEIGE-FM site while forest snow depths show a decrease in accumulation inward the forest.

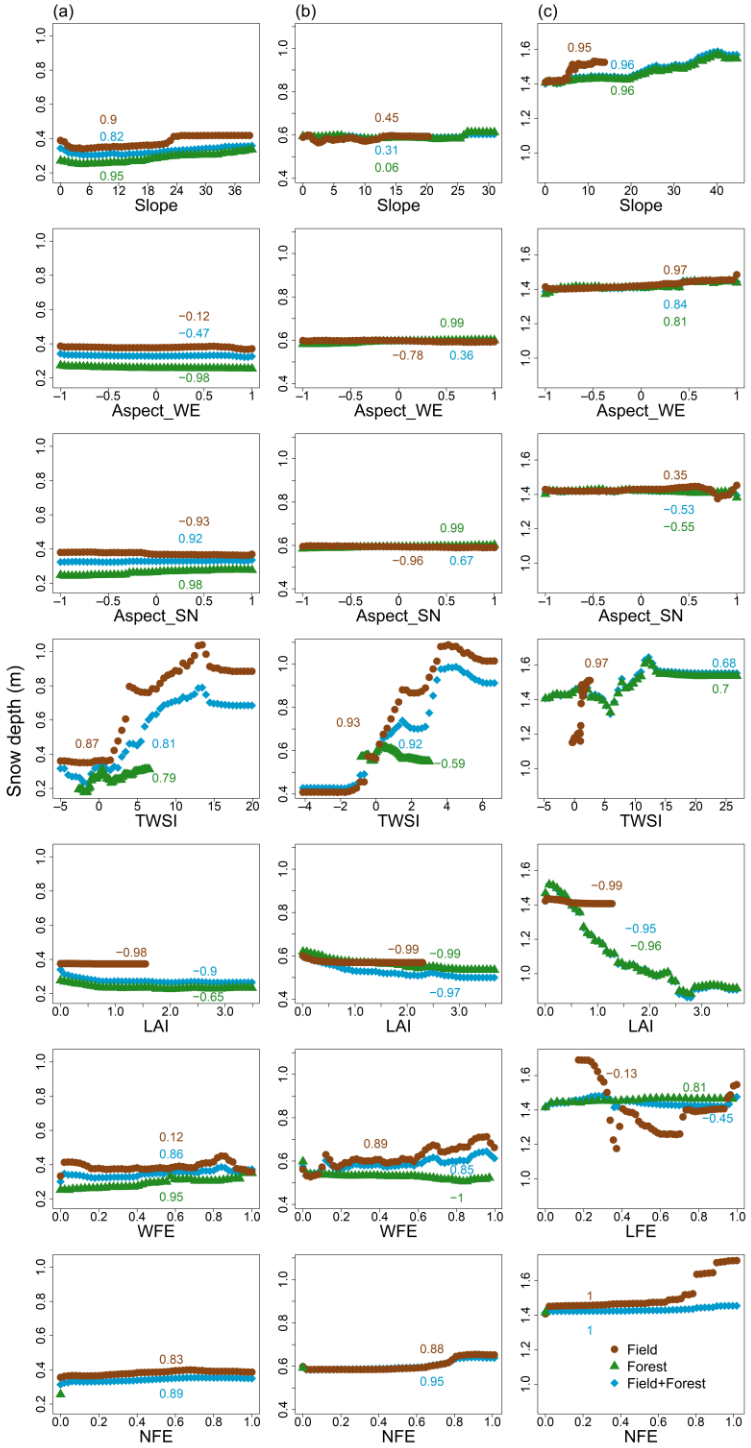

Figure 2.8. Partial relationship of landscape predictor variables with snow depth. **(a)** Sainte-Marthe, **(b)** Saint-Maurice and **(c)** Montmorency. Predictor variables are presented by rows and sites by columns.

2.3.3.3 Performance of RF Models at Each Site

Figure 2.9 displays the RF model estimates versus observed snow depth with corresponding OOB statistics for each site. Statistics are presented individually for the field, forest, and full domain (field+forest). Among the three sites, Sainte-Marthe RF model generally performs better with an OOB R^2 of 0.66 and RMSE of 0.083 m, and Montmorency shows the weakest performance with an R^2 of 0.30 and RMSE of 0.261 m. All field models perform comparatively better with higher R^2 and lower RMSEs values than the corresponding forest models.

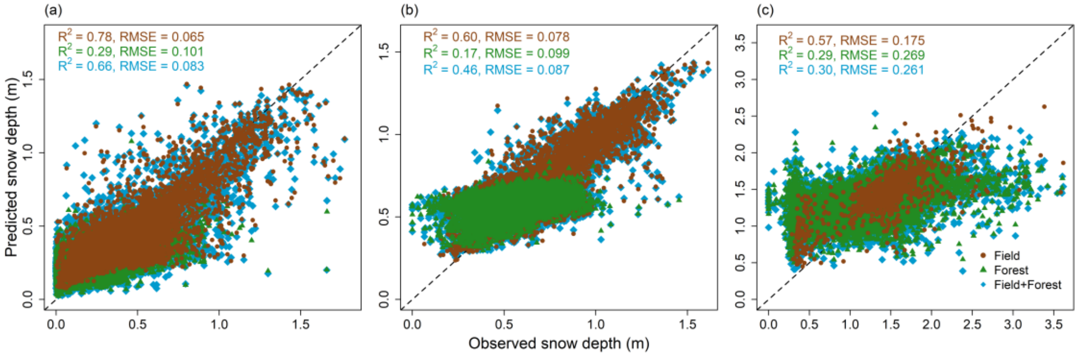

Figure 2.9. RF model performance against observed snow depths. **(a)** Sainte-Marthe, **(b)** Saint-Maurice and **(c)** Montmorency. The stippled line depicts the 1:1 relationship.

Table 2.3 shows the performance of RF models compared to MLR models using the same predictor variables. All RF models show better performances with higher R^2 and lower RMSE values than the corresponding MLR models.

Table 2.3. Comparison of RF and MLR model performances of study sites

	R^2			RMSE		
RF	Field	Forest	Field+Forest	Field	Forest	Field+Forest
Sainte-Marthe	0.78	0.29	0.66	0.07	0.10	0.08
Saint-Maurice	0.60	0.17	0.46	0.08	0.10	0.09
Montmorency	0.57	0.29	0.30	0.18	0.27	0.26
MLR						
Sainte-Marthe	0.18	0.04	0.21	0.12	0.12	0.13
Saint-Maurice	0.32	0.08	0.17	0.10	0.10	0.11
Montmorency	0.02	0.13	0.12	0.26	0.30	0.29

2.4 Discussion

2.4.1 Spatial Variability of Forest versus Field Snow Depths

Snow depths in Figure 2.4 show remarkable microtopographic variability across all sites. Our results in Sainte-Marthe underpin the previous finding that forested areas accumulate less snow than the adjacent open areas due to canopy interception and sublimation losses and sheltering from wind (Pomeroy and Granger, 1997; Hopkinson et al., 2004; Varhola et al., 2010a; Zheng et al., 2018; Hojatimalekshah et al., 2021). But the other two sites show on average a similar amount of snow accumulation in the field and forest. The dense coniferous canopy cover in Montmorency prevented laser shots from reaching the ground at some locations and consequently resulted in data gaps in the snow depth map (Figure 2.4c). The snow depth patterns in the coniferous site thus appear to be dominated by canopy closure, i.e., forest clearings have higher snow depths than adjacent canopies. Such patterns have been previously reported by both ALS and UAV lidar studies in western alpine/pre-alpine environments with different climates (Hopkinson et al., 2004; Zheng et al., 2016; Mazzotti et al., 2019; Jacobs et al., 2021). Several authors also highlighted that under-sampling of snow depths under the canopy could lead to an overestimation of the overall amount of snow in the forest when gaps (forest clearings) are prevalent, such as in Montmorency (Harpold et al., 2014; Zheng et al., 2016). This is because the lidar coverage can be biased towards the gaps, which accumulate more snow than under the canopy, hence the spatially-averaged snow depth is also biased.

At the agro-forested sites, the comparatively higher snow depths observed in the open field compared to the adjacent forest patches are in contrast to what Aygün et al. (2020) observed in similar environments in southern Québec. They measured a lower snow accumulation in exposed agricultural fields (excluding the canals and the forest edge) compared to the adjacent deciduous and mixed forests. Our results show that the higher snow depths at the two agro-forested sites principally correspond to canals and streams in the field and the forest edge, which trap the snow blown from the open field with greater fetches. Hence canals/streams and forest edges constitute the main structuring elements of snow spatial variability at these sites. However, if canals and forest edge snow depths are discarded, the agro-forested snow depth maps illustrate a somewhat similar phenomena to Aygün et al. (2020), where snow depths in the exposed field are slightly lower than those in the forest. In Saint-Maurice, clusters of high snow depth values in the central area of the field in Figure 2.4b could be due to local redeposition of snow by the wind in the microtopography, or larger-scale topographic effects. This could not be verified as unfortunately, the manual measurements in Saint-Maurice could not be retrieved due to a probe malfunctioning (Dharmadasa et al., 2022). Yet, the *TWSI* map (Supplement Figure S2.3) suggests that microtopographic wind sheltering could be the reason for the local snow deposition closer to the forest edge. The probable cause for the other larger high snow depth clusters between the two streams in the field could not be explained from the available predictors. They could be explained by the influence of the narrow riparian strips of bushes and shrubs surrounding the canals on blowing snow redistribution. Ultimately, as canopy interception and losses in deciduous and mixed forests are expected to be small (Hopkinson et al., 2012b; Aygün et al., 2020), the amount of differential snow depths between the open field and forest would mostly depend on the amount of erosion in the field, and perhaps snowmelt losses in the open field prior to peak snow accumulation. Moreover, the snow depth maps suggest that the redistribution of eroded snow in fields along the forest edges is a prime process in agro-forested landscapes.

2.4.2 Scaling Characteristics of Forest versus Field Snow Depths

2.4.2.1 Omnidirectional Semi-Variograms Analysis

Omnidirectional semi-variogram analyses revealed distinct scaling behaviors in forest versus field snow depths (Figure 2.5). Our results suggest a more variable (high semi-variance values) and more spatially continuous (larger scale break distance) snowpack in the Montmorency boreal forest compared to the temperate forest sites. The snowpack in the mixed forest at Saint-Maurice was less variable and more spatially continuous than that in the Sainte-Marthe deciduous forest. Compared to forested areas, the snowpack in field areas was less variable and more spatially continuous. We found the shortest scale break distance of 4.4 m for the dense deciduous forest in Sainte-Marthe, an intermediate distance of 5 m for the moderately dense mixed forest in Saint-Maurice, and a value of 6.5 m for the dense coniferous forest interspersed with gaps in Montmorency. Several studies reported scale break distances of 4 m for a shrub-dominated sparsely distributed subalpine site (Mendoza et al., 2020b), 7–9 m for high to moderately dense coniferous forests (Trujillo et al., 2007; Trujillo et al., 2009), 12 m for a moderately dense deciduous forest (Trujillo et al., 2007; Trujillo et al., 2009), 15.5 m for a dense coniferous forest with open meadows (Deems et al., 2006; Fassnacht and Deems, 2006), and 16.5 m for a sparse coniferous forest (Deems et al., 2006; Fassnacht and Deems, 2006). Our values are rather smaller than those reported by previous studies, except Mendoza et al. (2020b). This could be due to structural characteristics of the forests such as canopy density and size of open areas (gaps). It is also plausible that the dense point cloud provided by UAV (~150–600 points m^{-2}:

Zhang et al., 2019; Harder et al., 2020; Jacobs et al., 2021; Dharmadasa et al., 2022) was able to resolve spatially distributed snow depth patterns at finer scales than that permitted by previous ALS surveys, which had typical point densities of ~8–16 points m^{-2} (Kirchner et al., 2014; Broxton et al., 2015; Broxton et al., 2019; Currier et al., 2019). However, similar to the findings reported by Deems et al. (2006) and Trujillo et al. (2007) our topography+vegetation surface data show scale break distances at the same order of magnitude as the forest snow depths at all sites. This indicates that the variability of vegetation (trees) governs the pattern of snow deposition and distribution within the forest (Deems et al., 2006).

The relatively higher scale break distance in Montmorency forest snow depth could be due to the prevailing large gaps in the forest as a result of silvicultural practices and the higher efficient canopy interception of conifers. Coniferous trees have a substantial impact on snow depths as they intercept snow efficiently and unload it around the crown (Zheng et al., 2019). Thus, a longer correlation length (at least the diameter of a tree crown) is expected as well as greater variability of snow depth in coniferous environments compared to the more random deciduous tree structures which have reduced and more transient snow storage (Mendoza et al., 2020b). Leafless deciduous trees aid faster unloading of snow through branches as opposed to unloading around the crown in conifers and thus would result in a smaller correlation length in snow depth.

The difference in scale break distances in field snow depths compared to bare earth topography indicates that the bare ground surface in field areas was certainly altered by the snow accumulation. In Sainte-Marthe, snow accumulation increases the roughness of the bare ground whereas, in Saint-Maurice, snow accumulation results in a smooth surface compared to the ground underneath. i.e., interactions of snow with bare ground in Sainte-Marthe field change the scale invariance behavior to multi-scaling, and in Saint-Maurice, these interactions smooth the surface and resulted in a larger scale break distance than that of the bare ground. However, the larger scale break distance and gentler slope of the Sainte-Marthe field semi-variogram (Figure 2.5a) compared to Saint-Maurice (Figure 2.5b) suggests that the snowpack in Sainte-Marthe field is still smoother and more spatially continuous than that of Saint-Maurice. This interpretation is supported by the snow depth map in Figure 2.4a, which shows a smooth snow depth pattern that is only disrupted by preferential accumulation within irrigation canals/streams. In Montmorency field, rather than interactions of snow with bare ground, the meteorological station network appears to modify the snow accumulation and distribution patterns and resulted in different multi-scaling behavior than the bare ground. In general, large scale break distances (11–14 m) compared to forested areas were found in field snow depths at all sites except the short, first scale break distance (5.8 m) in Montmorency. With the absence of vegetation in the field in winter and its high exposure to wind at the two agro-forested sites (Figure 2.2a, b), these values are of similar magnitude to those reported for wind-exposed slopes in alpine environments (13.8–20.5 m) by Schirmer and Lehning (2011), Mott et al. (2011), Mendoza et al. (2020a), and Mendoza et al. (2020b). In the Montmorency field, mostly sheltered from the wind, the short and large-scale break distances could be due to the influence of preferential snow accumulation near the meteorological equipment (e.g., concentric snow accumulations patterns around the two double-fenced precipitation gauges in Figure 2.4c).

Generally, the scale break distances found in this study suggest that the scale selected for modeling or sampling in similar environments should be well below these values, in order to fully resolve the small-scale variability of the snow depth.

2.4.2.2 Directional Semi-Variograms Analysis

Sainte-Marthe field snow depths did not show any directionality, most probably as a result of the interactions of snow with two dominant and opposed wind directions. In contrast, Saint-Maurice field snow depths showed anisotropic behaviors along and perpendicular to the dominant wind direction. Narrow anisotropic patterns perpendicular to the dominant wind direction are due to the snow accumulation alongside canals. Even though the canals were discarded in semi-variogram analysis, as seen from Figure 2.4b, preferential snow accumulation is still significant from the canal margins up to a few meters into the field. Broader anisotropic patterns along the dominant wind direction are due to the influence of wind. This directionality is also shown in the snow depth map in Figure 2.4b, where the change of snow depth values along the direction perpendicular (northwest-southeast) to the dominant wind direction is more drastic than the change of snow depths along the dominant wind direction towards the forest. However, forest snow depths at both agro-forested sites show anisotropic behavior, although not very strong, parallel to dominant wind directions. This indicates an influence of blowing snow on the snow distribution patterns in the forest, and hence a possible penetration of blowing snow from field to forest. The isotropic behavior in the Montmorency field and forest, on the other hand, is not surprising given that the site is sheltered from the dominant winds (Figure 2.2c).

2.4.3 Relationship of Snow Depth to Topographic and Vegetation Characteristics

2.4.3.1 At the Agro-Forested Sites

At the two agro-forested sites, field snow depth variability is governed by preferential snow accumulation in canals/streams and the microtopography of the local terrain, as seen by the high relative importance factor of *TWSI* in Figure 2.7a, b, i.e., adding the *TWSI* reduces model errors significantly. As such, the highest wind sheltering values were found in canals/streams which accumulated more snow (Figure 2.4 and Supplement Figure S2.2, S2.3). Within the forested areas, the influence of forest structure (*LAI*) was not as strong as expected; instead, the influence of microtopography appeared to be mostly governing the snow depth variability. The lower influence of *LAI* at these sites probably reflects the abundance of leafless trees in winter, which reduce interception losses and concurrent spatial snowpack variability. Moreover, the microtopography of these landscapes is closely related to the surficial geology of the sites. Preserved forested patches in the St. Lawrence River lowlands often correspond to less favorable soil conditions, such as glacial till and/or bedrock outcrops and associated rougher microtopography. Conversely, agricultural fields are developed on glaciomarine or fluvioglacial sediments that are flatter in nature and also leveled by machinery (MFFP, Québec Research and Development Institute for the Agri-Environment (IRDA) and La Financière Agricole du Québec (FADQ)). Under limited wind transport, the rougher microtopography in forests creates a directional bias that promotes lateral transport of snow particles (bounce/ roll/ ejection) and therefore enhances the smoothing of the snow surface (Filhol and Sturm, 2019) which dominates the snow heterogeneity within the forest. The absence of apparent preferential snow accumulation on different slope orientations in agricultural fields suggests a smoothening of the topography by the snow cover due to wind redistribution in the field. The more rugged microtopography of the forested soil on the other hand seems to be preserved and to influence the snow cover through differential radiation loading, resulting in more snow accumulations on northerly slopes in the forest compared to that in the field (Figure 2.8a, b).

At the landscape scale (field+forest), *WFE* has the highest relative importance (Figure 2.7a, b); including *WFE* decreases the prediction error of the RF model by a factor of 0.97–0.99 (97–99 %) compared to a model excluding *WFE*. Thus, the agro-forested sites are dominated by blowing snow accumulation along the forest edges. This effect is well visible on the lidar-derived snow depth maps too (Figure 2.4a, b). Comparatively high wind speeds and more constrained dominant wind directions (Figure 2.2a, b) at these sites create favorable conditions for preferential deposition of blowing snow at the forest edge due to the large expanses of open terrain upwind of the windward forest edges. Preferential snow deposition by wind-induced snow drifting along the forest edge has been previously reported in alpine environments by Veatch et al. (2009), Essery et al. (2009), Broxton et al. (2015), and Currier and Lundquist (2018). However, there seems to be only limited penetration of blowing snow inside the forest in windward directions (*WFE* forest points in Figure 2.8a, b and Figure 2.6d, e).

Shading by the forest edge seemingly does not have a significant influence on the snow depth variability at these sites during the accumulation season. Shading effects would however probably have some influence on snow depth patterns during the melting season (Hojatimalekshah et al., 2021). The spatial heterogeneity of snow depths and associated processes challenge distributed snow modeling using hydrologic response units (HRUs) in agro-forested landscapes (Aygün et al., 2020), where HRUs are classified as field and forest patches but disregard boundary effects. Aygün et al., (2020) modelled (Nash–Sutcliffe efficiency of 0.57 over 23-year simulation of SWE) blowing snow transport in fields and the preferential accumulation in canals and streams, and assumed that once these were filled, any further blown snow accumulated in the forest. Our results confirm the preferential accumulation in field canals and streams but suggest that further blown snow first preferentially accumulates at the forest edge, which should eventually be represented as distinct HRUs in distributed hydrological models of agro-forested landscapes.

2.4.3.2 At the Boreal Forested Site

The findings in agro-forested sites are in contrast with the boreal forested environment, where forest structure (*LAI*) predominates on the variability of snow depth (Figure 2.7 and Figure 2.8). The small field appears to have fewer microtopographic features and is mostly sheltered from the most frequent winds coming from the northwest direction (Figure 2.2c). The relatively greater positive *TWSI* values at this site compared to agro-forested sites imply more rugged microtopography and a larger degree of wind sheltering in the forested terrain (Figure 2.8c and Supplement Figure S2.4). However, since wind is mostly impeded by the coniferous trees, the *TWSI*-snow depth relationship in the forest suggests that the snow displacement is driven by small-scale bounce/ejection/roll mechanisms, and preferential snow deposition is driven by immobilizing mechanisms such as adhesion, cohesion, and physical interlocking of snow particles (Filhol and Sturm, 2019) and unloading of snow by the canopy (Zheng et al., 2019). The lesser importance of *TWSI* (0.41 compared to 0.97 of *LAI*, the dominant predictor, Figure 2.7) as snow depth predictor in the coniferous forest compared to deciduous (*TWSI* = 0.74, the dominant predictor) and mixed (*TWSI* of 0.25 compared to 0.33 of *WFE*, the dominant predictor) forests, and the more or less constant snow depth values at higher *TWSI* values (Figure 2.8c) suggest that microtopography has a more restricted influence on deeper snowpack at this site compared to the shallower snowpack at the agro-forested sites. In other words, in the absence of wind, increasing snow depths reduce/inhibit surface undulations and promote more spatially continuous snow cover (Filhol and Sturm, 2019). The spatial arrangement of the trees may have a larger control on snow depths in the boreal forest, i.e., forest gaps in the coniferous forest with various slopes and aspects creating pronounced and distinct snow depth variabilities inside the forest (Woods et al., 2006). For instance, in Montmorency, superimposed *TWSI* and *LAI* maps (Supplement Figure S2.4) show that the high snow depth values associated with *TWSI* values of 10–12 (Figure 2.8c) are associated with a forest gap that likely prevents snow interception and accumulates more snow. Our results support the findings of previous studies that the snow depth distribution in coniferous environments is mainly governed by the canopy characteristics such as structure, distribution, and type of vegetation (Winkler et al., 2005; López-Moreno and Latron, 2008; Varhola et al., 2010a; Zheng et al., 2018; Safa et al., 2021; Koutantou et al., 2022). Our findings however show that the microtopography, even under wind-sheltered conditions in the forest, still explains some of the spatial variability in snow depths, although not as prominent as canopy characteristics.

2.4.4 Comparison of RF Model Performances

2.4.4.1 Comparison between the Sites

Our RF model showed variable performances, with overall OOB R^2 of 0.30–0.66 (Figure 2.9). All sites have different climates. The higher performance at Sainte-Marthe could be due to a combination of different factors. Early snowmelt due to frequent rain-on-snow events in this region (Paquotte and Baraer, 2021) might have contributed to a more structured snowpack in the Sainte-Marthe forest and hence improved the prediction of snow depth compared to the other agro-forested Saint-Maurice site. The high R^2 values in fields at all sites (0.78 in Sainte-Marthe, 0.60 in Saint-Maurice, and 0.57 in Montmorency) indicate that the models captured the most relevant processes through the predictor variables considered. In contrast, Saint-Maurice forest had the worst performance (0.17). This could be due to underlying processes/variables not considered in our model, possibly associated with the canopy structure of the mixed forest. Moreover, the reduced sampling under coniferous trees due to limited lidar penetration could also have affected grid-scale snow depth and resulting relationships with landscape metrics in the Montmorency forest.

2.4.4.2 Comparison with Previous Studies

The previous studies that used RF models to estimate snow depths/SWE (Bair et al., 2018; Yang et al., 2020) were mainly focused on mountainous watersheds with large elevation gradients and with less or no vegetation and reported average Nash–Sutcliffe efficiencies as high as ~0.7 and RMSEs of 44–73 mm, where the major part of this variance was explained by elevation. Safa et al. (2021) developed site-specific RF models to predict snow-covered areas using vegetation density, average incoming shortwave, and longwave radiation, total precipitation, and average air temperature and reported mean absolute errors of 0.05–0.12 m in mixed coniferous sites. In addition, the abundance of studies that employed MLR (Jost et al., 2007; Lehning et al., 2011; Grünewald et al., 2013; Revuelto et al., 2014; Fujihara et al., 2017) and BRT (Winstral et al., 2002; Anderton et al., 2004; Molotch et al., 2005; Revuelto et al., 2014) in alpine environments with rocky outcrops and pasture or no vegetation also reported R^2 of 0.25–0.91 where a substantial portion of the snow depth variability was explained by terrain parameters, mostly elevation. However, model performances are shown to be degraded with the presence of forests. Studies conducted in forested terrain with relatively small elevation ranges reported R^2 of 0.25–0.51 by MLR (Zheng et al., 2016; Zheng et al., 2018) and BRT (Erxleben et al., 2002; Veatch et al., 2009; Baños et al., 2011). Musselman et al. (2008) proved that including detailed vegetation information like micro-scale vegetation-induced solar radiation, distance to the canopy, and tree bole could improve BRT performance to 0.68 in a forested area. Compared to previous works in forested terrain, we believe our model fits (overall R^2 of 0.30–0.66) are in a reasonable range.

2.4.4.3 Comparison to MLR Models

The relatively good success of MLR in previous studies to study landscape control on snow accumulation is mostly attributed to elevational controls on snow accumulation, i.e., orographic enhancement of precipitation gradient and adiabatic cooling which promotes higher snowfall fraction and reduced ablation at higher elevations. However, in low elevation landscapes, more complex relationships are expected between snow depths, vegetation, and topography, which would likely be poorly captured by linear relationships. As shown in Table 2.3, our RF models show a significant improvement with higher R^2 and lower RMSE values compared to MLR models at all sites. Since the MLR models at each site were developed using the same predictors described in section 2.2.3.2., this suggests the deficiency of MLR models in capturing the underlying processes at these sites. Figure 2.8 shows that almost all variables have a nonlinear relationship with snow depth, which linear models are unable to capture. Our RF results thus highlight the importance of considering this nonlinearity in statistical models, as RF notably allows capturing nonlinear relationships between snow accumulation and landscape variables, while protecting against the typical overfitting of single decision trees.

2.4.5 Note on Potential Variables/Predictors in Similar Landscapes

One particularity of our sites (also related to the scale of the analysis) is the negligible elevation range. Many studies conducted in mountainous environments have shown the preponderant influence of elevation on the distribution of snow cover. While the elevation range becomes important over a larger extent on the Canadian shield (Montmorency-type physiography), the low elevation St. Lawrence lowlands (Sainte-Marthe and Saint-Maurice) remain mostly flat, and local topography (terrain roughness), land cover and land use are expected to control the spatial distribution of the snow cover. As confirmed by our results, in agro-forested land covers, wind-related forest edge effects will also have a substantial impact on snow deposition, and distribution patterns.

2.4.6 Limitations of the Study

This study provides insight into the scaling properties of the snowpack and the effect of different topographic, vegetation, and forest edge characteristics on snow depth variability in open versus forested areas with different canopy covers. However, there are potential limitations with some of the methods presented in this study. For instance, despite our efforts to incorporate processes/variables influencing the spatial distribution of snow depths with available data, the comparatively lower performance of RF models in Saint-Maurice and Montmorency indicates that there could still be some processes/variables that were unable to accounted for (e.g., soil parameters, snowpack state, and meteorological variables). Another limitation comes from the unexplained snow depth variability that is within the UAV lidar system detection limit. Especially in Montmorency, there were observation gaps by UAV lidar due to the thick canopy cover that eventually affected the accuracy of snow depth and ground surfaces rasters and derived landscape descriptors (e.g., slope, LAI, etc.). The problem of under-sampling of snow depth under canopies and associated effects on interpolation and spatial-averaging of snow depths has been long identified but is still not fully resolved. The dominant predictors identified in this study might also depend on the timing of the survey date (e.g., near peak snow accumulation versus early and mid-winter, or during the melt period). Hence, repeat surveys with UAV lidar to track the temporal evolution of the snowpack would be required to fully address this question in the future. However, the analysis presented here is thought to largely reflect the typical conditions at the sites and to portray key differences between agro-forested and boreal landscapes. The similar key processes identified at the two agro-forested sites suggest that findings at these sites could be extrapolated to similar environments. In absence of large-scale ALS surveys over snow in Québec as done, for example in the Sierra Nevada, USA (e.g., Zheng et al. (2019)), UAV lidar meanwhile provides opportunities to map snow depths and test hypotheses regarding the spatial variability of snow depths. While the statistical framework used in this study does not allow a full understanding of the driving processes, it provides a useful identification and ranking of the predictors associated with such processes, such as forest edge effects, forest structure, and microtopography and offers guidance for the development and application of process-based models in these environments.

2.5 Conclusions

In this study, including wind-related forest edge effects in agro-forested sites and incorporating canopy characteristics in the coniferous site increased the statistical prediction accuracy of snow depth spatial variability by more than 90 % compared to when these predictors are discarded from the RF model. This implies the importance of including and better representing these processes in physically-based models. Taken together, our results suggest that in agro-forested landscapes of the St. Lawrence valley, geomorphological assemblages drive the differential snow accumulation between field and forested areas, i.e., rugged glacial deposits with preserved forests favor more snow accumulation whereas flat glaciomarine sediments in the exposed fields promote snow erosion. The blowing snow redistributed from the fields gets trapped in canals/streams and accumulates along the forest edges, accounting for the highest local snow depths in these landscapes. Furthermore, within deciduous/mixed forests, it is rather the underlying topography and/or the forest edges that govern the snow depth variability, while within the coniferous environment, it is the forest structure variability. These processes are not fully represented in process-based models. For instance, models like CRHM (Pomeroy et al., 2007), and SnowModel (Liston and Sturm, 1998) prescribe a single, typical LAI for land cover classes. This ignores the variability within stands which could compromise larger scale estimates of snowpacks. The recent development of hyper-resolution process-based models does account for fine scale canopy structure (Mazzotti et al., 2020a; Mazzotti et al., 2020b), yet representing microtopographic characteristics like terrain roughness is still problematic. Our results suggest that snow redistribution at forest edges, spatial variability of forest structure, and better representation of microtopography and prominent topographical features such as canals are important processes/variables that should be taken into account in process-based models. This highlights the advantage of using high resolution data to characterize small-scale processes and therefore explicitly resolve snow depth variability.

In addition, since the selected sites are representative of typical agro-forested and boreal landscapes in southern Québec, the findings of this study could be applied/extrapolated to similar landscapes in the region and any similar environments where similar processes operate.

Acknowledgments

The authors extend their appreciation to the members of GlacioLab for their help during the fieldwork. Moreover, the authors are grateful to the Sainte-Marthe municipality, Québec, Canada and members of NEIGE_FM, Forêt Montmorency, Québec, Canada.

Supporting Information

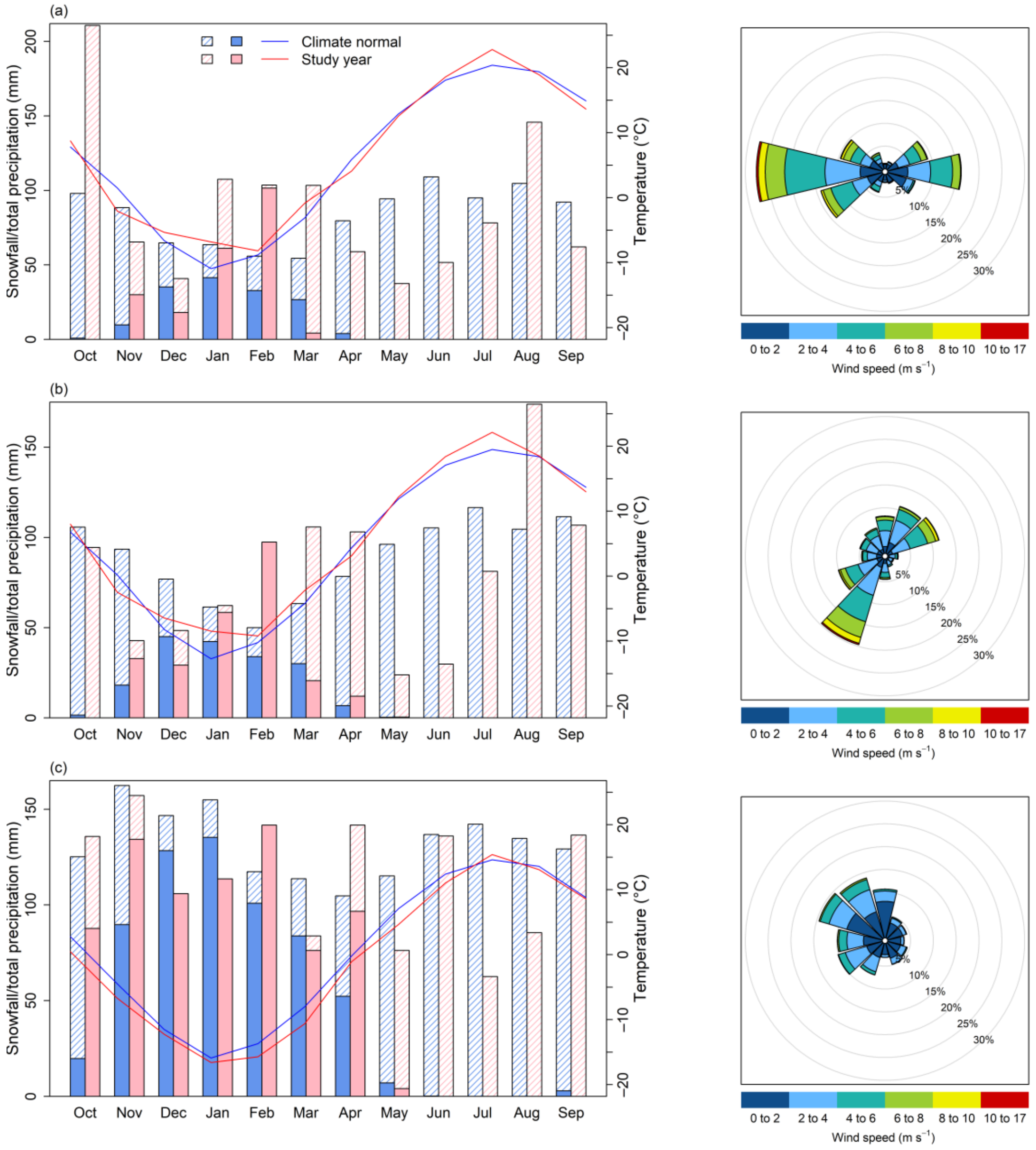

Figure S2.1. Long-term snowfall/total precipitation, average temperature, and wind rose plots at **(a)** Sainte-Marthe, **(b)** Saint-Maurice and **(c)** Montmorency. Stripped bars indicate total precipitation and solid color bars indicate snowfall. Long-term snowfall, total precipitation and average temperatures were derived from climate normal (averages for 1981–2010) for the same ECCC stations used in Table 2.1. Then they were plotted with snowfall/total precipitation and average temperature values of the study hydrological years (Oct-Sept) to place them in a climatological context. The long-term wind rose plots were derived from the nearest available wind stations to the sites for 2010–2020 (Station climate ID 7016470, 7018561, and 7042395 for Sainte-Marthe, Saint-Maurice, and Montmorency)

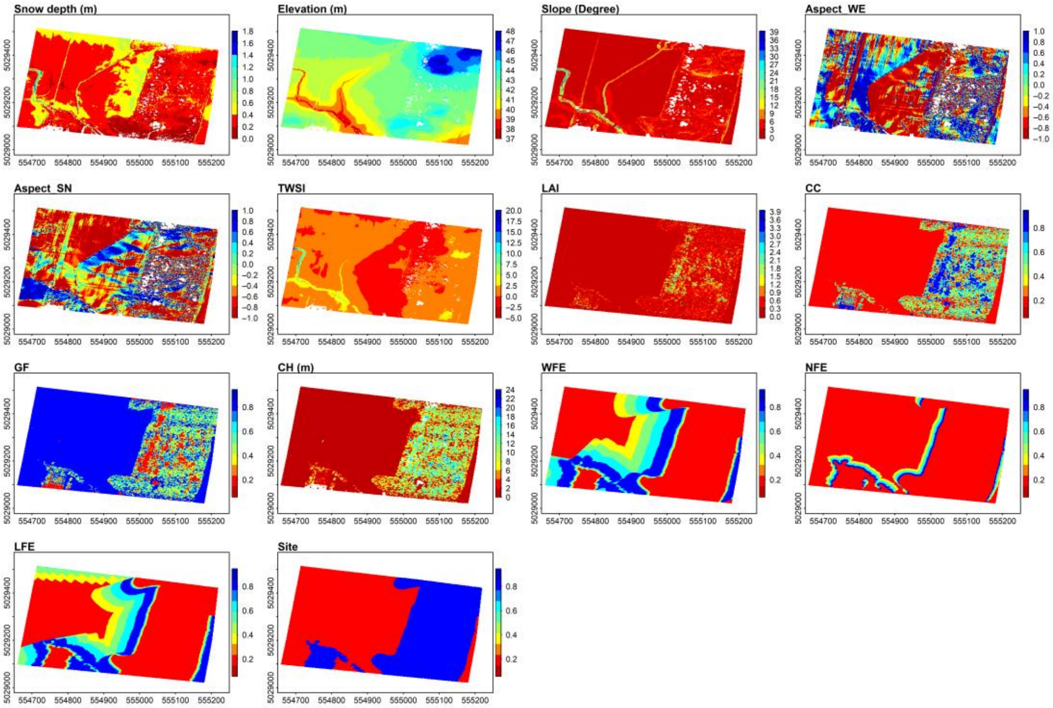

Figure S2.2. Sainte-Marthe snow depth and predictor variables maps. The elevation is presented as ellipsoidal height.

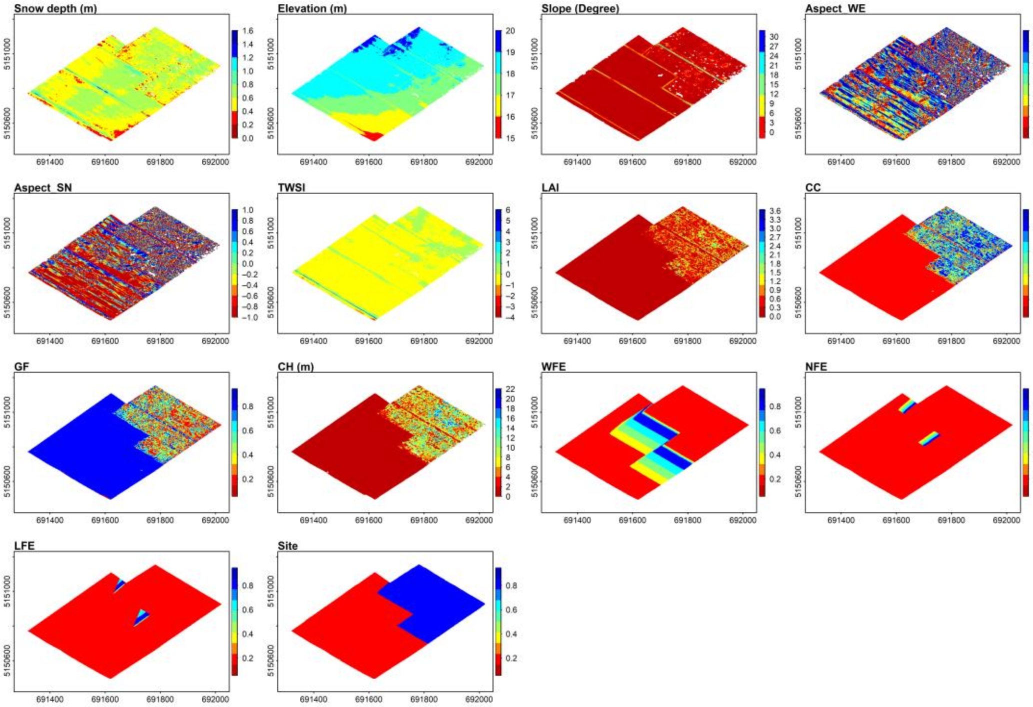

Figure S2.3. Saint-Maurice snow depth and predictor variables maps. The elevation is presented as ellipsoidal height.

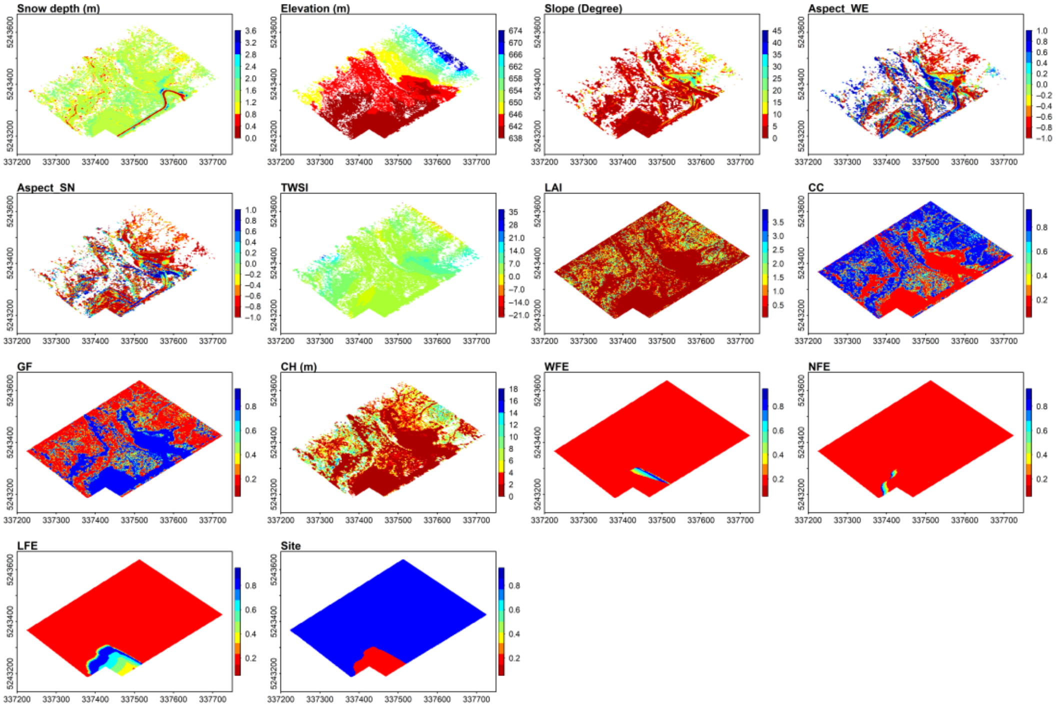

Figure S2.4. Montmorency snow depth and predictor variables maps. The elevation is presented as ellipsoidal height.

Table S2.1. RF model R^2 for different vegetation descriptors

	Sainte-Marthe			Saint-Maurice			Montmorency		
	Field+ Forest	Forest	Field	Field+ Forest	Forest	Field	Field+ Forest	Forest	Field
LAI	0.659	0.291	0.778	0.459	0.168	0.602	0.303	0.290	0.560
CC	0.659	0.292	0.778	0.459	0.167	0.602	0.304	0.294	0.562
CH	0.672	0.287	0.799	0.498	0.155	0.664	0.369	0.365	0.589
GF	0.659	0.290	0.777	0.459	0.166	0.602	0.304	0.292	0.563

Note: sensitivity of different vegetation descriptors was tested by keeping the other variables in RF models unchanged.

References

Anderton, S. P., White, S., and Alvera, B.: Evaluation of spatial variability in snow water equivalent for a high mountain catchment, Hydrological Processes, 18, 435–453, doi: 10.1002/hyp.1319, 2004.

Aygün, O., Kinnard, C., Campeau, S., and Krogh, S. A.: Shifting hydrological processes in a Canadian agroforested catchment due to a warmer and wetter climate, Water, 12, 739, 2020.

Bair, E. H., Abreu Calfa, A., Rittger, K., and Dozier, J.: Using machine learning for real-time estimates of snow water equivalent in the watersheds of Afghanistan, The Cryosphere, 12, 1579–1594, doi: 10.5194/tc-12-1579-2018, 2018.

Baños, I. M., García, A. R., Alavedra, J. M. i., Figueras, P. O. i., Iglesias, J. P., Figueras, P. M. i., and López, J. T.: Assessment of airborne lidar for snowpack depth modeling, Boletín de la Sociedad Geológica Mexicana, 63(1), 95–107, 2011.

Blue Marble Geographics: Global Mapper, Blue Marble Geographics, Hallowell, ME, USA, 2020.

Breiman, L.: Random Forests, Machine Learning, 45, 5–32, doi: 10.1023/A:1010933404324, 2001.

Brown, R. D.: Analysis of snow cover variability and change in Québec, 1948–2005, Hydrological Processes, 24, 1929–1954, 2010.

Broxton, P., Leeuwen, W. J. V., and Biederman, J.: Improving snow water equivalent maps with machine learning of snow survey and lidar measurements, Water Resour. Res, 55, 3739–3757, doi: 10.1029/2018WR024146, 2019.

Broxton, P. D., Harpold, A. A., Biederman, J. A., Troch, P. A., Molotch, N. P., and Brooks, P. D.: Quantifying the effects of vegetation structure on snow accumulation and ablation in mixed-conifer forests, Ecohydrology, 8, 1073–1094, 2015.

Cho, E., Hunsaker, A. G., Jacobs, J. M., Palace, M., Sullivan, F. B., and Burakowski, E. A.: Maximum entropy modeling to identify physical drivers of shallow snowpack heterogeneity using unpiloted aerial system (UAS) lidar, Journal of Hydrology, 602, 126722, doi: 10.1016/j.jhydrol.2021.126722, 2021.

Clark, M., Hendrikx, J., Slater, A., Kavetski, D., Anderson, B., Cullen, N. J., Kerr, T., Hreinsson, E., and Woods, R.: Representing spatial variability of snow water equivalent in hydrologic and land surface models: A review, Water Resour. Res, 47, W07539, doi: 10.1029/2011WR010745, 2011.

Clemenzi, I., Pellicciotti, F., and Burlando, P.: Snow depth structure, fractal behavior, and interannual consistency over Haut glacier d'Arolla, Switzerland, Water Resour. Res, 54, 7929–7945, doi: 10.1029/2017WR021606, 2018.

Currier, W., Pflug, J. M., Mazzotti, G., Jonas, T., Deems, J. S., Bormann, K., Painter, T., Hiemstra, C., Gelvin, A., Uhlmann, Z., Spaete, L., Glenn, N., and Lundquist, J. D.: Comparing aerial lidar observations with terrestrial lidar and snow probe transects from NASA's 2017 SnowEx campaign, Water Resour. Res, 55, 6285–6294, doi: 10.1029/2018WR024533, 2019.

Currier, W. R. and Lundquist, J. D.: Snow depth variability at the forest edge in multiple climates in the western United States, Water Resour. Res, 54, 8756–8773, doi: 10.1029/2018WR022553, 2018.

Deems, J. S., Fassnacht, S. R., and Elder, K. J.: Fractal distribution of snow depth from lidar data, Journal of Hydrometeorology, 7, 285–297, 2006.

Deems, J. S., Fassnacht, S. R., and Elder, K. J.: Interannual consistency in fractal snow depth patterns at two Colorado mountain sites, Journal of Hydrometeorology, 9, 977–988, doi: 10.1175/2008JHM901.1, 2008.

Deems, J. S., Painter, T. H., and Finnegan, D. C.: Lidar measurement of snow depth: a review, Journal of Glaciology, 59, 467–479, doi: 10.3189/2013JoG12J154, 2013.

Dharmadasa, V., Kinnard, C., and Baraër, M.: An accuracy assessment of snow depth measurements in agro-forested environments by UAV lidar, Remote Sensing, 14, 1649, doi: 10.3390/rs14071649, 2022.

Egli, L., Jonas, T., Grünewald, T., Schirmer, M., and Burlando, P.: Dynamics of snow ablation in a small Alpine catchment observed by repeated terrestrial laser scans, Hydrological Processes, 26, 1574–1585, doi: 10.1002/hyp.8244, 2012.

Elder, K., Michaelsen, J., and Dozier, J.: Small basin modelling of snow water equivalence using binary regression tree methods, Biogeochemistry of Seasonally Snow-Covered Areas, IAHS-AIHS and IUGG XXI General Assembly, Boulder, Colorado, July 1995, 129–139, 1995.

Elder, K., Rosenthal, W., and Davis, R. E.: Estimating the spatial distribution of snow water equivalence in a montane watershed, Hydrological Processes, 12, 1793–1808, 1998.

Environment and Climate Change Canada. Hourly Data Report. Retrieved July 16, 2021 https://climate.weather.gc.ca/, 2021a.

Environment and Climate Change Canada. Canadian Climate Normals 1981-2010, Edited. Retrieved August 10, 2020 https://climate.weather.gc.ca/, 2021b.

Erxleben, J., Elder, K., and Davis, R.: Comparison of spatial interpolation methods for estimating snow distribution in the Colorado Rocky Mountains, Hydrological Processes, 16, 3627–3649, 2002.

Essery, R., Rutter, N., Pomeroy, J., Baxter, R., Stähli, M., Gustafsson, D., Barr, A., Bartlett, P., and Elder, K.: SNOWMIP2 an evaluation of forest snow process simulations, Bulletin of the American Meteorological Society, 1120–1135, 2009.

Evans, J. S. and Hudak, A. T.: A multiscale curvature algorithm for classifying discrete return LiDAR in forested environments, IEEE Transactions on Geoscience and Remote Sensing, 45, 1029–1038 doi: 10.1109/TGRS.2006.890412, 2007.

Fassnacht, S. R. and Deems, J. S.: Measurement sampling and scaling for deep montane snow depth data, Hydrological Processes, 20, 829–838, 2006.

Filhol, S. and Sturm, M.: The smoothing of landscapes during snowfall with no wind, Journal of Glaciology, 65, 173–187, doi: 10.1017/jog.2018.104, 2019.

Fujihara, Y., Takase, K., Chono, S., Ichion, E., Ogura, A., and Tanaka, K.: Influence of topography and forest characteristics on snow distributions in a forested catchment, Journal of Hydrology, 546, 289–298, 2017.

Geodetics, I.: Geo-iNAV®,Geo-RelNAV®,Geo-PNT®,Geo-Pointer™,Geo-hNAV™,Geo-MMS™ and Geo-RR™ Commercial User Manual (Document 20134 Rev X), Geodetics, Inc., San Diego, CA, USA, 2018.

Geodetics, I.: LiDARTool™ User Manual (Document 20149 Rev I), Geodetics, Inc., San Diego, CA, USA, 2019.

Golding, D. L. and Swanson, R. H.: Snow distribution patterns in clearings and adjacent forest, Water Resour. Res, 22(13), 1931–1940, 1986.

GreenValley-International: LiDAR360 User Guide, GreenValley International, Ltd, Berkeley, CA, USA, 2020.

Grünewald, T., Stötter, J., Pomeroy, J., Dadj , R., Baños, I. M., Marturia, J., Spross, M., Hopkinson, C., Burlando, P., and Lehning, M.: Statistical modelling of the snow depth distribution in open alpine terrain, Hydrology and Earth System Sciences, 17, 3005–3021, doi: 10.5194/hess-17-3005-2013, 2013.

Harder, P., Pomeroy, J., and Helgason, W.: Improving sub-canopy snow depth mapping with unmanned aerial vehicles: Lidar versus structure-from-motion techniques, The Cryosphere, 14, 1919–1935, doi: 10.5194/tc-14-1919-2020, 2020.

Harder, P., Schirmer, M., Pomeroy, J., and Helgason, W.: Accuracy of snow depth estimation in mountain and prairie environments by an unmanned aerial vehicle, The Cryosphere, 10, 2559–2571, 2016.

Harpold, A. A., Guo, Q., Molotch, N., Brooks, P. D., Bales, R., Fernandez-Diaz, J. C., Musselman, K. N., and Swetnam, T. L.: Lidar-derived snowpack data sets from mixed conifer forests across the Western United States, Water Resour. Res, 50, 2749–2755, 2014.

Hedstrom, N. R. and Pomeroy, J. W.: Measurements and modelling of snow interception in the boreal forest, Hydrological Processes, 12, 1611–1625, 1998.

Helfricht, K., Schöber, J., Schneider, K., Sailer, R., and Kuhn, M.: Interannual persistence of the seasonal snow cover in a glacierized catchment, Journal of Glaciology, 60, 889–904, doi: 10.3189/2014JoG13J197, 2014.

Hojatimalekshah, A., Uhlmann, Z., Glenn, N., Hiemstra, C., Tennant, C., Graham, J., Spaete, L., Gelvin, A., Marshall, H., McNamara, J., and Enterkine, J.: Tree canopy and snow depth relationships at fine scales with terrestrial laser scanning, The Cryosphere, 15, 2187–2209, doi: 10.5194/tc-15-2187-2021, 2021.

Hopkinson, C., Sitar, M., Chasmer, L., and Treitz, P.: Mapping snowpack depth beneath forest canopies using airborne lidar, Photogrammetric Engineering & Remote Sensing, 70, 323–330, 2004.

Hopkinson, C., Collins, T., Anderson, A., Pomeroy, J., and Spooner, I.: Spatial snow depth assessment using lidar transect samples and public GIS data layers in the Elbow River watershed, Alberta, Canadian Water Resources Journal, 37, 69–87, 2012a.

Hopkinson, C., Pomeroy, J., Debeer, C., Ellis, C., and Anderson, A.: Relationships between snowpack depth and primary lidar point cloud derivatives in a mountainous environment, Remote Sensing and Hydrology, Jackson Hole, Wyoming, USA, 27–30 September 2010, 2012b.

Jacobs, J. M., Hunsaker, A. G., Sullivan, F. B., Palace, M., Burakowski, E. A., Herrick, C., and Cho, E.: Snow depth mapping with unpiloted aerial system lidar observations: a case study in Durham, New Hampshire, United States, The Cryosphere, 15, 1485–1500, doi: 10.5194/tc-15-1485-2021, 2021.

James, N. A. and Matteson, D. S.: ecp: An R package for nonparametric multiple change point analysis of multivariate data, Journal of Statistical Software, 62, 1–25, doi: 10.18637/jss.v062.i07, 2014.

Jennings, S. B., Brown, N. D., and Sheil, D.: Assessing forest canopies and understorey illumination: canopy closure, canopy cover and other measures, Forestry: An International Journal of Forest Research, 72, 59–74, doi: 10.1093/forestry/72.1.59, 1999.

Jerome, H. F.: Greedy function approximation: A gradient boosting machine, The Annals of Statistics, 29, 1189–1232, doi: 10.1214/aos/1013203451, 2001.

Jost, G., Weiler, M., Gluns, D. R., and Alila, Y.: The influence of forest and topography on snow accumulation and melt at the watershed-scale, Journal of Hydrology, 347, 101–115, 2007.

Kirchner, P. B., Bales, R. C., Molotch, N. P., Flanagan, J., and Guo, Q.: Lidar measurement of seasonal snow accumulation along an elevation gradient in the southern Sierra Nevada, California, Hydrology and Earth System Sciences, 18, 4261–4275, 2014.

Koutantou, K., Mazzotti, G., and Brunner, P.: UAV-based lidar high-resolution snow depth mapping in the swiss alps: Comparing flat and steep forests, Int. Arch. Photogramm. Remote Sens. Spatial Inf. Sci., XLIII-B3-2021, 477–484, doi: 10.5194/isprs-archives-XLIII-B3-2021-477-2021, 2021.

Koutantou, K., Mazzotti, G., Brunner, P., Webster, C., and Jonas, T.: Exploring snow distribution dynamics in steep forested slopes with UAV-borne LiDAR, Cold Regions Science and Technology, 200, 103587, doi: 10.1016/j.coldregions.2022.103587, 2022.

Lehning, M., Grünewald, T., and Schirmer, M.: Mountain snow distribution governed by an altitudinal gradient and terrain roughness, Geophysical Research Letters, 38, L19504, doi: 10.1029/2011GL048927, 2011.

Lendzioch, T., Langhammer, J., and Jenicek, M.: Tracking forest and open area effects on snow accumulation by unmanned aerial vehicle photogrammetry, International Archives of the Photogrammetry, Remote Sensing and Spatial Information Sciences, XLI-B1, 917–923, 2016.

Liaw, A. and Wiener, M.: Classification and Regression by randomForest, R News, 2/3, 18–22, 2002.

Liston, G. E. and Elder, K.: A distributed snow-evolution modeling system (SnowModel), Journal of Hydrometeorology, 7, 1259–1276, 2006.

Liston, G. E. and Sturm, M.: A snow-transport model for complex terrain, Journal of Glaciology, 44(148), 498–516, 1998.

López-Moreno, J. I. and Latron, J.: Spatial heterogeneity in snow water equivalent induced by forest canopy in a mixed beech-fir stand in the Pyrenees, Annals of Glaciology, 49, 83–90, 2008.

Mazzotti, G., Essery, R., Moeser, C. D., and Jonas, T.: Resolving small-scale forest snow patterns using an energy balance snow model with a one-layer canopy, Water Resour. Res, 56, e2019WR026129, doi: 10.1029/2019WR026129, 2020a.

Mazzotti, G., Essery, R., Webster, C., Malle, J., and Jonas, T.: Process-level evaluation of a hyper-resolution forest snow model using distributed multisensor observations, Water Resour. Res, 56, e2020WR027572, doi: 10.1029/2020WR027572, 2020b.

Mazzotti, G., Currier, W., Deems, J. S., Pflug, J. M., Lundquist, J. D., and Jonas, T.: Revisiting snow cover variability and canopy structure within forest stands: Insights from airborne lidar data, Water Resour. Res, 55, 6198–6216, doi: 10.1029/2019WR024898, 2019.

Mendoza, P. A., Musselman, K. N., Revuelto, J., Deems, J. S., López-Moreno, J. I., and McPhee, J.: Interannual and seasonal variability of snow depth scaling behavior in a subalpine catchment, Water Resour. Res, 56, e2020WR027343, doi: 10.1029/2020WR027343, 2020a.

Mendoza, P. A., Shaw, T. E., McPhee, J., Musselman, K. N., Revuelto, J., and MacDonell, S.: Spatial distribution and scaling properties of lidar-derived snow depth in the extratropical Andes, Water Resour. Res, 56, e2020WR028480, doi: 10.1029/2020WR028480, 2020b.

Molotch, N. P., Colee, M. T., Bales, R. C., and Dozier, J.: Estimating the spatial distribution of snow water equivalent in an alpine basin using binary regression tree models: The impact of digital elevation data and independent variable selection, Hydrological Processes, 19, 1459–1479, 2005.

Morsdorf, F., Kötz, B., Meier, E., Itten, K. I., and Allgöwer, B.: Estimation of LAI and fractional cover from small footprint airborne laser scanning data based on gap fraction, Remote Sensing of Environment, 104, 50–61, 2006.

Mott, R., Schirmer, M., and Lehning, M.: Scaling properties of wind and snow depth distribution in an Alpine catchment, Journal of Geophysical Research, 116, D06106, doi: 10.1029/2010JD014886, 2011.

Musselman, K. N., Molotch, N. P., and Brooks, P. D.: Effects of vegetation on snow accumulation and ablation in a mid-latitude sub-alpine forest, Hydrological Processes, 22, 2767–2776, doi: 10.1002/hyp.7050, 2008.

Painter, T., Berisford, D., Boardman, J., Bormann, K. J., Deems, J., Gehrke, F., Hedrick, A., Joyce, M., Laidlaw, R., Marks, D., Mattmann, C., Mcgurk, B., Ramirez, P., Richardson, M., Skiles, S., Seidel, F., and Winstral, A.: The Airborne Snow Observatory: Fusion of scanning lidar, imaging spectrometer, and physically-based modeling for mapping snow water equivalent and snow albedo, Remote Sensing of Environment, 184, 139–152, 2016.

Paquotte, A. and Baraer, M.: Hydrological behavior of an ice-layered snowpack in a non-mountainous environment, Hydrological Processes, 36, e14433, doi: 10.1002/hyp.14433, 2021.

Plattner, C., L. N. , A., B., and Brenning: The spatial variability of snow accumulation on Vernagtferner, Austrian Alps, in Winter 2003/2004, Zeitschrift für Gletscherkunde und Glazialgeologie, 39, 43–57, 2004.

Pomeroy, J. W. and Granger, R. J.: Sustainability of the western Canadian boreal forest under changing hydrological conditions-Snow accumulation and ablation, Sustainability of Water Resources under Increasing Uncertainty (Proceedings of an international Symposium S1), Rabat, Morocco, 23 April–3 May 1997, 237–242, 1997.

Pomeroy, J. W., Parviainen, J., Hedstrom, N., and Gray, D. M.: Coupled modelling of forest snow interception and sublimation, Hydrological Processes, 12, 2317–2337, 1998.

Pomeroy, J. W., Gray, D. M., Brown, T., Hedstrom, N. R., Quinton, W. L., Granger, R. J., and Carey, S. K.: The cold regions hydrological model: a platform for basing process representation and model structure on physical evidence, Hydrological Processes, 21, 2650–2667, doi: 10.1002/hyp.6787, 2007.

Probst, P. and Boulesteix, A.-L.: To tune or not to tune the number of trees in random forest, Journal of Machine Learning Research 18, 6673–6690, 2017.

Revuelto, J., López-Moreno, J., Azorin-Molina, C., and Vicente-Serrano, S. M.: Topographic control of snowpack distribution in a small catchment in the central Spanish Pyrenees: Intra- and inter-annual persistence, The Cryosphere, 8, 1989–2006, doi: 10.5194/tc-8-1989-2014, 2014.

Richardson, J. J., Moskal, L. M., and Kim, S.-H.: Modeling approaches to estimate effective leaf area index from aerial discrete-return lidar, Agricultural and Forest Meteorology, 149, 1152–1160, 2009.

Roth, T. R. and Nolin, A. W.: Forest impacts on snow accumulation and ablation across an elevation gradient in a temperate montane environment, Hydrology and Earth System Sciences, 21, 5427–5442, 2017.

Royer, A., Roy, A., Jutras, S., and Langlois, A.: Review article: Performance assessment of radiation-based field sensors for monitoring the water equivalent of snow cover (SWE), The Cryosphere, 15, 5079–5098, doi: 10.5194/tc-15-5079-2021, 2021.

Safa, H., Krogh, S. A., Greenberg, J., Kostadinov, T. S., and Harpold, A. A.: Unraveling the controls on snow disappearance in montane conifer forests using multi-site lidar, Water Resour. Res, 57, e2020WR027522, doi: 10.1029/2020WR027522, 2021.

Schirmer, M. and Lehning, M.: Persistence in intra-annual snow depth distribution: 2. Fractal analysis of snow depth development, Water Resour. Res, 47, W09517, doi: 10.1029/2010WR009429, 2011.

Sena, N., Chokmani, K., Gloaguen, E., and Bernier, M.: Analyse multi-échelles de la variabilité spatiale de l'équivalent en eau de la neige (EEN) sur le territoire de l'Est du Canada, Hydrological Sciences Journal, 62(3), 359–377, 2017.

SPH-Engineering: UgCS Desktop application version 3.2 (113) User Manual, SPH Engineering, Baložu Pilsēta, Latvia, 2019.

Sun, W., Xu, G., Gong, P., and Liang, S.: Fractal analysis of remotely sensed images: A review of methods and applications, International Journal of Remote Sensing, 27, 4963–4990, doi: 10.1080/01431160600676695, 2006.

Tinkham, W. T., Smith, A. M. S., Marshall, H., Link, T., Falkowski, M., and Winstral, A.: Quantifying spatial distribution of snow depth errors from lidar using random forest, Remote Sensing of Environment, 141, 105–115, doi: 10.1016/j.rse.2013.10.021, 2014.

Trujillo, E., Ramı´rez, J. A., and Elder, K. J.: Topographic, meteorologic, and canopy controls on the scaling characteristics of the spatial distribution of snow depth fields, Water Resour. Res, 43, W07409, 1–17, 2007.

Trujillo, E., Ramírez, J. A., and Elder, K.: Scaling properties and spatial organization of snow depth fields in sub alpine forest and alpine tundra, Hydrological Processes, 23, 1575–1590, doi: 10.1002/hyp.7270, 2009.

Tyralis, H., Papacharalampous, G., and Langousis, A.: A brief review of random forests for water scientists and practitioners and their recent history in water resources, Water, 11, 910, 2019.

Valence, E., Baraer, M., Rosa, E., Barbecot, F., and Monty, C.: Drone-based ground-penetrating radar (GPR) application to snow hydrology, The Cryosphere, 16, 3843–3860, doi: 10.5194/tc-16-3843-2022, 2022.

Varhola, A., Coops, N. C., Weiler, M., and Moore, R. D.: Forest canopy effects on snow accumulation and ablation: An integrative review of empirical results, Journal of Hydrology, 392, 219–233, 2010a.

Varhola, A. s., Coops, N. C., Bater, C. W., Teti, P., Boon, S., and Weiler, M.: The influence of ground- and lidar-derived forest structure metrics on snow accumulation and ablation in disturbed forests, Canadian Journal of Forest Research, 40, 812–821, 2010b.

Veatch, W., Brooks, P. D., Gustafson, J. R., and Molotch, N. P.: Quantifying the effects of forest canopy cover on net snow accumulation at a continental, mid-latitude site, Ecohydrology, 2, 115–128, 2009.

Webster, R. and Oliver, M.: Geostatistics for environmental scientists, second edition, in, Chichester, England: John Wiley & Sons Ltd., doi: 10.1002/9780470517277.ch1, 2007.

Wilcoxon, F.: Individual comparisons by ranking methods, Biometrics, 1(6), 80–83, 1945.

Winkler, R. D., Spittlehouse, D. L., and Golding, D. L.: Measured differences in snow accumulation and melt among clearcut, juvenile, and mature forests in southern British Columbia, Hydrological Processes, 19, 51–62, 2005.

Winstral, A. and Marks, D.: Simulating wind fields and snow redistribution using terrain based parameters to model snow accumulation and melt over a semi arid mountain catchment, Hydrological Processes, 16, 3585–3603, doi: 10.1002/hyp.1238, 2002.

Winstral, A., Elder, K., and Davis, R. E.: Spatial snow modeling of wind-redistributed snow using terrain-based parameters, Journal of Hydrometeorology, 3, 524–538, doi: 10.1175/1525-7541(2002)003<0524:Ssmowr>2.0.Co;2, 2002.

Woods, S. W., Ahl, R., Sappington, J., and McCaughey, W.: Snow accumulation in thinned lodgepole pine stands, Montana, USA, Forest Ecology and Management, 235, 202–211, 2006.

Yang, J., Jiang, L., Luojus, K., Pan, J., Lemmetyinen, J., Takala, M., and Wu, S.: Snow depth estimation and historical data reconstruction over China based on a random forest machine learning approach, The Cryosphere, 14, 1763–1778, doi: 10.5194/tc-14-1763-2020, 2020.

Zhang, X., Gao, R., Sun, Q., and Cheng, J.: An automated rectification method for unmanned aerial vehicle LiDAR point cloud data based on laser intensity, Remote Sensing, 11, 811, doi: 10.3390/rs11070811, 2019.

Zheng, Z., Kirchner, P. B., and Bales, R. C.: Topographic and vegetation effects on snow accumulation in the southern Sierra Nevada: A statistical summary from lidar data, The Cryosphere, 10, 257–269, 2016.

Zheng, Z., Ma, Q., Qian, K., and Bales, R. C.: Canopy effects on snow accumulation: observations from lidar, canonical-view photos, and continuous ground measurements from sensor networks, Remote Sensing, 10, 1769, doi: 10.3390/rs10111769, 2018.

Zheng, Z., Ma, Q., Jin, S., Su, Y., Guo, Q., and Bales, R. C.: Canopy and terrain interactions affecting snowpack spatial patterns in the Sierra Nevada of California, Water Resour. Res, 55, 8721–8739, doi: 10.1029/2018wr023758, 2019.

CHAPTER III

A NEW INTERPOLATION METHOD TO RESOLVE UNDER-SAMPLING BENEATH THE CANOPY IN CONIFEROUS ENVIRONMENTS BY UAV-LIDAR

Vasana Dharmadasa [1,2,3], Christophe Kinnard [1,2,3] and Michel Baraër [4]

[1] Department of Environmental Sciences, University of Québec at Trois-Rivières,
Trois-Rivieres, QC G8Z 4M3, Canada

[2] Center for Northern Studies (CEN), Quebec City, QC GV1 0A6, Canada

[3] Research Centre for Watershed-Aquatic Ecosystem Interactions (RIVE), University of Québec at Trois-Rivières, Trois-Rivieres, QC G8Z 4M3, Canada

[4] Department of Construction Engineering, École de Technologie Supérieure,
Montreal, QC H3C 1K3, Canada

Corresponding author: vasana.sandamali.dharmadasa@uqtr.ca

This article is in review for the journal of *Cold Regions Science and Technology*.

Abstract

Obtaining accurate snow depth estimates under dense canopies using airborne lidar (light detection and ranging) techniques is challenging due to the under-sampling of ground and snow surfaces. Existing interpolation techniques do not adequately address this problem and they often result in an overestimation of under-canopy snow depths. To address this issue, we introduce and evaluate a new interpolation method that incorporates intra-canopy snow depth variability to provide more accurate estimations at unsampled locations. Four interpolation methods were tested, considering systematic trends (landscape trend, canopy vs. gap trend, and intra-canopy trend) along with spatial interpolation of the residuals. Our results show that spatial interpolation methods without consideration of trends are sufficient to capture and reconstruct the small-scale variability of snow depths below a point separation distance of 1 m, (i.e., ground surface point density > 1 pt m^{-2}). However, beyond a point separation distance of 2.5–3 m (point density < 0.33–0.40 pt m^{-2}), spatial interpolation based on proximity alone becomes unreliable because point separation becomes larger than the snow depth spatial correlation scale. Within these limiting distances, the method that incorporates trends along with spatial interpolation techniques can resolve the small-scale variability and thereby reduce the likely overestimation of snow depths under the canopy.

Key words: UAV-lidar; under-sampling; interpolation; systematic trends

3.1 Introduction

Airborne (both piloted and unpiloted) lidar (light detection and ranging) scanning has been increasingly used in recent years to monitor snowpacks in forested environments due to its strong penetration ability through the forest canopy to detect underlying snow cover and ground (Hopkinson et al., 2004; Morsdorf et al., 2006; Hopkinson et al., 2012b; Deems et al., 2013; Harpold et al., 2014; Zheng et al., 2016; Currier and Lundquist, 2018; Zheng et al., 2018; Mazzotti et al., 2019; Harder et al., 2020; Jacobs et al., 2021; Dharmadasa et al., 2022; Koutantou et al., 2022; Dharmadasa et al., 2023). In forested environments, ground returns point density depends on forest cover type, understory vegetation, laser spot size, laser pulse rate, and the scan angle of the laser sensor (Deems et al., 2013). As such, dense canopies, especially snow-laden conifer canopies, pose challenges for under-canopy snow depth detection by reflecting and attenuating larger amounts of lidar pulses and thereby preventing laser shots from reaching the ground/snow surface (Varhola et al., 2010; Hopkinson et al., 2012b; Harpold et al., 2014; Tinkham et al., 2014; Broxton et al., 2015; Zheng et al., 2016; Mazzotti et al., 2019; Zheng et al., 2019; Jacobs et al., 2021; Koutantou et al., 2022; Dharmadasa et al., 2023). Consequently, this under-sampling of snow under canopies introduces errors upon averaging or interpolating snow depth points to a different resolution (Tinkham et al., 2014; Zheng et al., 2016). Since forest openings (gaps) generally accumulate more snow than under canopies and have higher lidar point densities (Hopkinson et al., 2012a; Broxton et al., 2015; Revuelto et al., 2015; Hojatimalekshah et al., 2021), aggregating or interpolating point snow depths can results in an overestimation bias in the resulting averaged snow depth map (Tinkham et al., 2014; Zheng et al., 2016). For example, in a dense mixed-conifer forest in the southern Sierra Nevada, Zheng et al. (2016) found that 28 % of the area had no lidar returns, which resulted in at least a 10 cm overestimation error in average snow depth for the whole area when using snow depths in the open area as estimates of under-canopy snow depths. In addition, along with the influence of coniferous tree canopy interception, sublimation, longwave emittance, and unloading of snow from the canopy lead to relatively lower snow depths closer to the tree trunk and a gradual increase in snow depth up to a distance coinciding with the canopy crown (Pomeroy and Dion, 1996; Musselman et al., 2008; Revuelto et al., 2015; Zheng et al., 2019), resulting in significant, but somewhat predictable, intra-canopy variability of snow depths in coniferous forests. Existing interpolation techniques such as inverse distance weighting (Burrough, 1986; Guo et al., 2010; Michele et al., 2016), geostatistical methods (Isaaks and Srivastava, 1989; Guo et al., 2010; Mazzotti et al., 2019; Koutantou et al., 2022), regression and tree-based methods (Winstral et al., 2002; Jost et al., 2007; López-Moreno et al., 2010; Lehning et al., 2011; Revuelto et al., 2014; Zheng et al., 2018), or a combination of these methods (Erxleben et al., 2002) do not fully address the aforementioned caveats. Koutantou et al. (2022) emphasized the need for a more sophisticated gap-filling algorithm to avoid likely overestimation of under-sampled under-canopy snow depths. In this study, we address and explore the problem of biased snow depth distributions due to under-canopy under-sampling in coniferous environments, and introduce and evaluate a new interpolation method that incorporates the intra-canopy snow depth variability and thus providing more accurate estimations at unsampled locations. This method seeks to decompose and model the overall lidar snow depth variability into systematic components (landscape trend, preferential accumulation in gaps, intra-canopy variability) and remaining stochastic variability, for an optimal interpolation of lidar snow depths in coniferous forests and more accurate landscape-wide snow depth distribution estimates. To determine the optimal method, four methods were assessed, which combined the systematic trends and spatial interpolation of residuals.

3.2 Study Area

The study site, Forêt Montmorency (hereafter Montmorency) is a dense boreal forest with a mean canopy density of 60–80 %, located north on the Canadian Shield (47.3 °N, 71.1 °W) in southern Québec, eastern Canada (Figure 3.1). Dominant tree species of the site are balsam fir (*Abies balsamea*), black spruce (*Picea mariana*), and white spruce (*Picea glauca*). One of the characteristics of the area is forest gaps associated with clear-cutting and regeneration practices (Québec Ministry of Forests, Wildlife, and Parks (MFFP)). Lidar data acquisition of the site was conducted in summer 2019 for the snow-off surface (13 June 2019) and winter for the snow-on surface (29 March 2019) with a GeoMMS system mounted onto a DJI M600 Pro UAV platform. A 100 x 100 m representative area (Figure 3.1) from the broader survey conducted in Montmorency by Dharmadasa et al. (2022) was used in this study. More details on data acquisition and equipment specifications are described in Dharmadasa et al. (2022). As observed in the field campaign, the sparse mixed forest area in Figure 3.1 is mostly composed of forest gaps.

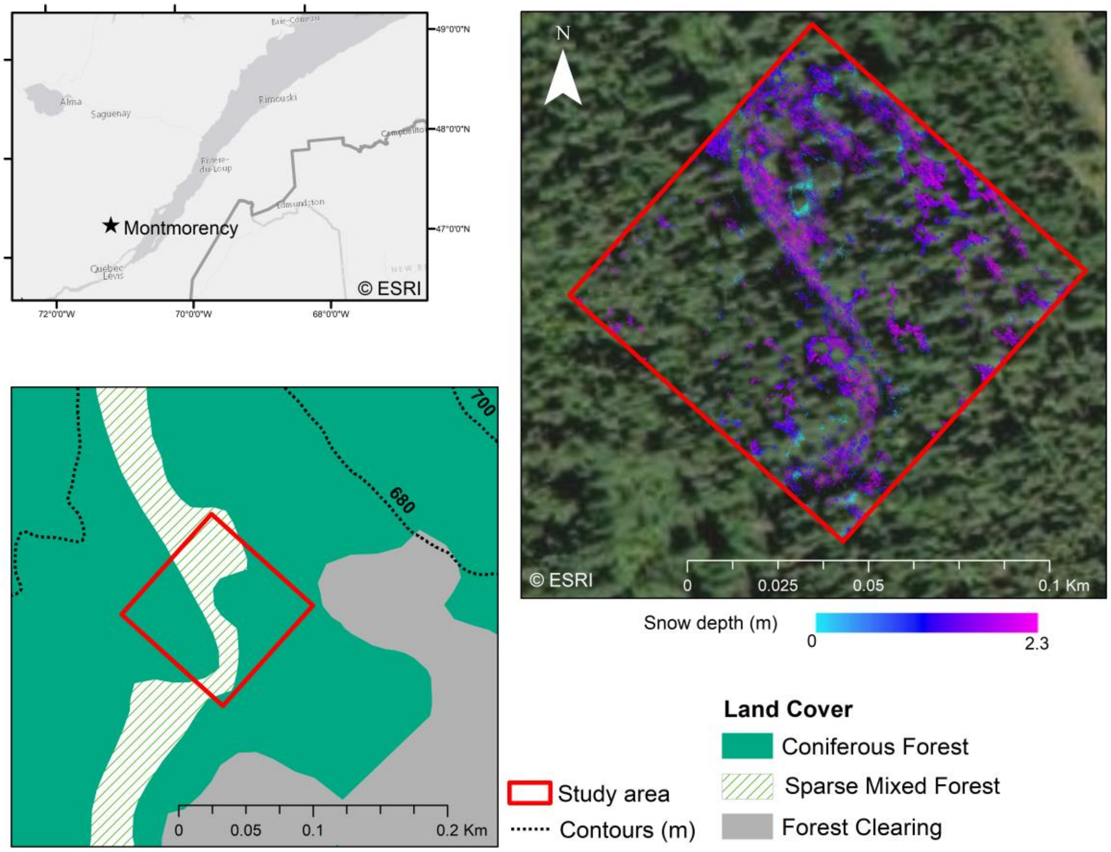

Figure 3.1. Montmorency site showing the 100x100 study area (demarcated in red) and lidar snow depth of the study area at 0.1 m resolution (see Methods).

3.3 Methods

The post-processed and classified lidar point clouds obtained from Dharmadasa et al. (2022) were used to produce a digital elevation model (DEM) of snow depths and for further analyses in this study. A detailed presentation of lidar point cloud processing is given by Dharmadasa et al. (2022). The workflow presented in Figure 3.2 depicts the sequence of steps utilized in this study, incorporating both the methods developed specifically for this study and those adapted from Dharmadasa et al. (2022).

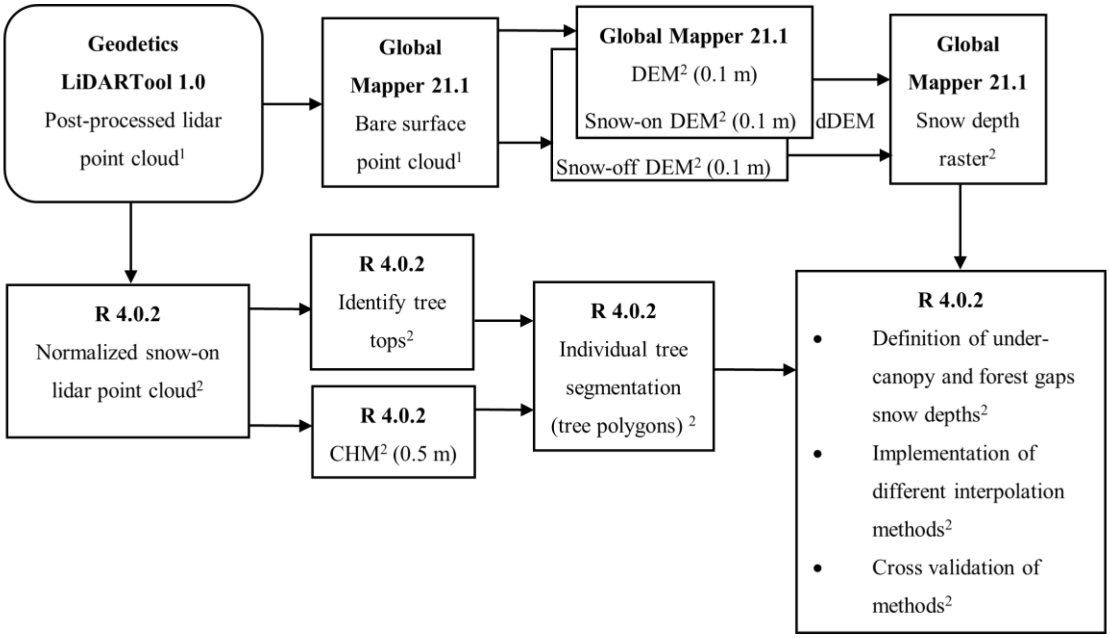

Figure 3.2. Workflow adopted for the study. Each box shows the software used (bold) with the corresponding end product. [1] adapted from Dharmadasa et al. (2022). [2] developed for this study.

3.3.1 Producing Snow Depth Map

Snow depth maps were produced at 0.1 m grid resolution (Figure 3.1), following the same procedure described in Dharmadasa et al. (2022) and Dharmadasa et al. (2023), to account for the variability of snow depth within the canopy. i.e., bare surface points were aggregated to a grid resolution of 0.1 m using the binning method in Global Mapper (Blue Marble Geographics, 2020). Rather than interpolating, this method uses the average of the bare surface points within a grid cell, hence preserving the observation gaps in the data.

3.3.2 Segmenting Individual Trees

We developed a canopy height model (CHM) at 0.5 m resolution and identified the tree tops in the winter point cloud normalized by bare surface point elevations in the R package lidR (Roussel et al., 2020; Roussel et al., 2022). A local maximum was detected to identify tree tops using flexible window sizes ranging from 3–5 m. We used the region-growing algorithm developed by Dalponte and Coomes (2016) for tree segmentation on our data. Figure 3.3 shows the tree tops and tree polygons (canopy crowns) identified by the tree segmentation algorithm. Note that, at times, for a cluster of trees with interlocking crowns, only a single tree top was identified. This is still acceptable for the purpose of our study, as confirmed during the field works, these clusters of trees act as a single unit when accumulating snow underneath the canopy. Zheng et al. (2018) also found that the canopy surrounding within a few meters of a tree have a stronger effect on the snow accumulation on the ground when the trees are clustered together versus a single tree. After the segmentation of individual trees, all snow depth points within the tree polygons were defined as “under-canopy”, whereas the snow depth points outside the tree polygons were defined as “forest gaps”. A similar approach for tree segmentation was previously used by Hojatimalekshah et al. (2021) on terrestrial laser scanning data collected across Grand Mesa, Colorado, USA.

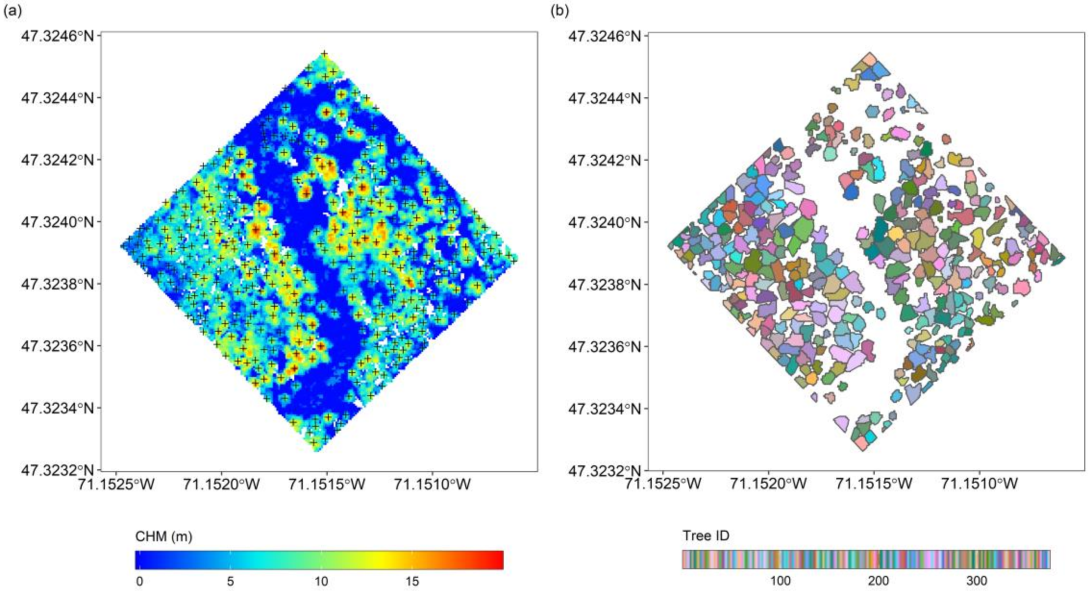

Figure 3.3. Results of tree segmentation. (a) tree tops plotted as crosses (+) over the canopy height model (CHM); (b) tree polygons identified for each tree top

3.3.3 Snow Depth Interpolation Methods

We implemented four different interpolation methods on snow depth points. The methods differed in which of the systematic trends (landscape trend, canopy vs. gap trend, and intra-canopy trend) were considered, or not, during the interpolation process. Method 1 only considered the landscape trend of the snow depths; method 2 considered the landscape trend and the canopy vs. gap trend; Method 3 considered the landscape trend and the intra-canopy trend in snow depths; finally, method 4 considered all systematic trends (landscape trend, canopy vs. gap trend and intra-canopy trend). For each method, the systematic trends were modelled and removed, and the residuals were spatially interpolated using either local-inverse distance weighting (IDW) or the geostatistical ordinary kriging (OK) method. With IDW, the weight of each point is inversely proportional to the distance between the samples (Burrough, 1986). With OK, a semi-variogram that summarizes the spatial structure of the snow depth points is used to calculate the weighting factor that corresponds to each point to estimate snow depth at unsampled locations (Isaaks and Srivastava, 1989). Both methods were tested separately for the interpolation of residuals. In addition, spatial interpolation of raw snow depths using OK and IDW approaches was used as a benchmark to show the effect of including systematic trends. All analyses were done in R 4.0.2. Figure 3.4 summaries the methods interrelations.

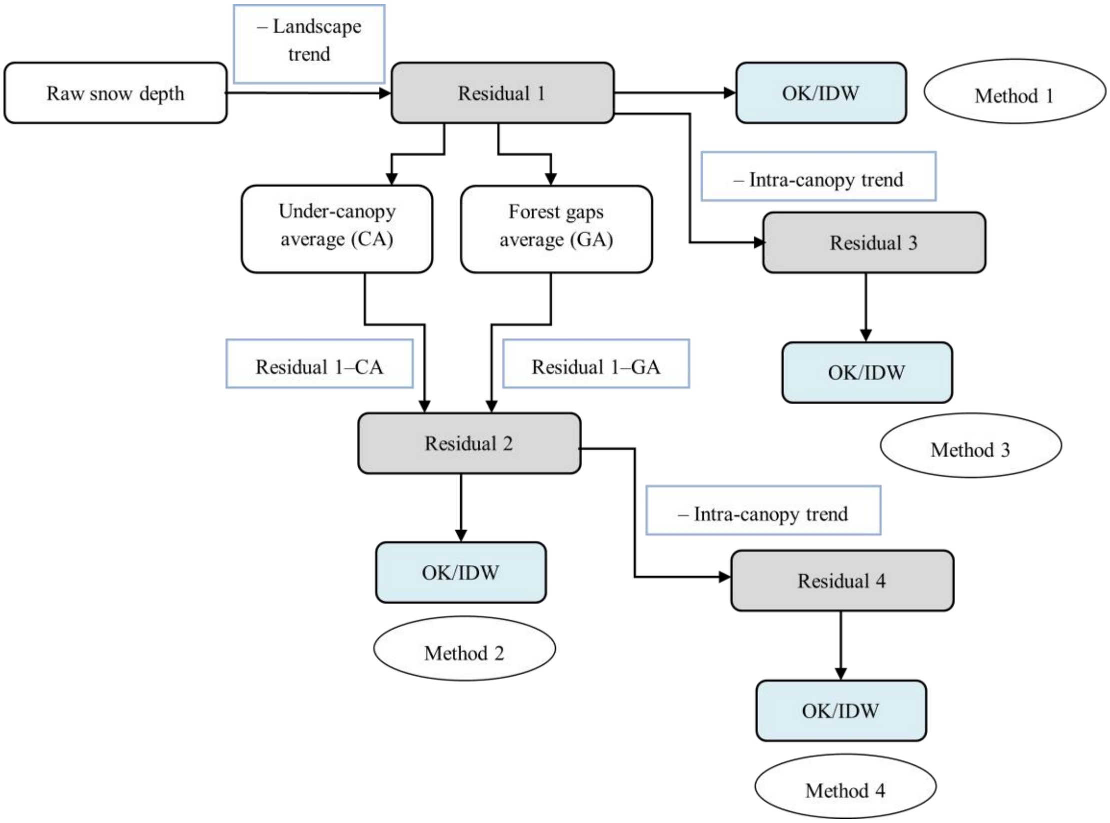

Figure 3.4. Schematic illustration of the interpolation methods.

3.3.3.1 Method 1

In method 1, we first removed the landscape trend in snow depth points by fitting a second-order polynomial trend surface using the spatial package in R (Venables and Ripley, 2002). Then, the snow depth residuals (raw snow depth – landscape trend: 'residual 1' on Figure 3.4) were spatially interpolated using OK and IDW. The landscape trend is then added back to the interpolated residuals to obtain the estimated snow depths in unsampled areas.

3.3.3.2 Method 2

In method 2, the detrended snow depth data from method 1 (residual 1) was used to calculate the canopy vs. gap trend. For this, the average snow depth under-canopy and within forest gaps were calculated and subtracted from residual 1, yielding the 2nd-level residuals ('residual 2' in Figure 3.4). This operation thus removes the potentially systematic positive bias in gaps relative to canopies. Then, the 2nd-level residuals were spatially interpolated with OK and IDW. The landscape trend and the canopy vs. gap trends are then added back to the interpolated residuals to obtain the estimated snow depths in unsampled areas.

3.3.3.3 Method 3

In method 3, the detrended snow depth data from method 1 (residual 1) was used to determine the intra-canopy snow depth patterns. A number of studies reported increasing snow depths with increased distance from tree stems toward the tree canopy (Musselman et al., 2008; Revuelto et al., 2015; Zheng et al., 2019). As such, the correlation between snow depth under the canopy and the scaled distance from the tree stem was investigated. For each snow depth point located within a canopy, the distance from the tree stem location (as identified by tree tops) to the snow depth point was calculated and then scaled by the total distance from the tree stem to the tree canopy edge. A scaled distance was used to account for the different tree canopy sizes. Then, a second-order polynomial function was fitted to snow depth residual 1 and corresponding scaled distances (Figure 3.5) to estimate the intra-canopy trend. Since the point density tended to increase from the tree stem towards the canopy edges, the polynomial model was weighed according to point density over the scaled distance. The point density was estimated with a gaussian kernel window with a 0.1 scaled distance bandwidth (standard deviation = 0.1). An interaction term with tree height was included, to account for the different intra-canopy trends with tree sizes (Figure 3.5). The fitted polynomial function showed an adjusted R^2 of 0.70. Finally, the intra-canopy trend was removed from residual 1, and the residuals from the intra-canopy trend ('residual 3' in Figure 3.4) were spatially interpolated using OK and IDW (Figure 3.4).

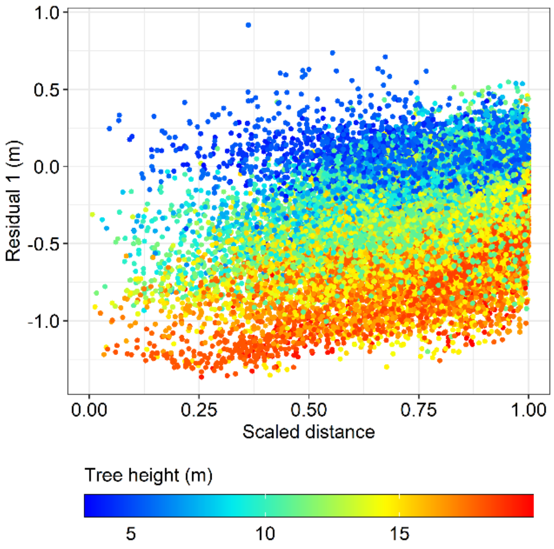

Figure 3.5. Variation of snow depth residual 1 with scaled distance. Points are colored by the tree height.

3.3.3.4 Method 4

Method 4 removed both the landscape trend and the canopy vs. gap trend (yielding the 2nd order residuals in Figure 3.4). The polynomial model described in method 3 was then fitted on the 2nd order residuals to obtain the intra-canopy trend (Figure 3.4). The fitted polynomial function showed an adjusted R^2 of 0.7. Subtracting the intra-canopy trend from residual 2 yielded the 4th-level residuals ('residual 4' in Figure 3.4), which were then spatially interpolated using OK and IDW.

3.3.4 Cross-validation of the Interpolation Methods

Cross-validation was used to estimate the prediction performance of the respective interpolation methods. One-hundred random snow depth points were used as test points. To investigate the effect of the distance between the sampled and unsampled points on the prediction (i.e., the effect of the local point density on the quality of the interpolation), all the surrounding training (sampled) points within a distance D to each of the test (unsampled) points were removed from the training set, and then the snow depth at the test points was estimated from the remaining training points (Figure 3.6). D was varied from 0 to 5 m, with a 0.5 interval. The whole procedure was repeated 20 times to reduce the sampling uncertainty. The root mean squared error (RMSE), bias, and correlation coefficient were used as validation statistics and reported as a function of the mean distance between the unsampled (test) points and the three closest training points. The validation statistics for the four interpolation methods described above and the same methods without imposing spatial interpolation (i.e., only estimating snow depths with trends) were compared with the benchmark method (spatial interpolation of raw snow depths using OK and IDW approaches) to investigate the effect of incorporating trends in snow depth estimates.

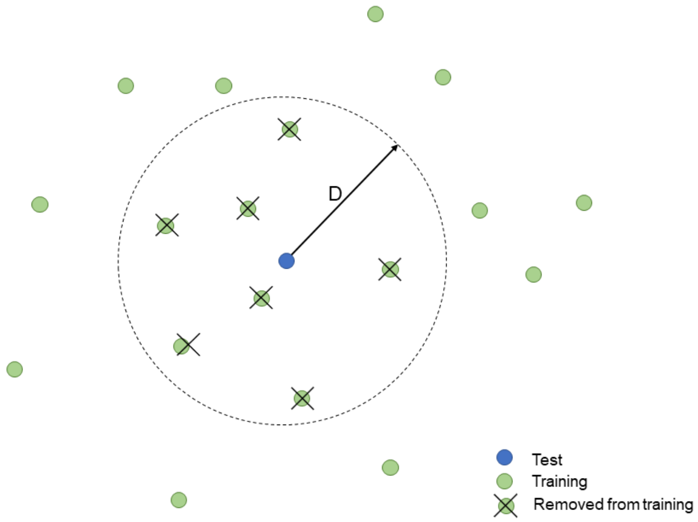

Figure 3.6. Illustration of the cross validation scheme. Selected test points (blue) are chosen randomly and training points within a separation distance (D) are eliminated to investigate the impact of lidar sampling density on the interpolation performance.

3.4 Results and Discussion

3.4.1 Interpolated Snow Depth Maps

Figure 3.7 shows the interpolated snow depth obtained by the different methods. Snow depth maps derived from the OK (top row) method show negligible to no visible difference to the corresponding IDW (mid row) snow depth estimates. Snow depth patterns obtained by the four interpolated methods are overall similar, but fine scale differences are apparent (Figure 3.7a–d and e–h). For instance, the area west of the large gap is covered by a dense canopy (Figure 3.3) and consequently shows more observation gaps due to few lidar returns in this area (Figure 3.1). The snow depths interpolated by method 1 in this area display smoothed spatial variability, notably between under-canopy and forest gaps (Figure 3.7a, e). Consideration of the measured canopy vs. gap snow depth trend in method 2 shows some disruptions in the previously smoothed snow depth variability in this area, i.e., snow depth differences under-canopy and forest gaps (Figure 3.7b, f). Compared to methods 1 and 2, the consideration of intra-canopy snow depth trend in methods 3 and 4 shows clear differences in snow depths under-canopy and forest gaps and variability of snow depth under the canopy (Figure 3.7c, d, g, h). Methods 3 and 4 do not exhibit any visual difference between snow depth maps, implying that it is rather the intra-canopy trend that causes differential snow depths between under-canopy and forest gaps.

Snow depth differences between methods illustrate the relative effect of the different interpolation methods (Figure 3.7 -bottom row). Since both OK and IDW yielded similar snow depth maps, differences are only shown using OK approach. Negligible differences in snow depths between method 1 and the benchmark method (Figure 3.7i) indicate that the landscape trend is not pronounced in the data. Large snow depth differences between methods 2 and 1 (Figure 3.7j) show the substantial impact of including canopy vs. gap snow depth trend. Figure 3.7k shows comparatively large differences in snow depths between methods 3 and 1 and adding the intra-canopy trend on residual 1 tends to smooth the sharper gap vs canopy pattern introduced by method 2. It further suggests that method 1 overestimates snow depths at some locations (negative values in Figure 3.7k) and underestimates (positive values in Figure 3.7k) at others compared to method 3. Similar patterns are observed in Figure 3.7l, which shows the effect of adding the intra-canopy trend on residual 2. Snow depth patterns within the canopy are also visible in both figures (Figure 3.7k, l).

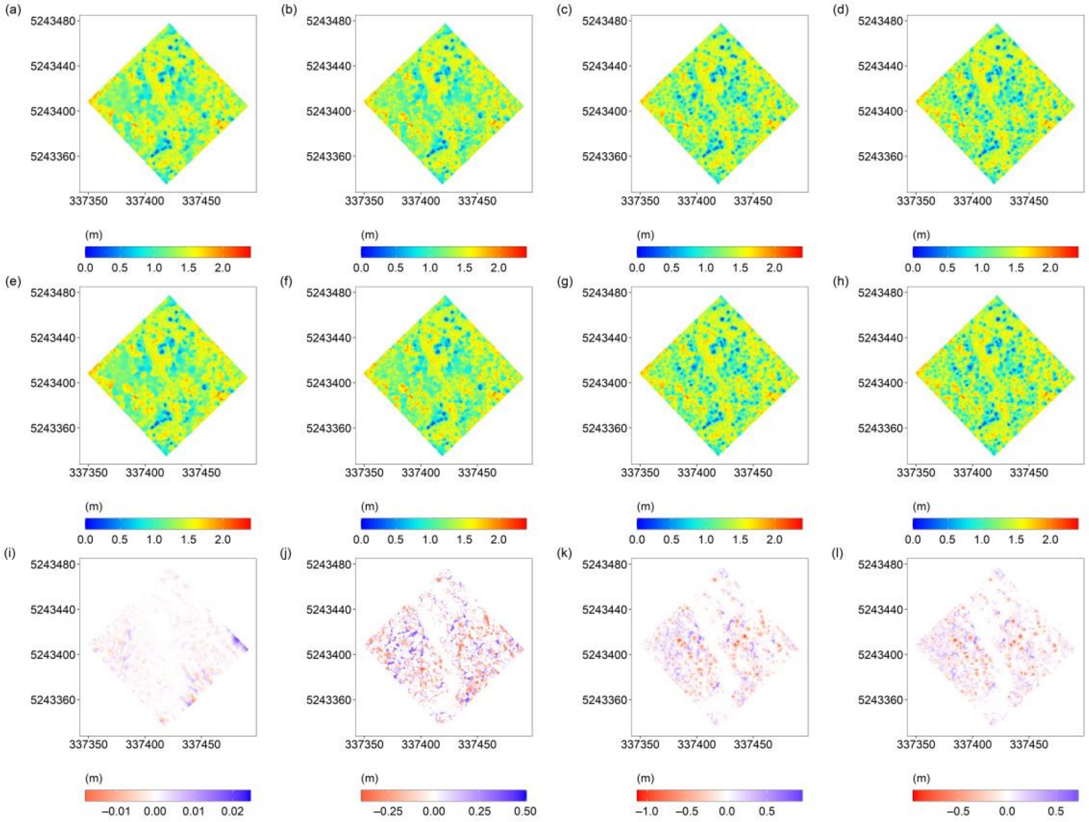

Figure 3.7. Interpolated snow depth products (a) method 1 with OK, (b) method 2 with OK, (c) method 3 with OK, (d) method 4 with OK, (e) method 1 with IDW, (f) method 2 with IDW, (g) method 3 with IDW, (h) method 4 with IDW, (i) method 1 with OK – benchmark, (j) method 2 with OK – method 1 with OK, (k) method 3 with OK – method 1 with OK, and (l) method 4 with OK – method 2 with OK

The different interpolation methods resulted in different snow depth distributions over the study area (Figure 3.8). Only the results from OK are shown in Figure 3.8 as both OK and IDW approaches produced similar snow depths. Density distributions for the IDW are included in Supplement Figure S3.1.

The higher snow depth observed in forest gaps compared to under-canopy in Figure 3.8 corroborates results found in previous studies (Musselman et al., 2008; Revuelto et al., 2015; Uhlmann et al., 2018; Mazzotti et al., 2019). This difference becomes more evident once the snow depths are interpolated, as the snow depth distributions below the canopy become more skewed towards smaller values. The snow depth distribution using the raw (not interpolated) data appears to be biased by the higher snow depths in forest gaps. This is not surprising due to the over-sampling and under-sampling of snow depths in forest gaps and under-canopy, respectively (see snow depth map in Figure 3.1). All the interpolated methods implemented here seem to rectify this issue. Moreover, the similar distributions of snow depths in forest gaps obtained by all the interpolation methods indicate that these have the least effect in the forest gaps, where the point density is highest, than in the forest. In canopies, benchmark (spatial interpolation of raw snow depths using OK), methods 1 and 2 show noisier and tighter (less variable) distributions, whereas methods 3 and 4 show similar, smoother, and wider (more variable) distributions. These results show that estimating area-wide snow depth distributions and their summary statistics from sparse lidar snow depths in forested areas entails a significant error and interpolation is necessary to eliminate the bias due to canopy under-sampling.

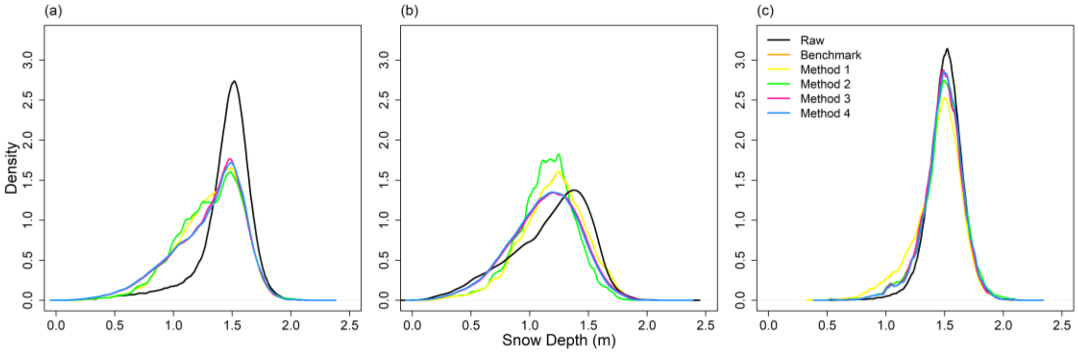

Figure 3.8. Probability density distributions of snow depths interpolated by OK for (a) full domain, (b) under-canopy, and (c) forest gaps. The density distributions were computed using a gaussian kernel with a standard deviation of 0.01. The Raw distributions correspond to snow depths not interpolated.

3.4.2 Cross-validation

Of all the methods with spatial interpolation (trends + spatial interpolation of residuals; column one in Figure 3.9), method 1 shows the lowest interpolation performance with higher RMSE, bias, and lower correlation coefficient. Moreover, method 1 exhibits negligible differences with the benchmark method in which spatial interpolation techniques were directly applied to the raw data (black vs pink graphs in Figure 3.9a, c, e). This suggests an absence of pronounced landscape trend in the study area; hence, removing or not the trend does not have a substantial effect on interpolation. However, in larger areas and/or with more pronounced elevation ranges where orographic and lapse rate gradients start to impact snow accumulation, the landscape trend would be expected to be important and would need to be considered. Among the four methods, method 4 shows the highest performance with lower RMSE, bias, and higher correlation coefficient. Methods 3 and 2 scored second and third in terms of RMSE and correlation coefficient, though showing similar biases (Figure 3.9c). The OK and IDW spatial interpolation techniques generally yield similar accuracies in snow depth estimates among all methods. All methods show degrading accuracies with increasing distance between unsampled and sampled snow depth points.

Column two in Figure 3.9 shows the prediction error when using only the systematic trends, without spatial interpolation of residuals, and allows seeing the effect of incorporating trends within the interpolation methods. Similar to the methods with spatial interpolation (Figure 3.9, column one), methods 1 and 4 show the lowest and highest performances respectively, while methods 3 and 2 show intermediate performances. However, the noticeable bias reported in method 3 (which ignores the canopy vs. gap trend) in Figure 3.9d indicates that consideration of average under-canopy and forest gap snow depth difference might be more important when spatial interpolation is not used. In general, column two shows that incorporating trends within the interpolation methods slows the degradation of the prediction accuracy with increasing distance between unsampled and sampled points.

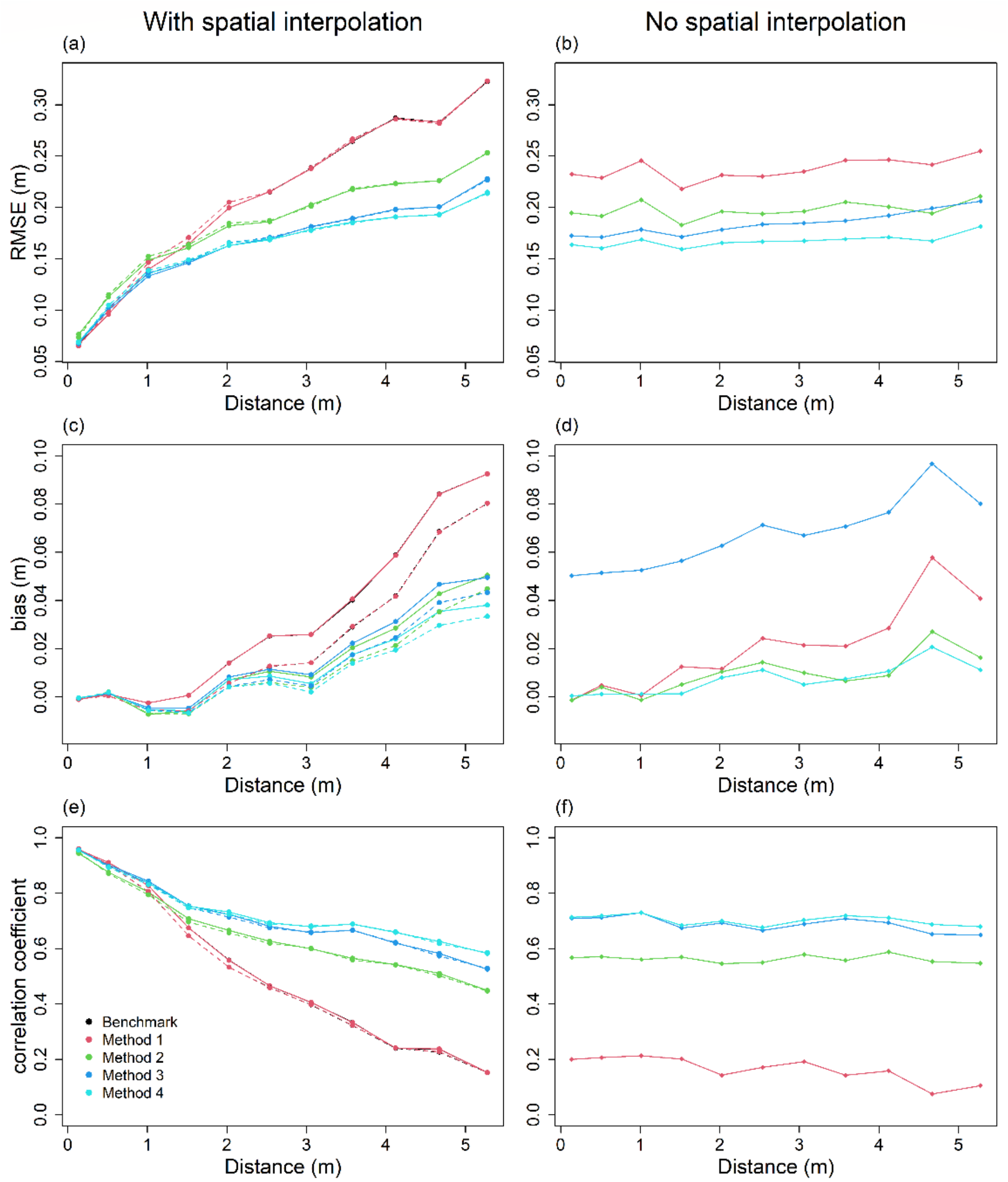

Figure 3.9. Error statistics with the distance between unsampled and sampled points (a, b) RMSE (c, d) bias, and (e, f) correlation coefficient. Panels in the first column show the effect with spatial interpolation and the second column is without spatial interpolation, i.e., only considering trends. In the first column, methods with OK are shown as solid lines whereas methods with IDW are represented by stippled lines. Benchmark indicates spatial interpolation of raw snow depths with OK and IDW.

Figure 3.9 also provides an indication of two limiting distances within which these interpolation methods can be used. As observed from the first column, up to ~1 m of distance all methods show similar and comparatively better performances compared to when the inter-point separation distances increase by > 1m. This suggests that when the distance between unsampled and sampled points is < 1 m, (i.e., ground surface point density is > 1 pt m^{-2}) spatial interpolation techniques like OK and IDW have sufficient information to resolve and reconstruct small-scale snow depth patterns. This is in agreement with the threshold ground surface point density found by Guo et al. (2010) and Zheng et al. (2019) for airborne lidar surveys in order to generate high-accuracy DEMs and to capture the tree well snow surfaces. Similar to Guo et al. (2010), we found an RMSE of less than 0.15 m for interpolated snow depths when ground surface point density is larger than 1 pt m^{-2}. However, Zheng et al. (2019) emphasized that the effect of point density is more significant in densely forested areas like Montmorency than in more sparsely forested areas, as with moderate forest density, the under-sampling under the canopy and over-sampling in forest gaps can offset the overestimation and underestimation of snow depths. Above 1 m, the performance of the different methods is no longer similar and starts degrading at a slower rate than that below 1 m. Column one shows that past 1 m, incorporating trends slows the degradation of accuracies with increasing inter-point distances, and canopy vs. gap and intra-canopy trends (method 2, 3, and 4) significantly improve the interpolation performances compared to benchmark. This highlights the necessity of modeling trends past this distance. This also suggests that these trends are not well sampled past a separation distance of 1 m and hence not adequately represented by OK/IDW approaches.

A comparison of the two columns in Figure 3.9 suggests another limiting distance at ~2.5–3 m. After this distance, the interpolation of trend residuals with OK/IDW (Figure 3.9 a, c, e) degrades the performance compared to using the trends alone for prediction (Figure 3.9 b, d, f). This is particularly evident in the RMSE and correlation coefficient plots. This suggests that when the distance between sampled and unsampled points is larger than 2.5–3 m (point density of 0.33–0.40 pts m^{-2}), the points are too separated to inform each other, i.e., to provide meaningful interpolation. The resulting interpolated snow depth fields thus sustain high uncertainties. As such, when the ground surface point density is lower, the modelled systematic trends (landscape, canopy vs. gap, and intra-canopy) would provide more accurate gap-filled snow depth maps than using spatial interpolation methods. This limiting distance of 2.5–3 m is in the same order of magnitude as the maximum canopy radii (7 m) found in Montmorency, and half of the scale break distance (4.5 m in bare earth topography+trees and 6.5 m in snow depth) found for Montmorency by Dharmadasa et al. (2023). Therefore, when the distance between sampled and unsampled points is larger than this threshold, we risk interpolating data points with no spatial correlation (i.e., points within and outside the canopy), hence degrading the accuracy of gap-filling. Especially beneath the canopy, intra-canopy trends help preserving the variability of snow depths when ground point density is lower.

3.5 Conclusions

Given the typical under-sampling of lidar ground surface points under the canopy, our results suggest that the spatial interpolation method that incorporates systematic trends in snow accumulation at the landscape, canopy vs. gaps, and intra-canopy scales yield significant improvements for gap-filling when the distance between sampled and unsampled lidar snow depth points is larger than 1 m (ground point density of < 1 pt m^{-2}). Beyond a point separation distance of 2.5–3 m (point density < 0.33–0.40 pt m^{-2}), the point separation becomes larger than the snow depth spatial correlation scale, and spatial interpolation based on proximity alone becomes useless. Below a separation distance of 1 m, (i.e., ground surface point density > 1 pt m^{-2}), spatial interpolation methods without consideration of trends are sufficient to capture and reconstruct the small-scale variability of snow depths. This suggests that consideration of the trends only becomes useful for areas with a ground surface point density of < 1 pt m^{-2}. Within these limiting distances, consideration of trends along with spatial interpolation techniques can resolve the small-scale variability and thereby reduce the likely overestimation of snow depths under the canopy. In this context, within the prescribed range, method 4 yields the best performance followed by methods 3, 2, and 1, respectively.

The proposed interpolation method in this study can be easily applied to any area subjected to fine-tuning of window size for tree top identification. However, it is worth noting that running the R script (Supplement) on a standard computer can be somewhat computationally intensive. For instance, on a Core i7 computer equipped with 32 Gb RAM and a 3.2 GHz processor, the R script (Supplement) took approximately 1.5 hr to execute (excluding the cross-validation part) for a 100x100 m area. In contrast, on a Core i7 computer with 64 Gb RAM and a 3.6 GHz processor, the same took 0.7 hr to complete. Therefore, we expect that the computational demand of the method will be lower when implemented on a high-performance computing system.

Supporting Information

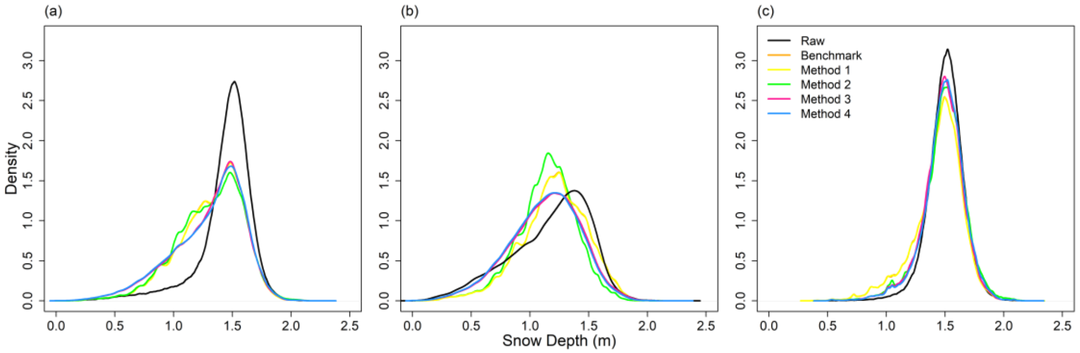

Figure S3.1. Kernel density estimates of snow depths by IDW in (a) full domain, (b) under-canopy, and (c) forest gaps

Code

```
start_time <- Sys.time()
library(raster)
library(sf)
library(lidR)
library(spatial)
library(proj4)
library(sp)
library(foreach)
library(doParallel)
library(proxy)
library(units)
library(gstat)
library(ggplot2)
library(Metrics)
library(beepr)
library(pracma)

#--------------------------------------input---------------------------------------------------
setwd() # set directory
SD=raster("/SD.tif") # snow depth raster
Las = readLAS("/Las.las") # las file
Area= shapefile("/Area.shp") # shape file of area of interest
#-------------------------------------------------------------------------------------------------

nlas2 <- normalize_height(Las, knnidw()) # normalize las file with ground points
```

```
hist(filter_ground(nlas2)$Z,  main = "", xlab = "Elevation") # check if ground points are zero in normalized point cloud
chm_2 <- rasterize_canopy(nlas2, 0.5, p2r(subcircle = 0), pkg = "raster") # create chm using normalized point cloud

f2 <- function(x) {              # function for flexible window size
  y <- 2.6 * (-(exp(-0.08*(x-2)) - 1)) + 3
  y[x < 3] <- 4
  y[x > 12] <- 5
  return(y)
}
# identify tree tops
ttops <- locate_trees(nlas2, lmf(f2))
plot(chm_2, col = height.colors(50));
plot(sf::st_geometry(ttops), add = TRUE, pch = 3)

# segment point cloud to individual trees
algo1 <- dalponte2016(chm_2, ttops, max_cr = 12)
las_seg <- segment_trees(nlas2, algo1)
plot(las_seg, bg = "white", size = 4, color = "treeID") # visualize trees

# delineate tree polygons (canopies)
crowns1 <- crown_metrics(las_seg, func = NULL, attribute = "treeID", geom = "concave")
plot(crowns1, col = pastel.colors(200))

# merge tree tops and canopies in to one data frame
crowns1.df= as.data.frame(crowns1)
ttops.df= as.data.frame(ttops)
c.ttops.df= merge(crowns1.df, ttops.df, by.x= "treeID",by.y= "treeID" )
c.ttops.df= cbind(c.ttops.df, st_coordinates(c.ttops.df$geometry.y))
co.treexy.sf = st_as_sf(c.ttops.df, coords = c("X","Y")) # coordinates of tree xy as sf
co.treexy.df = as.data.frame(co.treexy.sf[,c(1,6)])
c.ttops.df= merge(c.ttops.df, co.treexy.df, by.x= "treeID",by.y= "treeID" )
rm(co.treexy.df)
c.ttops.df= c.ttops.df[,-c(3,4,9)]
colnames(c.ttops.df)<- c("treeID", "crown_polygon", "tree_x", "tree_y", "tree_H", "tree_xy")
st_crs(c.ttops.df$tree_xy)<- 32619 # assign coordinate system projection to tree xy column
c.ttops.sf= sf::st_as_sf(c.ttops.df)

# landscape trend--------------------------------------------
```

```
SD.df = as.data.frame(SD) # convert SD raster to dataframe
co = xyFromCell(SD,1:ncell(SD)) # extract x,y coordinates
co.df = as.data.frame(co)
SD.df = cbind(co.df,SD.df)
colnames(SD.df) <- (c("cellx","celly","Raw_SD"))
# trend fitting
ind = !is.na(SD.df$Raw_SD)  #logical index for non NA rows
fit_poly = surf.ls(2, SD.df$cellx[ind],SD.df$celly[ind],SD.df$Raw_SD[ind])
# predict over all xy
sd.pred = predict(fit_poly,SD.df$cellx,SD.df$celly)
SD.df$trend =  sd.pred
SD.df$residual1 = SD.df$Raw_SD - SD.df$trend
rm(sd.pred,SD_detrend,SD_trend,SD_trend_allxy)
co.sf = st_as_sf(co.df, coords = c("x","y")) # set SD coordinates as simple feature
SD.df = cbind(SD.df, co.sf)
rm(co.sf)
colnames(SD.df) <- (c("cellx","celly","Raw_SD","trend","residual1","xy"))

# under canopy vs gap snow depth trend -------------------------------
r<- raster(ncol=ncol(SD),nrow=nrow(SD))
extent(r)= extent(SD)
rp<- rasterize(crowns1, r)
co_rp = xyFromCell(rp,1:ncell(rp))
rp.df = as.data.frame(rp)
rp.df= cbind(co_rp, rp.df)
rm(co_rp)
gapind = is.na(rp.df$treeID)
canopyind = !gapind
rp.df$canopy_gap[gapind] = 0
rp.df$canopy_gap[canopyind] = 1
SD.df = base::cbind(SD.df,dplyr::select(rp.df,treeID,canopy_gap))
rm(rp.df)
hist((SD.df$Raw_SD[SD.df$canopy_gap==1]), freq=F) #under canopy
hist((SD.df$Raw_SD[SD.df$canopy_gap==0]), freq=F) #gap

# intra-canopy trend ----------------------------------------------
SD.df = merge.data.frame(SD.df, c.ttops.df, by.x="treeID", by.y = "treeID", all.x = T)
rm(c.ttops.df)
st_crs (SD.df$xy) <- 32619
# distance from tree trunk to SD point
SD.df$sd_tree = sqrt((SD.df$cellx - SD.df$tree_x)^2+(SD.df$celly - SD.df$tree_y)^2)

# distance from SD point to canopy
```

```
cores = detectCores()
cl <- makeCluster(cores[1]-1) #not to overload your computer
registerDoParallel(cl)
nosnow_ind = is.na(SD.df$Raw_SD)
snow_ind = !nosnow_ind
D = foreach(i = 1:
nrow(SD.df), .combine=rbind, .packages=c('sf','proxy','units')) %dopar% {
if (SD.df$canopy_gap[i]==1){
  x = st_geometry(obj = SD.df$crown_polygon[i])  # extract polygon
  x = st_cast(x, to = 'LINESTRING')
  D1 = st_distance(x, y = SD.df$xy[i], which = 'Euclidean') # distance between SD
point and polygon
  } else {
    D1 = NA
  }
  D = D1
}
stopCluster(cl)
SD.df$sd_crown = D[,1]
rm(D)

# total distance from tree trunk to canopy
SD.df$tree_crown = SD.df$sd_tree + SD.df$sd_crown
# scaled distance
# distance from tree to SD/total distance from tree to crown
SD.df$scaled.dis = SD.df$sd_tree/ SD.df$tree_crown

# remove under canopy vs gap trend
canopy_avg = mean(SD.df$residual1[SD.df$canopy_gap==1], na.rm=T)
gap_avg = mean(SD.df$residual1[SD.df$canopy_gap==0], na.rm=T)
canopyind = SD.df$canopy_gap==1
gapind = SD.df$canopy_gap==0
SD.df$c.g.avg[canopyind] = canopy_avg
SD.df$residual2[canopyind] = SD.df$residual1[canopyind] - canopy_avg
SD.df$c.g.avg[gapind] = gap_avg
SD.df$residual2[gapind] = SD.df$residual1[gapind] - gap_avg

# intra-canopy trend fitting
SD.df_na = na.omit(SD.df) # for fitting purposes
dx = density(SD.df_na$scaled.dis, bw = 0.1) # bin point density in 0.1 m moving
window
dy = approx(dx$x,dx$y,xout=SD.df_na$scaled.dis) # returns x,y  coordinates;
# quadratic model fitting
```

```
fit_poly2int_res2 = lm(residual2 ~ scaled.dis
                + I(scaled.dis^2)
                + tree_H
                + tree_H:scaled.dis,
                weight = 1/(dy$y),   # assign a weight according to point density
                data = SD.df_na)
summary(fit_poly2int_res2)

# predict snow depth below canopies
notreeind = is.na(SD.df$tree_H)
treeind = !notreeind
SD.df$canopy.trend.res2[treeind] = predict(fit_poly2int_res2,SD.df[treeind,])
SD.df$residual4[treeind] = SD.df$residual2[treeind]-SD.df$canopy.trend.res2[treeind]
SD.df$canopy.trend.res2[notreeind] = NA
SD.df$residual4[notreeind] = SD.df$residual2[notreeind]

# calculate variograms and interpolate residuals with OK & IDW--------------------
SD.df2 = SD.df
SD.sf0 = st_as_sf(SD.df2, coords = c("cellx", "celly"), crs = 32619) %>%
  cbind(st_coordinates(.)) # Convert to (Painter et al.) because that is the best way to
store spatial points
SD.sf = SD.sf0[!is.na(SD.sf0$Raw_SD),] # remove SD NAs
# variogram on residual 4
SD.sf_res4_vario <- automap::autofitVariogram(residual4~X+Y, as(SD.sf,
"Spatial"))$var_model # find the fitted variogram model to data
# create a raster/grid as same size as SD raster for interpolation
r0<- raster(ncol=ncol(SD),nrow=nrow(SD)) # create a raster of the same size as SD
extent(r0)= extent(SD)
crs(r0) <- 32619
SD_grid <- rasterToPoints(r0, spatial = TRUE) # Convert raster to spatial pixel to work
with gstat
gridded(SD_grid) <- TRUE
SD_grid <- as(SD_grid, "SpatialPixels")

# Ordinary Kriging
SD_OK_res4 <- krige(
  residual4~1,
  as(SD.sf, "Spatial"),
  SD_grid,
  nmax =8,
  model = SD.sf_res4_vario
)
# IDW
```

```
SD_idw_res4 <- gstat::idw(
  residual4~1,
  as(SD.sf, "Spatial"),
  nmax=8,
  SD_grid,
)
SD_OK_res4.r = raster(SD_OK_res4)
SD_idw_res4.r = raster(SD_idw_res4)
masked_SD_OK_res4 = mask(SD_OK_res4.r, Area) # mask rasters, making data
outside area to NA
masked_SD_idw_res4 = mask(SD_idw_res4.r, Area)

# add OK to main dataframe
SD_OK.df0 = as.data.frame(masked_SD_OK_res4) # convert to dataframe
co.ok=xyFromCell(masked_SD_OK_res4,1:ncell(masked_SD_OK_res4))
SD_OK.df = cbind(as.data.frame(co.ok), SD_OK.df0)
colnames(SD_OK.df) <- (c("cellx","celly","var1.pred"))
SD.df1 = merge.data.frame(SD.df, SD_OK.df , by.x=c("cellx","celly"), by.y =
c("cellx","celly"), all.x = T) # merge sd, canopy_gap, tree coordinates with crown
polygon
names(SD.df1)[names(SD.df1) == 'var1.pred'] <- 'OK_res4'
# add IDW to main dataframe
SD_idw.df0 = as.data.frame(masked_SD_idw_res4)
co.idw=xyFromCell(masked_SD_idw_res4,1:ncell(masked_SD_idw_res4))
SD_idw.df = cbind(as.data.frame(co.idw), SD_idw.df0)
colnames(SD_idw.df) <- (c("cellx","celly","var1.pred"))
SD.df2 = merge.data.frame(SD.df1, SD_idw.df , by.x=c("cellx","celly"), by.y =
c("cellx","celly"), all.x = T) # merge sd, canopy_gap, tree coordinates with crown
polygon
names(SD.df2)[names(SD.df2) == 'var1.pred'] <- 'IDW_res4'

# get the final snow depths ----------------------------------
# ******************  reminder ***************************
# residual4 = SD - landscape trend - canopy vs gap - intra-canopy trend

# points with snow: do not interpolate
snowind = !is.na(SD.df2$Raw_SD)
SD.df2$test4_OK[snowind] = SD.df2$Raw_SD[snowind]
SD.df2$test4_IDW[snowind] = SD.df2$Raw_SD[snowind]
# points below canopy
canind = is.na(SD.df2$Raw_SD) & SD.df2$canopy_gap==1
SD.df2$test4_OK[canind] = SD.df2$trend[canind] + SD.df2$c.g.avg[canind] +
SD.df2$canopy.trend.res2[canind] + SD.df2$OK_res4[canind]
```

```
SD.df2$test4_IDW[canind] = SD.df2$trend[canind] + SD.df2$ c.g.avg[canind] +
SD.df2$canopy.trend.res2[canind] + SD.df2$IDW_res4[canind]
# points in gaps
gapind = is.na(SD.df2$Raw_SD) & SD.df2$canopy_gap==0
SD.df2$test4_OK[gapind] = SD.df2$trend[gapind] + SD.df2$ c.g.avg[gapind] +
SD.df2$OK_res4[gapind]
SD.df2$test4_IDW[gapind] = SD.df2$trend[gapind] + SD.df2$ c.g.avg[gapind] +
SD.df2$IDW_res4[gapind]

# set negative values to zero
negok4= which(SD.df2$test4_OK<0)
negidw4= which(SD.df2$test4_IDW<0)
SD.df2$test4_OK[negok4]=0
SD.df2$test4_IDW[negidw4]=0

# plot interpolated DEMs
test4_OK = cbind.data.frame(SD.df2$cellx, SD.df2$celly, SD.df2$test4_OK)
test4_OK_r = rasterFromXYZ(test4_OK, crs = '+proj=utm +zone=19
+datum=WGS84')
plot(test4_OK_r, main="Test4_OK")
test4_IDW = cbind.data.frame(SD.df2$cellx, SD.df2$celly, SD.df2$test4_IDW)
test4_IDW_r = rasterFromXYZ(test4_IDW, crs = '+proj=utm +zone=19
+datum=WGS84')
plot(test4_IDW_r, main="Test4_IDW")

end_time <- Sys.time()
end_time - start_time

#----------------------- cross validation -------------------------------------------------------
SD.cv = dplyr::select(SD.df2,cellx,celly,Raw_SD,canopy_gap,tree_H,scaled.dis) # all
that is needed to calibrate the interpolation models
SD.cv = SD.cv[!is.na(SD.cv$Raw_SD),] # remove all rows with no snow depth
SD.cv.sf = st_as_sf(SD.cv, coords = c("cellx", "celly"), crs = 32619) %>%
   cbind(st_coordinates(.)) # Convert to (Painter et al.) because that is the best way to
store spatial points

RMSE <- function(observed, predicted) {
  sqrt(mean((predicted - observed)^2, na.rm=TRUE))
}

# parameters for density-based CV:
sampdist = seq(0,5,by=0.5)
sampdensity = 1/sampdist^2  # in pts/m2
```

```
samprop = sampdist[1]/sampdist
nsnow = sum(!is.na(SD.df$Raw_SD))
sampn = round(nsnow*samprop)
n = length(sampdist)

variables = 5+5+4+1+1  # 5 OK test,  5 IDW tests, 4 no interp test + 1 distance + n
train...
nrep = 20 # number of random sampling iterations... increasing it = more computing
time!
someData <- rep(NaN, n*variables*nrep)
rmseCV <- array(someData,c(n,variables,nrep))
biasCV <- array(someData,c(n,variables,nrep))
corCV <- array(someData,c(n,variables,nrep))

# CV loop:
for (i in 1:n) {
  for (j in 1:nrep) {
    # option for density-based CV:
    testcases = sample(seq(1,nsnow, by=1),100)  # 100 pts for validation
    traincases = !(seq(1,nsnow,by=1) %in% testcases) # the rest for training, indexing
TRUE for cases not selected as testcases
    train <- SD.cv.sf[traincases,]
    test <- SD.cv.sf [testcases,]
    #
    # calculate closed distance to snow point
    D2 = st_distance(train,test, which = "Euclidean")
    D2ind = D2<set_units(sampdist[i],m)
    keepind = !apply(D2ind,1,any)
    train = train[keepind,] # remove close points
    D2 = D2[keepind,]
    sortdist = apply(D2,2,sort)
    mindist = apply(sortdist[1:3,],2,mean) # mean distance from test point to three
closest training points

    #--train--
    fit_poly = surf.ls(2, train$X,train$Y,train$Raw_SD)
    train$trend = predict(fit_poly,train$X,train$Y)
    gapind = train$canopy_gap==0
    canopyind = train$canopy_gap==1
    train$res1 = resid(fit_poly)
    gapavg = mean(train$res1[gapind],na.rm = T)
    canopyavg = mean(train$res1[canopyind],na.rm = T)
    train$res2[gapind] = train$res1[gapind] - gapavg
```

```
   train$res2[canopyind] = train$res1[canopyind] - canopyavg

   # fit intra canopy trends over res 2 train period
   dx = density(train$scaled.dis[!is.na(train$scaled.dis)], bw = 0.1)
   dy = approx(dx$x,dx$y,xout=train$scaled.dis)

   fit_poly2int_res2 = lm(res2 ~ scaled.dis
                   + I(scaled.dis^2)
                   + tree_H
                   + tree_H:scaled.dis,
                   weight = 1/(dy$y),
                   data = train)
   summary(fit_poly2int_res2)

   train$canopytrend_res2[canopyind] = predict(fit_poly2int_res2,train[canopyind,])
   train$canopytrend_res2[gapind] = NA
   train$res4[canopyind] = train$res2[canopyind] - train$canopytrend_res2[canopyind]
   train$res4[gapind] = train$res2[gapind]

   #--test--
   gapind = test$canopy_gap==0
   canopyind = test$canopy_gap==1
   test$trend = predict(fit_poly,test$X,test$Y)
   test$canopytrend_res2[canopyind] = predict(fit_poly2int_res2,test[canopyind,])
   test$canopytrend_res2[gapind] = NA

   # interpolation of training residuals to test period:`
   train.sf = st_as_sf(train, coords = c("X", "Y"), crs = 32619) %>%
     cbind(st_coordinates(.))
   test.sf = st_as_sf(test, coords = c("X", "Y"), crs = 32619) %>%
     cbind(st_coordinates(.))

   # OK-on res4 (** variogram must be re-estimated on train period))
   vario_res4_train <- automap::autofitVariogram(res4~X+Y, as(train.sf,
"Spatial"))$var_model
   m <- gstat(formula=res4~1, locations=train.sf, model=vario_res4_train, nmax=8)
   p1 <- predict(m, newdata=test.sf, debug.level=0)$var1.pred
   #IDW- on res4
   m <- gstat(formula=res4~1, locations=train.sf,  set = list(idp=2), nmax=8)
   p2 <- predict(m, newdata=test.sf, debug.level=0)$var1.pred

   # --------------final snow depth predictions
   #final snow depths WITH RESIDUALS
```

```
    test$test4_OK[canopyind] = test$trend[canopyind]  + canopyavg +
test$canopytrend_res2[canopyind] + p1[canopyind] # residual4 = SD - trend -
canopygap - canopy trend
    test$test4_OK[gapind] = test$trend[gapind]  + gapavg + p1[gapind]

    test$test4_IDW[canopyind] = test$trend[canopyind]  + canopyavg +
test$canopytrend_res2[canopyind] + p2[canopyind]
    test$test4_IDW[gapind] = test$trend[gapind]  + gapavg + p2[gapind]

    # final snow depths WITHOUT RESIDUALS
    test$test4_nores[canopyind] = test$trend[canopyind]  + canopyavg +
test$canopytrend_res2[canopyind]
    test$test4_nores[gapind] = test$trend[gapind]  + gapavg

  # put negative snow depths to zero
    negok4= which(test$test4_OK<0)
    negidw4= which(test$test4_IDW<0)
    test$test4_OK[negok4]=0
    test$test4_IDW[negidw4]=0
    negnores4= which(test$test4_nores<0)
    test$test4_nores[negnores4]=0

    #----- global stats------
    rmseCV[i,1,j] <- RMSE(test$Raw_SD, test$test4_OK)
    rmseCV[i,2,j] <- RMSE(test$Raw_SD, test$test4_IDW)
    rmseCV[i,3,j] <- RMSE(test$Raw_SD, test$test4_nores)
    rmseCV[i,4,j] <- mean(mindist)
    rmseCV[i,5,j] <- sum(keepind)

    biasCV[i,1,j] <- bias(test$Raw_SD, test$test4_OK)
    biasCV[i,2,j] <- bias(test$Raw_SD, test$test4_IDW)
    biasCV[i,3,j] <- bias(test$Raw_SD, test$test4_nores)
    biasCV[i,4,j] <- mean(mindist)
    biasCV[i,5,j] <- sum(keepind)

    corCV[i,1,j] <- cor(test$Raw_SD, test$test4_OK)
    corCV[i,2,j] <- cor(test$Raw_SD, test$test4_IDW)
    corCV[i,3,j] <- cor(test$Raw_SD, test$test4_nores)
    corCV[i,4,j] <- mean(mindist)
    corCV[i,5,j] <- sum(keepind)
   }
  disp(i)
  beepr::beep()
```

```
 }

rmseCV = drop(rmseCV)  # in case nrep is set to 1!
biasCV = drop(biasCV) # 1:11, 1:16, 1:20 arrey
corCV = drop(corCV)

columnnames =   c("test4_OK","test4_IDW","test4_nores","meandist","Ntrain")
# average over nrep
if (length(size(rmseCV))==3)
  rmseCV = apply(rmseCV, c(1,2), mean, na.rm=T) # 1:11, 1:16 matrix
  biasCV = apply(biasCV, c(1,2), mean, na.rm=T)
  corCV  = apply(corCV, c(1,2), mean, na.rm=T)

rmseCV <- as.data.frame(rmseCV)
colnames(rmseCV) <- columnnames
biasCV <- as.data.frame(biasCV)
colnames(biasCV) <- columnnames
corCV <- as.data.frame(corCV)
colnames(corCV) <- columnnames

# for plotting--------------
sortind = sort(rmseCV$meandist, index.return = T)  # sort by mean distance for plotting
sortind = sortind$ix
rmseCV = rmseCV[sortind,]
biasCV = biasCV[sortind,]
corCV = corCV[sortind,]
```

References

Blue Marble Geographics: Global Mapper, Blue Marble Geographics, Hallowell, ME, USA, 2020.

Broxton, P. D., Harpold, A. A., Biederman, J. A., Troch, P. A., Molotch, N. P., and Brooks, P. D.: Quantifying the effects of vegetation structure on snow accumulation and ablation in mixed-conifer forests, Ecohydrology, 8, 1073–1094, doi: 10.1002/eco.1565, 2015.

Burrough, P. A.: Principles of geographical information systems for land resources assessment, Geocarto International, 1, 54–54, doi: 10.1080/10106048609354060, 1986.

Currier, W. R. and Lundquist, J. D.: Snow depth variability at the forest edge in multiple climates in the western United States, Water Resour. Res, 54, 8756–8773, doi: 10.1029/2018WR022553, 2018.

Dalponte, M. and Coomes, D. A.: Tree-centric mapping of forest carbon density from airborne laser scanning and hyperspectral data, Methods in Ecology and Evolution, 7, 1236–1245, doi: 10.1111/2041-210X.12575, 2016.

Deems, J. S., Painter, T. H., and Finnegan, D. C.: Lidar measurement of snow depth: a review, Journal of Glaciology, 59, 467–479, doi: 10.3189/2013JoG12J154, 2013.

Dharmadasa, V., Kinnard, C., and Baraër, M.: An accuracy assessment of snow depth measurements in agro-forested environments by UAV lidar, Remote Sensing, 14, 1649, doi: 10.3390/rs14071649, 2022.

Dharmadasa, V., Kinnard, C., and Baraër, M.: Topographic and vegetation controls of the spatial distribution of snow depth in agro-forested environments by UAV lidar, The Cryosphere, 17, 1225–1246, doi: 10.5194/tc-17-1225-2023, 2023.

Erxleben, J., Elder, K., and Davis, R.: Comparison of spatial interpolation methods for estimating snow distribution in the Colorado Rocky Mountains, Hydrological Processes, 16, 3627–3649, doi: 10.1002/hyp.1239, 2002.

Guo, Q., Li, W., Yu, H., and Alvarez, O.: Effects of topographic variability and lidar sampling density on several DEM interpolation methods, Photogrammetric Engineering and Remote Sensing, 76(6), 701–712, doi: 10.14358/PERS.76.6.701, 2010.

Harder, P., Pomeroy, J., and Helgason, W.: Improving sub-canopy snow depth mapping with unmanned aerial vehicles: Lidar versus structure-from-motion techniques, The Cryosphere, 14, 1919–1935, doi: 10.5194/tc-14-1919-2020, 2020.

Harpold, A. A., Guo, Q., Molotch, N., Brooks, P. D., Bales, R., Fernandez-Diaz, J. C., Musselman, K. N., and Swetnam, T. L.: Lidar-derived snowpack data sets from mixed conifer forests across the Western United States, Water Resour. Res, 50, 2749–2755, doi: 10.1002/ 2013WR013935., 2014.

Hojatimalekshah, A., Uhlmann, Z., Glenn, N., Hiemstra, C., Tennant, C., Graham, J., Spaete, L., Gelvin, A., Marshall, H., McNamara, J., and Enterkine, J.: Tree canopy and snow depth relationships at fine scales with terrestrial laser scanning, The Cryosphere, 15, 2187–2209, doi: 10.5194/tc-15-2187-2021, 2021.

Hopkinson, C., Sitar, M., Chasmer, L., and Treitz, P.: Mapping snowpack depth beneath forest canopies using airborne lidar, Photogrammetric Engineering & Remote Sensing, 70, 323–330, 2004.

Hopkinson, C., Collins, T., Anderson, A., Pomeroy, J., and Spooner, I.: Spatial snow depth assessment using lidar transect samples and public GIS data layers in the Elbow River watershed, Alberta, Canadian Water Resources Journal, 37, 69–87, doi: 10.4296/cwrj3702893, 2012a.

Hopkinson, C., Pomeroy, J., Debeer, C., Ellis, C., and Anderson, A.: Relationships between snowpack depth and primary lidar point cloud derivatives in a mountainous environment, Remote Sensing and Hydrology, Jackson Hole, Wyoming, USA, 27–30 September 2010, 2012.

Isaaks, E. H. and Srivastava, R. M.: Applied Geostatistics, Oxford University Press, 1989.

Jacobs, J. M., Hunsaker, A. G., Sullivan, F. B., Palace, M., Burakowski, E. A., Herrick, C., and Cho, E.: Snow depth mapping with unpiloted aerial system lidar observations: a case study in Durham, New Hampshire, United States, The Cryosphere, 15, 1485–1500, doi: 10.5194/tc-15-1485-2021, 2021.

Jost, G., Weiler, M., Gluns, D. R., and Alila, Y.: The influence of forest and topography on snow accumulation and melt at the watershed-scale, Journal of Hydrology, 347, 101–115, doi: 10.1016/j.jhydrol.2007.09.006, 2007.

Koutantou, K., Mazzotti, G., Brunner, P., Webster, C., and Jonas, T.: Exploring snow distribution dynamics in steep forested slopes with UAV-borne LiDAR, Cold

Regions Science and Technology, 200, 103587, doi: 10.1016/j.coldregions.2022.103587, 2022.

Lehning, M., Grünewald, T., and Schirmer, M.: Mountain snow distribution governed by an altitudinal gradient and terrain roughness, Geophysical Research Letters, 38, L19504, doi: 10.1029/2011GL048927, 2011.

López-Moreno, J. I., Latron, J., and Lehmann, A.: Effects of sample and grid size on the accuracy and stability of regression-based snow interpolation methods, Hydrological Processes, 24, 1914–1928, doi: 10.1002/hyp.7564, 2010.

Mazzotti, G., Currier, W., Deems, J. S., Pflug, J. M., Lundquist, J. D., and Jonas, T.: Revisiting snow cover variability and canopy structure within forest stands: Insights from airborne lidar data, Water Resour. Res, 55, 6198–6216, doi: 10.1029/2019WR024898, 2019.

Michele, C., Avanzi, F., Passoni, D., Barzaghi, R., Pinto, L., Dosso, P., Ghezzi, A., Gianatti, R., and Vedova, G. D.: Using a fixed-wing UAS to map snow depth distribution: An evaluation at peak accumulation, The Cryosphere, 10, 511–522, doi: 10.5194/tc-10-511-2016, 2016.

Morsdorf, F., Kötz, B., Meier, E., Itten, K. I., and Allgöwer, B.: Estimation of LAI and fractional cover from small footprint airborne laser scanning data based on gap fraction, Remote Sensing of Environment, 104, 50–61, doi: 10.1016/j.rse.2006.04.019, 2006.

Musselman, K. N., Molotch, N. P., and Brooks, P. D.: Effects of vegetation on snow accumulation and ablation in a mid-latitude sub-alpine forest, Hydrological Processes, 22, 2767–2776, doi: 10.1002/hyp.7050, 2008.

Pomeroy, J. W. and Dion, K.: Winter radiation extinction and reflection in a boreal pine canopy: Measurements and modelling, Hydrological Processes, 10, 1591–1608, 1996.

Revuelto, J., López-Moreno, J., Azorin-Molina, C., and Vicente-Serrano, S. M.: Topographic control of snowpack distribution in a small catchment in the central Spanish Pyrenees: Intra- and inter-annual persistence, The Cryosphere, 8, 1989–2006, doi: 10.5194/tc-8-1989-2014, 2014.

Revuelto, J., López-Moreno, J., Azorin-Molina, C., and Vicente-Serrano, S. M.: Canopy influence on snow depth distribution in a pine stand determined from terrestrial laser data, Water Resour. Res, 51, 3476–3489, doi: 10.1002/2014WR016496, 2015.

Roussel, J.-R., Auty, D., Boissieu, F. D., Meador, A. S., Jean-François, B., Demetrios, G., Steinmeier, L., and Adaszewski, S.: Airborne LiDAR data manipulation and visualization for forestry applications. R package version 4.0.2, 2022.

Roussel, J.-R., Auty, D., Coops, N. C., Tompalski, P., Goodbody, T. R. H., Meador, A. S., Bourdon, J.-F., de Boissieu, F., and Achim, A.: lidR: An R package for analysis of Airborne Laser Scanning (ALS) data, Remote Sensing of Environment, 251, 112061, doi: 10.1016/j.rse.2020.112061, 2020.

Tinkham, W. T., Smith, A. M. S., Marshall, H., Link, T., Falkowski, M., and Winstral, A.: Quantifying spatial distribution of snow depth errors from lidar using random forest, Remote Sensing of Environment, 141, 105–115, doi: 10.1016/j.rse.2013.10.021, 2014.

Uhlmann, Z., Glenn, N. F., Spaete, L. P., Hiemstra, C., Tennant, C., and McNamara, J.: Resolving the influence of forest-canopy structure on snow depth distributions with terrestrial laser scanning, IGARSS 2018 - 2018 IEEE International Geoscience and Remote Sensing Symposium, Valencia, Spain, 22-27 July 2018, 6284–6286, doi: 10.1109/IGARSS.2018.8517911,

Varhola, A. s., Coops, N. C., Bater, C. W., Teti, P., Boon, S., and Weiler, M.: The influence of ground- and lidar-derived forest structure metrics on snow accumulation and ablation in disturbed forests, Canadian Journal of Forest Research, 40, 812–821, doi: 10.1139/X10-008, 2010.

Venables, W. N. and Ripley, B. D.: Modern applied statistics with S. Fourth edition, Springer, New York, 2002.

Winstral, A., Elder, K., and Davis, R. E.: Spatial snow modeling of wind-redistributed snow using terrain-based parameters, Journal of Hydrometeorology, 3, 524–538, doi: 10.1175/1525-7541(2002)003<0524:Ssmowr>2.0.Co;2, 2002.

Zheng, Z., Kirchner, P. B., and Bales, R. C.: Topographic and vegetation effects on snow accumulation in the southern Sierra Nevada: A statistical summary from lidar data, The Cryosphere, 10, 257–269, doi: 10.5194/tc-10-257-2016, 2016.

Zheng, Z., Ma, Q., Qian, K., and Bales, R. C.: Canopy effects on snow accumulation: observations from lidar, canonical-view photos, and continuous ground measurements from sensor networks, Remote Sensing, 10, 1769, doi: 10.3390/rs10111769, 2018.

Zheng, Z., Ma, Q., Jin, S., Su, Y., Guo, Q., and Bales, R. C.: Canopy and terrain interactions affecting snowpack spatial patterns in the Sierra Nevada of

California, Water Resour. Res, 55, 8721–8739, doi: 10.1029/2018wr023758, 2019.

CHAPTER IV

CHARACTERIZATION OF METEOROLOGICAL CONTROL ON SNOW DEPTH IN AN AGRO-FORESTED ENVIRONMENT BY A MEASUREMENT-BASED APPROACH: A CASE STUDY IN SAINTE-MARTHE, EASTERN CANADA

Vasana Dharmadasa [1,2,3], Christophe Kinnard [1,2,3] and Michel Baraër [4]

[1] Department of Environmental Sciences, University of Québec at Trois-Rivières, Trois-Rivieres, QC G8Z 4M3, Canada

[2] Center for Northern Studies (CEN), Quebec City, QC GV1 0A6, Canada

[3] Research Centre for Watershed-Aquatic Ecosystem Interactions (RIVE), University of Québec at Trois-Rivières, Trois-Rivieres, QC G8Z 4M3, Canada

[4] Department of Construction Engineering, École de Technologie Supérieure, Montreal, QC H3C 1K3, Canada

Corresponding author: vasana.sandamali.dharmadasa@uqtr.ca

This article is in review for the journal of *Agricultural and Forest Meteorology.*

Highlights

- We used measurements to explore energy exchanges in an agro-forested snowpack.
- Differences in energy fluxes between open, forest, and gap areas were significant.
- Longwave radiation had a greater influence on energy balance during accumulation.
- Latent heat fluxes and solar radiation absorption dominated snowpack melting.
- Blowing snow influenced the energy budget through negative feedback effects.

Abstract

A lack of field studies measuring snow mass and energy balance in open and forest patches hinders the holistic understanding of snowpack dynamics and makes it difficult to validate modeling efforts in agro-forested environments. In such context, this study explores the energy exchanges within snowpacks in an agro-forested environment in eastern Canada, with a focus on measuring energy fluxes and assessing temporal variability and meteorological controls on the snowpack. The results showed that there are considerable differences in energy fluxes between open, forest, and gap areas, with net radiation dominating the snow surface energy balance. During the accumulation period, longwave radiation had a greater influence on the variability of the energy balance, while during the ablation period, latent heat fluxes and solar radiation absorption dominated the variability of the energy balance and snowpack melting. Blowing snow also influenced the energy budget in the open area through negative feedback effects. Despite the negative feedback effects, results showed that the decreased air stability in response to the reduced temperature gradient between the atmosphere and snowpack counterbalanced the reduced vapor pressure gradient and resulted in slightly increased latent heat (sublimation) losses from the snowpack during blowing snow. This shows that the feedback of blowing snow on snowpack sublimation is contingent on the choice of stability function in the bulk aerodynamic method. Furthermore, our analysis showed reduced influxes of sensible heat and longwave radiation to the snowpack in response to the blowing snow cooling feedback on the atmosphere. These results emphasize the significant role of blowing snow for the energy exchanges in large wind-exposed open areas in humid continental agro-forested landscapes. Furthermore, the different snowpack and energy balance conditions between the open and forested patches of agro-forested landscapes highlighted in this study could have important implications for snowmelt infiltration patterns and resulting catchment-scale hydrology.

Keywords: Snow energy budget; agro-forested environment; blowing snow

4.1 Introduction

Snow cover is an integral component of the climate system in cold climate regions. It represents a major part of the terrestrial water storage during the winter season and produces a significant spring runoff with the onset of snowmelt. Snow accumulation and the timing, intensity, and duration of snowmelt depend on meteorological and physiographic variables such as regional climate, elevation, vegetation presence/absence, and forest structure (Elder et al., 1998; Golding and Swanson, 1986; Pomeroy et al., 1998a; Roth and Nolin, 2017; Zheng et al., 2018). Snowpack energy budget is a key element to understand the spatial and temporal evolution of snowpack in different climatic and physiographic settings. For instance, compared to open areas, forest cover reduces the incoming shortwave radiation, increases longwave radiation, dampens wind speed, and hence reduces turbulent heat transfers within the canopy (Helgason and Pomeroy, 2012a; Pomeroy and Dion, 1996; Pomeroy and Granger, 1997; Pomeroy and Gray, 1994; Pomeroy et al., 1998a; Pomeroy et al., 1998b; Prévost et al., 1991; Tarboton, 1994). In turn, the snowpack dynamics within a forest differ from that in an open area. A significant amount of literature reported reduced snow accumulation in forested areas compared to adjacent open areas due to canopy interception and sublimation losses and slower snowmelt rates in spring due to shading by the canopy, or, in a humid climate, faster snowmelt due to increased longwave radiation with higher canopy density- the ‘radiative paradox’ (Hojatimalekshah et al., 2021; Hopkinson et al., 2004; Lundquist et al., 2013; Pomeroy and Granger, 1997; Varhola et al., 2010; Zheng et al., 2018). Snow accumulation and melt also differ significantly between different forest stands with distinct structural differences, due to the impact of forest structure on the energy balance, dominated by radiative heat fluxes (Winkler et al., 2005). Accumulation and melt rates generally decline with increasing canopy density and leaf area (Pomeroy et al., 2002). For example, larger canopy interception and losses in coniferous forests result in less snow on the ground than that in deciduous and mixed forests (Aygün et al., 2020; Hopkinson et al., 2012). Open areas on the other hand are generally characterized by large fetch distances and high wind speeds that promote erosion of the snow cover by increased blowing snow fluxes and sublimation losses (Pomeroy and Gray, 1994). High wind speeds also significantly increase turbulent energy exchanges in open areas which eventually increase snow sublimation (Roth and Nolin, 2017). The importance of blowing snow fluxes in shaping the open terrain snow cover and its ultimate influence on the magnitude and timing of snowmelt has been well documented (Essery and Pomeroy, 2004; Liston et al., 2007; Mott et al., 2018; Pomeroy and Gray, 1994; Pomeroy et al., 1998a; Prasad et al., 2001). For example, in the Canadian prairies, 8–19 % of annual snowfall is removed by blowing snow fluxes (by saltation and suspension), and 15–40 % or more of annual snowfall is lost through blowing snow sublimation (Pomeroy and Gray, 1995; Pomeroy et al., 1993). Several authors reported substantial differences in snow accumulation and melt in forest clearings or gaps compared to adjacent forests and open areas (e.g., Broxton et al., 2015; Conway et al., 2018; Golding and Swanson, 1986; Pomeroy et al., 2012; Pomeroy and Gray, 1994; Pomeroy et al., 2002; Swanson, 1988; Troendle and Leaf, 1980; Woods et al., 2006). Collectively, they demonstrate that small gaps (~2–5 times the tree height diameter) are often still sheltered by trees, while large gaps are exposed to wind erosion that eventually reduces the overall snow accumulation.

The knowledge on energy exchanges between the snowpack, atmosphere, and the ground is important for the prediction of snowmelt rates in hydrological applications (Mas et al., 2018), determination of land surface-atmosphere interactions for climate modeling and weather forecasting (Pomeroy et al., 1998a), and prediction of avalanche hazards (Brun et al., 1989). Indeed, many of the snow physics models developed for such applications are based on energy budget estimation. Since their early developments, these models have been greatly improved with the addition of new parameterizations for turbulent energy transfer (Andreas et al., 2010), blowing snow (Liston et al., 2007; Pomeroy et al., 2007; Pomeroy et al., 1993), and snow metamorphism (Lehning et al., 2002). However, despite these advances, in a snowmelt model intercomparison project, Rutter et al. (2009) reported that snowmelt models do not consistently produce acceptable results in all environments. This is partly due to the inability to robustly simulate the snowpack processes and snow-atmosphere-ground interactions (Rutter et al., 2009). However, the availability of calibration data could solve a major portion of this issue by reducing the parameter uncertainty and thereby offsetting model deficiencies (Essery et al., 2009). This highlights the importance of having detailed meteorological and/or energy flux measurements in different environments.

The snowpack energy exchanges in different environments are well documented in large open areas like the Canadian prairies (Harder et al., 2018; Harder et al., 2017; Pomeroy and Gray, 1994; Pomeroy et al., 1993; Pomeroy et al., 1998a) and Arctic (Boike et al., 2003; Lackner et al., 2022; Liston and Sturm, 1998; Price and Dunne, 1976), forested environments (Barry et al., 1990; Lundquist et al., 2013; Pomeroy and Granger, 1997; Prévost et al., 1991), and mountainous regions (Bair et al., 2018; Helgason and Pomeroy, 2012b; Hoelzle et al., 2022; Kuipers Munneke et al., 2009; Mott et al., 2011b; Mott et al., 2017; Roth and Nolin, 2017). Collectively, these studies show marked differences in snow mass and energy fluxes in different environments depending on vegetation and topographical settings, which in turn have a substantial effect on snowmelt and regional hydrology. On the other hand, agro-forested catchments, which are composed of alternate patches of open lands (mostly agricultural) and forest, have been little studied. Snow-affected agro-forested landscapes characterize much of eastern Canada (Jobin et al., 2014), but also part of the Midwest and northeastern USA (Gootman and Hubbart, 2021; Jacobs et al., 2021), and northern Europe (Luomaranta et al., 2019). Differences in snow mass and energy balance within agro-forested environments would be expected to exert a significant influence on regional hydrology (Aygün et al., 2020; Aygün et al., 2022). However, the lack of field studies simultaneously measuring snow mass and energy balance in open and forest patches hampers the holistic understanding of snowpack dynamics and makes it difficult to validate the modeling efforts in these agro-forested landscapes (Aygün et al., 2020; Brown, 2010; Paquotte and Baraer, 2021; Sena et al., 2017). Therefore, the objective of this study is to simultaneously measure and estimate energy fluxes and assess the temporal variability and meteorological controls on snow energy transfer between open ground, forest, and forest clearing (gap) within an agro-forested environment in eastern Canada. We also measure blowing snow fluxes and investigate their influence on the energy budget, which is largely understudied in agro-forested, humid continental climates. In view of the lack of observational studies, our study is expected to provide a baseline for energy partitioning in agro-forested landscapes using a measurement-based approach that would benefit future modeling applications.

4.2 Study Sites and Measurements

The study was conducted at three sites within the experimental watershed of Sainte-Marthe in southern Québec, eastern Canada (Figure 4.1). The watershed has an extent of 9 km^2 with a mixed wood forest in the upper catchment and agricultural areas downstream. The climate of the region is characterized by a sub-humid continental climate (Paquotte and Baraer, 2021; Valence et al., 2022). Automatic weather station (AWS) measurements from three contrasted sites were used in this study: (i) an "open" site located in an open agricultural area (45.40°N, 74.31°W), (ii) a "forest" site in the mixed wood forest (mostly deciduous, 45.43°N, 74.28°W), and (iii) a "gap" site in a clearing zone of approximately 20x30 m in the mixed wood forest area (45.42°N, 74.28°W). Although the open station is located a little outside the watershed boundary due to logistical reasons, it shares the same climatic conditions. Also, the proximity of the sites and their similar topographic settings (flat, within an elevation range of 69–110 m asl (above sea level)), allow isolating the effect of land use on the snow energy and mass balance. The gap station is in operation since 2016 and the open and forest stations are operational since December 2019. Figure 4.1 shows the study locations and Table 4.1 outlines the details of the individual measurements at each site.

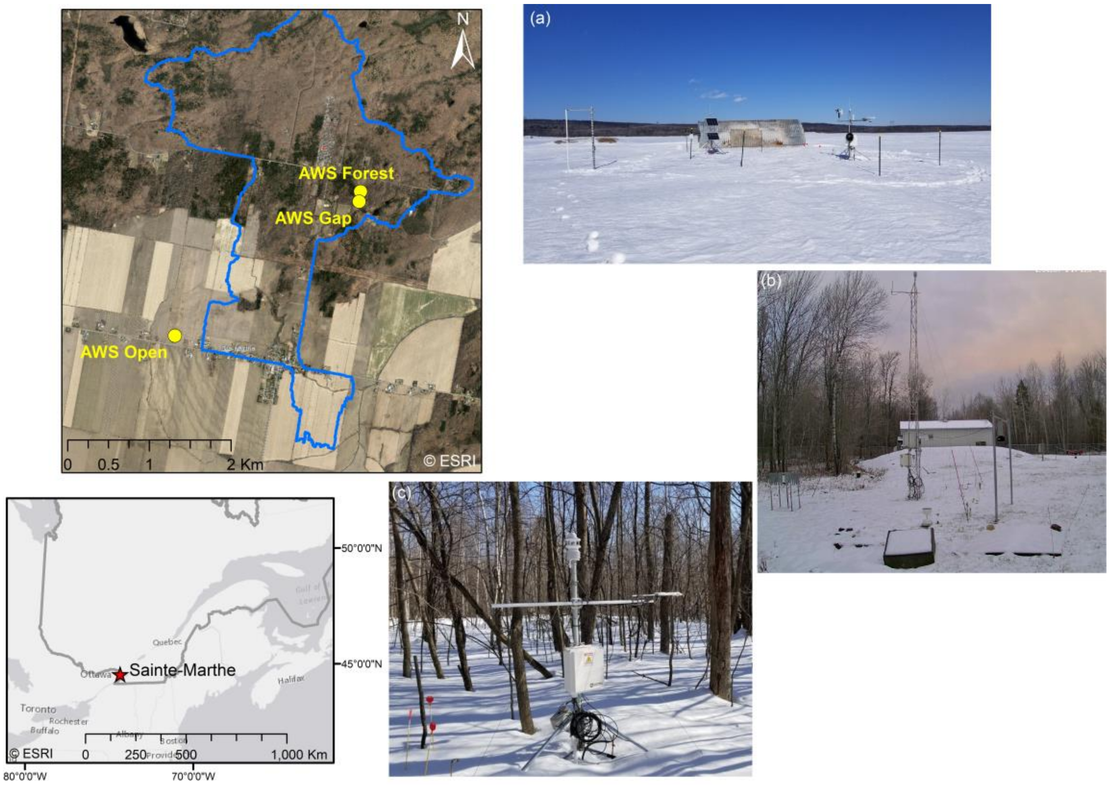

Figure 4.1. Study site locations in the Sainte-Marthe watershed a) open, b) gap, and c) forest

Table 4.1. List of instruments used and their characteristics at the three different sites

Parameters	Sensors	Manufacturer	Range	Accuracy	Station
Shortwave and longwave radiation	Pyranometer and pyrgeometer (CNR4)	Kipp & Zonen	0.3–2.8 µm, 4.5–42 µm	±10 % [a], ±10 % [a]	Open Gap Forest
Air Temperature and relative humidity	HMP155A probe	Vaisala	–80–60 °C, 0–100 %	±0.5 °C, ±1.5 %	Open
	Platinum thermocouple HygroClip (HC-S3L)	Rotronic Instrument Corp	–40–60 °C, 0–100 %	±0.6 °C, ±1.5 %	Gap
	WS700-UMB	Lufft	–50–60 °C, 0–100 %	±0.2 °C, ±2 %	Forest

Atmospheric pressure	Barometer (CS106)	Vaisala	500–1100 hPa	±1.5 hPa	Open
	Barometer (CS106)	Vaisala	500–1100 hPa	±1.5 hPa	Gap
	WS700-UMB	Lufft	300–1200 hPa	±0.5 hPa	Forest
Wind speed and wind direction	Anemometer (5103-L)	R. M. Young	0–100 m s^{-1}, 0–360 °	±0.3 m s^{-1}, ±3 °	Open
	Anemometer (5103-L)	R. M. Young	0–100 m s^{-1}, 0–360 °	±0.3 m s^{-1}, ±3 °	Gap
	WS700-UMB	Lufft	0–100 m s^{-1}, 0–360 °	±0.3 m s^{-1}, < 3 °	Forest
Precipitation	WS700-UMB	Lufft	0.3–5 mm drop size 0–200 mm h^{-1} intensity	±2 %	Gap
Snow depth	Sonic telemetry sensor (SR50A)	Campbell Scientific	0.5–10 m	±1 cm	Open Gap Forest
Snow and ground temperatures	Temperature probes (107)	Campbell Scientific	–35–50 °C	±0.2 °C	Open Gap Forest
Soil moisture (volumetric water content)	Reflectometer (CS-655)	Campbell Scientific	0–100 %	±1 or ± 3 %	Open Gap
Blowing snow	FlowCapt	IAV Technologies	0–250 g m^{-2} s^{-1}	±5 %	Open

[a] : accuracy for daily totals.

All data were recorded at hourly intervals using a CR3000 data logger (Campbell Scientific) in the open, at hourly intervals using a CR1000 data logger in the forest, and at 15 min intervals using a CR1000 data logger in the gap. Temperatures within the snowpack were measured from 0 to +30 cm at a 10 cm interval. Ground temperatures were measured at depths from 0 to –60 cm at a 10 cm interval and ground volumetric water content was measured from 0 to –40 cm at the same interval. Ground temperature and soil moisture sensors in the forest malfunctioned soon after their deployment. With the proximity of the forest site to the gap site, ground temperature measurements from the gap station were therefore used for the analysis in the forest. Snow water equivalent (SWE) was only measured at the gap station at 6 hr intervals using a passive gamma SWE sensor (CS725, accuracy of ±15 mm). Two Hydroinnova SWE sensors (Hydroinnova, 2019) installed in the open and forest were found to be not functioning well, and hence were not considered in the analysis. The precipitation radar sensor was installed at a height of 10 m above the ground. SR50 sensors were installed at 2 m, 2 m, and 1.5 m height above the ground in open, forest, and gap station respectively. Installation height of wind sensors from ground surface are 2.4 m, 2.5 m, and 1.5 m in open, forest, and gap station respectively.

The open site is equipped with two second-generation FlowCapt acoustic sensors to measure hourly blowing snow fluxes vertically integrated between 0–1 m and 1–2 m above the ground surface (Chritin et al., 1999; Cierco et al., 2007; IAV Technologies, 2019; Trouvilliez et al., 2015). A number of studies in the Swiss and French Alps (Lehning and Fierz, 2008; Naaim-Bouvet et al., 2010; Trouvilliez et al., 2015; Vionnet et al., 2018), the Indian Himalayas and Central Asia (Das et al., 2012; Zhang et al., 2022), the Arctic region (Jaedicke, 2001), and in Antarctica (Amory, 2020; Trouvilliez et al., 2014) have demonstrated the capability of the FlowCapt sensor to detect blowing snow. However, the accuracy of the FlowCapt sensor for quantitatively measuring the blowing snow fluxes has been debated in the literature (Cierco et al., 2007; Lehning and Fierz, 2008; Naaim-Bouvet et al., 2010; Trouvilliez et al., 2015). The second-generation sensor (used in this study) has significant improvements (Trouvilliez et al., 2015) overcoming many drawbacks of its first-generation counterpart (Cierco et al., 2007). Trouvilliez et al. (2015) found that the sensor still underestimates the snow fluxes quantities compared to a snow particle counter S7 sensor during a winter season in the French Alps, particularly during concurrent snowfall. However, they also showed its promising capability as a blowing snow event detector. Several other authors highlight the usefulness of the second-generation FlowCapt as a good aeolian snow transport event detector with a high level of confidence, together with its robustness to withstand hostile weather conditions for prolonged periods (e.g., polar environments), and its low power consumption (Amory, 2020; Trouvilliez et al., 2014).

4.3 Methods

The snowpack behavior at the three sites was examined from December 2020–April 2021 by computing the energy exchange components. Prior to calculating the energy budget components, all the raw measurements were visually inspected, and missing, and/or suspected erroneous values were screened, inventoried, and gap-filled accordingly. Then, at the open and forest stations hourly measurements were directly used for the energy flux calculations. At the gap station, all data recorded in 15-minute time steps were aggregated to hourly data for the energy flux calculations.

4.3.1 Data Quality Control and Preprocessing

No data gaps were identified for the open and gap stations for the study period. Twenty isolated missing values were identified for the WS700-UMB measurements at the forest station and were filled with linear interpolation. Isolated snow depth outliers were deleted and corrected manually with measurements from neighboring time steps. Specific processing for the other meteorological variables and radiation fluxes are described in subsequent sections.

4.3.1.1 Solar Radiation Correction

Negative incoming and outgoing shortwave radiations during the night were set to zero. Corrections were made for snow covering and shading the upward-looking pyranometer sensor, specifically at the forest station where low winds were less efficient to clear the snow on the sensors. These periods were identified by available time-lapse photos and high albedo during daytime (>0.9). In such situations, the incoming radiation data were corrected by using an albedo for fresh snow ($\propto_{raw}$= 0.85; Oke (1987)) and multiplying it by the outgoing radiation (e.g., Conway et al., 2018; Hoelzle et al., 2022). However, this correction only accounted for a smaller portion of the study period, i.e., 0.05 % of hourly measurements in the forest.

Additionally, solar radiation data were corrected for patchy snowpack conditions at the beginning and end of the study periods at all sites by considering the snow cover fraction within the sensor footprint (Essery et al., 2013). The snow cover fraction (SCF) was approximated as:

$$SCF = \min\left(1, \frac{snow\ depth}{d_0}\right) \qquad \text{Equation 4.1}$$

d_0 was taken as 0.1 m in all sites. This value was decided by plotting daily raw albedo versus snow depth, which showed that albedo was influenced by exposed soil below 0.1 m of snow depth (Supplement Figure S4.1). The raw snow albedo ($\propto_{raw}$) was then corrected using the snow cover fraction.

$$\propto_{corr} = \frac{\propto_{raw} - (1 - SCF)\ \propto_{soil}}{SCF} \qquad \text{Equation 4.2}$$

Where soil albedo ($\propto_{soil}$) was set to 0.15 based on snow-free observations in the fall. Then, the outgoing shortwave radiation was corrected by multiplying the incoming shortwave radiation by the corrected albedo ($\propto_{corr}$).

This correction was applied for 49, 46, and 34 days from the total of 135 days in the open, forest, and gap respectively.

4.3.1.2 Longwave Radiation Correction

In terms of correcting outgoing longwave radiation for snow cover fraction, a maximum value of 316 W m^{-2} was imposed on outgoing longwave radiation to avoid the bias from warmer snow-free soil in the sensor footprint (e.g., melting snow surface with a patchy snowpack). This maximum value was obtained by calculating outgoing longwave radiation (Q_{LWout}) for a snow surface temperature, T_s, of 273.15 K (0 °C) using Equation 4.3 (Dewalle and Rango, 2008).

$$Q_{LWout} = \varepsilon\sigma\, T_s^4 + (1-\varepsilon)Q_{LWin} \qquad \text{Equation 4.3}$$

Where the emissivity ε is taken as 0.98 (Anderson, 1976), σ is the Stefan-Boltzmann constant ($5.67\text{x}10^{-8}$ W m^{-2} K^{-4}), and Q_{LWin} is the incoming longwave radiation.

The heater/ventilator unit in CNR4 sensor prevents the formation and deposition of dew and frost on the pyrgeometer and pyrgeometer window, hence the errors due to dew and frost for radiation measurements are expected to be negligible. Snow covering the sensor only accounted for a smaller portion for the study period (see solar radiation correction), hence incoming longwave radiations were not corrected for those periods.

4.3.1.3 Local Precipitation Data Preparation

In a recent study at the gap station, Paquotte and Baraer (2021) used precipitation data from the Pierre-Elliott-Trudeau station (YUL), situated 40 km east of the study site (Environment and Climate Change Canada, 2021) reasoning that it is situated in the same precipitation corridor as Sainte-Marthe, and in a similar physiographic context. The authors used the data from November 2018 to April 2019, before the deployment of the WS700-UMB sensor at the site. We compared the total cumulative precipitation of the WS700-UMB with YUL for the 2020–2021 winter season which showed that they are in the same order of magnitude (Supplement Figure S4.2). Therefore, the local precipitation data from the WS700-UMB measurements at the gap station was used for all three sites in this study. However, since the automatic separation of the precipitation into rainfall and snowfall by the WS700-UMB sensor appeared to be erroneous, the precipitation phase separation was done by adopting a 2 °C temperature threshold based on the mean winter relative humidity of 90 % during the precipitation events at the site (Jennings et al., 2018b).

4.3.1.4 Local Wind Data Preparation

No outlier wind speed values were found during the initial quality control process in all sites. A minimum wind speed threshold of 0.3 m s^{-1} was imposed at all sites to avoid suppressing turbulent fluxes completely at low wind speeds (Conway and Cullen, 2013; Martin and Lejeune, 1998).

4.3.1.5 Calculation of Mean Snowpack Temperature

The mean snowpack temperature was obtained by averaging the four thermistor measurements within the snowpack when the snow depth was higher than 35 cm. When snow depth was below 35 cm, only the thermistors located 5 cm or more below the snow surface were used for averaging, in order to avoid direct solar radiation effects on thermistors.

4.3.1.6 Calculation of Specific Humidity

The specific humidity, q, was calculated from the relative humidity measurements at each site (Armstrong and Brun, 2008).

$$q = 0.622\ RH\ \rho_w / (\rho_a - \rho_w) \qquad \text{Equation 4.4}$$

Where RH is the relative humidity as a factor, ρ_w is the density of water vapor (kg m^{-3}), and ρ_a is the density of air (kg m^{-3}).

4.3.2 Calculation of Surface Energy Balance

The energy balance for the snowpack was calculated at an hourly time step, using Equation 4.5 (adapted from Dewalle and Rango (2008)).

$$Q_M + \frac{dU}{dt} = Q_{SW} + Q_{LW} + Q_S + Q_L + Q_R + Q_{SF} + Q_G \quad \text{Equation 4.5}$$

Where U is the internal energy of the snowpack, Q_{SW} is the net shortwave radiation heat flux, Q_{LW} is the net longwave radiation heat flux, Q_S is the sensible heat flux, and Q_L is the latent heat flux caused by evaporation, sublimation, or condensation. Q_R is the sensible and latent heat flux associated with rain-on-snow events, Q_{SF} is the sensible heat associated with solid precipitation (snowfall), Q_G is the heat exchange at the snow-ground interface, and Q_M is the heat available for melt. All fluxes on the right side of the energy balance equation, except Q_S and Q_L were derived from the raw measurements collected at the respective weather station at each site. $Q_M + \frac{dU}{dt}$ was solved as the residual of the other energy fluxes as depicted in Equation 4.5. All energy terms are expressed in W m^{-2} and are positive when received by the snowpack and negative when lost by the snowpack. The analysis was calculated from December 2020 to April 2021. All energy fluxes were calculated at hourly time steps and then aggregated to daily values first. Then, the daily surface energy fluxes calculated for days with snow depths less than 5 cm (i.e., snow cover fraction less than 0.5) were omitted because of the high uncertainty involved with a very thin snowpack. Mean weekly values were then calculated from daily values to simplify the presentation and interpretation of the results.

4.3.2.1 *Radiation Fluxes*

Q_{SW} and Q_{LW} were measured directly at each site using CNR4 sensors (Table 4.1) and were corrected as described in sections 4.3.1.1 and 4.3.1.2.

4.3.2.2 *Turbulent Sensible and Latent Heat Flux*

The turbulent fluxes were calculated using the bulk aerodynamic method (Oke, 1987; Price and Dunne, 1976).

$$Q_S = \rho_a c_p C_h u_a (T_a - T_s) \qquad \text{Equation 4.6}$$

$$Q_L = 0.622\, \rho_a L C_e u_a (e_a - e_s)/P_a \qquad \text{Equation 4.7}$$

Where C_h and C_e are the bulk exchange coefficients for the sensible and latent heat fluxes, respectively, ρ_a is the density of air (kg m^{-3}), c_p is the specific heat of air at constant pressure (1005 J kg^{-1} K^{-1}), u_a is the wind speed (m s^{-1}), T_a is the air temperature (K), T_s is the snow surface temperature (K), which was measured using the outgoing (Q_{LWout}) and incoming (Q_{LWin}) longwave radiation measurements and rearranging the longwave radiation balance, Equation 4.3 (Helgason and Pomeroy, 2012a; Steiner et al., 2018). L is the latent heat of vaporization (2.501x10^{6} J kg^{-1}) when T_s = 0 °C or sublimation (2.835x10^{6} J kg^{-1}) when T_s < 0 °C, e_a is the atmospheric vapor pressure (Pa), e_s is the vapor pressure at the snow surface (Pa) which is estimated for ice surface when T_s < 0 °C or liquid water surface when T_s = 0 °C, and P_a is the atmospheric pressure (Pa).

Both bulk exchange coefficients for sensible and latent heat under neutral atmospheric conditions, C_n, was estimated using Equation 4.8 (Conway and Cullen, 2013).

$$C_n = \frac{k^2}{[ln(z_a/z_0)]^2} \qquad \text{Equation 4.8}$$

Where the von Karman constant k is 0.4, z_a is the height of the wind measurement from the snow surface and z_0 is the snow roughness. z_0 reported in the literature generally varies from 0.0002 m to 0.02 m for smooth to rough snowpack conditions (Dewalle and Rango, 2008). Some studies assumes scaler roughness lengths for snow surface , i.e., 1/10 th of the average height of roughness obstacles (Dewalle and Rango, 2008). However, given the sensitivity and uncertainity involved with this parameter for estimating turbulent fluxes (Armstrong and Brun, 2008), z_0 was assumed to be at 0.0005 m, which is similar to that used by Paquotte and Baraer (2021) in the same study area. In situations of non-neutral atmospheric conditions, C_n should be corrected according to the relevant atmospheric stability to obtain C_h and C_e. Atmospheric stability can generally be assessed by the Richardson number, R_{iB} (Oke, 1987; Boike et al., 2003; Mas et al., 2018).

$$R_{iB} = g\, z_a(T_a - T_s)/T_m u_a^2 \qquad \text{Equation 4.9}$$

Where g is the acceleration of gravity (9.8 m s^{-2}) and T_m is (T_a+ T_s)/2.

If the conditions are stable ($R_{iB} > 0$), the bulk exchange coefficient is (Boike et al., 2003; Price and Dunne, 1976):

$$C_e = C_h = \frac{C_n}{(1 + 10R_{iB})} \qquad \text{Equation 4.10}$$

and for unstable conditions:

$$C_e = C_h = C_n\,(1 - 10R_{iB}) \qquad \text{Equation 4.11}$$

As mentioned in section 4.3.1.4, a minimum of 0.3 m s^{-1} was imposed on u_a to avoid suppressing turbulent fluxes completely at low wind speeds (Martin and Lejeune, 1998). In addition, a sensitivity analysis was carried out for the turbulent flux calculation using four different wind threshold values, a windless coefficient, and two other stability correction methods to check the sensitivity of the residual energy balance,

$Q_M + \frac{dU}{dt}$, to the different calculation methods (Supplement Table S4.1 and Figure S4.3). Error statistics for the different methods did not vary considerably, except when including a windless coefficient (Supplement Table S4.2 and Table S4.3).

4.3.2.3 Rainfall Energy Flux

Heat flux due to rain-on-snow was calculated in two stages (Dewalle and Rango, 2008) as:

$$Q_R = Q_{r1} + Q_{r2} \qquad \text{Equation 4.12}$$

The first source of energy input by rain is the sensible heat brought to the snow surface and used to bring it to the freezing point, 0 °C:

$$Q_{r1} = P_r c_w \rho_w (T_r - 0) \qquad \text{Equation 4.13}$$

Where P_r is the rainfall intensity (m s^{-1}), c_w is the specific heat of liquid water (4187 J kg^{-1} °C^{-1}), ρ_w is the density of liquid water (1000 kg m^{-3}), T_r is the temperature of rain (°C), which is assumed to be equal to T_a in this study.

The second source of energy input is the release of latent heat of fusion when rain freezes on a subfreezing snowpack (< 0 °C).

$$Q_{r2} = P_r \rho_w L_f \qquad \text{Equation 4.14}$$

Where L_f is the latent heat of fusion (0.334x10^6 J kg^{-1}).

4.3.2.4 Snowfall Energy Flux

The sensible heat flux advected by snowfall was calculated as:

$$Q_{SF} = P_{SF} c_i \rho_w (T_{SF} - 0) \qquad \text{Equation 4.15}$$

Where P_{SF} is the snowfall intensity (m s^{-1}), c_i is the specific heat of ice (2100 J kg^{-1} °C^{-1}), ρ_w is the density of liquid water (1000 kg m^{-3}), T_{SF} is the temperature of snowfall (°C), which is assumed here to be equal to T_a.

4.3.2.5 Ground Heat Flux

The ground heat conduction to the base of the snowpack was be computed as (Dewalle and Rango, 2008):

$$Q_g = k_g \frac{dT_g}{dz} \approx \frac{k_g(T_{10} - T_0)}{\frac{10}{100}} \qquad \text{Equation 4.16}$$

Where k_g denotes the thermal conductivity of soil (W m^{-1} °C^{-1}), T_{10} is the temperature measured 10 cm below the ground surface, and T_0 is the temperature measured at the ground surface (base of the snowpack). We used the temperature gradient between the base of the snowpack and the 10 cm depth ($\frac{dT_g}{dz}$, °C m^{-1}) for the ground heat calculation, as it was observed from the measurements that the ground temperature did not fluctuate much below 10 cm. k_g generally varies with the moisture and organic matter content of the soil, typically between 0.2 and 2.2 W m^{-1} °C^{-1} (Oke, 1987). In this study, k_g was calculated using the porosity (φ) of the soil at each site. The maximum measured volumetric water content in the spring was used to estimate the soil porosity, assuming the pores were saturated by the beginning of spring with snowmelt. Then, by taking a typical thermal conductivity of the dry soil (k_{dry}) for each site (Oke, 1987) and ice ($k_{ice} = 2.24$) , k_g is given by:

$$k_g = k_{dry}(1 - \varphi) + k_{ice}\varphi \qquad \text{Equation 4.17}$$

Table 4.2 shows the k_g values obtained using respective φ and k_{dry} values at each site. Soil types at each site were obtained from the Institute for Agri-Environments (IRDA).

Table 4.2. Soil types, parameters, and thermal conductivity of soil (k_g) at each site

	Open	Gap	Forest
Soil type	Clay	Sandy loam	Sandy loam
φ	0.40	0.45	0.45
k_{dry} (W m^{-1} °C^{-1})	0.25	0.30	0.30
k_g (W m^{-1} °C^{-1})	1.05	1.17	1.17

4.3.2.6 Residual Energy Flux

The residual energy flux, or net energy balance, is a combination of melt energy (Q_M) and change of internal energy (cold content) of the snowpack $\left(\frac{dU}{dt}\right)$. Q_M is equal to 0 when the right hand side of the energy balance equation (Equation 4.5) is negative (snowpack cooling). Otherwise, $Q_M + \frac{dU}{dt}$ is equal to the right member of the energy balance equation, whose value represents the minimum melt estimate, i.e., snowpack melting given that the available energy is large enough to eliminate the cold content and induce melt, else only warming of the snowpack occurs. $\frac{dU}{dt}$ was not calculated separately in this study due to the absence of continuous snow pit or SWE measurements and the high uncertainty involved with the calculation process (Dewalle and Rango, 2008; Helgason and Pomeroy, 2012a; Jennings et al., 2018a). More often, $\frac{dU}{dt}$ is modeled with a multilayer snowpack assumption (Conway et al., 2018; Helgason and Pomeroy, 2012a; Jennings et al., 2018a; Parajuli et al., 2021). However, by keeping $\frac{dU}{dt}$ at the left side of Equation 4.5, we are still able to explain the different snowpack behaviors observed at each site by the changes of the right members of the energy balance equation.

4.3.3 Blowing Snow Analysis at Open Site

Mean hourly blowing snow fluxes measured by the two FlowCapt sensors (measurements along the height 0–1 m and 1–2 m) were summed and analyzed from mid-January 2021 to March 2021 when a stable snow cover was present and before significant snowmelt began at the study site (Accumulation period in Figure 4.2). For the analysis, snow flux measurements higher than the lower detection limit of the FlowCapt (0.002 g m^{-2} s^{-1} considering both sensors) were considered as blowing snow events. First, we examined and analyzed the general trends/observations in blowing snow measurements. Blowing snow events with and without concurrent snowfall were compared against hourly meteorological measurements such as wind speed, air temperature, and relative humidity to assess the relationship between blowing snow events and meteorological conditions. Then, we examined the weather conditions associated with the blowing snow events and the thermodynamic feedback effects of blowing snow on energy balance in the open under snowfall-free conditions. The former was investigated by comparing relative humidity, air temperature, atmospheric pressure, wind speed, and wind direction between blowing snow and no-blowing snow events in the open. The latter was achieved by comparing the changes in energy fluxes and associated meteorological parameters between the open and gap sites during blowing snow and no-blowing snow time steps recorded by the FlowCapt. Given the proximity of the sites, the weather conditions triggering blowing snow fluxes would have similar influences on these differences between open and gap, and hence are expected to reflect the feedback effect of blowing snow on energy fluxes and associated meteorological variables at the open site. We specifically tested the hypothesis that blowing snow events under snowfall-free conditions modify the snowpack latent heat and sensible heat exchanges calculated by the bulk aerodynamic method, which was shown by previous modeling studies (e.g., Déry et al., 1998; Le Toumelin et al., 2021; Vionnet et al., 2014). Radiative feedbacks were also investigated for incoming longwave radiation but not for incoming shortwave radiation, as the reference gap site is largely shaded by surrounding trees which precludes meaningful comparisons with the open site using hourly data. Absolute (AE) and relative (RE) effects of blowing snow on these fluxes and associated meteorological variables were calculated as follows.

$$AE = \overline{(open - gap)_{BS}} - \overline{(open - gap)_{No\ BS}} \qquad \text{Equation 4.18}$$

Where $\overline{(open - gap)_{BS}}$ indicates the mean difference between open and gap measurements during blowing snow periods and $\overline{(open - gap)_{No\ BS}}$ indicates the mean difference between open and gap measurements during no-blowing snow periods. AE should be near zero if blowing snow has no thermodynamic impacts at the open site.

$$RE = (AE/(\overline{open_{BS}} - AE)) * 100 \qquad \text{Equation 4.19}$$

Where $\overline{open_{BS}}$ indicates the mean observed meteorological variable or energy flux during blowing snow periods.

4.4 Results

4.4.1 Measured Meteorological Variables

During the observation period, the highest maximum snow depth of 0.68 m was found in the gap, and the lowest maximum snow depth of 0.52 m was found in the open site, with an intermediate snow depth of 0.60 m being found in the forest site (Figure 4.2a). Similarly, the highest average snow depth was observed in the gap (0.27 m), lowest in the open (0.19 m), and intermediate in the forest (0.22 m). The snowpack disappeared on the same date (26/03/2021) in the open and forest and lasted longer in the gap (29/03/2021). Based on the evolution of the snow depth, the study period could be characterized into three periods: a first “Early winter period” from December to mid-

January when the snowpack is thin (<10 cm) and transient, a second “Accumulation period” from mid-January to February 28th (starting date of ablation) when the snowpack is thickening, and a third “Ablation period” from February 28th onward with sustained ablation of the snowpack. High air temperature throughout the winter at the forest site compared to the gap and open sites indicates a comparatively warmer climate in the forest (Figure 4.2b). The mean air temperature was –3.3 °C at the open site, –3.0 °C in the gap, and –1.9 °C in the forest throughout the observation period. The mean snowpack temperature shows a substantial variation in the open compared to the forest and gap (Figure 4.2c). The snowpack at the open site was the coldest among the sites, the forest snowpack the warmest, and the gap snowpack falling in between. Similarly, the ground surface (snowpack base) temperature was colder and more variable at the open site, compared to the forest site while the gap showed an intermediate behavior (Figure 4.2d). The ground surface temperature at the forest and gap sites displayed freezing events in early winter, while a prolonged zero-curtain effect (near-zero temperature) is observed during the accumulation and ablation period. The open site stands out with a near-continuous frozen state throughout winter. Significant rainfall events are observed in the early winter and ablation periods, but not in the accumulation period (Figure 4.2e). Specific humidity did not vary much between the sites indicating almost similar moisture contents in all the sites (Figure 4.2f). Wind speed was substantially higher in the open compared to forest and gap. Being sheltered by trees, the forest shows the lowest wind speeds during the study period (Figure 4.2g).

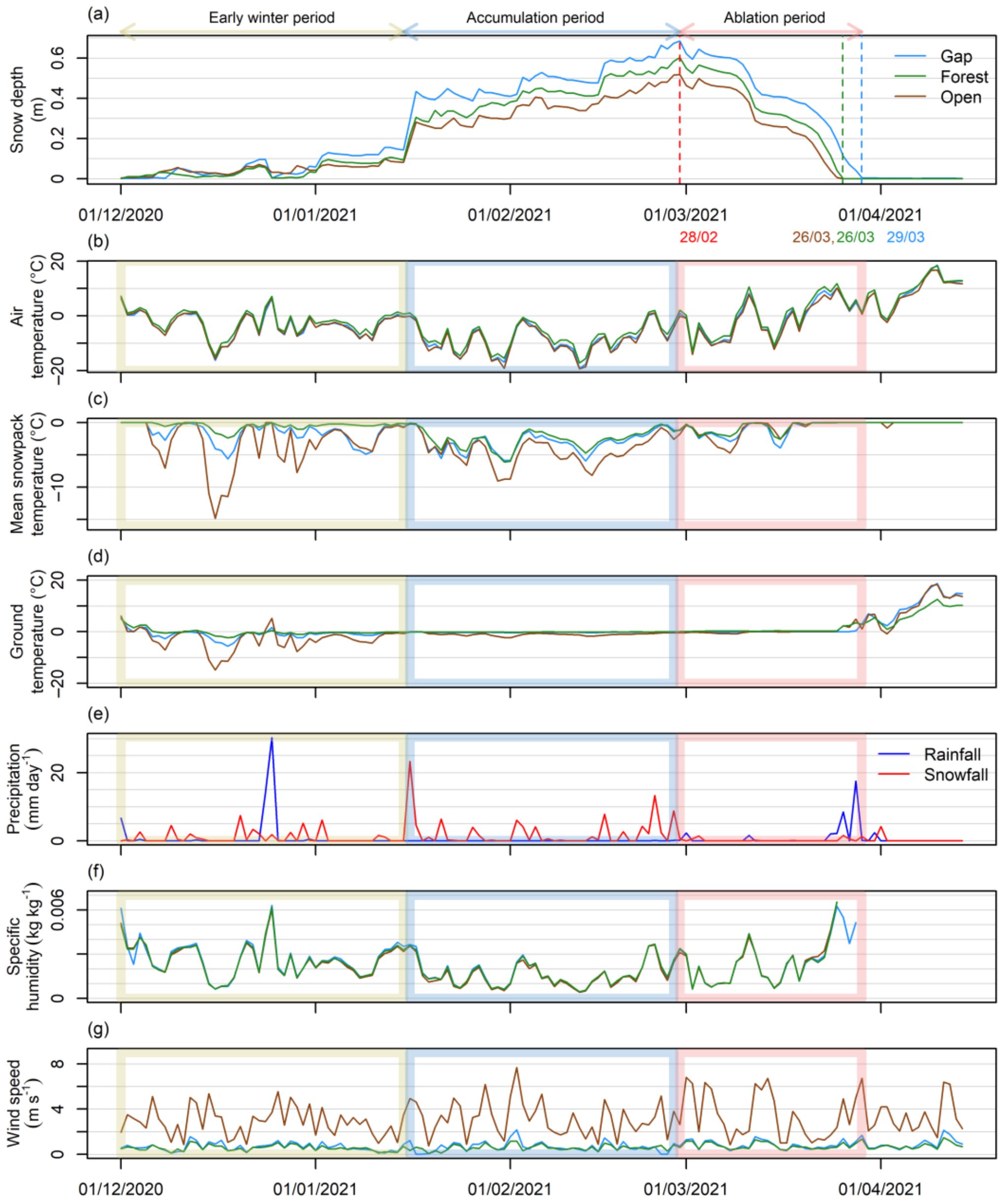

Figure 4.2. Meteorological conditions and snowpack characteristics at the three study sites during winter 2020–2021 with a) daily snow depth, with the start (red) and end (brown, blue, green) of the ablation period indicated by stippled vertical lines and corresponding dates; b) daily air temperature; c) daily mean snowpack temperature; d) daily ground (snowpack base) temperature; e) snowfall and rainfall; f) specific humidity; and g) wind speed. Early winter, accumulation, and ablation periods are demarcated by yellow, blue, and red colors and are further explained in the text.

With the absence of SWE data, snowpack evolution was analyzed using the changes in snow depth. During the ablation period, negative snow depths estimated using the measured snow depths were used to compare the snowpack evolution between the sites (Figure 4.3). Despite having a considerable difference in snow depths (Figure 4.2a), almost similar negative snow depth changes were observed between the sites (Figure 4.3).

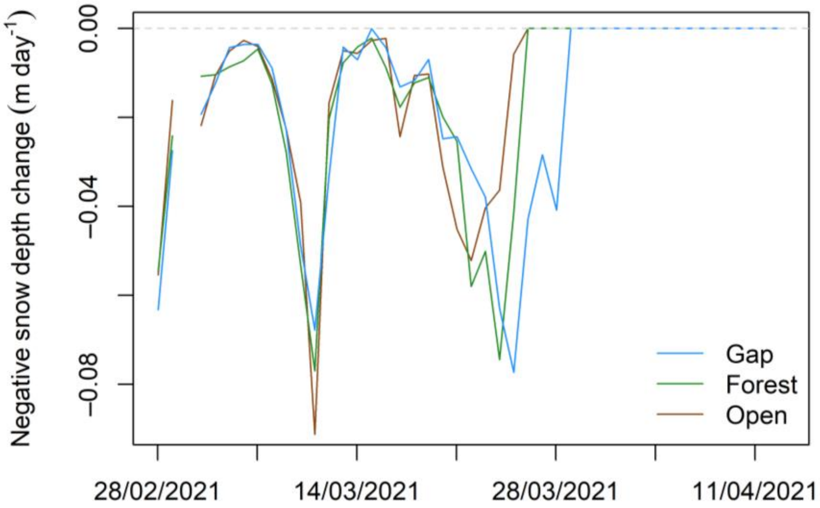

Figure 4.3. Negative snow depth changes in the three sites

4.4.2 Energy balance components

The weekly variation of energy flux components and associated mean energy fluxes are portrayed in Figure 4.4 and Table 4.3 for the early winter, accumulation, and ablation periods between the sites. Table 4.4 shows the partial correlation coefficient values between energy terms and the residual energy flux, or net energy balance ($Q_M + \frac{dU}{dt}$). In Figure 4.4, the energy balance components were plotted by moving all the energy terms to the right side of Equation 4.5, so that the sum of all terms is zero. In other words, when the right-hand side of Equation 4.5 is negative, the plotted $Q_M + \frac{dU}{dt}$

(grey color bar) is positive and vice versa. Therefore, in Figure 4.4, a positive $Q_M + \frac{dU}{dt}$ indicates the accumulation of a cold content (heat loss) in the snowpack. Conversely, a negative $Q_M + \frac{dU}{dt}$ indicates an energy surplus and snowmelt, except at subfreezing temperatures, then the excess energy should indicate a warming of the snowpack.

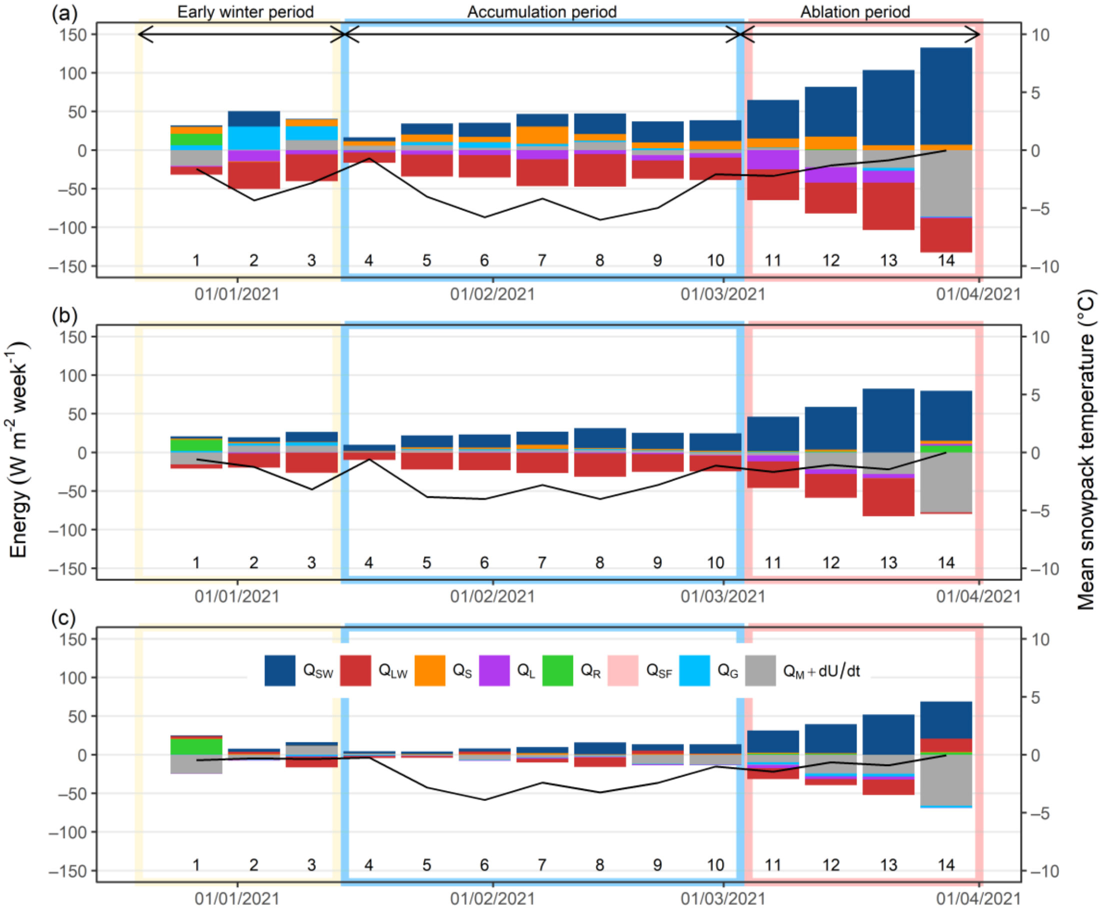

Figure 4.4. Mean weekly variation of energy fluxes and mean snowpack temperatures (black lines) at the three study sites: a) open; b) gap; c) forest

Table 4.3. Mean values and standard deviation of the energy balance components, and their contribution (%) for the total energy budget in the three periods. Q_{SW}: Mean net shortwave radiation, Q_{LW}: Mean net longwave radiation, Q_S: Mean sensible heat flux, Q_L: Mean latent heat flux, Q_R: Mean rainfall energy flux, Q_{SF}: Mean snowfall energy

flux, Q_G: Mean ground heat flux, and Q_M+dU/dt: Mean net energy balance.

	Open		Gap		Forest	
	W m^{-2}	% of total energy budget[1]	W m^{-2}	% of total energy budget[1]	W m^{-2}	% of total energy budget[1]
Early winter period						
Q_{SW}	5.72 ± 9.51	9.1	5.72 ±.16 5.24	17.9	3.04 ± 2.03	14.7
Q_{LW}	–24.11 ± 12.63	38.5	–15.44 ± 8.87	48.3	–2.47 ± 9.90	11.9
Mean net radiation	*–18.39 ± 10.98*	*47.7*	*–9.72 ± 5.21*	*66.2*	*0.57 ± 8.69*	*26.6*
Q_S	6.28 ± 4.84	10.0	1.07 ± 0.47	3.3	0.64 ± 0.17	3.1
Q_L	–6.53 ± 5.49	10.4	–0.47 ± 0.36	1.5	–0.46 ± 0.27	2.2
Q_R	3.71 ± 7.41	5.9	3.58 ± 7.16	11.2	6.66 ± 11.54	32.2
Q_{SF}	–0. 09 ± 0.14	0.1	–0.07 ± 0.09	0.2	–0.13 ± 0.16	0.7
Q_G	15.57 ± 10.84	24.9	3.04 ± 0.84	9.5	–0.98 ± 0.99	4.7
Q_M+dU/dt	0.54 ± 14.06		–2.57 ± 11.97		6.30 ± 17.95	
Accumulation period						
Q_{SW}	19.18 ± 8.23	27.3	17.98 ± 5.86	39.4	7.72 ± 4.73	44.7
Q_{LW}	–28.59 ± 8.97	40.7	–21.95 ± 6.27	48.1	–2.08 ± 5.64	12.1
Mean net radiation	*–9.41 ± 7.86*	*68.1*	*–3.97 ± 3.57*	*87.5*	*5.63 ± 5.29*	*56.8*
Q_S	10.28 ± 5.63	14.7	2.26 ± 1.63	5.0	0.91 ± 0.51	5.3
Q_L	–6.36 ± 2.72	9.1	–0.70 ± 0.78	1.5	–0.62 ± 0.32	3.6
Q_R	0.00 ± 0.00	0.0	0.00 ± 0.00	0.0	0.00 ± 0.00	0.0
Q_{SF}	–0.15 ± 0.09	0.2	–0.16 ± 0.09	0.3	–0.10 ± 0.12	0.6
Q_G	2.75 ± 2.54	3.9	1.02 ± 0.42	2.2	–0.61 ± 0.37	3.5
Q_M+dU/dt	–2.88 ± 5.93		–1.54 ± 2.33		5.23 ± 5.37	
Ablation period						
Q_{SW}	84.41 ± 34.00	44.4	61.70 ± 16.20	46.7	41.57 ± 10.57	47.7
Q_{LW}	–46.41 ± 10.21	24.4	–29.13 ± 19.54	22.1	–6.08 ± 16.29	7.0
Mean net radiation	*37.99 ± 30.85*	*68.9*	*32.57 ± 22.31*	*68.8*	*35.49 ± 21.39*	*54.6*
Q_S	10.31 ± 4.84	5.4	1.74 ± 1.97	1.3	0.72 ± 0.66	0.8
Q_L	–15.35 ± 10.20	8.1	–4.21 ± 4.49	3.2	–3.03 ± 2.02	3.5
Q_R	0.23 ± 0.43	0.1	2.51 ± 4.10	1.9	1.30 ± 1.20	1.5
Q_{SF}	–0.01 ± 0.03	0.0	–0.01 ± 0.04	0.0	–0.01 ± 0.03	0.0
Q_G	–1.02 ± 1.96	0.5	0.09 ± 0.33	0.1	–3.30 ± 0.42	3.8
Q_M+dU/dt	32.14 ± 37.80		32.69 ± 31.54		31.17 ± 24.32	

[1] The % contribution of each energy flux to the total energy budget was calculated by dividing the absolute value of the energy flux by the sum of the absolute value of all the energy fluxes. Net radiation is the sum of shortwave and longwave radiation.

Table 4.4. Partial correlation coefficients between individual energy terms and net energy balance (Q_M+dU/dt). EW = Early winter period, Acc. = Accumulation period, and Abl. = Ablation period.

	Open			Gap			Forest		
	EW	Acc.	Abl.	EW	Acc.	Abl.	EW	Acc.	Abl.
Q_{SW}	0.57	0.81	0.75	0.78	0.86	0.62	0.72	0.80	0.75
Q_{LW}	0.59	0.92	0.75	0.95	0.93	0.42	0.96	0.93	0.68
Q_S	–0.08	0.62	0.71	0.50	0.48	0.28	–0.49	0.22	0.38
Q_L	0.37	0.44	0.85	0.20	0.21	0.77	0.22	0.22	0.69
Q_R	0.24	0.43	0.28	–0.42	0.07	0.22	0.32	0.28	0.55
Q_{SF}	–0.12	0.34	0.42	–0.53	0.13	0.26	–0.52	0.31	0.03
Q_G	0.49	0.67	–0.30	0.45	0.15	–0.11	0.70	–0.13	–0.13

During the entire winter period, energy exchanges were highest in the open and lowest in the forest (Table 4.3). Similarly, the weekly variation of the energy fluxes was most pronounced in the open and more subdued in the forest (Figure 4.4). The gap site displayed an intermediate amount and variation of the weekly energy fluxes (Figure 4.4 and Table 4.3). The partitioning of the energy flux components between the sites during the three periods is of particular interest and is presented in the subsequent sections.

4.4.2.1 *Early Winter Period*

Throughout the early winter period, net longwave radiation was the most important energy flux in open and gap (with an average contribution of 38.5 % and 48.3 % at the open and gap respectively, from Table 4.3). Sensible heat fluxes were always positive except for week 2, during which it was slightly negative at the open. Latent heat fluxes were always negative at all sites. Snowpacks at all sites received a negligible amount of energy from rainfall, except during week 1 as a result of the 30 mm rainfall event that occurred in the early winter period (see Figure 4.2e). Energy advected due to snowfall was insignificant at all sites. Nevertheless, the most striking difference in energy fluxes during the early winter period compared to the later periods is the significant ground heat fluxes at all sites (4.7–24.9 %), though more pronounced at the open and gap (Figure 4.4 and Table 4.3). The net energy balance at all sites was generally negative (positive bar in Figure 4.4), hence reflecting cooling of the snowpack. The highest partial correlation coefficient between individual fluxes and the net energy balance at all sites was for net longwave radiation (Table 4.4). This indicates that the most significant control of the net energy balance came from longwave radiation. However, the application of the energy balance equation in the early winter period when the snowpack is thin (less than 10 cm), comes with some limitations and a higher degree of uncertainty, which will be commented in the discussion section.

4.4.2.2 Accumulation Period

Net radiation (both shortwave and longwave components) was the most important energy balance component at all sites, while turbulent fluxes (sensible and latent components) were only substantial at the open site (Figure 4.4 and Table 4.3). During the study period, the net radiation component accounted for 68.1 %, 87.5 %, and 56.8 % of the total energy budget in the open, gap, and forest respectively (Table 4.3). Turbulent flux contributions to the energy budget were 23.7 %, 6.5 %, and 8.9 % in the open, gap, and forest respectively. Net radiation was negative at the open and gap, but positive in the forest (both weekly and on average). As seen in Figure 4.4, negative net radiations at open and gap were often associated with smaller positive net shortwave and larger negative net longwave radiations throughout the accumulation period whereas, at the forest, positive net radiations were associated with slightly larger net shortwave radiations and smaller negative or sometimes even positive (in weeks 6 and 9) net longwave radiations. At all sites, although more prominent at open, sensible heat fluxes were always positive, and latent heat fluxes always negative. The ground heat flux and the energy advected by precipitation (both rainfall and snowfall) were negligible throughout the accumulation period. The net energy balance was negative (positive bar in Figure 4.4) throughout the accumulation period at the open and gap indicating cooling of the snowpack, but became positive during the last two weeks of the period (weeks 9 and 10). In contrast, the net energy balance was slightly positive (negative bar in Figure 4.4) throughout the accumulation period in the forest, indicating warming/and or melting of the snowpack. Similar to the early winter period, the net longwave radiation exerted the greatest control on the net energy balance (Table 4.4).

4.4.2.3 Ablation Period

The transition from the accumulation to the ablation period was accompanied by a clear increase in net shortwave radiation at all sites (Figure 4.4 and Table 4.3). Net radiation remained positive throughout the ablation period. Sensible heat fluxes were still positive, indicating an energy source for snowpacks at all sites. There was an increase in latent heat fluxes during the ablation period at all sites. However, net radiation still had the highest contribution to the total energy budget (68.9 % at open, 68.8 % at gap, and 54.6 % at forest). There was negligible ground heat flux and energy advected by precipitation (both rainfall and snowfall) at all sites. However, the forest snowpack shows a comparatively higher ground heat transfer from the snowpack base to the ground compared to the other two sites throughout the ablation period (Figure 4.4c). The net energy balance was generally positive (negative bars in Figure 4.4) at all sites, indicating a warm and melting snowpack. In the forest, net longwave radiation also contributed to snowmelt in week 14. However, latent heat fluxes had the greatest control over the net energy balance at the sites, except in the forest, where shortwave radiation correlated slightly better with the net energy balance (Table 4.4).

4.4.3 Blowing Snow

Hourly blowing snow measurements varied from 0.002–8.6 g m^{-2} s^{-1} in the accumulation period (presented on a log-scale for better interpretability in Figure 4.5). Most events with concurrent snowfall had higher intensity fluxes (Figure 4.5a–c) while most events under snowfall-free conditions are clustered in low-intensity snow fluxes, except for a few events (Figure 4.5d–f). Irrespective of snowfall or snowfall-free conditions, the intensity of blowing snow fluxes increases with increasing wind speeds (Figure 4.5a and d). The relationship is more linear for snowfall events (Figure 4.5a), which may reflect the fact that a large part of the blown snow comes from snowfall, whose flux would increase proportionally with wind speed. In contrast, under snowfall free conditions, higher fluxes only begin above wind speeds of 4 m s^{-1}, whereas the blowing snow flux measurements below this wind speed are very small in magnitude. No simple relationships emerge between blowing snow fluxes and air temperature and humidity. However most blowing snow events, especially the high-intensity ones, appear to occur between –10 °C and 0 °C (Figure 4.5b and e), while both the frequency and intensity of blowing snow fluxes tend to increase with increasing relative humidity (Figure 4.5c and f). Of all the hourly blowing snow events, 75 % occurred during snowfall-free conditions. Blowing snow with concurrent snowfall does not show a clear trend towards either increase (deposition) or decrease (erosion) in snow depth measured by SR50. However, in contrast to expected erosion, deposition (increasing snow depth) predominated over erosion at the AWS location for high-intensity blowing snow fluxes under snowfall-free conditions. As such, at the end of the study period, snow depth showed a net gain of 0.16 m (total gain of 0.99 m and total loss of 0.83 m from the AWS snow depth measurements) at the AWS location due to blowing snow fluxes under snowfall-free conditions. This corresponds to 29 % of the maximum hourly snow depth of 0.55 m during the study period.

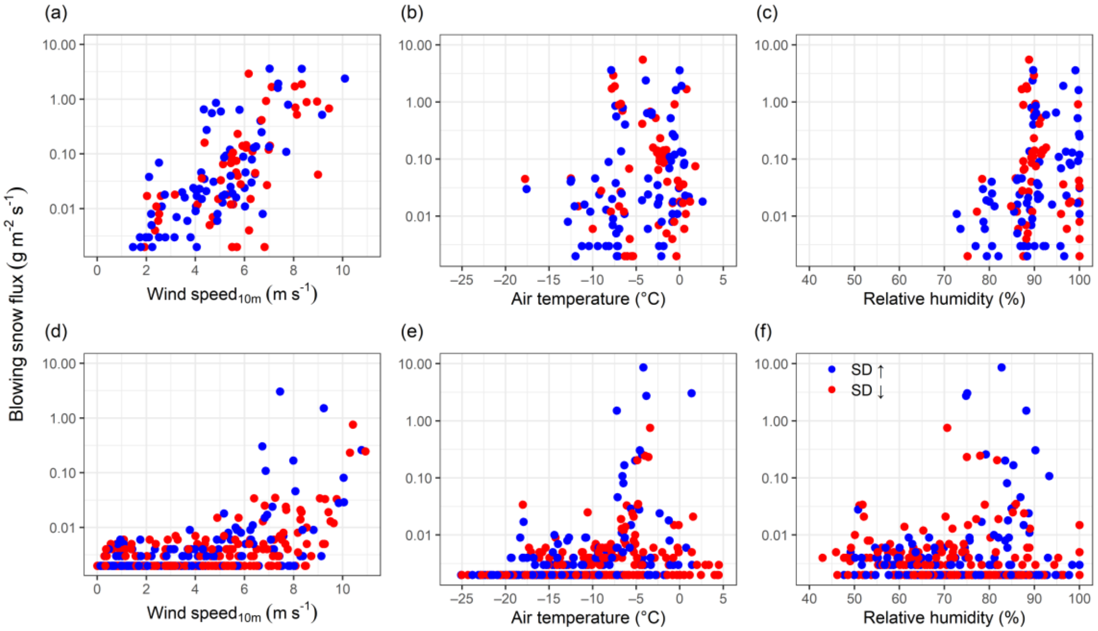

Figure 4.5. Relationship between hourly blowing snow fluxes and meteorological conditions. Blue (red) dots indicate events with an increase (decrease) in snow depth recorded by SR50. Top row: events with concurrent snowfall; bottom row; snowfall-free conditions. a, d) wind speed at 10 m height from snow surface (extrapolated using wind logarithmic profile); b, e) air temperature; c, f) relative humidity. All y-axes are displayed in log scale for better visibility of the data distribution.

4.4.3.1 Weather Conditions Associated with Blowing Snow Events

Blowing snow fluxes under snowfall-free conditions occurred during periods with colder air temperature and lower relative humidity (Figure 4.6a, b), and higher atmospheric pressure and wind speed (Figure 4.6c, d) compared to periods with no blowing snow fluxes. Wind directions were generally similar in both scenarios, i.e., predominantly from the West (Figure 4.6e).

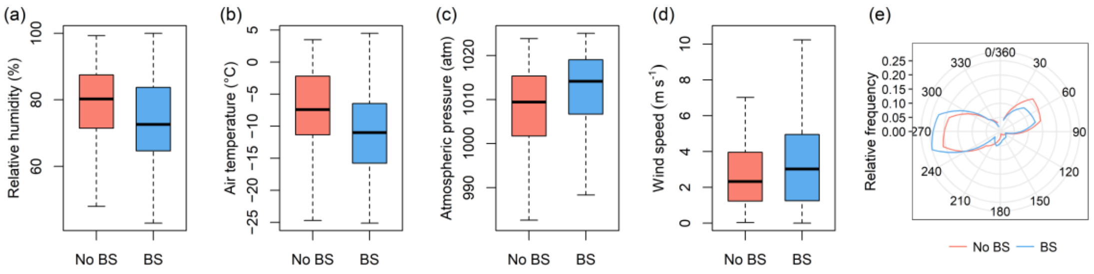

Figure 4.6. Meteorological conditions during no-blowing snow (red) versus blowing snow (blue) under snowfall-free conditions. a) relative humidity; b) air temperature; c) atmospheric pressure; d) wind speed; e) relative frequency of wind direction in 30-degree bins.

4.4.3.2 Feedback Effects of Blowing Snow on Energy Balance

Nonparametric Wilcoxon rank-sum test (Wilcoxon, 1945) showed that the difference between no bowing snow (No BS) and blowing snow (BS) were statistically significant, reflecting the feedback effects of blowing snow on meteorological variables and energy fluxes in the open site. Compared to no-blowing snow periods, blowing snow periods under snowfall-free conditions show higher snowpack latent heat losses (more negative Q_L, Figure 4.7a), lower sensible heat gains (less positive Q_S, Figure 4.7b), and a decrease in incoming longwave radiation (Q_{LWin}, Figure 4.7c). Increased relative humidity (Figure 4.7d) and air vapor pressure (e_a, Figure 4.7e), a cooling of air temperature (T_a, Figure 4.7f), an increase in wind speed (Figure 4.7g), and a decrease in vapor pressure difference (e_a-e_s, Figure 4.7h) and temperature difference (T_a-T_s, Figure 4.7i) are also observed in the open relative to gap. Both latent and sensible heat fluxes are higher in the open than in the gap and are on average negative and positive, respectively (Figure 4.4, Table 4.3, and Supplement Figure S4.4). Hence, the negative increase in Δ latent heat flux and decrease in Δ sensible heat flux in Figure 4.7 suggest that snowpack latent heat losses are accentuated, and sensible heat gains attenuated, in the open during blowing snow periods. On average, incoming longwave radiation, relative humidity, and air vapor pressure are higher in the gap than that in open (Supplement Figure S4.4 and negative averages in Figure 4.7c, d, and e). Therefore, the negative increase in Δ incoming longwave radiation indicates reduced incoming longwave radiation in the open during blowing snow events. Similarly, the negative decreases in Δ relative humidity and Δ air vapor pressure suggest that blowing snow results in an increase in relative humidity and air vapor pressure in the open. This increase in vapor pressure is driving a reduction of the vapor pressure difference between the air and snowpack (i.e., less negative e_a-e_s). The vapor pressure difference is mostly positive in the gap and negative in the open (Supplement Figure S4.4). While air temperature is slightly cooler in the open than in the gap during no-blowing snow conditions (Supplement Figure S4.4), this difference accentuates during blowing snow, indicating a cooling effect of blowing snow in the open. The temperature difference between the air and snowpack is mostly positive in open and gap (thereby driving positive sensible heat fluxes, Supplement Figure S4.4). Hence the cooling effect of blowing snow sublimation results in a reduced positive temperature gradient in the open. The increase in Δ wind speed shows that wind speeds increase more in the open than at the gap during blowing snow events, due to the sheltered conditions at the gap (Figure 4.2g and Supplement Figure S4.4).

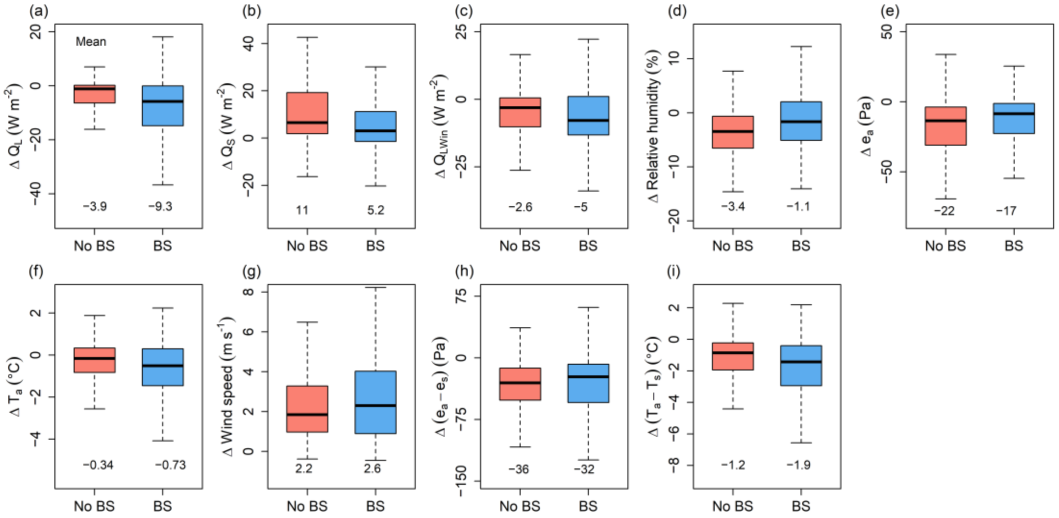

Figure 4.7. Feedback effects of blowing snow in terms of the difference between open and gap in a) latent heat flux; b) sensible heat flux; c) incoming longwave radiation; d) relative humidity; e) air vapor pressure; f) air temperature; g) wind speed; h) vapor

pressure difference between air and snowpack surface; i) temperature difference between air and snowpack surface. Mean differences are reported in each panel.

To discard the effect of the notable different wind regimes between the open and gap on snowpack latent and sensible heat fluxes, the latent and sensible heat fluxes at the gap were recalculated using wind speed at the open. Under the same wind regime, and despite the reduced vapor pressure gradient (Figure 4.7h) the snowpack latent fluxes were still slightly greater (more negative) in the open during blowing snow periods compared to no-blowing snow periods (Figure 4.8a). The sensible heat gains were still lower during blowing snow (Figure 4.8b, Supplement Figure S4.5), in accordance with the reduced positive temperature gradient in the open (Figure 4.7i). To further investigate the other possible causes for the altered latent and sensible heat fluxes due to blowing snow, we also compared changes in air stability (Richardson number R_{iB}: Figure 4.8c), bulk exchange coefficient (C_e: Figure 4.8d), and air density and atmospheric pressure between open and gap as these fluxes also depend on these factors (Equation 4.6, 4.7) (Table 4.5). Results show that blowing snow resulted in an average 4 % increase in snowpack latent heat loss, 42 % decrease in sensible heat gain, 47 % decrease in air stability (R_{iB}), 23 % increase in C_e, 8 % decrease in vapor pressure gradient, and 33 % decrease in temperature gradient due to blowing snow fluxes (Table 4.5). Changes in air density and atmospheric pressure due to blowing snow were negligible (Table 4.5), hence not presented in Figure 4.8.

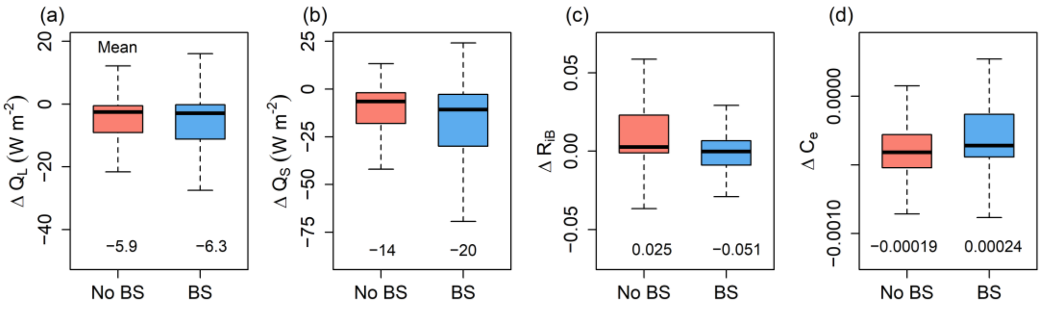

Figure 4.8. Under open wind speeds, differences between the open and gap in a) latent

heat flux; b) sensible heat flux; c) Richardson number; d) bulk exchange coefficient. Mean differences are reported in each panel.

Table 4.5. Absolute and relative effects of blowing snow on meteorological conditions and associated energy fluxes

Energy flux/variable	Absolute effect	Relative effect (%)
Q_L (W m^{-2})	–0.40 (W m^{-2})	4
Q_S (W m^{-2})	–6.00 (W m^{-2})	–42
R_{iB}	–0.08 (-)	–47
C_e	0.0004 (-)	23
e_a-e_s (Pa)	4.00 (Pa)	–8
T_a-T_s (°C)	–0.70 (°C)	–33
Air density (kg m^{-3})	0.0006 (kg m^{-3})	0.04
Atmospheric pressure (Pa)	0.00 (Pa)	0

4.5 Discussion

4.5.1 Snowpack Behavior Between Sites

The variation and evolution of the snow depth substantially differed between the sites over the study winter. The snowpack at the gap is characterized by comparatively higher snow depths and later snow disappearance date, which is in contrast to what Pomeroy and Granger (1997) observed in a clear-cut in Saskatchewan, Canada. However, the size of the gap plays an important role in snow accumulation and ablation in a gap, compared to the adjacent forest (Golding and Swanson, 1986; Pomeroy et al., 2002). Large gaps that are exposed to wind erosion reduce the overall snow accumulation compared to small gaps sheltered by trees, while small gaps (2–5 times the tree height diameter) are expected to accumulate a larger amount of snow (Pomeroy and Gray, 1994; Pomeroy et al., 2002; Swanson, 1988; Troendle and Leaf, 1980; Woods et al., 2006; Ellis et al., 2013). Similarly, our gap site, with a size of approximately 2–3 times the typical tree height in the adjacent forest (13 m), accumulated more snow, due to sheltering from the wind (Figure 4.2g). Conversely, the snowpack at the open site had lower snow depths and an earlier snow disappearance date. Although forest snow depths were consistently higher than that at the open site, the snow disappearance date was the same for both sites. The comparison of the snow depth variation with wind speed (Figure 4.2a and g) suggests that the higher wind speeds played a significant role in shaping the snowpack at the open site. For instance, higher wind speeds generally promote snow erosion, higher sublimation losses due to increased latent heat fluxes (Figure 4.6 and 4.7), and densification of snow by wind compaction (Jenicek et al., 2017; Mott et al., 2018; Pomeroy and Gray, 1995; Pomeroy et al., 1998a; Vionnet et al., 2013). This resulted in lower snow depths at the open site. Although snow pit measurements were unfortunately not available in the study year due to logistical reasons, snow pits measurements carried out in early February 2020 reported a density of 440 kg m^{-3} in the open site with a ~10 cm basal ice layer, and a density of 300 kg m^{-3} in the forest with no visible basal ice layers. These measurements suggest the mechanisms described above were present during the winter of 2020. In contrast, the dampened wind speeds in the forest and the gap (Figure 4.2g) would have suppressed blowing snow transport and wind compaction. The comparatively lower snow depths in the forest compared to the gap could be due to the canopy interception losses in the forest. Reba et al.(2012) previously observed similar patterns in air temperature and wind speed in open versus sheltered environments in mountainous environment in western USA, i.e., comparatively colder air temperatures and higher wind speeds over open snowpack. Our results show that large differences in energy transfers occurred whether the ground was fully or partially snow-covered at all the sites. The subsequent sections discuss in detail the difference in this energy partitioning between the sites during the three main periods of the winter: early winter, accumulation, and ablation.

4.5.1.1 Early Winter Period

The early winter period was characterized by a patchy snowpack less than 10 cm deep at all sites. The more variable mean snowpack temperatures in the open and comparatively steady variation in the gap, and even more in the forest, (Figure 4.2c) is reflected by similar variations of energy fluxes at the sites (Figure 4.4). Indeed, the more variable energy fluxes in the open resulted in more variable mean snowpack temperature, while steadier variations of energy fluxes in the forest resulted in more stable snowpack temperatures, with the gap site falling in between these two behaviors. Snowpack temperatures were more strongly correlated with air temperature under a thin snowpack, due to the reduced insulation, which is particularly prominent at the open site (Figure 4.2b). Although forest and gap ground surface temperatures showed some freezing events early in the winter, the prolonged near-zero temperatures afterward indicate that even a thin layer of snow (< 10 cm) was sufficient to insulate the ground from freezing at these sites, despite the cold air temperatures (Figure 4.2d). But in the open, more than 10 cm of snow layer was required to insulate the ground and stabilize its temperature. The energy partitioning shows a substantial ground heat influx received by the snowpack during early winter (Figure 4.4), which is more pronounced in the open and the gap. For instance, the highest ground heat flux was reported during week 2 in the open. During this week, the sensible heat flux did not compensate for the radiative cooling (negative net longwave radiation); heat transfer from the soil to the snowpack and net shortwave radiation compensated the radiative cooling in the open, whereas, in the forest and gap, ground heat influxes were insufficient to fill the energy deficit. However, estimating energy fluxes during the early winter period is associated with higher uncertainties. One of the uncertainties comes from the possibility of shortwave penetration through a thin snowpack (Armstrong and Brun, 2008; Dewalle and Rango, 2008; Helgason and Pomeroy, 2012a; Oke, 1987). Significant solar energy can penetrate up to 10 cm depth in the snowpack, and can even warm the underlying surface (e.g., soil), which can bias the temperatures measured within and below a thin snowpack (Armstrong and Brun, 2008; Oke, 1987). High absorption of shortwave radiation in the surface layers of the snowpack can also increase the snow surface temperature (Dewalle and Rango, 2008). For a snowpack less than 10 cm like in early winter in our study, this could cause erroneous snowpack temperature measurements due to warming by direct solar radiation and associated inaccurate energy estimates. Moreover, Pomeroy and Granger (1997) and Armstrong and Brun (2008) reported that in the presence of a patchy snowpack, the snowpack could receive energy by advection through the overlaying air mass as a result of the radiant energy absorbed by the ground patches. This turbulent transfer of energy would neither be detected by the energy balance instrumentation nor in bulk approach calculations. This implies the challenges in the application of the energy balance equation for patchy, thin snowpacks. Despite our effort to correct for a patchy snowpack by implementing the snow cover fraction approach and discarding energy estimates for very shallow daily snow depths (< 5 cm), the energy components calculated for the remaining days with thin snow depth (5–10 cm) might still suffer from these unaccounted processes.

4.5.1.2 Accumulation Period

Throughout the accumulation period the snowpack was stable (> 10 cm), and so were the ground surface (snowpack base) temperatures (Figure 4.2d). Snowpack base temperatures at gap and forest were consistently at 0 °C, indicating melting at the base, while temperatures at open were consistently lower than 0 °C most of the time. This suggests more frequent freezing at the base of the shallower snowpack and restricted infiltration in the open. A small ground heat influx received by the snowpack base throughout the accumulation period (Figure 4.4a) indicates that the snowpack base was consistently colder than the soil beneath in the open. More variable energy flux exchanges resulted in more variable mean snowpack temperatures at the open (Figure 4.4 and Figure 4.2c). In contrast, energy exchanges were more attenuated within the forest, which resulted in more stable snowpack temperatures than in the open, with the gap snowpack falling in between. Radiative cooling due to longwave radiation losses was highest in the open. This, and the consistent negative net energy balance (positive grey bars in Figure 4.4a) suggests a high cold content in the open, hence requiring more energy to warm the snowpack to 0 °C. Radiative cooling was lowest in the forest, and during weeks 6 and 9 the net longwave radiation even became an energy source for the forest snowpack (positive net longwave radiation in Figure 4.4c), indicating more incoming longwave radiation within the forest. This and the continuously positive net energy balance (negative grey bars in week 5–10 in Figure 4.4c) in the forest suggest much lower cold content for the forest snowpack, hence requiring less energy to trigger melting. The gap snowpack shows an intermediate behavior between the open and forest. It received and lost more energy than the forest, but less than the open hence requiring more energy than the forest and less energy than the open to bring the snowpack to 0 °C. The high correlation between net longwave radiation and the net energy balance (Table 4.4) suggests that radiative cooling was the most influential and crucial energy component during the accumulation period, i.e., determining how cold or warm the snowpack would be. Large temperature gradients between the atmosphere and snow surface and high wind speeds produced large sensible heat fluxes in the open that partly compensated for the radiative cooling during the accumulation period. The large negative latent heat fluxes suggest high sublimation rates at the open. Not surprisingly, dampened wind speeds suppressed the turbulent fluxes at the forest and gap. Similar observations in radiation and turbulent fluxes were previously reported in open versus forested environments (e.g., Pomeroy and Granger, 1997; Reba et al., 2012; Roth and Nolin, 2017).

Collectively, energy exchanges resulted in the coldest snowpack in the open, a comparatively warmer snowpack in the forest, and intermediate conditions at the gap, a conclusion also supported by the mean snowpack temperature variations (Figure 4.4 and Figure 4.2c).

4.5.1.3 Ablation Period

From the beginning of the ablation period, the noticeable increase in net shortwave radiation and latent heat fluxes as the ablation period progressed at all sites suggests the increasing importance of these energy components for snowpack melting. The decrease in cold content and the warming and melting of the snowpack are reflected by the decline of longwave radiation losses and the positive net energy balance (negative grey bars in Figure 4.4). In turn, the snowpack temperature gradually increased. The influence of net longwave radiation gradually diminished during the transition of the snowpack from the accumulation period to the ablation period and onward. However, during the last week of the ablation (week 14), net longwave radiation was positive in the forest, implying higher incoming longwave radiation within the forest, while it was slightly negative in the gap and markedly more negative in the open. Incoming longwave radiation is generally high within the forest due to longwave emittance by trees (Lundquist et al., 2013; Pomeroy and Granger, 1997). We hypothesize that the increase of incoming longwave radiation by the warming of trees and the decrease of outgoing longwave radiation due to the melting snowpack would be the reason for this positive net longwave radiation in week 14. Similar to the accumulation period, the sensible heat flux acted as an energy source during the ablation period. Latent heat fluxes were negative, implying a continuous sublimation flux. Many studies documented the importance of net radiation for snowmelt in clear-cuts and forests (Armstrong and Brun, 2008; Lundquist et al., 2013; Pomeroy and Granger, 1997). Several studies also showed that the contribution of turbulent fluxes becomes particularly important late in the melt period (Reba et al., 2012; Harder et al., 2017; Mott et al., 2011a; Mott et al., 2017). Despite the high contribution of net shortwave radiation to the energy budget, our results show that the correlation between net shortwave radiation and net energy balance was secondary to that of latent heat fluxes at the open and gap. However, the opposite occurred in the forest, where shortwave radiation acted as the primary factor driving net energy balance, while the latent heat flux was secondary. Collectively, this thus implies that it is the difference in both shortwave radiation and latent heat flux that governs the daily ablation between these sites. Another interesting finding in the ablation period is that despite the dissimilar snow depths and dissimilar energy budgets between open, forest, and gap sites, almost similar negative snow depth changes were observed (Figure 4.3).

4.5.2 Blowing Snow

Hourly blowing snow fluxes measured at our site (0.002–8.6 g m^{-2} s^{-1}) are rather small compared to the measurements made elsewhere with the FlowCapt sensor, e.g. in the Swiss and French Alps (up to 90 g m^{-2} s^{-1}: Lehning and Fierz, 2008; Trouvilliez et al., 2015), Indian Himalayas (up to 40 g m^{-2} s^{-1}: Das et al., 2012), Central Asia (up to 192 g m^{-2} s^{-1}: Zhang et al., 2022), the Arctic region (up to 200 g m^{-1} s^{-1}: Jaedicke, 2001), and in Antarctica (up to 1200 g m^{-2} s^{-1}: Amory, 2020; Trouvilliez et al., 2014). Despite its relatively small magnitude, blowing snow events under snowfall-free conditions at our open site still account for substantial changes in snow depth over the course of accumulation period (deposition of 0.99 m and erosion of 0.83 m), with a net snow depth gain of 0.16 m equal to 29 % of the peak winter snow depth at the AWS site. This highlights the significance of blowing snow fluxes in altering snow-mass in the open fields of agro-forested landscapes with a cold-continental climate type.

4.5.2.1 Weather Conditions Associated with Blowing Snow

Our analysis shows that at an hourly scale, blowing snow fluxes have a substantial and rapid impact on changing the snow depths and modifying the energy budget in the open. At our open site, the occurrence of blowing snow was found to be associated with cold dry air, elevated atmospheric pressure together with gusty weather, all typical of a passing cold front (Figure 4.6). Our analysis shows a shift from negligible to a substantial increase in blowing snow fluxes above ~4 m s^{-1} wind speed (Figure 4.5), which is in agreement with the threshold wind speed of 4–11 m s^{-1} found by Li and Pomeroy (1997) for dry snow transport in the Canadian prairies. They further noted that low temperatures produce snow covers with low cohesion and low transport threshold wind speeds which in turn increase the frequency of blowing snow events. Our blowing snow measurements in the open generally showed increasing blowing snow flux transport with increasing wind speeds and increasing relative humidity (Figure 4.5d-f) which is in agreement with previous findings in the Canadian prairies (Pomeroy and Gray, 1995; Pomeroy and Gray, 1994), but showed no correlation with air temperature. Our analysis shows that when sufficient snow is available on the ground, such as in the present case, the occurrence of blowing snow flux transport depends more on whether the snowpack is exposed to high wind speeds, low temperatures, and high relative humidity (Figure 4.5d-f) rather than to snowfall. However, the occurrence of blowing snow events can also be closely related to the state of the snowpack, such as surface layer density, snow grain shape and size, and surface hardness (Dewalle and Rango, 2008; Doorschot et al., 2004; Mott et al., 2018; Vionnet et al., 2014), which were not measured in this study.

4.5.2.2 Feedback Effects of Blowing Snow

Similar to previous studies (Barral et al., 2014; Bintanja, 2001a; Déry et al., 1998; Groot Zwaaftink et al., 2011; Le Toumelin et al., 2021; Vionnet et al., 2014; Yang et al., 2010) our analysis demonstrates thermodynamic feedback effects of blowing snow -wetting and cooling of the air above the snowpack due to blowing snow sublimation- which led to increased relative humidity, decreased vapor pressure gradient, and colder air temperature (Figure 4.7). However, contrary to the aforementioned studies and the negative feedback observed on the vapor pressure gradient, the snowpack latent heat losses (surface sublimation) estimated by the bulk aerodynamic method still increased slightly during blowing snow events under no snowfall, even after correcting for the differences in wind speed between the two sites (Figure 4.8). This happened because the cooling effect of blowing snow decreased the temperature gradient between the atmosphere and the snow surface, thereby decreasing air stability (R_{iB}). This led to an increase in the latent heat transfer coefficient (C_e: 23 %) which surpassed the decrease in vapor pressure gradient (–8 %) during blowing snow periods in the open (Table 4.5). Our analysis showed that the reduced temperature gradient during blowing snow periods also decreased the sensible heat gains to the snowpack during blowing snow events. Here the reduction in temperature gradient (–33 %) surpassed the increase in C_e (23 %), which led to reduced sensible flux gains. The reduced incoming longwave radiation reported during blowing snow periods can be ascribed to the cooling feedback of blowing snow sublimation, since the wetting feedback of blowing snow would rather increase the emissivity of the air and longwave radiation; and also because incoming longwave radiation is very sensitive to air temperature (Dewalle and Rango, 2008; Oke, 1987). Collectively, our analyses show that blowing snow is an important element in energy exchanges during the accumulation season in wind-exposed open areas of agro-forested landscapes with humid continental climates.

4.5.3 Limitations and Way Forward

One strong limitation of this study is the availability of a single measurement year. While the original design included two monitoring years, the data from the first winter suffered from large data gaps due to a power failure of the stations and the malfunction of some sensors. Future analyses would be useful to assess if the same patterns of energy partitioning persist over several years and to establish long-term trends between the open, forest, and gap snowpacks in agro-forested environments. Also, continuous SWE monitoring at the open and forest sites failed due to sensor malfunction. Concurrent snow depth and SWE measurements, also providing the snowpack density, would be useful to obtain a more complete understanding of the snowpack mass balance between the sites. For instance, even though a significant difference in snow depth was observed between the open and forest, both sites might have had the same

SWE considering the wind-compacted denser snow at the open site. Therefore, deploying new passive SWE measuring sensors and snow pit measurements would be an added value in the future.

Another limitation in this study stems from the parameter uncertainty. For instance, the roughness length (z_0) has a significant influence on turbulent flux estimations by bulk aerodynamic method. A future study that explores the sensitivity of this parameter across open, gap, and forest snowpacks would be deemed to obtain optimum z_0 values for the sites. Since we only investigated the sensitivity of stability correction methods by Richardson number, a comparison of them with Monin Obhukhov similarity theory would provide more insights into the uncertainties involved in different methods.

4.6 Conclusions

Our results show that there are considerable differences in energy fluxes between open, forest, and forest gap in an agro-forested landscape with a humid continental climate. Large variations in energy fluxes throughout the analyzed period caused more variation in snowpack and ground temperatures in the open, whereas the opposite occurred in the forest and the gap exhibited an intermediate behavior. Net radiation dominated the snow surface energy balance in varying quantities between the sites, while turbulent fluxes were only significant at the wind-exposed open site. During the accumulation period, longwave radiation exerted a greater control on the variability of the net energy through radiative cooling. However, during the ablation period, latent heat fluxes and the absorption of solar radiation dominated the variability of the energy balance and snowpack melting.

Our analysis demonstrates that blowing snow fluxes have a substantial influence on changing snowpack dynamics in the open site at hourly scales. Blowing snow events under snowfall-free conditions outnumbered the events with concurrent snowfall by

75 %, resulting in a net snow depth gain equal to 29 % of the peak winter snow depth at the AWS location in the open site. Our results suggest that when sufficient snow is available on the ground, the occurrence of blowing snow events depends more on the intensity of wind speed, cold air temperature, and relative humidity rather than on concurrent snowfall. In addition to influencing the mass changes of the snowpack by accumulation and erosion processes, blowing snow modified the energy budget in the open through negative feedback effects. The observed increase in relative humidity and related decrease in vapor pressure gradient, and cooling of air temperature suggest a decrease in snowpack sublimation during blowing snow events. However, contrary to modelling (Bintanja, 2001a; Déry et al., 1998; Groot Zwaaftink et al., 2011; Le Toumelin et al., 2021; Vionnet et al., 2014; Yang et al., 2010) and observational (Bintanja, 2001b) studies that showed reduced snowpack sublimation during blowing snow events, our results rather showed that the decreased air stability in response to the decreased temperature gradient between the atmosphere and snowpack counterbalanced the reduced vapor pressure gradient and resulted in slightly increased latent heat (sublimation) losses from the snowpack during blowing snow. This shows the feedback of blowing snow on snowpack sublimation is contingent on the choice of stability function in the bulk aerodynamic method. Furthermore, our analysis showed reduced influxes of sensible heat and longwave radiation to the snowpack in response to the blowing snow cooling feedback on the atmosphere. These results emphasize the significant role of blowing snow for the energy exchanges in large wind-exposed open areas in humid continental agro-forested landscapes.

Our study also highlights how dissimilar energy budgets can lead to comparable ablation patterns in open, forest, and forest gap environments. The ablation mainly differed between the sites due to the difference in latent heat fluxes and changes in shortwave radiation. The different snowpack and energy balance conditions between the open and forested patches of agro-forested landscapes highlighted in this study could have important implications for snowmelt infiltration patterns (Lundberg et al.,

2016) and resulting catchment-scale hydrology (Aygün et al., 2020). For instance, our results show that the snowpack in the open was conductive to ground freezing and ice layer formation, while the forest snowpack and ground were warmer and devoid of ice layers. This has a great implication for infiltration patterns and thus the partition of meltwater between recharge and runoff in the region. As such, open agricultural areas are expected to produce more runoff, while forested areas would favor groundwater recharge, thereby influencing regional hydrology and flood regimes in the region. While these results are focused on southern Québec where such environments prevail, they have a broader implication for other cold agro-forested environments and they underscore the importance of incorporating blowing snow in physically based snow cover and hydrological models to correctly represent snow dynamics in such landscapes.

Acknowledgments

The authors extend their appreciation to the members of GlacioLab for their help during the fieldwork. Moreover, the authors are grateful to the Sainte-Marthe municipality, Québec, Canada.

Supporting Information

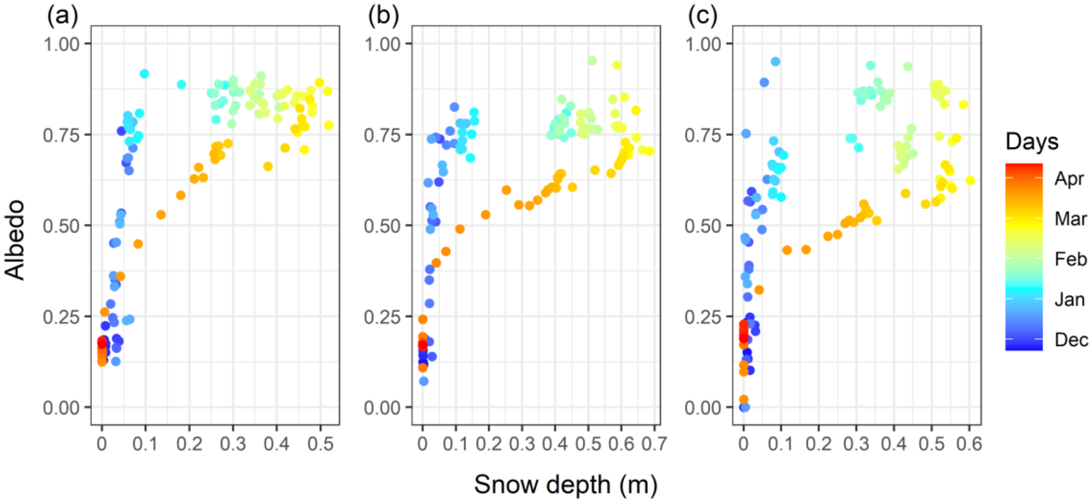

Figure S4.1. Albedo vs snow depth for the period of December 2020 to April 2021 in a) Open; b) gap; c) forest

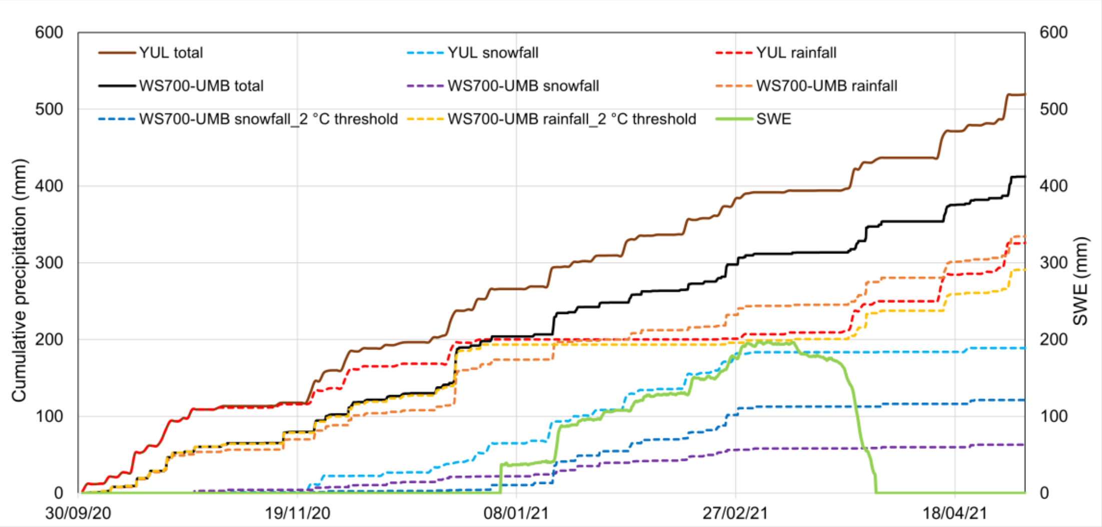

Figure S4.2. Cumulative precipitation YUL and gap stations with gap SWE for the hydrological year 2020–2021. YUL shows precipitation data extracted from Pierre-Elliott-Trudeau station and WS700-UMB is the precipitation from the deployed sensor at the gap. WS700-UMB snowfall and rainfall shows the automatic separation of snowfall and rainfall by the sensor and suffix _2 °C threshold indicates the precipitation separated with 2 °C threshold.

Sensitivity of turbulent flux calculation using different methods

Turbulent fluxes were calculated using seven methods and the ultimate effect on each method on the cumulative residual energy ($Q_M + \frac{dU}{dt}$) were investigated. Methods used include four different wind thresholds, a windless coefficient, and three stability correction methods.

Stability correction methods:

Method 1:
Here, the method described in the main text was used to calculate the bulk transfer coefficient (using Equation 4.10 and 4.11 in the main text).

Method 2:
Bulk transfer coefficient was calculated using equations based on Oke (1987) and (Dewalle and Rango, 2008). If the conditions are stable ($R_{iB} > 0$):

$$C_e = C_h = C_n(1 - 5R_{iB})^2 \quad \text{Equation S4.1}$$

and for unstable conditions ($R_{iB} \leq 0$):

$$C_e = C_h = C_n(1 - 16R_{iB})^{0.75} \quad \text{Equation S4.2}$$

This method has upper limit of R_{iB} = 0.2. i.e., at R_{iB} = 0.2, C_e= C_h= 0 and suppress the turbulent flux transfers. Mas et al. (2018)

Method 3:
Stability correction described in was used here. They introduced an approach to account for the heat exchange between the air and the snowpack surface when the atmospheric conditions are stable (even when R_{iB} ≥ 0.2).

If $R_{iB} \leq 0$:

$$C_e = C_h = C_n(1 - 16R_{iB})^{0.75} \quad \text{Equation S4.3}$$

If $0 < R_{iB} \leq 0.2$:

$$C_e = C_h = \frac{C_n}{1 + k_{tur}\frac{R_{iB}}{0.2}} \qquad \text{Equation S4.4}$$

If $R_{iB} > 0.2$:

$$C_e = C_h = \frac{C_n}{1 + k_{tur}} \qquad \text{Equation S4.5}$$

Where k_{tur} is 4.

Wind thresholds:
Wind thresholds tested were 0.1 m s^{-1}, 0.3 m s^{-1}, 0.45 m s^{-1}, and 1 m s^{-1}.

Windless coefficient:
A windless coefficient of 1 W m^{-2} K^{-1} used (Jordan, 1991) to calculate turbulent fluxes.

Then the updated equations of sensible and latent heat fluxes are:

$$Q_S = 1 + \rho_a c_p C_h u_a (T_a - T_s) \qquad \text{Equation S4.6}$$

$$Q_L = 1 + 0.622\, \rho_a L C_e u_a (e_a - e_s)/P_a \qquad \text{Equation S4.7}$$

Following table outlines the seven options used to calculate turbulent fluxes.

Table S4.1. Details of the different calculation methods

Option	Stability correction method	Wind threshold (m s^{-1})	Windless coefficient (W m^{-2} K^{-1})
1	Method 1	0.3	-
2	Method 2	0.3	-
3	Method 3	0.3	-
4	Method 1	0.1	-
5	Method 1	0.45	-
6	Method 1	1	-
7	Method 1	-	1

Figure S4.3 illustrates the effect of different calculation methods on the cumulative residual flux. Table S4.2 and S4.3 show the error statistics of each method. In Table S4.3, relative error was calculated with relative to the option 1.

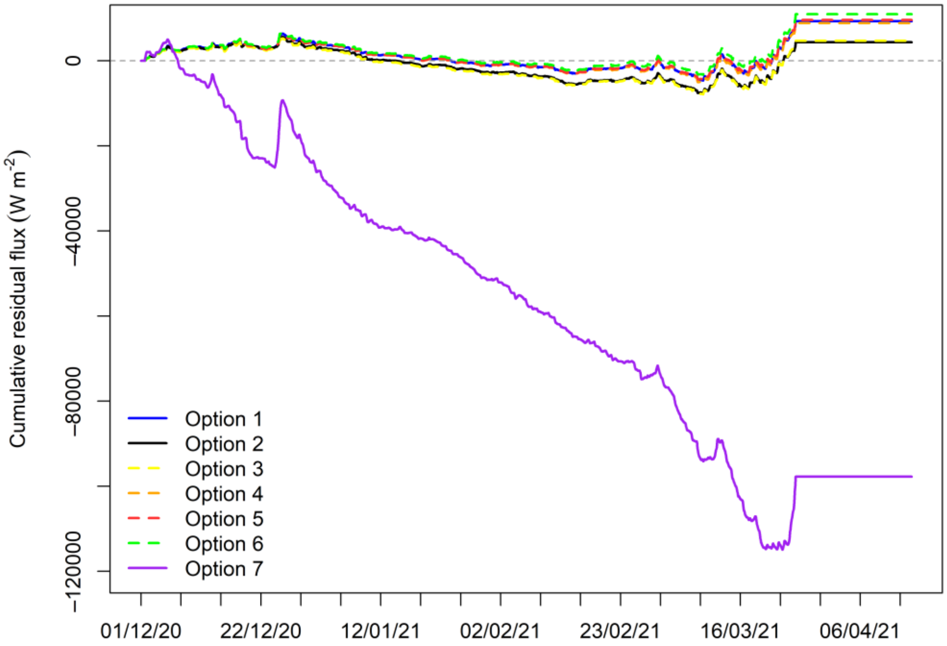

Figure S4.3. Cumulative residual fluxes for different calculation method

Table S4.2. Error statistics of different calculation methods

	Option 1	Option 2	Option 3	Option 4	Option 5	Option 6	Option 7
mean	3.42	1.60	1.73	3.25	3.52	4.03	–36.04
Standard deviation	67.42	65.18	64.18	68.16	67.22	66.61	143.78
RMS	67.51	65.20	64.20	68.24	67.31	66.73	148.23

Table S4.3. Mean relative error of different methods compared to Option 1

Option 2	Option 3	Option 4	Option 5	Option 6	Option 7
–0.53	–0.49	–0.05	0.03	0.18	–11.53

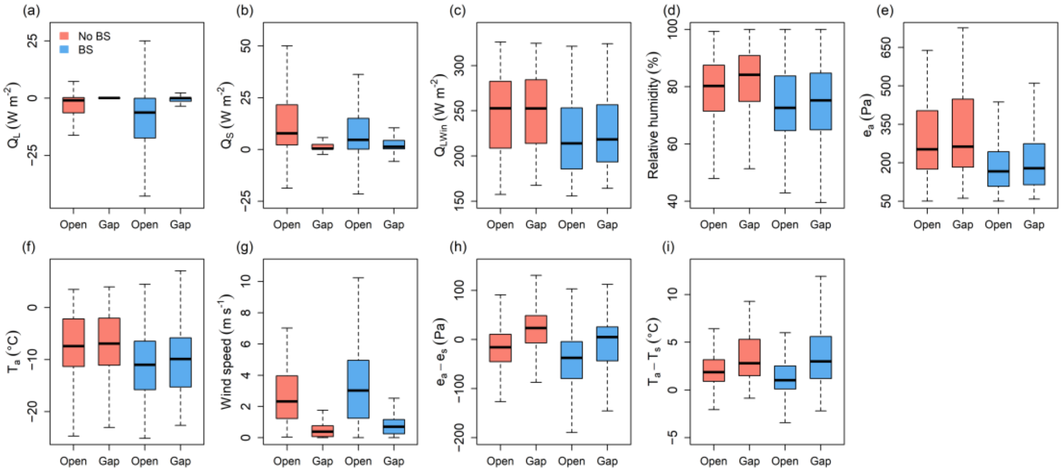

Figure S4.4. Energy fluxes and other variables in open and gap during periods of no blowing snow (no BS) and blowing snow (BS). a) latent heat flux; b) sensible heat flux; c) incoming longwave radiation; d) relative humidity; e) air vapor pressure; f) air temperature; g) wind speed; h) vapor pressure difference between air and snowpack surface; i) temperature difference between air and snowpack surface

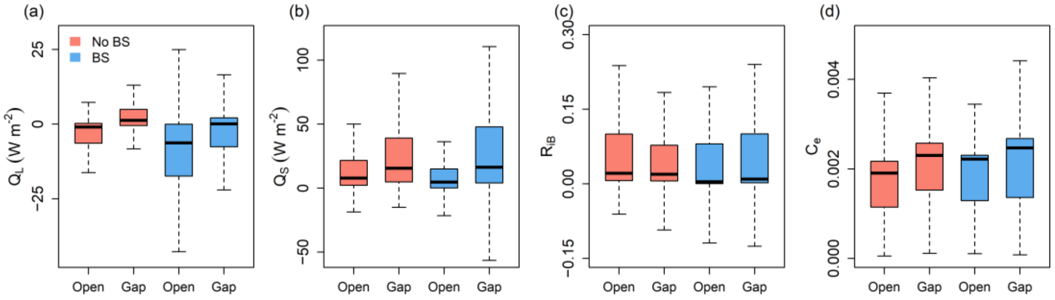

Figure S4.5. Energy fluxes and other variables in open and gap during periods of no blowing snow (no BS) and blowing snow (BS) under open wind conditions. a) latent heat flux; b) sensible heat flux; c) Richardson number; d) bulk exchange coefficient.

References

Amory, C. 2020. Drifting-snow statistics from multiple-year autonomous measurements in Adélie Land, East Antarctica. The Cryosphere 14(5), 1713–1725.

Anderson, E.A. 1976 A point energy and a mass balance model of a snow cover, NOAA Technical Report NWS 19, USA.

Andreas, E.L., Horst, T.W., Grachev, A.A., Persson, P.O.G., Fairall, C.W., Guest, P.S. and Jordan, R.E. 2010. Parametrizing turbulent exchange over summer sea ice and the marginal ice zone. Quarterly Journal of the Royal Meteorological Society 136(649), 927–943.

Armstrong, R.L. and Brun, E. (2008) Snow and Climate-physical processes, surface energy exchange and modeling, Cambridge University Press, New York, USA.

Aygün, O., Kinnard, C., Campeau, S. and Krogh, S.A. 2020. Shifting hydrological processes in a Canadian agroforested catchment due to a warmer and wetter climate. Water 12(3), 739.

Aygün, O., Kinnard, C., Campeau, S. and Pomeroy, J.W. 2022. Landscape and climate conditions influence the hydrological sensitivity to climate change in eastern Canada. Journal of Hydrology 615, 128595.

Bair, E.H., Davis, R.E. and Dozier, J. 2018. Hourly mass and snow energy balance measurements from Mammoth Mountain, CA USA, 2011–2017. Earth System Science Data 10, 549–563.

Barral, H., Genthon, C., Trouvilliez, A., Brun, C. and Amory, C. 2014. Blowing snow in coastal Adélie Land, Antarctica: three atmospheric-moisture issues. The Cryosphere 8(5), 1905–1919.

Barry, R., Prévost, M., Stein, J. and Plamondon, A.P. 1990. Application of a snow cover energy and mass balance model in a balsam fir forest. Water Resour. Res 26(5), 1079–1092.

Bintanja, R. 2001a. Modelling snowdrift sublimation and its effect on the moisture budget of the atmospheric boundary layer. Tellus A 53(2), 215–232.

Bintanja, R. 2001b. Snowdrift sublimation in a katabatic wind region of the Antarctic ice sheet. Journal of Applied Meteorology 40(11), 1952–1966.

Boike, J., Roth, K. and Ippisch, O. 2003. Seasonal snow cover on frozen ground: Energy balance calculations of a permafrost site near Ny-Ålesund, Spitsbergen. Journal of Geophysical Research: Atmospheres 108(D2), 8163.

Brown, R.D. 2010. Analysis of snow cover variability and change in Québec, 1948–2005. Hydrological Processes 24, 1929–1954.

Broxton, P.D., Harpold, A.A., Biederman, J.A., Troch, P.A., Molotch, N.P. and Brooks, P.D. 2015. Quantifying the effects of vegetation structure on snow accumulation and ablation in mixed-conifer forests. Ecohydrology 8, 1073–1094.

Brun, E., Martin, E., Simon, V., Gendre, C. and Coléou, C. 1989. An energy and mass model of snow cover suitable for operational avalanche forecasting. Journal of Glaciology 35, 333–342.

Chritin, V., Bolognesi, R. and Gubler, H. 1999. FlowCapt: a new acoustic sensor to measure snowdrift and wind velocity for avalanche forecasting. Cold Regions Science and Technology 30(1), 125—133.

Cierco, F.-X., Naaim-Bouvet, F. and Bellot, H. 2007. Acoustic sensors for snowdrift measurements: How should they be used for research purposes? Cold Regions Science and Technology 49(1), 74–87.

Conway, J., Pomeroy, J., Helgason, W. and Kinar, N. 2018. Challenges in modeling turbulent heat fluxes to snowpacks in forest clearings. Journal of Hydrometeorology 19, 1599–1616.

Conway, J.P. and Cullen, N.J. 2013. Constraining turbulent heat flux parameterization over a temperate maritime glacier in New Zealand. Annals of Glaciology 54(63), 41–51.

Das, R.K., Datt, P. and Acharya, A. 2012. An assessment of the FlowCapt acoustic sensor for measuring snowdrift in the Indian Himalayas. Journal of Earth System Science 121, 1483–1491.

Déry, S., Taylor, P. and Xiao, J.B. 1998. The thermodynamic effects of sublimating, blowing snow in the atmospheric boundary layer. Boundary-Layer Meteorology 89(2), 251–283.

Dewalle, D.R. and Rango, A. (2008) Principles of Snow Hydrology, Cambridge University Press, New York, USA.

Doorschot, J.J., Lehning, M. and Vrouwe, A. 2004. Field measurements of snow-drift threshold and mass fluxes, and related model simulations. Boundary-Layer Meteorology 113(3), 347–368.

Elder, K., Rosenthal, W. and Davis, R.E. 1998. Estimating the spatial distribution of snow water equivalence in a montane watershed. Hydrological Processes 12, 1793–1808.

Environment and Climate Change Canada 2021 Hourly Data Report.

Ellis, C. R., Pomeroy, J. W., and Link, T. E. (2013). Modeling increases in snowmelt yield and desynchronization resulting from forest gap-thinning treatments in a northern mountain headwater basin. Water Resources Research, 49(2), 936–949. doi:10.1002/wrcr.20089

Essery, R. and Pomeroy, J. 2004. Vegetation and topographic control of wind-blown snow distributions in distributed and aggregated simulations for an Arctic tundra basin. Journal of Hydrometeorology 5, 735–744.

Essery, R., Rutter, N., Pomeroy, J., Baxter, R., Stähli, M., Gustafsson, D., Barr, A., Bartlett, P. and Elder, K. 2009. SNOWMIP2 an evaluation of forest snow process simulations. Bulletin of the American Meteorological Society 90(8), 1120–1135.

Essery, R.L.H., Morin, S., Lejeune, Y. and Ménard, C.B. 2013. A comparison of 1701 snow models using observations from an alpine site. Advances in Water Resources 55, 131–148.

Golding, D.L. and Swanson, R.H. 1986. Snow distribution patterns in clearings and adjacent forest. Water Resour. Res 22(13), 1931–1940.

Gootman, K.S. and Hubbart, J.A. 2021. Rainfall, runoff and shallow groundwater response in a mixed-use, agro-forested watershed of the northeast, USA. Hydrological Processes 35(8), e14312.

Groot Zwaaftink, C.D., Löwe, H., Mott, R., Bavay, M. and Lehning, M. 2011. Drifting snow sublimation: A high-resolution 3-D model with temperature and moisture feedbacks. Journal of Geophysical Research: Atmospheres 116, D16107.

Harder, P., Helgason, W.D. and Pomeroy, J.W. 2018. Modeling the snowpack energy balance during melt under exposed crop stubble. Journal of Hydrometeorology 19(7), 1191–1214.

Harder, P., Pomeroy, J.W. and Helgason, W. 2017. Local-scale advection of sensible and latent heat during snowmelt. Geophysical Research Letters 44(19), 9769–9777.

Helgason, W. and Pomeroy, J. 2012a. Problems closing the energy balance over a homogeneous snow cover during midwinter. Journal of Hydrometeorology 13, 557–572.

Helgason, W. and Pomeroy, J.W. 2012b. Characteristics of the near-surface boundary layer within a mountain valley during winter. Journal of Applied Meteorology and Climatology 51(3), 583–597.

Hoelzle, M., Hauck, C., Mathys, T., Noetzli, J., Pellet, C. and Scherler, M. 2022. Long-term energy balance measurements at three different mountain permafrost sites in the Swiss Alps. Earth Syst. Sci. Data 14(4), 1531–1547.

Hojatimalekshah, A., Uhlmann, Z., Glenn, N., Hiemstra, C., Tennant, C., Graham, J., Spaete, L., Gelvin, A., Marshall, H., McNamara, J. and Enterkine, J. 2021. Tree canopy and snow depth relationships at fine scales with terrestrial laser scanning. The Cryosphere 15, 2187–2209.

Hopkinson, C., Pomeroy, J., Debeer, C., Ellis, C. and Anderson, A. 2012 Relationships between snowpack depth and primary lidar point cloud derivatives in a mountainous environment, IAHS Publ. 352, Jackson Hole, Wyoming, USA.

Hopkinson, C., Sitar, M., Chasmer, L. and Treitz, P. 2004. Mapping snowpack depth beneath forest canopies using airborne lidar. Photogrammetric Engineering & Remote Sensing 70(3), 323–330.

Hydroinnova 2019 SnowFox.

IAV Technologies 2019 User guide-operating instructions for ISAW sensors, Tannay, Switzerland.

Jacobs, J.M., Hunsaker, A.G., Sullivan, F.B., Palace, M., Burakowski, E.A., Herrick, C. and Cho, E. 2021. Snow depth mapping with unpiloted aerial system lidar observations: a case study in Durham, New Hampshire, United States. The Cryosphere 15(3), 1485–1500.

Jaedicke, C. 2001. Acoustic snowdrift measurements: experiences from the FlowCapt instrument. Cold Regions Science and Technology 32, 71–81.

Jenicek, M., Pevna, H. and Matejka, O. 2017. Canopy structure and topography effects on snow distribution at a catchment scale: Application of multivariate approaches. Journal of Hydrology and Hydromechanics 66, 43–54.

Jennings, K.S., Kittel, T.G.F. and Molotch, N.P. 2018a. Observations and simulations of the seasonal evolution of snowpack cold content and its relation to snowmelt and the snowpack energy budget. The Cryosphere 12(5), 1595–1614.

Jennings, K.S., Winchell, T.S., Livneh, B. and Molotch, N.P. 2018b. Spatial variation of the rain–snow temperature threshold across the Northern Hemisphere. Nature Communications 9(1), 1148.

Jobin, B., Latendresse, C., Baril, A., Maisonneuve, C., Boutin, C. and Côté, D. 2014. A half-century analysis of landscape dynamics in southern Québec, Canada. Environmental Monitoring and Assessment 186(4), 2215–2229.

Jordan, R.E. 1991 A one-dimensional temperature model for a snow cover : technical documentation for SNTHERM.89, U.S. Army Corps of Engineers, Cold Regions Research & Engineering Laboratory, USA.

Kuipers Munneke, P., van den Broeke, M.R., Reijmer, C.H., Helsen, M.M., Boot, W., Schneebeli, M. and Steffen, K. 2009. The role of radiation penetration in the energy budget of the snowpack at Summit, Greenland. The Cryosphere 3(2), 155–165.

Lackner, G., Domine, F., Nadeau, D.F., Parent, A.C., Anctil, F., Lafaysse, M. and Dumont, M. 2022. On the energy budget of a low-Arctic snowpack. The Cryosphere 16(1), 127–142.

Le Toumelin, L., Amory, C., Favier, V., Kittel, C., Hofer, S., Fettweis, X., Gallée, H. and Kayetha, V. 2021. Sensitivity of the surface energy budget to drifting snow as simulated by MAR in coastal Adelie Land, Antarctica. The Cryosphere 15(8), 3595–3614.

Lehning, M., Bartelt, P., Brown, B., Fierz, C. and Satyawali, P. 2002. A physical SNOWPACK model for the Swiss avalanche warning Part II. Snow microstructure. Cold Regions Science and Technology 35(3), 147–167.

Lehning, M. and Fierz, C. 2008. Assessment of snow transport in avalanche terrain. Cold Regions Science and Technology 51(2), 240–252.

Li, L. and Pomeroy, J.W. 1997. Estimates of threshold wind speeds for snow transport using meteorological data. Journal of Applied Meteorology 36(3), 205–213.

Liston, G.E., Haehnel, R.B., Sturm, M., Hiemstra, C.A., Berezovskaya, S. and Tabler, R.D. 2007. Instruments and Methods-Simulating complex snow distributions in windy environments using SnowTran-3D. Journal of Glaciology 53(181), 214–256.

Liston, G.E. and Sturm, M. 1998. A snow-transport model for complex terrain. Journal of Glaciology 44(148), 498–516.

Lundberg, A., Ala-Aho, P., Eklo, O., Klöve, B., Kværner, J. and Stumpp, C. 2016. Snow and frost: implications for spatiotemporal infiltration patterns – a review. Hydrological Processes 30(8), 1230–1250.

Lundquist, J.D., Dickerson-Lange, S.E., Lutz, J.A. and Cristea, N.C. 2013. Lower forest density enhances snow retention in regions with warmer winters: A global framework developed from plot-scale observations and modeling. Water Resour. Res 49, 6356–6370.

Luomaranta, A., Aalto, J. and Jylhä, K. 2019. Snow cover trends in Finland over 1961–2014 based on gridded snow depth observations. International Journal of Climatology 39(7), 3147–3159.

Martin, E. and Lejeune, Y. 1998. Turbulent fluxes above the snow surface. Annals of Glaciology 26, 179–183.

Mas, A., Baraer, M., Arsenault, R., Poulin, A. and Préfontaine, J. 2018. Targeting high robustness in snowpack modeling for Nordic hydrological applications in limited data conditions. Journal of Hydrology 564, 1008–1021.

Mott, R., Egli, L., Grünewald, T., Dawes, N., Manes, C., Bavay, M. and Lehning, M. 2011a. Micrometeorological processes driving snow ablation in an Alpine catchment. The Cryosphere 5(4), 1083–1098.

Mott, R., Schirmer, M. and Lehning, M. 2011b. Scaling properties of wind and snow depth distribution in an Alpine catchment. Journal of Geophysical Research 116, D06106.

Mott, R., Schlögl, S., Dirks, L. and Lehning, M. 2017. Impact of extreme land surface heterogeneity on micrometeorology over spring snow cover. Journal of Hydrometeorology 18(10), 2705–2722.

Mott, R., Vionnet, V. and Grünewald, T. 2018. The seasonal snow cover dynamics: review on wind-driven coupling processes. Frontiers in Earth Science 6:197.

Naaim-Bouvet, F., Bellot, H. and Naaim, M. 2010. Back analysis of drifting-snow measurements over an instrumented mountainous site. Annals of Glaciology 51(54), 207–217.

Oke, T.R. (1987) Boundary layer climates, Routledge, New York, USA.

Paquotte, A. and Baraer, M. 2021. Hydrological behavior of an ice-layered snowpack in a non-mountainous environment. Hydrological Processes 36(1), e14433.

Parajuli, A., Nadeau, D.F., Anctil, F. and Alves, M. 2021. Multilayer observation and estimation of the snowpack cold content in a humid boreal coniferous forest of eastern Canada. The Cryosphere 15(12), 5371–5386.

Pomeroy, J., Fang, X. and Ellis, C. 2012. Sensitivity of snowmelt hydrology in Marmot Creek, Alberta, to forest cover disturbance. Hydrological Processes 26(12), 1891–1904.

Pomeroy, J. and Gray, D.M. 1995 Snowcover: accumulation, relocation and management, p. 144, National Hydrology Research Institute Science report No. 7, Environment Canada, Saskatoon, Canada.

Pomeroy, J.W. and Dion, K. 1996. Winter radiation extinction and reflection in a boreal pine canopy: Measurements and modelling. Hydrological Processes 10, 1591–1608.

Pomeroy, J.W. and Granger, R.J. 1997 Sustainability of the western Canadian boreal forest under changing hydrological conditions-Snow accumulation and ablation, pp. 237–242, IAHS Publ. no. 240, Rabat, Morocco.

Pomeroy, J.W. and Gray, D.M. 1994 Sensitivity of snow relocation and sublimation to climate and surface vegetation, pp. 213–225, IAHS Publ. no. 223, Yokohama, Japan.

Pomeroy, J.W., Gray, D.M., Brown, T., Hedstrom, N.R., Quinton, W.L., Granger, R.J. and Carey, S.K. 2007. The cold regions hydrological model: a platform for basing process representation and model structure on physical evidence. Hydrological Processes 21(19), 2650–2667.

Pomeroy, J.W., Gray, D.M., Hedstrom, N.R. and Janowicz, J.R. 2002. Prediction of seasonal snow accumulation in cold climate forests. Hydrological Processes 16, 3543–3558.

Pomeroy, J.W., Gray, D.M. and Landine, P.G. 1993. The Prairie Blowing Snow Model: characteristics, validation, operation. Journal of Hydrology 144, 165–192.

Pomeroy, J.W., Gray, D.M., Shook, K.R., Toth, B., Essery, R.L.H., Pietroniro, A. and Hedstrorm, N. 1998a. An evaluation of snow accumulation and ablation processes for land surface modelling. Hydrological Processes 12, 2339–2367.

Pomeroy, J.W., Parviainen, J., Hedstrom, N. and Gray, D.M. 1998b. Coupled modelling of forest snow interception and sublimation. Hydrological Processes 12, 2317–2337.

Prasad, R., Tarboton, D.G., Liston, G.E., Luce, C.H. and Seyfried, M.S. 2001. Testing a blowing snow model against distributed snow measurements at Upper Sheep Creek, Idaho, United States of America. Water Resour. Res 37(5), 1341–1350.

Prévost, M., Barry, R., Stein, J. and Plamondon, A.P. 1991. Snowmelt modeling in a balsam fir forest: Comparison between an energy balance model and other simplified models. Canadian Journal of Forest Research 21, 1–10.

Price, A.G.S. and Dunne, T. 1976. Energy balance computations of snowmelt in a subarctic area. Water Resour. Res 12, 686–694.

Reba, M. L., Pomeroy, J., Marks, D., and Link, T. E. (2012). Estimating surface sublimation losses from snowpacks in a mountain catchment using eddy covariance and turbulent transfer calculations. Hydrological Processes, 26(24), 3699–3711. doi:10.1002/hyp.8372

Roth, T.R. and Nolin, A.W. 2017. Forest impacts on snow accumulation and ablation across an elevation gradient in a temperate montane environment. Hydrology and Earth System Sciences 21, 5427–5442.

Rutter, N., Essery, R., Pomeroy, J., Altimir, N. and Andreadis, K. 2009. Evaluation of forest snow processes models (SnowMIP2). Journal of Geophysical Research 114, Paper 8.

Sena, N., Chokmani, K., Gloaguen, E. and Bernier, M. 2017. Analyse multi-échelles de la variabilité spatiale de l'équivalent en eau de la neige (EEN) sur le territoire de l'Est du Canada. Hydrological Sciences Journal 62(3), 359–377.

Steiner, J.F., Litt, M., Stigter, E.E., Shea, J., Bierkens, M.F.P. and Immerzeel, W.W. 2018. The importance of turbulent fluxes in the surface energy balance of a debris-covered glacier in the Himalayas. Frontiers in Earth Science 6:144.

Swanson, R. 1988 The effect of in situ evaporation on perceived snow distribution in partially clear-cut forests, pp. 87–92.

Tarboton, D.G. 1994 Measurements and modeling of snow energy balance and sublimation from snow, Utah Water Research Laboratory, Utah State University, Logan, USA.

Troendle, C. and Leaf, C. 1980 Hydrology. An approach to water resources evaluation of non-point silviculture sources, pp. 1–173, Environmental Research Laboratory, Athens, GA.

Trouvilliez, A., Naaim-Bouvet, F., Bellot, H., Genthon, C. and Gallée, H. 2015. Evaluation of the FlowCapt acoustic sensor for the aeolian transport of snow. Journal of Atmospheric and Oceanic Technology 32, 1630–1641.

Trouvilliez, A., Naaim-Bouvet, F., Genthon, C., Piard, L., Favier, V., Bellot, H., Agosta, C., Palerme, C., Amory, C. and Gallée, H. 2014. A novel experimental study of aeolian snow transport in Adelie Land (Antarctica). Cold Regions Science and Technology 108, 125–138.

Valence, E., Baraer, M., Rosa, E., Barbecot, F. and Monty, C. 2022. Drone-based ground-penetrating radar (GPR) application to snow hydrology. The Cryosphere 16, 3843–3860.

Varhola, A., Coops, N.C., Weiler, M. and Moore, R.D. 2010. Forest canopy effects on snow accumulation and ablation: An integrative review of empirical results. Journal of Hydrology 392, 219–233.

Vionnet, V., Guyomarc'h, G., Lafaysse, M., Naaim-Bouvet, F., Giraud, G. and Deliot, Y. 2018. Operational implementation and evaluation of a blowing snow scheme for avalanche hazard forecasting. Cold Regions Science and Technology 147, 1–10.

Vionnet, V., Martin, E., Masson, V., Guyomarc'h, G., Naaim-Bouvet, F., Prokop, A., Durand, Y. and Lac, C. 2014. Simulation of wind-induced snow transport and sublimation in alpine terrain using a fully coupled snowpack/atmosphere model. The Cryosphere 8(2), 395–415.

Vionnet, V., Naaim-Bouvet, F., Martin, E., Durand, Y., Bellot, H., Bel, C. and Pugliese, P. 2013. Occurrence of blowing snow events at an alpine site over a 10-year period: Observations and modelling. Advances in Water Resources 55, 53–63.

Wilcoxon, F.: Individual comparisons by ranking methods, Biometrics, 1(6), 80–83, 1945.

Winkler, R.D., Spittlehouse, D.L. and Golding, D.L. 2005. Measured differences in snow accumulation and melt among clearcut, juvenile, and mature forests in southern British Columbia. Hydrological Processes 19, 51–62.

Woods, S.W., Ahl, R., Sappington, J. and McCaughey, W. 2006. Snow accumulation in thinned lodgepole pine stands, Montana, USA. Forest Ecology and Management 235, 202–211.

Yang, J., Yau, M.K., Fang, X. and Pomeroy, J.W. 2010. A triple-moment blowing snow-atmospheric model and its application in computing the seasonal wintertime snow mass budget. Hydrol. Earth Syst. Sci. 14(6), 1063–1079.

Zhang, W., He, J., Chen, A.a., Wu, X. and Shen, Y. 2022. Observations of drifting snow using FlowCapt sensors in the Southern Altai mountains, Central Asia. Water 14(6), 845.

Zheng, Z., Ma, Q., Qian, K. and Bales, R.C. 2018. Canopy effects on snow accumulation: observations from lidar, canonical-view photos, and continuous ground measurements from sensor networks. Remote Sensing 10, 1769.

CONCLUSIONS

Synthesis and Concluding Discussions

This chapter presents a synthesis of this thesis's contribution to the research on the impact of landscape heterogeneity on snow cover. In view of utilizing UAV lidar in snow depth monitoring, this dissertation provided a comprehensive overview of the accuracy assessment of lidar-derived snow depths within and between agro-forested and boreal environments in eastern Canada and recommendations for future applications. This research characterized and assessed the small-scale variability of lidar-derived snow depths within and between the aforementioned landscapes and discussed the landscape-induced impacts on the snow depths. The work in this thesis also shed light on resolving the likely overestimation of snow depths in coniferous forests due to under-sampling under the thick canopies by UAV lidar and proposed a new method to mitigate it. Moreover, this dissertation provides an analysis of how snow depths respond to meteorological factors in agro-forested environments by a measurement-based approach in eastern Canada.

Subsequent sections present the main conclusions obtained for the specific objectives proposed in Introduction to fulfill the main objective of this thesis; "exploring how landscape heterogeneity modulates the snow cover at the microscale (< 100 m) level by combining high-resolution lidar and detailed meteorological and energy flux measurements".

Objective 1: Investigate how accurate the lidar-derived snow depths are in open versus forested environments with different canopy covers.

UAV lidar data acquired in two agro-forested sites (Sainte-Marthe and Saint-Maurice) and a boreal forested site (Montmorency) in eastern Canada in 2019 and 2020 were assessed for point clouds and subsequent snow depth accuracies (Chapter I). An automatic strip alignment algorithm was tested on lidar data to assess whether it can improve upon the manual boresight calibration procedure. The accuracy of lidar-derived snow depths was assessed by the discrepancy between the lidar and manual snow depths in the open (field) and forest at each site.

The validation of lidar-derived snow depths with ground-based measurements showed a good agreement, however with higher uncertainties observed in forested areas compared with open areas. Results show that the deterioration of the absolute accuracy of the point cloud by the strip alignment method caused large errors in strip-aligned snow depths compared with ground-based measurements. RMSE values for lidar-derived snow depths found in this study were less than 0.16 m in open environments (including a basal ice layer), less than 0.08 m in the deciduous forested environment, and less than 0.19 m in the coniferous environment which is comparable to previous efforts in open and forested environments by ALS and UAV. Nevertheless, in Montmorency, the higher RMSE values had a relatively smaller impact due to the deeper snowpack observed at the site.

Overall, the results show that careful boresight calibration provides centimeter-level accuracy of lidar data without strip alignment enhancement, therefore, should receive paramount attention in the data processing workflow. A well-formulated flight plan that addresses IMU tuning and favorable weather conditions (i.e., wind speed) plays a critical role in reducing system errors. Furthermore, the deployment of ground control points can ensure an absolute check of data in situations where no distinct structures are visible from airborne sensors. The final accuracy of the snow depths also depends on successful ground point classification, hence should be given utmost importance in the data processing.

Objective 2: Characterize the small-scale variability of snow depth between and within the forested and open environments using lidar-derived data.

UAV lidar-derived snow depths in two agro-forested sites (Sainte-Marthe and Saint-Maurice) and the boreal forested site (Montmorency) in Chapter I were analyzed in Chapter II for inter (agro-forested versus coniferous) and intra (open versus forest) site variability of snow depths. The scaling behavior of snow depths was explored by semi-variogram analysis. To investigate the effect of vegetation and topographic variables on the spatial variability of snow depth, random forest (RF) regression models were applied on rasters derived from lidar data. In addition, RF model performance at each site was compared to traditional multiple linear regression (MLR) model performances.

Results in two agro-forested sites show that canals/streams in the field and the forest edges trap snow blown from the open field and correspond to the highest snow depths at those sites. When these elements are discarded open areas in two agro-forested sites showed slightly lower snow accumulation than the adjacent forest. In the boreal forested site, the snow depth difference between the open field and the forest was not significant.

Semi-variogram analysis shows more variable snow depths in the forest than in open snow depths at all sites. Snow depths are more variable in coniferous forests than in deciduous and mixed forests. Snow depth in forested areas at all three sites shows a typical multi-scaling behavior with a scale break located at distances less than 10 m. Open areas show larger scale break distances (11–14 m) at all sites. Directional semi-variograms suggest an influence of blowing snow on the snow distribution patterns in the forest, and hence a possible penetration of blowing snow from field to forest in agro-forested sites. The scale break distances found in this study suggest that the scale selected for modeling or sampling in similar environments should be well below these values, in order to fully resolve the small-scale variability of the snow depth.

Significantly better performances of RF models compared to MLRs at all sites suggest the deficiency of MLR models in capturing the underlying processes at these sites. Moreover, almost all variables have a nonlinear relationship with snow depth, which linear models are unable to capture. Results of RF models show that the underlying topography and the wind-redistribution of snow along forest edges (windward forest edge matrices) govern the snow depth variability at agro-forested sites, while forest structure variability dominates snow depth variability in the coniferous environment.

Objective 3: Develop an interpolation method to resolve the effects of under-sampling under the canopy in coniferous environments by UAV lidar.

A 100 m x 100 m area extracted from processed, classified lidar data of the boreal forested site, Montmorency in Chapter I was used in this chapter. Snow depth for the selected area was derived at 0.1 m resolution to take into account the variability within the canopy. Then, tree segmentation and canopy (tree polygon) delineation were implemented on the classified point cloud. Four interpolation methods were tested. The first method only considered the landscape trend of the snow depths. The second method considered landscape trend and the canopy versus gap snow depth trend. The third method considered the landscape trend and the intra-canopy trend in snow depths. The fourth method considered the landscape trend, canopy versus gap snow depth trend, and intra-canopy trend in snow depths. Each method was completed by spatial interpolation of residuals using inverse distance weighting (IDW) and ordinary kriging (OK) methods (altogether giving eight scenarios). The performance of interpolation methods was evaluated by cross-validation.

When the distance between unsampled and sampled points is < 1 m, (i.e., ground surface point density is > 1 pt m^{-2}), all methods show similar RMSEs, indicating that spatial interpolation techniques like OK and IDW have sufficient information to resolve and reconstruct small-scale patterns of data. When the sampled and unsampled points are sparser than 2.5–3 m (i.e., ground surface point density is < 0.33–0.40 pt m^{-2}), snow depth estimates by spatial interpolation techniques cause high uncertainties. This limiting distance of 2.5–3 m is in the same order of magnitude as half of the maximum canopy diameter (7 m) found in Montmorency, and half of the scale break distance (4.5 m in DSM and 6.5 m in snow depth) found for Montmorency forest in Chapter II, suggesting that beyond this distance we risk interpolating data points with no spatial correlation. Between these limiting distances, the fourth method yields the most accurate estimates of snow depths at unsampled locations.

Objective 4: Analyze snow energy partitioning between forested and open environments.

Automatic weather station measurements from an open agricultural area, a mixed wood forest (mostly deciduous), and a forest clearing in Sainte-Marthe were used to estimate energy budget components for the 2020–2021 winter in this chapter. The energy balance for snowpacks in three sites was calculated using the energy balance equation developed by Anderson (1976). Snow energy partitioning between sites was compared and analyzed for early winter, accumulation, and ablation periods in the 2020–2021 winter. Changes in latent, sensible, and incoming longwave radiation fluxes in the open agricultural area compared to forest clearing during measured blowing snow events without concurrent snowfall were analyzed to investigate the effect of blowing snow fluxes on the energy budget.

The results show that a high variation of energy fluxes throughout the analyzed period caused more variation in snowpack and ground temperatures in the open environment whereas the opposite occurred in the forest. Snowpack in forest clearing exhibited an intermediate behavior. Net radiation dominated the snow surface energy balance in varying quantities between the sites. Turbulent fluxes are only significant in the wind-exposed open site. During the accumulation period, longwave radiation exerts greater control of the net energy balance through radiative cooling at all sites. However, during the ablation period, latent heat fluxes and the absorption of solar radiation dominate the energy balance, and snowpack melting. Blowing snow demonstrated thermodynamic feedback effects leading to increased relative humidity, decreased vapor pressure gradient, and colder air temperature at the open site similar to previous studies. However, a slight increase in latent heat losses was found due to decreasing air stability (R_{iB}) (thereby increasing bulk exchange coefficient, C_e: 23 %) surpassing the decrease in vapor pressure gradient (–8 %) during blowing snow periods. Moreover, the reduction in temperature gradient (–33 %) that surpassed the increase in C_e led to reduced sensible flux gains during blowing snow periods. Cooling feedback of blowing snow also reduced the incoming longwave radiation reported during blowing snow periods. Collectively, our analysis shows that blowing snow is an important element in energy exchanges during the accumulation season in wind-exposed open areas.

Concluding Remarks

This research used UAV lidar measurements and meteorological and snow energy flux measurements to assess the impact of landscape heterogeneity on snow cover in agro-forested and boreal environments. Results revealed that landscape settings have a significant influence in modifying the snow accumulation and distribution patterns between and within these landscapes.

It was found that in agro-forested environments, the assemblage of agricultural and forested areas drives the differential snow accumulation between open fields and forested areas. Such that, the snow depth variability in open fields is governed by preferential snow accumulation in canals and streams and the microtopography of the underlying terrain, and within deciduous/mixed forests it is rather governed by the underlying topography and/or the forest edges. The results show that blowing snow redistributed from the open fields gets trapped in canals and streams and accumulates along the forest edges accounting for the highest local snow accumulation in agro-forested landscapes. Apart from snow accumulation and distribution by blowing snow, results from blowing snow measurements at the open agricultural site showed that they influence the energy budget by modifying the energy exchanges between snowpack, ground, and atmosphere. These results highlight the importance of considering blowing snow in modeling efforts in such landscapes. They also suggest the better representation of canals and streams and the use of distinct spatial units such as HRUs to represent preferential snow accumulation along the forest edges in distributed hydrological models of such landscapes. Furthermore, the different snowpack and energy balance conditions between open fields and forest patches of agro-forested landscapes highlighted in this research have important implications for snowmelt infiltration patterns (Lundberg et al., 2016) and resulting catchment-scale hydrology (Aygün et al., 2020). For example, our results show that ground freezing and ice layer formation in the open agricultural areas would likely generate more runoff while warmer ground in the forested areas would encourage groundwater recharge, thereby influencing regional hydrology and flood regimes in cold agro-forested environments.

Landscape in boreal forested environments acts differently on snow cover than that in agro-forested environments. Our results show that snow depth variability in these environments mainly comes from forest structure variability. Such that, the canopy interception and unloading of snow from the canopies govern the snow accumulation and distribution patterns in boreal forested environments. Our results demonstrate that UAV lidar can successfully be used to monitor this forest structure variability. However, UAV lidar-derived snow depths in the boreal forested site highlight the prevailing observation gaps due to the occlusion of airborne measurements by the thick canopy cover. To mitigate the effect of likely overestimation of snow depths under canopies due to this under-sampling and to obtain more representative intra-canopy snow depth variability, the new interpolation method introduced in this research can be used. Taken together, our results emphasize that a better representation of snow depth variability and associated forest structure variability would be beneficial in obtaining more accurate snowmelt estimates in these landscapes.

Collectively, the findings of this research have important implications for snowmelt modeling, flood forecasting, water management strategies, and land management practices (e.g., agriculture, regeneration of forests, and clear cuttings) in cold agro-forested and boreal landscapes. In events where high-resolution data is not affordable, our results provide opportunities for sub-grid parameterization, upscaling, and validating modeling efforts in these landscapes.

Outlook

This thesis provides insight into how different land use types (e.g., forested versus open, deciduous versus coniferous) modulates the snow cover distribution. However, there are potential limitations with some of the methods presented in this study.

For instance, despite our efforts to incorporate processes and variables influencing the spatial distribution of snow depths with available data, the comparatively lower performance of RF models in Saint-Maurice and Montmorency indicates that there could still be some processes/variables that were unable to accounted for (e.g., soil parameters, snowpack state, and meteorological variables). Furthermore, the unexplained snow depth variability that is within the UAV lidar system detection limit (especially in Montmorency) also affected the accuracy of snow depth and ground surface rasters and derived landscape descriptors. For instance, the observation gaps in ground returns in Montmorency by UAV lidar suggest that airborne remote sensing techniques alone may not be sufficient to retrieve a comprehensive snow depth distribution pattern under a coniferous canopy. Therefore, a combination of UAV lidar and ground-based manual measurement or under-and-above canopy UAV lidar (Hyyppä et al., 2020) would be beneficial to obtain more representative and extensive snow depth measurements, however at the cost of increased manual labor. In the event that observational gaps are unavoidable, the interpolation method introduced in Chapter III of this thesis shows significant improvements in the gap-filling of snow depths while considering the spatial variability within canopies in forested environments.

The timing of the UAV lidar survey date also posed another limitation in the study. The dominant predictors identified in this study during near-peak accumulation might differ from those acting during mid-winter, or the melt period. Hence, repeated surveys with UAV lidar to track the temporal evolution of the snowpack would be required to fully address this question in the future. The statistical framework used in this study only provides identification and ranking of predictors associated with driving processes in agro-forested and boreal forested landscapes. Obtaining a complete understanding of the processes would require physically-based modeling.

Another limitation of this study is the availability of a single measurement year for meteorological variables and associated energy fluxes. The original design included two monitoring years, but data gaps from the first winter due to power failure and dysfunctional sensors led to the use of data from only one year. Future analyses are needed to determine if energy partitioning patterns persist over several years and to establish long-term trends in agro-forested environments. During the study period, continuous SWE monitoring at the open and forest sites failed due to sensor malfunction. Concurrent snow depth and SWE measurements (by deploying new passive SWE measuring sensors and snow pit measurements), also providing the snowpack density, would be essential in obtaining a more comprehensive understanding of the snowpack mass balance between the sites in the future.

REFERENCES

Anderson, E. A. (1976). *A point energy and a mass balance model of a snow cover*. Retrieved from NOAA Technical Report NWS 19, USA: https://repository.library.noaa.gov/view/noaa/6392

Andreas, E. L., Horst, T. W., Grachev, A. A., Persson, P. O. G., Fairall, C. W., Guest, P. S., et al. (2010). Parametrizing turbulent exchange over summer sea ice and the marginal ice zone. *Quarterly Journal of the Royal Meteorological Society, 136*(649), 927–943. doi:10.1002/qj.618

Aygün, O., Kinnard, C., Campeau, S., and Krogh, S. A. (2020). Shifting hydrological processes in a Canadian agroforested catchment due to a warmer and wetter climate. *Water, 12*(3), 739. doi:10.3390/w12030739

Aygün, O., Kinnard, C., Campeau, S., and Pomeroy, J. W. (2022). Landscape and climate conditions influence the hydrological sensitivity to climate change in eastern Canada. *Journal of Hydrology, 615*, 128595. doi:10.1016/j.jhydrol.2022.128595

Baños, I. M., García, A. R., Alavedra, J. M. i., Figueras, P. O. i., Iglesias, J. P., Figueras, P. M. i., et al. (2011). Assessment of airborne lidar for snowpack depth modeling. *Boletín de la Sociedad Geológica Mexicana, 63(1)*, 95–107.

Bayesmap Solutions. (2020). *BayesStripAlign 2.1 Software Manual*. Retrieved from Mountain View, CA, USA: http://bayesmap.com/

Bouchard, B., Nadeau, D. F., and Domine, F. (2022). Comparison of snowpack structure in gaps and under the canopy in a humid boreal forest. *Hydrological Processes, 36*(9), e14681. doi:10.1002/hyp.14681

Breiman, L. (2001). Random Forests. *Machine Learning, 45*(1), 5–32. doi:10.1023/A:1010933404324

Brown, R. (2011). Snow. Retrieved March 03, 2019, from The Canadian Encyclopedia https://www.thecanadianencyclopedia.ca/en/article/snow

Brown, R., Tapsoba, D., and Derksen, C. (2018). Evaluation of snow water equivalent datasets over the Saint-Maurice river basin region of southern Québec. *Hydrological Processes, 32*, 2748–2764. doi:10.1002/hyp.13221

Brown, R. D. (2010). Analysis of snow cover variability and change in Québec, 1948–2005. *Hydrological Processes, 24*, 1929–1954. doi:10.1002/hyp.7565

Brown, R. D., Brasnett, B., and Robinson, D. (2003). Gridded North American monthly snow depth and snow water equivalent for GCM evaluation. *Atmosphere-Ocean, 41(1)*, 1–14.

Brown, R. D., and Goodison, B. E. (1996). Interannual variability in reconstructed Canadian snow cover, 1915-1992. *Journal of Climate, 9*, 1299–1318.

Broxton, P. D., Harpold, A. A., Biederman, J. A., Troch, P. A., Molotch, N. P., and Brooks, P. D. (2015). Quantifying the effects of vegetation structure on snow accumulation and ablation in mixed-conifer forests. *Ecohydrology, 8*, 1073–1094. doi:10.1002/eco.1565

Canada, G. o. (2018). State of Canada's forest report. Retrieved March 03, 2019, from Government of Canada https://www.nrcan.gc.ca

Chokmani, K., Bernier, M., and Royer, A. (2013). A merging algorithm for regional snow mapping over eastern Canada from AVHRR and SSM/I data. *Remote Sensing, 5*(11), 5463–5487. doi:10.3390/rs5115463

Chokmani, K., Bernier, M., and Slivitzky, M. (2005). Validation of a method for snow cover extent monitoring over Québec (Canada) using NOAA-AVHRR data. *EARSeL eProceedings, 4(1)*, 106–118.

Clark, M., Hendrikx, J., Slater, A., Kavetski, D., Anderson, B., Cullen, N. J., et al. (2011). Representing spatial variability of snow water equivalent in hydrologic and land surface models: A review. *Water Resources Research, 47*, W07539. doi:10.1029/2011WR010745

Conway, J., Pomeroy, J., Helgason, W., and Kinar, N. (2018). Challenges in modeling turbulent heat fluxes to snowpacks in forest clearings. *Journal of Hydrometeorology, 19*, 1599–1616. doi:10.1175/JHM-D-18-0050.1

Currier, W. R., and Lundquist, J. D. (2018). Snow depth variability at the forest edge in multiple climates in the western United States. *Water Resources Research, 54*(11), 8756–8773. doi:10.1029/2018WR022553

Deems, J. S., Fassnacht, S. R., and Elder, K. J. (2006). Fractal distribution of snow depth from lidar data. *Journal of Hydrometeorology, 7*, 285–297.

Deems, J. S., Painter, T. H., and Finnegan, D. C. (2013). Lidar measurement of snow depth: a review. *Journal of Glaciology, 59*(215), 467–479. doi:10.3189/2013JoG12J154

Dong, C. (2018). Remote sensing, hydrological modeling and in situ observations in snow cover research: a review. *Journal of Hydrology, 561*, 573–583. doi:10.1016/j.jhydrol.2018.04.027

Eitel, J. U. H., Höfle, B., Vierling, L. A., Abellán, A., Asner, G. P., Deems, J. S., et al. (2016). Beyond 3-D: The new spectrum of lidar applications for earth and ecological sciences. *Remote Sensing of Environment, 186*, 372–392. doi:10.1016/j.rse.2016.08.018

Elder, K., Dozier, J., and Michaelsen, J. (1991). Snow accumulation and distribution in an Alpine watershed. *Water Resources Research, 27(7)*, 1541–1552. doi:10.1029/91WR00506

Elder, K., Rosenthal, W., and Davis, R. E. (1998). Estimating the spatial distribution of snow water equivalence in a montane watershed. *Hydrological Processes, 12*, 1793–1808.

Essery, R., Rutter, N., Pomeroy, J., Baxter, R., Stähli, M., Gustafsson, D., et al. (2009). SNOWMIP2 an evaluation of forest snow process simulations. *Bulletin of the American Meteorological Society, 90*(8), 1120–1135. doi:10.1175/2009BAMS2629.1

Fieber, K. D., Davenport, I. J., Tanase, M. A., Ferryman, J. M., Gurney, R. J., Walker, J. P., et al. (2014). Effective LAI and CHP of a single tree from small-footprint full-waveform lidar. *IEEE Geoscience and Remote Sensing Letters, 11(9)*, 1634–1638. doi:10.1109/LGRS.2014.2303500

Geodetics, I. (2019). *Geo-MMS User Manual (Document 20160 Rev B)*. Retrieved from San Diego, CA, USA: https://geodetics.com/

Golding, D. L., and Swanson, R. H. (1986). Snow distribution patterns in clearings and adjacent forest. *Water Resources Research, 22(13)*, 1931–1940.

Grünewald, T., Bühler, Y., and Lehning, M. (2014). Elevation dependency of mountain snow depth. *The Cryosphere, 8*, 2381–2394. doi:10.5194/tc-8-2381-2014

Harder, P., Helgason, W. D., and Pomeroy, J. W. (2018). Modeling the snowpack energy balance during melt under exposed crop stubble. *Journal of Hydrometeorology, 19*(7), 1191–1214. doi:10.1175/JHM-D-18-0039.1

Harder, P., Pomeroy, J., and Helgason, W. (2020). Improving sub-canopy snow depth mapping with unmanned aerial vehicles: Lidar versus structure-from-motion techniques. *The Cryosphere, 14*, 1919–1935. doi:10.5194/tc-14-1919-2020

Harder, P., Schirmer, M., Pomeroy, J., and Helgason, W. (2016). Accuracy of snow depth estimation in mountain and prairie environments by an unmanned aerial vehicle. *The Cryosphere, 10*, 2559–2571. doi:10.5194/tc-10-2559-2016

Harpold, A. A., Guo, Q., Molotch, N., Brooks, P. D., Bales, R., Fernandez-Diaz, J. C., et al. (2014). Lidar-derived snowpack data sets from mixed conifer forests across the Western United States. *Water Resources Research, 50*, 2749–2755. doi:10.1002/ 2013WR013935.

Helgason, W., and Pomeroy, J. (2012). Problems closing the energy balance over a homogeneous snow cover during midwinter. *Journal of Hydrometeorology, 13*, 557–572. doi:10.1175/JHM-D-11-0135.1

Hopkinson, C., Collins, T., Anderson, A., Pomeroy, J., and Spooner, I. (2012a). Spatial snow depth assessment using lidar transect samples and public GIS data layers in the Elbow River watershed, Alberta. *Canadian Water Resources Journal, 37*(2), 69–87. doi:10.4296/cwrj3702893

Hopkinson, C., Pomeroy, J., Debeer, C., Ellis, C., and Anderson, A. (2012b). *Relationships between snowpack depth and primary lidar point cloud derivatives in a mountainous environment.* Paper presented at the Remote Sensing and Hydrology, Jackson Hole, Wyoming, USA, 27–30 September 2010.

Hopkinson, C., Sitar, M., Chasmer, L., and Treitz, P. (2004). Mapping snowpack depth beneath forest canopies using airborne lidar. *Photogrammetric Engineering & Remote Sensing, 70*(3), 323–330.

Hydro-Québec. (2023). How Hydro-Québec installations reduce the impact of spring runoff. Retrieved March 14, 2023 https://www.hydroquebec.com/generation/spring-runoff/

Hyyppä, E., Hyyppä, J., Hakala, T., Kukko, A., Wulder, M. A., White, J. C., et al. (2020). Under-canopy UAV laser scanning for accurate forest field measurements. *ISPRS Journal of Photogrammetry and Remote Sensing, 164*, 41–60. doi:10.1016/j.isprsjprs.2020.03.021

Hyyppä, H., Hyyppä, J., Kaartinen, H., Kaasalainen, S., Honkavaara, E., and Rönnholm, P. (2005). *Factors affecting the quality of DTM generation in forested areas.* Paper presented at the Proceedings of the ISPRS Workshop Laser scanning 2005, Enschede, the Netherlands, 12–14 September 2005.

Jacobs, J. M., Hunsaker, A. G., Sullivan, F. B., Palace, M., Burakowski, E. A., Herrick, C., et al. (2021). Snow depth mapping with unpiloted aerial system lidar observations: a case study in Durham, New Hampshire, United States. *The Cryosphere, 15*(3), 1485–1500. doi:10.5194/tc-15-1485-2021

Jobin, B., Latendresse, C., Baril, A., Maisonneuve, C., Boutin, C., and Côté, D. (2014). A half-century analysis of landscape dynamics in southern Québec, Canada. *Environmental Monitoring and Assessment, 186*(4), 2215–2229. doi:10.1007/s10661-013-3531-6

Jost, G., Weiler, M., Gluns, D. R., and Alila, Y. (2007). The influence of forest and topography on snow accumulation and melt at the watershed-scale. *Journal of Hydrology, 347*, 101–115. doi:10.1016/j.jhydrol.2007.09.006

Kirchner, P. B., Bales, R. C., Molotch, N. P., Flanagan, J., and Guo, Q. (2014). Lidar measurement of seasonal snow accumulation along an elevation gradient in the southern Sierra Nevada, California. *Hydrology and Earth System Sciences, 18*, 4261–4275. doi:10.5194/hess-18-4261-2014

Koutantou, K., Mazzotti, G., Brunner, P., Webster, C., and Jonas, T. (2022). Exploring snow distribution dynamics in steep forested slopes with UAV-borne LiDAR. *Cold Regions Science and Technology, 200*, 103587. doi:10.1016/j.coldregions.2022.103587

Lehning, M., Bartelt, P., Brown, B., Fierz, C., and Satyawali, P. (2002). A physical SNOWPACK model for the Swiss avalanche warning Part II. Snow microstructure. *Cold Regions Science and Technology, 35*(3), 147–167.

Liston, G. E., and Elder, K. (2006). A distributed snow-evolution modeling system (SnowModel). *Journal of Hydrometeorology, 7*, 1259–1276.

Liston, G. E., Haehnel, R. B., Sturm, M., Hiemstra, C. A., Berezovskaya, S., and Tabler, R. D. (2007). Instruments and Methods-Simulating complex snow distributions in windy environments using SnowTran-3D. *Journal of Glaciology, 53(181)*, 214–256.

Lundberg, A., Ala-Aho, P., Eklo, O., Klöve, B., Kværner, J., and Stumpp, C. (2016). Snow and frost: implications for spatiotemporal infiltration patterns – a review. *Hydrological Processes, 30*(8), 1230–1250. doi:10.1002/hyp.10703

Lundquist, J. D., Dickerson-Lange, S. E., Lutz, J. A., and Cristea, N. C. (2013). Lower forest density enhances snow retention in regions with warmer winters: A global framework developed from plot-scale observations and modeling. *Water Resources Research, 49*, 6356–6370. doi:10.1002/wrcr.20504, 2013

Mas, A., Baraer, M., Arsenault, R., Poulin, A., and Préfontaine, J. (2018). Targeting high robustness in snowpack modeling for Nordic hydrological applications in limited data conditions. *Journal of Hydrology, 564*, 1008–1021. doi:10.1016/j.jhydrol.2018.07.071

Mazzotti, G., Currier, W., Deems, J. S., Pflug, J. M., Lundquist, J. D., and Jonas, T. (2019). Revisiting snow cover variability and canopy structure within forest stands: Insights from airborne lidar data. *Water Resources Research, 55*, 6198–6216. doi:10.1029/2019WR024898

Moeser, D., Stähli, M., and Jonas, T. (2015). Improved snow interception modeling using canopy parameters derived from airborne lidar data. *Water Resources Research, 51*, 5041–5059. doi:10.1002/2014WR016724

Morsdorf, F., Kötz, B., Meier, E., Itten, K. I., and Allgöwer, B. (2006). Estimation of LAI and fractional cover from small footprint airborne laser scanning data based on gap fraction. *Remote Sensing of Environment, 104*, 50–61. doi:10.1016/j.rse.2006.04.019

Musselman, K. N., Molotch, N. P., and Brooks, P. D. (2008). Effects of vegetation on snow accumulation and ablation in a mid-latitude sub-alpine forest. *Hydrological Processes, 22*(15), 2767–2776. doi:10.1002/hyp.7050

Painter, T., Berisford, D., Boardman, J., Bormann, K. J., Deems, J., Gehrke, F., et al. (2016). The Airborne Snow Observatory: Fusion of scanning lidar, imaging spectrometer, and physically-based modeling for mapping snow water equivalent and snow albedo. *Remote Sensing of Environment, 184*, 139–152. doi:10.1016/j.rse.2016.06.018

Paquotte, A., and Baraer, M. (2021). Hydrological behavior of an ice-layered snowpack in a non-mountainous environment. *Hydrological Processes, 36*(1), e14433. doi:10.1002/hyp.14433

Parajuli, A., Nadeau, D. F., Anctil, F., and Alves, M. (2021). Multilayer observation and estimation of the snowpack cold content in a humid boreal coniferous forest of eastern Canada. *The Cryosphere, 15*(12), 5371–5386. doi:10.5194/tc-15-5371-2021

Pomeroy, J., Fang, X., and Ellis, C. (2012). Sensitivity of snowmelt hydrology in Marmot Creek, Alberta, to forest cover disturbance. *Hydrological Processes, 26*(12), 1891–1904. doi:10.1002/hyp.9248

Pomeroy, J. W., and Dion, K. (1996). Winter radiation extinction and reflection in a boreal pine canopy: Measurements and modelling. *Hydrological Processes, 10*, 1591–1608.

Pomeroy, J. W., and Granger, R. J. (1997). *Sustainability of the western Canadian boreal forest under changing hydrological conditions-Snow accumulation and ablation.* Paper presented at the Sustainability of Water Resources under Increasing Uncertainty (Proceedings of an international Symposium S1), Rabat, Morocco, 23 April–3 May 1997.

Pomeroy, J. W., and Gray, D. M. (1994). *Sensitivity of snow relocation and sublimation to climate and surface vegetation.* Paper presented at the Snow and Ice Covers: Interactions with the Atmosphere and Ecosystems (Proceedings of Yokohama Symposia), Yokohama, Japan, July 1993.

Pomeroy, J. W., Gray, D. M., Brown, T., Hedstrom, N. R., Quinton, W. L., Granger, R. J., et al. (2007). The cold regions hydrological model: a platform for basing process representation and model structure on physical evidence. *Hydrological Processes, 21*(19), 2650–2667. doi:10.1002/hyp.6787

Pomeroy, J. W., Gray, D. M., Hedstrom, N. R., and Janowicz, J. R. (2002). Prediction of seasonal snow accumulation in cold climate forests. *Hydrological Processes, 16*, 3543–3558. doi:10.1002/hyp.1228

Pomeroy, J. W., Gray, D. M., and Landine, P. G. (1993). The Prairie Blowing Snow Model: characteristics, validation, operation. *Journal of Hydrology, 144*, 165–192. doi:10.1016/0022-1694(93)90171-5

Pomeroy, J. W., Gray, D. M., Shook, K. R., Toth, B., Essery, R. L. H., Pietroniro, A., et al. (1998a). An evaluation of snow accumulation and ablation processes for land surface modelling. *Hydrological Processes, 12*, 2339–2367.

Pomeroy, J. W., Parviainen, J., Hedstrom, N., and Gray, D. M. (1998b). Coupled modelling of forest snow interception and sublimation. *Hydrological Processes, 12*, 2317–2337.

Prévost, M., Barry, R., Stein, J., and Plamondon, A. P. (1991). Snowmelt modeling in a balsam fir forest: Comparison between an energy balance model and other simplified models. *Canadian Journal of Forest Research, 21*, 1–10. doi:10.1139/x91-001

Qin, H., Wang, C., Xi, X., Tian, J., and Zhou, G. (2017). Simulating the effects of the airborne lidar scanning angle, flying altitude, and pulse density for forest foliage profile retrieval. *Applied Sciences, 7*, 712. doi:10.3390/app7070712

Revuelto, J., López-Moreno, J., Azorin-Molina, C., and Vicente-Serrano, S. M. (2015). Canopy influence on snow depth distribution in a pine stand determined from terrestrial laser data. *Water Resources Research, 51*, 3476–3489. doi:10.1002/2014WR016496

Revuelto, J., Vionnet, V., López-Moreno, J., Lafaysse, M., and Morin, S. (2016). Combining snowpack modeling and terrestrial laser scanner observations improves the simulation of small scale snow dynamics. *Journal of Hydrology, 533*, 291–307. doi:10.1016/j.jhydrol.2015.12.015

Richardson, J. J., Moskal, L. M., and Kim, S.-H. (2009). Modeling approaches to estimate effective leaf area index from aerial discrete-return lidar. *Agricultural and Forest Meteorology, 149*, 1152–1160. doi:10.1016/j.agrformet.2009.02.007

Roth, T. R., and Nolin, A. W. (2017). Forest impacts on snow accumulation and ablation across an elevation gradient in a temperate montane environment. *Hydrology and Earth System Sciences, 21*, 5427–5442. doi:10.5194/hess-21-5427-2017

Roth, T. R., and Nolin, A. W. (2019). Characterizing maritime snow canopy interception in forested mountains. *Water Resources Research, 55*(6), 4564–4581. doi:10.1029/2018wr024089

Royer, A., Roy, A., Jutras, S., and Langlois, A. (2021). Review article: Performance assessment of radiation-based field sensors for monitoring the water equivalent of snow cover (SWE). *The Cryosphere, 15*(11), 5079–5098. doi:10.5194/tc-15-5079-2021

Rutter, N., Essery, R., Pomeroy, J., Altimir, N., and Andreadis, K. (2009). Evaluation of forest snow processes models (SnowMIP2). *Journal of Geophysical Research, 114*, Paper 8.

Schirmer, M., and Pomeroy, J. (2020). Processes governing snow ablation in alpine terrain-detailed measurements from the Canadian Rockies. *Hydrology and Earth System Sciences, 24*, 143–157. doi:10.5194/hess-24-143-2020

Sena, N., Chokmani, K., Gloaguen, E., and Bernier, M. (2017). Analyse multi-échelles de la variabilité spatiale de l'équivalent en eau de la neige (EEN) sur le territoire de l’Est du Canada. *Hydrological Sciences Journal, 62(3)*, 359–377. doi:10.1080/02626667.2015.1022552

Sena, Y. N., Chokmani, K., Gloaguen, E., and Bernier, M. (2019). Critical analysis of the snow survey network according to the spatial variability of snow water equivalent (SWE) on eastern mainland Canada. *Hydrology, 6*, 55. doi:10.3390/hydrology6020055

Shaw, T. E., Gascoin, S., Mendoza, P. A., Pellicciotti, F., and McPhee, J. (2020). Snow depth patterns in a high mountain Andean catchment from satellite optical tristereoscopic remote sensing. *Water Resources Research, 56*(2), e2019WR024880. doi:10.1029/2019WR024880

Tarboton, D. G. (1994). *Measurements and modeling of snow energy balance and sublimation from snow*. Retrieved from Utah State University, Logan, USA: https://digitalcommons.usu.edu/water_rep/61

Teufel, B., Sushama, L., Huziy, O., Diro, G. T., Jeong, D. I., Winger, K., et al. (2019). Investigation of the mechanisms leading to the 2017 Montreal flood. *Climate Dynamics, 52*(7), 4193–4206. doi:10.1007/s00382-018-4375-0

Tinkham, W. T., Smith, A. M. S., Marshall, H., Link, T., Falkowski, M., and Winstral, A. (2014). Quantifying spatial distribution of snow depth errors from lidar using random forest. *Remote Sensing of Environment, 141*, 105–115. doi:10.1016/j.rse.2013.10.021

Trujillo, E., Ramı´rez, J. A., and Elder, K. J. (2007). Topographic, meteorologic, and canopy controls on the scaling characteristics of the spatial distribution of snow depth fields. *Water Resources Research, 43*, W07409. doi:10.1029/2006WR005317

Turcotte, B., Burrell, B., and Beltaos, S. (2019). *The impact of climate change on breakup ice jams in Canada: State of knowledge and research approaches*. Paper presented at the 20th Workshop on the Hydraulics of ice Covered Rivers, Ottawa, Ontario, Canada.

Valence, E., Baraer, M., Rosa, E., Barbecot, F., and Monty, C. (2022). Drone-based ground-penetrating radar (GPR) application to snow hydrology. *The Cryosphere, 16*, 3843–3860. doi:10.5194/tc-16-3843-2022

Varhola, A., Coops, N. C., Weiler, M., and Moore, R. D. (2010a). Forest canopy effects on snow accumulation and ablation: An integrative review of empirical results. *Journal of Hydrology, 392*, 219–233. doi:10.1016/j.jhydrol.2010.08.009

Varhola, A., Frazer, G. W., Teti, P., and Coops, N. C. (2012). Estimation of forest structure metrics relevant to hydrologic modelling using coordinate transformation of airborne laser scanning data. *Hydrology and Earth System Sciences, 16*, 3749–3766. doi:10.5194/hess-16-3749-2012

Varhola, A. s., Coops, N. C., Bater, C. W., Teti, P., Boon, S., and Weiler, M. (2010b). The influence of ground- and lidar-derived forest structure metrics on snow accumulation and ablation in disturbed forests. *Canadian Journal of Forest Research, 40*, 812–821. doi:10.1139/X10-008

Wallace, L. O., Lucieer, A., and S.Watson, C. (2012). *Assessing the feasibility of UAV-based lidar for high resolution forest change detection.* Paper presented at the ISPRS Congress, Melbourne, Austrailia, 25 August–1 September 2012.

Webster, R., and Oliver, M. (2007). Geostatistics for environmental scientists, second edition. In. Chichester, England: John Wiley & Sons Ltd.

Whitfield, P. H., and Cannon, A. J. (2000). Recent variations in climate and hydrology in Canada. *Canadian Water Resources Journal, 25(1)*, 19–65. doi:10.4296/cwrj2501019

Winkler, R. D., Spittlehouse, D. L., and Golding, D. L. (2005). Measured differences in snow accumulation and melt among clearcut, juvenile, and mature forests in southern British Columbia. *Hydrological Processes, 19*, 51–62. doi:10.1002/hyp.5757

Woods, S. W., Ahl, R., Sappington, J., and McCaughey, W. (2006). Snow accumulation in thinned lodgepole pine stands, Montana, USA. *Forest Ecology and Management, 235*, 202–211. doi:10.1016/j.foreco.2006.08.013

Zahmatkesh, Z., Kumar Jha, S., Coulibaly, P., and Stadnyk, T. (2019). An overview of river flood forecasting procedures in Canadian watersheds. *Canadian Water Resources Journal / Revue canadienne des ressources hydriques, 44*(3), 213–229. doi:10.1080/07011784.2019.1601598

Zheng, Z., Kirchner, P. B., and Bales, R. C. (2016). Topographic and vegetation effects on snow accumulation in the southern Sierra Nevada: A statistical summary from lidar data. *The Cryosphere, 10*, 257–269. doi:10.5194/tc-10-257-2016

Zheng, Z., Ma, Q., Jin, S., Su, Y., Guo, Q., and Bales, R. C. (2019). Canopy and terrain interactions affecting snowpack spatial patterns in the Sierra Nevada of California. *Water Resources Research, 55*(11), 8721–8739. doi:10.1029/2018wr023758

Zheng, Z., Ma, Q., Qian, K., and Bales, R. C. (2018). Canopy effects on snow accumulation: observations from lidar, canonical-view photos, and continuous ground measurements from sensor networks. *Remote Sensing, 10*, 1769. doi:10.3390/rs10111769